

## Dissertation

# Hot deformation and properties of PRTi alloys

ausgeführt zum Zwecke der Erlangung des akademischen Grades eines Doktors der technischen Wissenschaften unter der Leitung von

o. Univ. Prof. Dr. H. P. Degischer  
E308

Institut für Werkstoffwissenschaft und Werkstofftechnologie

eingereicht an der Technischen Universität Wien

**Fakultät für Maschinenwesen und Betriebswissenschaften**

von

Dipl. Ing. M. Cecilia Poletti

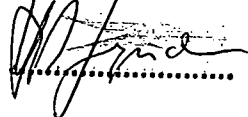

Matr. Nr.: 0027173

Burggasse 93/14  
A-1070. Wien

Wien, am 18. Juli 2005

  
Cecilia Poletti

Diese Dissertation haben begutachtet:

 .....  
 .....

Nada está perdido si se tiene por fin el valor de proclamar  
que todo está perdido y que hay que empezar de nuevo.

(Julio Cortázar)

## **Acknowledgments.**

First of all, I would like to thank to Prof. H. P. Degischer for his scientific and human support along these three years. Without his invaluable experimental suggestions, hours dedicated to discussions, help to clarify the most important concepts combined to an easygoing atmosphere this work would not be possible.

Thanks of course to Prof. Julio Vivas Hohl, for helping me in the initial and hard steps of this long travel to Europe, and for showing me, 5 years ago, new perspectives of my career.

I am also very grateful to Prof. B. Buchmayr for accepting to read this work, and for the interesting comments and suggestions to it.

The financial support from Böhler Schmiedetechnik (Kapfemberg, Austria) through the Austrian Aeronautic Research Network, and the meetings and discussions with Dr. W. Marketz and Dr. S. Kremmer made also possible this work.

I will not forget the help of my colleagues from this and other institutes. Thanks to: Heide and Jana Knoblich for the long hours in front of my samples; Zoran Ignjatov for the whole chapter of dilatometry, the hard work, and the discussions; C. Zaruba for knowing the secrets of Mr. B. Gates; Dr. A. Merstallinger for the wear tests in ARCS; Dr. Th. Schubert for the trails on the SiC reinforced materials in IFAM, Dresden; C. Heering for the compression tests in RWTH Aachen, A. Lasagni and C. Holzapfel for the EBSD tests, and J. Castillo and C. Stocker for the nice pictures after IBE in ECHEM. Thanks also to the Mercosur colegas!

Thank you my friends, the ones who are here: the people from the WGs in the Lederer(Peter)-Laudon(Dani)-Schopenhauer(Guille)gasse and from the ex-Hörnesgasse WG and the visitors who virtually live there, and the others friends who always are...: Kurt, Sil, Fernanda, Adri, Sergio, Sole, Gabi, and la banda completa. Thank you for holding me, for hearing me and for sharing with me a piece of your lives.

Finally but not less important, I would like to thanks to my family: ma, pa and Diego and my love Fer, for the force and the love that you always gave me, and for your thrust.

## Kurzfassung.

Die Konzeption eines neuen Verbundwerkstoffes erfordert Modelle, es erlauben, die Erreichbarkeit gewünschter mechanischer Eigenschaften ab zu schätzen. Zusätzlich wissen die Parameter der industriellen Fertigungen, Sekundärprozessen in Betracht gezogen werden.

In dieser Arbeit wird das Verbesserungspotential einiger mechanischer Eigenschaften (Steifigkeit, Fließgrenze, Stauchwiderstand) und der Verschleißbeständigkeit von Ti-Legierungen durch die Zugabe von Teilchenverstärkungen untersucht. Die Warmverformbarkeit der Teilchenverstärkten Materialien wird gegenüber den unverstärkten wesentlich erschwert, weshalb Warmstauchversuche bei verschiedenen Temperaturen und Verformungsgeschwindigkeiten untersucht wurden.

Zwei Beispiele neuer Titanmatrixverbundwerkstoffes, die durch Pudermetallurgie hergestellt wurde. Unverstärkte Ti-6Al-6V-2Sn und mit 12 und 20% TiC Teilchen, sowie unverstärkte Ti-6Al-4V und mit 12% TiC Teilchen verstärkt wurden geprüft.

Druckversuche bei hohen Temperaturen (650-950°C) wurden mit einer Gleeble ® 1500 Maschine und einer SERVOTEST-Maschine durchgeführt, um die Deformationsmechanismen der Materialien zu studieren und die *Processing maps* und die Instabilitätsdiagramme zu ermitteln, die mit den Dynamischen Material Modell (DMM) und den modifizierten DMM errechnet wurden.

Die E-Module der Werkstoffe wurden bis 350°C ermittelt, wobei eine Verbesserung der Steifigkeit beobachtet wurde, wenn der Prozentsatz der keramischen Teilchen erhöht wurde.

Die Verstärkung von Ti662 mit TiC Teilchen (12 und 20%vol) verbessert deutlich die Druckfestigkeit bei hohen Temperaturen.

Pin on ring Versuche der Titanlegierungen gegen Stahl als Gegenstückmaterial zeigte eine geringe Verbesserung der Verschleißwiderstand bei niedrigen Drücken durch die Hinzufügung der TiC Partikel.

Aufgrund von herstellungsbedingten Defekten ergibt die mit SiC Partikeln verstärkte Ti64 Legierung keine Eigenschaftsverbesserung.



## **Abstract.**

The design of a new composite material requires models to estimate the achievability of the desired mechanical properties. In addition, processing considerations such as method, parameters and secondary processing have to be taken into account.

In this work, the potential improvement of some mechanical properties (stiffness, yield strength, compression strength) and of the wear resistance of Ti-alloys by adding ceramic particles is investigated. The hot formability of particle reinforced Ti is expected to be limited and therefore has been tested by hot compression tests.

Two examples of new titanium matrix composite produced by powder metallurgy were studied. Ti6Al-6V-2Sn unreinforced and reinforced with 12 and 20% of TiC particles as well as Ti6Al-4V unreinforced and reinforced with 12% of TiC particles were tested.

Compression tests at high temperatures (650-950°C) were carried out with a Gleeble ® 1500 machine and a SERVOTEST machine in order to study the deformation mechanisms of the materials and to obtain the processing and the instability maps calculated with the Dynamic Materials Model (DMM) and the modified DMM.

The Young's moduli of the materials were determined up to 350°C, and significant improvement of the stiffness was observed with increasing the percentage of ceramic particles added.

The reinforcement of Ti662 with TiC particles (12 and 20%vol) improves markedly the compressive strength at high temperatures as well.

Pin on ring tests of the titanium alloys using steel as a counterpart material showed a slight improvement of the wear resistance at low pressures by the addition of TiC particles.

Owing to processing defects, the properties of Ti64 reinforced with SiC particles are not promising.

# Index

<b>1</b>	<b>Introduction.</b>	<b>1</b>
<b>2</b>	<b>State of the Art.</b>	<b>4</b>
2.1	Titanium alloys.	4
2.1.1	Titanium Applications.	4
2.1.2	Alpha-beta transformation.	6
2.2	Metal matrix composites.	9
2.2.1	Classification of the MMCs.	9
2.2.2	Processing methods.	9
2.2.3	Composite mechanics.	13
2.2.4	Strengthening mechanisms of the particulate composites.	13
2.2.5	Titanium Matrix composites.	15
2.3	Thermomechanical concepts.	17
2.3.1	Deformation maps.	17
2.3.2	Thermodynamics.	18
2.3.3	Dynamic Materials Model (DMM).	18
2.3.4	Modified DMM.	21
2.4	Behaviour at high temperatures.	23
2.4.1	Deformation at high temperatures.	23
2.4.2	Hot compression tests.	24
2.5	Objectives of this work.	25
<b>3</b>	<b>Experimental.</b>	<b>26</b>
3.1	Materials.	26
3.1.1	Materials description.	26
3.1.2	Production methods.	27
3.1.3	Density measurements.	29
3.1.4	Reinforcing titanium alloys with SiC particles.	30
3.2	Metallography.	30
3.2.1	Sample preparation.	30
3.2.2	Microscopy.	31
3.2.3	Ion Beam Etching (IBE).	32
3.2.4	Microhardness.	32
3.3	Image Analysis.	33
3.4	EBSD.	34
3.5	Diffractionmetry.	34
3.6	Dilatometry.	35
3.6.1	Equipment.	35
3.6.2	Tests.	35

3.6.3	Limitations of the technique.....	36
3.6.4	Calculation of the CTE.....	38
3.7	Dynamical Mechanical Analysis.....	39
3.7.1	Equipment and Young's Modulus.....	39
3.7.2	DMA Tests.....	40
3.8	Hot compression tests.....	40
3.8.1	Gleeble® 1500.....	40
3.8.2	SERVOTEST TMTS Test System.....	41
3.8.3	Parameters and tests.....	41
3.9	Wear tests.....	43
3.9.1	Description of the equipment.....	43
3.9.2	Surface and subsurface studies.....	43
3.9.3	Wear rate and friction coefficient.....	44
<b>4</b>	<b>Results.....</b>	<b>45</b>
4.1	Microstructure features.....	45
4.1.1	As received.....	45
4.1.2	Ion Beam Etching pictures.....	48
4.1.3	SiC reinforced Ti64.....	50
4.1.4	Microstructures after heat treatments.....	55
4.1.5	Microstructures after deformation.....	56
4.1.6	Microstructure during dilatometry.....	70
4.2	Microhardness.....	71
4.3	Image Analysis.....	72
4.4	EBSD.....	74
4.5	Diffractionmetry.....	75
4.6	Dilatometry Results.....	78
4.6.1	Change in length.....	78
4.7	Young's modulus.....	84
4.7.1	Dependence of the Young's modulus with the orientation.....	86
4.8	Compression tests.....	87
4.8.1	Flow curves.....	87
4.8.2	Maximum Strength.....	93
4.8.3	Temperature changes.....	95
4.8.4	Effect of holding time at 650°C.....	97
4.8.5	Effect of holding time at 900°C.....	98
4.8.6	Effect of holding time at 1000°C.....	98
4.9	Wear rate and friction.....	99
4.9.1	Wear rate and friction coefficient results.....	99

4.9.2	Worn surfaces .....	102
4.9.3	Topography .....	107
<b>5</b>	<b>Interpretation of the results.....</b>	<b>109</b>
5.1	Microstructure features.....	109
5.1.1	SiC reinforced material .....	109
5.1.2	Globular and lamellar microstructures .....	109
5.1.3	Alpha beta changes .....	110
5.2	Trials of a new material .....	111
5.3	Young's modulus.....	112
5.4	Deformation mechanisms. ....	114
5.4.1	Dynamic Materials Model and modified Dynamic Materials Model.....	114
5.4.2	Processing and instability maps. ....	115
5.5	Wear mechanisms.....	127
<b>6</b>	<b>Discussion. ....</b>	<b>130</b>
6.1	Analysis of the experimental methods.....	130
6.1.1	Alpha-beta quantification with Image Analysis. ....	130
6.1.2	Dilatometry .....	130
6.1.3	Gleeble vs. Servotest. ....	131
6.2	Deformation behaviour.....	132
6.2.1	Ti662 Ingot: globular microstructure. ....	132
6.2.2	Ti662 PM: lamellar microstructure. ....	137
6.2.3	Ti64 PM alloy: lamellae microstructure.....	140
6.2.4	Composites. Influence of the TiC particles in the deformation behaviour.....	141
6.2.5	Dynamic material model and modified DMM. ....	147
6.2.6	Considerations for forging. ....	147
6.3	Wear mechanisms.....	149
6.3.1	Running-in state. ....	149
6.3.2	Steady state .....	150
6.3.3	Wear behaviour. ....	151
6.3.4	Interface damage .....	152
6.3.5	TiC influence.....	152
6.4	Young's modulus.....	153
6.5	Alpha beta transformations.....	154
6.6	Trials on the production of a new material.....	155
<b>7</b>	<b>Conclusions. ....</b>	<b>156</b>
<b>8</b>	<b>References. ....</b>	<b>158</b>

# 1 Introduction.

Titanium alloys show high specific properties (e.g., strength/density, modulus/density) up to high temperatures, and corrosion resistance, that make them attractive not only for aerospace components, but also for automotive, industrial and medical applications [1,2].

Ceramic reinforcement can further improve some mechanical properties, and the wear resistance, which is very poor for titanium alloys in general [3]. The goal of Ti matrix composite development here is to improve the thermo-mechanical and tribological properties of the titanium alloys.

Figure 1 shows in an Ashby diagram [4, 5] the specific stiffness of a tensile/compression rod ( $E/\rho$ ) and of a bending beam ( $\sqrt{E/\rho}$ ) of the commercial structural alloys compared to the titanium alloys reinforced with ceramic particles, and SiC monofilaments (transverse and parallel to the direction of the fibres).

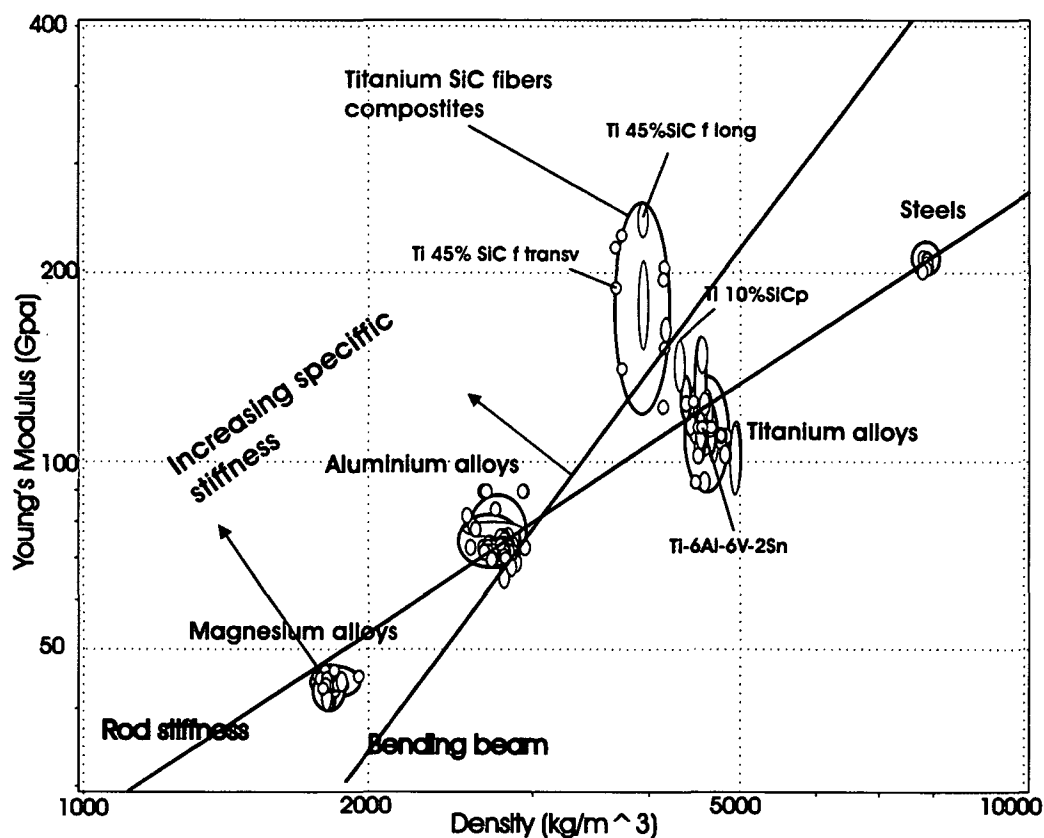


Figure 1. Theoretical comparison of the specific stiffness of Ti alloys with that of Ti matrix composites reinforced with particles and fibres as well as with those of steel, magnesium and aluminium alloys [4, 5].

The specific moduli of the composites are markedly higher than for the unreinforced materials. What's more, the improvement of the specific stiffness given by the addition of SiC particles is more significant than that given by the TiC particles. In the diagram, the specific bending stiffness of TiC/SiC/20p is approaching that of Al – alloys to 95%.

An increase in strength at room temperature was also observed in previous works with different particulate reinforced Titanium composites [6, 7].

Figure 2 shows the specific tensile strength vs. specific Young's modulus for light alloys, steels and titanium matrix composites, showing that the titanium matrix composites have high performance.

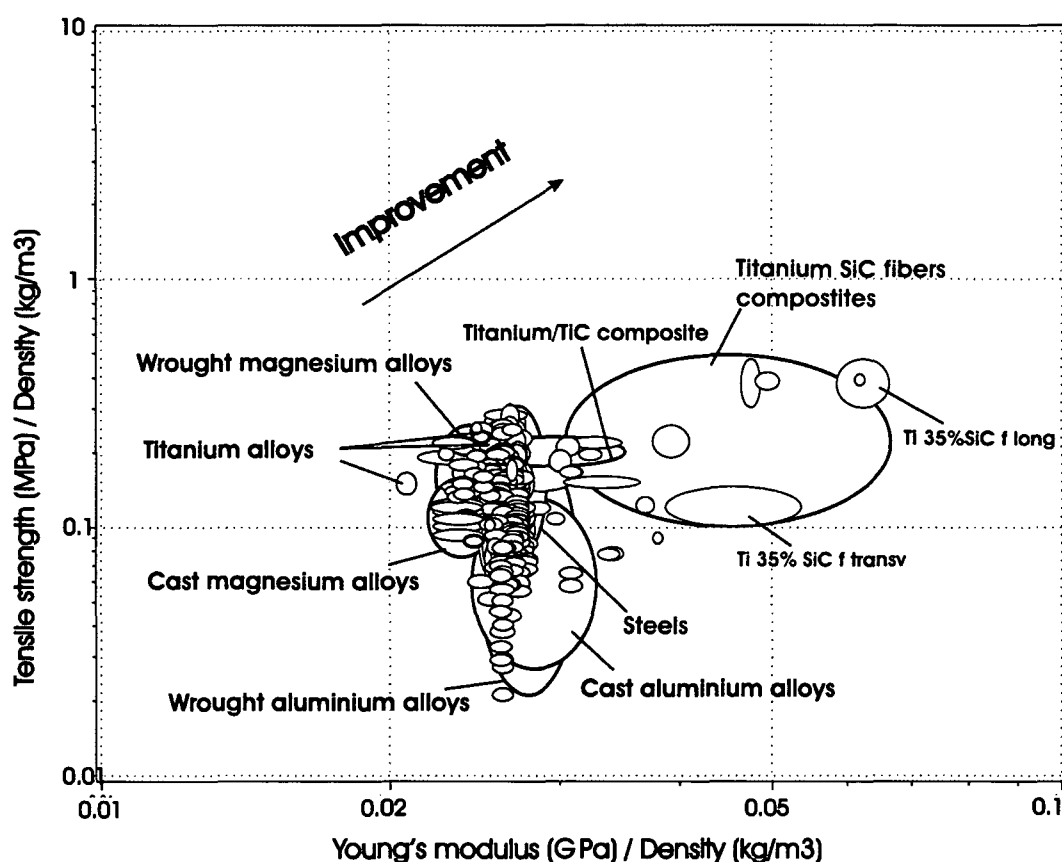


Figure 2. Specific tensile strength as a function of the specific elastic modulus for light alloys (magnesium, aluminium and titanium alloys), steels and titanium matrix composites [4, 5].

The wear resistance should also be improved, depending on the wear conditions, due to the high hardness of the ceramic particles. In the case of aluminium alloys, the addition of 10-20% of SiC particles yielded higher wear resistance than bearing steel [8]. On the other hand, the ductility is not expected to be as good as for the conventional titanium alloys, and this point will be also discussed in this work, as well as the optimal forging parameters of unreinforced and reinforced Ti662.

In Chapter 2, the basic, mechanical and descriptive concepts related to titanium alloys and metal matrix composite (MMCs) are exposed.

Chapter 3 describes the equipment and the materials used, as well as the experimental procedures applied.

The resulting flow curves, wear rates and friction values, the Young's moduli and the metallographs are shown in Chapter 4.

In Chapter 5 the deformation behaviour presented by the stability and processing maps comparing the Prasad et al model to the Nageswara Rao et al model. The wear and friction results are plotted as isovalues in order to illustrate the influence of the sliding speed and of the load. Some other physical and mechanical properties are correlated here.

The discussions of the deformation and wear mechanisms and of the alpha-beta transformations are presented in Chapter 6. In this chapter are exposed the advantages and disadvantages of each experimental method. Furthermore, the influence of the ceramic particles in the elastic modulus, the deformation and the wear behaviour was analysed.

The whole work is closed in the Chapter 7 with the conclusions.

## 2 State of the Art.

### 2.1 Titanium alloys.

Titanium is the fourth most abundant structural metal in the earth, after aluminium, iron and magnesium. Its name was taken from the Titans, the elder and powerful gods in the Greek mythology. Titanium can be found as  $\text{TiO}$  and  $\text{FeTiO}_3$ , and the most common extraction of titanium nowadays is made via  $\text{TiCl}_4$  using the Kroll process described elsewhere [9]. Although the material is expensive due to high effort in energy to convert  $\text{TiO}$  into the pure metal, some new developments are been studied in order to decrease its price [10,11], which is the main marketing limit.

#### 2.1.1 Titanium Applications

Because of their high specific strength and stiffness, and creep resistance, the main applications of titanium alloys are airframes and aeroengines [12]. The planes Boeing 7E7 and Airbus 380 (Figure 3a)) have reached percentages of titanium of about 15% and 10% [13] respectively.



**Figure 3.** Aerospace and automobile applications a) Airbus 380 with almost 10% of titanium b). satellite developed by United Titanium Inc. c) suspension springs: titanium (right) compared to steel (left) on a balance.

Titanium alloys are also good candidates for space applications [14, 15] (Figure 3 b)), where light weight is required to decrease the high costs in combustible; it is possible to save up to 54000 € in the combustible costs per reduced kg of weight. Potential parts have been identified in the automotive engine area [16, 17], such as valves, valve springs and connecting rods, pipes and the exhaust system and in the car body area, bolts, fasteners, suspension springs Figure 3c), are made of titanium alloys and titanium aluminides.



Titanium's corrosion resistance, low weight and high strength make it a material ideally suited for long life cycle (LLC) offshore applications. Titanium does not corrode in seawater and therefore benefits from a lower maintenance cost and extended periods between downtime.

Due to their high biocompatibility [18, 19], Commercial Pure (CP) titanium and vanadium free titanium alloys are widely used in the medical field mostly for bone replacement implantations and surgery tools (Figure 4a)) as well as the spectacle frames. Sports requiring high strength materials and light weight represent also a good market for titanium based materials, such as goods for golf, cycling and tennis (Figure 4 b) and c)).

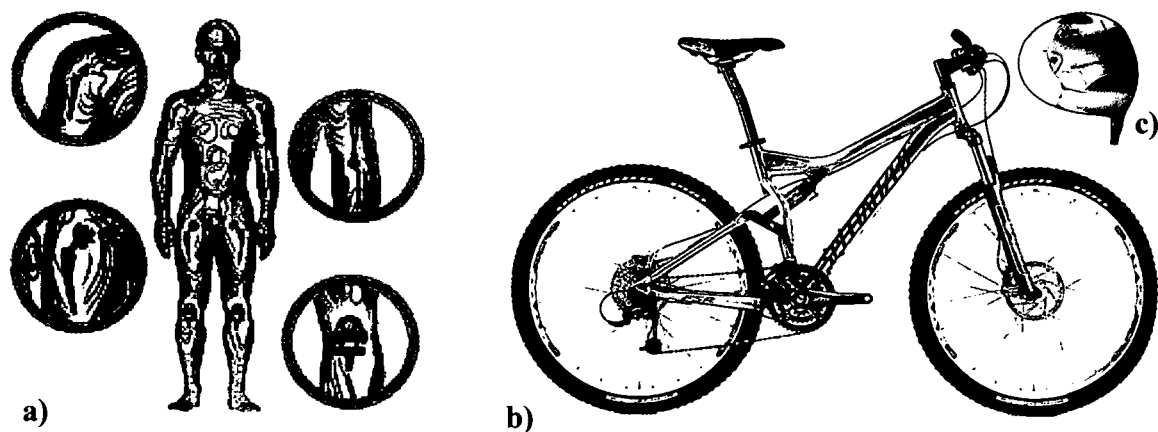


**Figure 4. Health and sports: a) Typical titanium implants b) bicycle frame and c) golf wedge.**

Chemical and Energy producer industries, where corrosion and creep resistance and high strength at high temperatures are required, find some of their materials solutions with the titanium alloys such as the industrial boiler made of titanium alloy showed in Figure 5a).

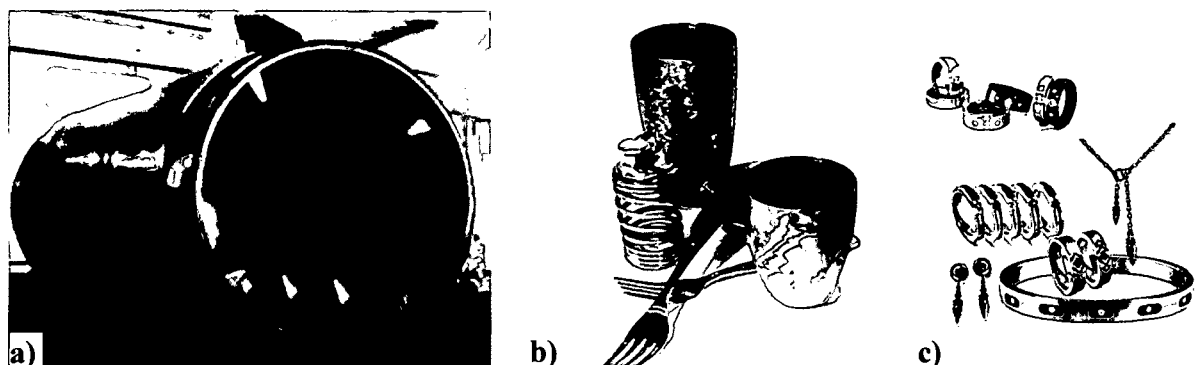


**Figure 5. a) Chemical industry applications: boiler (Fenggang Titanium Equipment) b) cutlery and beakers (Edward Rosenberg designs) and c) jewels (Edward Mirell collection).**

Finally, structural applications such as exterior walls and roofing material have emerged as a new market for titanium, and the Guggenheim-Bilbao, in Spain, and the Fukuoka Dome, in Japan, are

good examples. Titanium has also taken place in the new jewel generation, the design and the art world, as shown in Figure 5b) as the result of the possibility to create nice and colourful surfaces by oxidation [20]. The golden appearance of TiN is well known.

### **2.1.2 *Alpha-beta transformation.***

Titanium exists in two crystal structures: hexagonal close-packed (hcp) called alpha phase ( $\alpha$ ) and beta phase ( $\beta$ ), which has a body-centred cubic (bcc) structure [2].

The phase transformation temperature is known as the beta transus temperature above which, the  $\alpha$  phase is transformed completely into the  $\beta$  phase.

For pure titanium, the cell parameters are: alpha,  $a = 0.295\text{nm}$ ,  $c=0.468\text{nm}$  (at  $25^\circ\text{C}$ ), and beta,  $a=0.331\text{ nm}$  (at  $900^\circ\text{C}$ ) [21]. The transformation of the bcc  $\beta$  phase to the hexagonal  $\alpha$  phase can either occur martensitically, at higher cooling rate or by diffusion controlled nucleation and growth process, at lower cooling rate [12] at a temperature of  $882^\circ\text{C}$ . As the hexagonal phase is less dense than the beta phase at the same temperature, then the phase transformation from beta into alpha results in an expansion of the volume of about 0.1% [22]. An in-situ SEM- EBSD study [23] concluded that the transformation of alpha into beta in commercially pure titanium nucleates and grows at and along the alpha grain boundaries as allotriomorphs (a crystal that does not reflect its internal crystalline symmetry) and within the alpha grains as plates. Furthermore, the phase transformation results in a large grained microstructure with a near-equilibrium triple junction arrangement ( $120^\circ$ ). Finally, the resulting texture of the beta phase can be correlated directly with that of the alpha phase.

According to its allotropy, the alloying elements of titanium are usually classified into alpha or beta stabilizers (Figure 6), depending on if they increase or decrease the beta transus temperature. The phase transformation in the alloys does not occur at a defined temperature, but via a two-phase region, and the diffusion of the alloying elements can control the alpha-beta transformation kinetics which proceeds from nucleation to diffusion controlled growth and ripening.

The  $\alpha$  stabilising elements tend to preferentially concentrate in the  $\alpha$  phase and raise the  $\beta$  transus. The beta-stabilisers can be subdivided into  $\beta$ -isomorphous and  $\beta$ -eutectoid forming elements. Commercial titanium alloys are classified into  $\alpha$ , near- $\alpha$ ,  $\alpha+\beta$ , near- $\beta$  and  $\beta$  alloys, with different contributions of the  $\alpha$  and  $\beta$  phases to their microstructures.

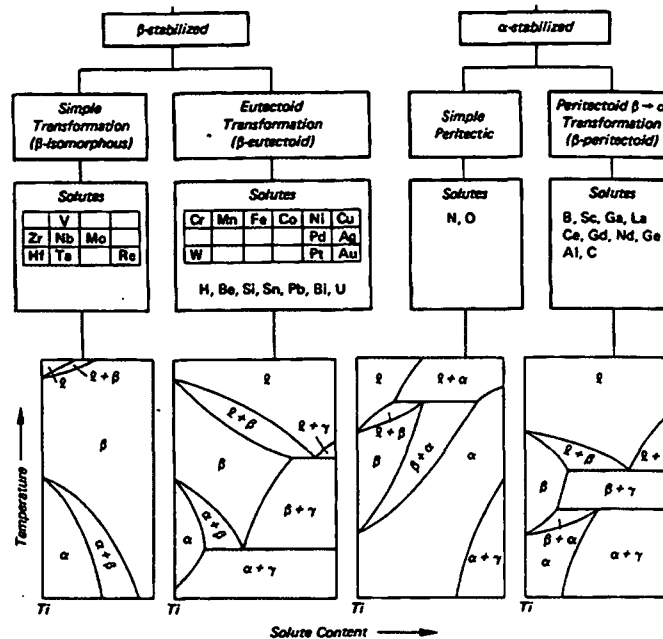


Figure 6. Effect of alloying elements on the phase diagrams of titanium alloys [24].

The most widely used titanium alpha-beta alloy is the Ti-6Al-4V (Ti64), which presents high specific strength, thermal stability up to 400°C, excellent machinability, good weldability and good corrosion resistance [24].

Ti6Al6V2Sn (Ti662) is a higher strength version of the Ti64 [24] and it is used in applications requiring higher strength at temperatures up to 315°C where the use is limited to secondary structures and the strength efficiency is minimized by lower fracture toughness.

For titanium alloys, the phase transformation kinetics depends on the diffusion coefficients of the alloys elements and the transformation is not from  $\alpha$  into  $\beta$ , but from  $\alpha + \beta$  into  $\beta$ . A model for Ti64 was proposed by Szkiliniarz and Smolka [22] in order to determine the grade of transformation ( $p$ ) with the temperature, the changes in the cell parameters of each phase, the specific volume of the phases, and the transformation volume effect. During transformations of  $\alpha + \beta$  into  $\beta$ , the V content in beta changes from 28% at room temperature to 4,5% according to the solubility limits of the phase diagram. Figure 7 shows the semi-binary phase diagram of Ti4Al and V [2], where the abrupt variation of the V in the beta phase during phase transformation above 650°C is observed. On the other hand, the specific volume of the beta phase increases by decreasing the V content. Using the rule of mixtures proposed by Smolka, and the value of cell parameter for the vanadium of  $a = 0.3040\text{nm}$  and  $a = 0.32763\text{nm}$  for beta titanium at room temperature, then a volume variation up to 2% is expected when the vanadium content is decreased due to the phase transformation.

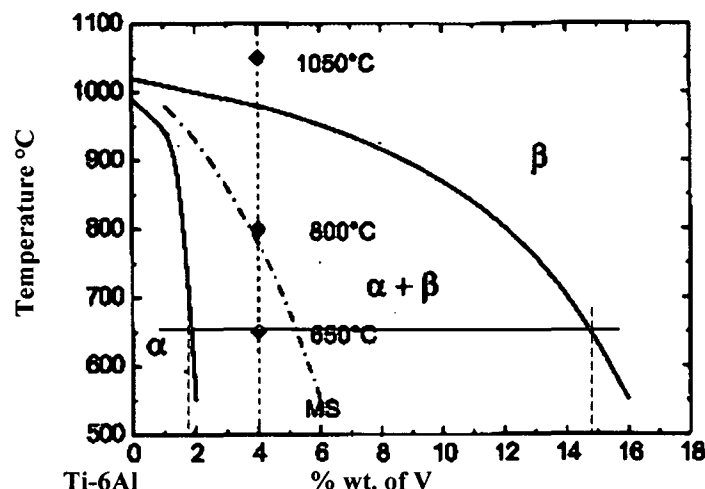


Figure 7. Cut of ternary diagram Ti-Al-V at 6% wt. Al. Following the horizontal line and using the lever rule at 650°C is possible to find up to 15% wt of V in the beta phase, and less than 2% wt in the alpha phase [2]

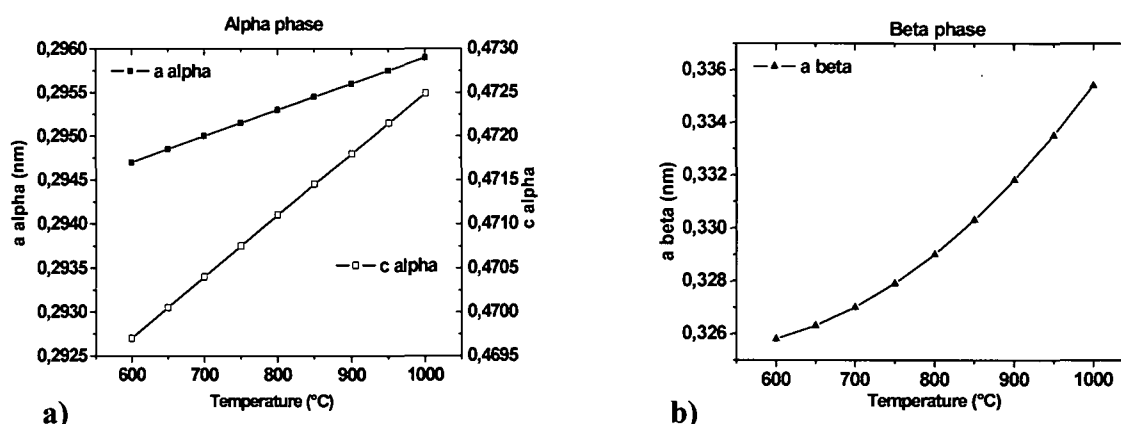


Figure 8 Cell parameters as a function of temperature for a)  $\alpha$  phase and b)  $\beta$  phase [22]

The results of the cell parameters using this model are shown in Figure 8 a) and b). Figure 9 shows the volume variation of both phases and of the alloys (full line). A total volume variation of -0,77% was observed due to the transformation at 6K/min of heating rate. These results [22] were also confirmed using dilatometry by Ignjatov [25].

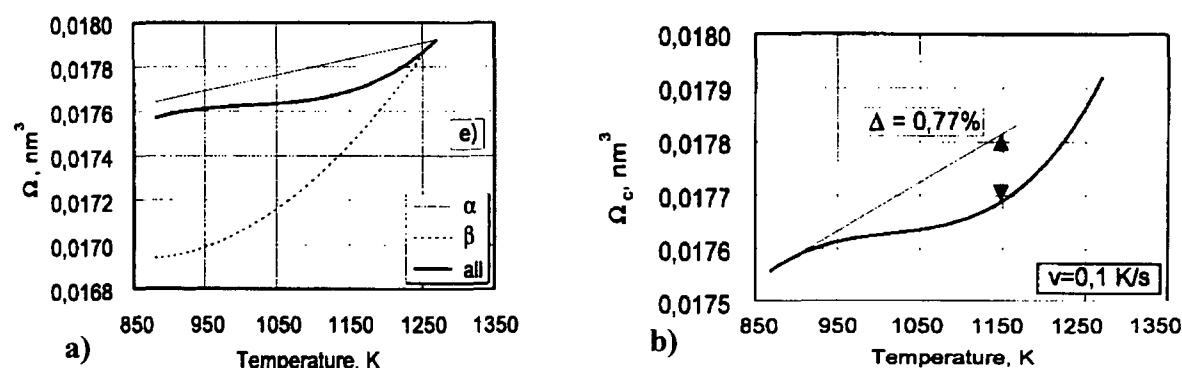


Figure 9. Volume variations as a function of the temperature [22], showing a) the changes in the alpha and beta phases at 6K/min of heating rate and b) changes in the volume of -0,77% when transforming into beta

## 2.2 Metal matrix composites.

The metal matrix composite (MMC) is defined as a material produced by the mixture of at least two components: one metallic, and the other/s non metallic (commonly ceramics). The metallic component is then the continuous system, called matrix, where the reinforcement is the embedded system.

### 2.2.1 Classification of the MMCs.

The MMCs can be classified according to the form of the reinforcement (Figure 10):

- *Continuous fibre reinforcement*: If the fibres are embedded in the matrix uni-directionally, the composite properties are anisotropic. Depending on the diameter, the reinforcements are known as continuous fibres available in tows of single fibres with diameters less than  $30\mu\text{m}$  or monofilaments with diameters larger than  $100\mu\text{m}$ . The strengthening is basically done by longitudinal global load transfer and transverse similar to PRM.
- *Discontinuous reinforcement*: short fibres, whiskers and particles are the most common discontinuous reinforcements. The strengthening is basically done by load transfer in the case of the fibres and due to the internal stresses provoked by the CTE mismatch between the reinforcement and the matrix. A modification of the microstructure of the matrix by the reinforcement has to be considered as well. If the fibres or whiskers are randomly oriented, the properties are isotropic, like they are with particle reinforcements.

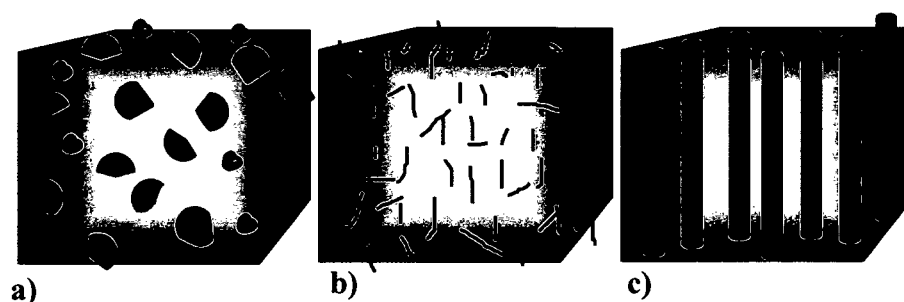


Figure 10. Types of reinforcement in the MMCs: discontinuous: a) particulate (PRM) and b) short fibres (SFRM) or whiskers (WRM) and c) continuous monofilaments (MFRM).

### 2.2.2 Processing methods

The selection of the adequate fabrication processes for a specific metal matrix composite is governed by the type of the reinforcement, the component size and shape, the physical properties, the matrix and the desired microstructure of the final product.

The processing methods can be divided according to the physical state of the matrix as follows:

- *Liquid phase.* The at least partially molten metal matrix is brought into contact with the reinforcement. Surface tensions as well as chemical reaction between both ingredients sometimes have to be controlled (non wetability or contact times at high temperatures respectively), when porous and/or brittle reaction products can be produced.

1) *Slurry casting.* The cheapest and easiest way to produce MMC is to stir mix the liquid metal with solid ceramic particles and then to solidify the mixture. Some problems inherent to the method make it practicable only for some particulate reinforced materials [26, 27]. The increase of viscosity on adding solid could be really severe, and particularly for ceramic fibres. The concept of rheocasting (compocasting for composites) is based on a semisolid of  $> 40\%$  of liquid metal, and the result is an increase of the viscosity no more than a factor of two by the addition of 25% of ceramic particles. Other problems such as inhomogeneities produced by particle agglomeration and sedimentation in the melt, gas bubble entrapment, porosity, particle segregation, and interfacial reaction usually cause low performance of the resulting material [28, 29].

2) *Infiltration of preform.* The molten metal is made to fill, spontaneously or using external mechanical work, pores within a preform of the reinforcement. In the spontaneous infiltration the matrix penetrates spontaneously the preform without added force, while the in the forced infiltration the application of mechanical force onto matrix or reinforcement is required. Some forced processes can be listed:

- a) *Pressure infiltration.* A hydrostatic pressure is applied onto the molten matrix surface to drive the liquid into the preform.
- b) *Vacuum infiltration.* A hydrostatic pressure of one bar applied by the atmosphere onto the molten matrix drives it into an evacuated preform.
- c) *Gas pressure infiltration:* a pressure infiltration process which uses pressurized gas to apply pressure on the metal surface driving the liquid into a preform.
- d) *Squeeze casting.* The squeeze casting consists in moving the liquid metal in laminar flow into a mould by pressure using a single hydraulically activated ram. The final product shows in general a fine microstructure and low porosity. The squeeze infiltration uses the same principle, but applied to MMC, where the liquid metal is injected into the interstices of an assembly of reinforcement called perform.

3) *Spray deposition.* A stream of metallic droplets is impinged on the reinforcement to build up a composite. The resultant material can contain pores, a low content of oxides and

inhomogeneities in the reinforcement distribution [30]. A following consolidation process reduces porosity.

- *Solid phase.* Solid phase method requires normally fine metal powders; but the increment on the price is exponential to the decrement of the powder size.

1) *Powder consolidation.* This method is mostly used for particulate reinforcements [31], because the fibres and even the whiskers tend to persist in the form of tangled agglomerates with interstitial spaces far too small for the penetration of metallic powder. The powder blending is carried out dry or in a liquid suspension, such as glycerine, or water.  $\text{Al}_2\text{O}_3$  balls can be used to break the oxide layer and also to produce the mechanical alloy (milling) [32, 33]. According to Cocks [34] the manufacturing process for powder metallurgical components can be divided into: filling die, powder transfer, powder compaction, ejection, sintering and machining. After filling the die, the powder is transferred within the die through a series of tool motions to produce a compact approaching to the final shape. In the compaction process there is first a rearrangement of the particles, then the metallic particles deformed plastically (open pores), and in the final stage the network of interconnected channels pinch off to form a distribution of isolated pores. The ejection of the green part from the die results in the relaxation of the constraints and can result in the distortion of the part from the die geometry due to elastic spring back. The sintering of the green parts is made normally in a reducing furnace and this results in the particles bonding together and the closing of the pores by diffusion. In studies of the fundamentals of sintering, dimensional changes are determined as the difference of dimensions between green and sintered compacts [35]. The transition in microstructure from that of a green compact to that of a well-sintered compact is a function of sintering temperature and time (Figure 11 [36]).

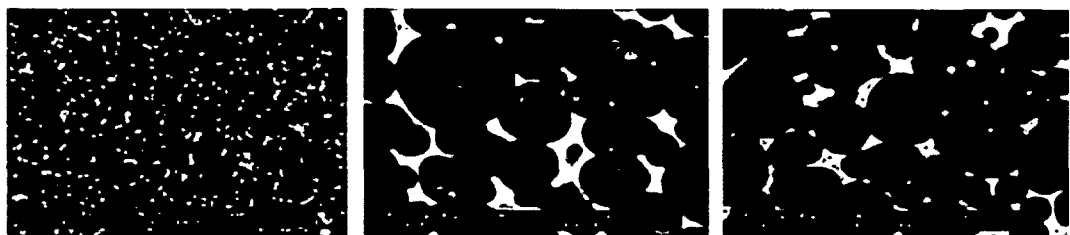
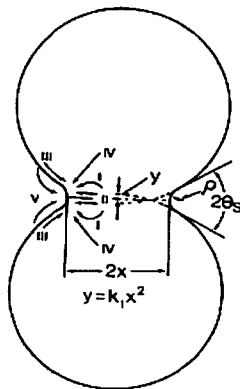


Figure 11. VC 90% plus 10% Co sintered during 1 hr at a) 1350°C, b) 1400°C and c) 1450°C [36]

The principal driving forces for the sintering without external forces that tend to decrease the surfaces and the interfacial areas are capillary forces due to the surface and interfacial tensions.

Typical model for the initial stage of sintering is shown in Figure 12 [37], where  $x$  is the contact radius,  $\rho$  is the minimum principle radius of curvature of the neck surface, and  $2\theta$  is the angle of contact between the two particles.



contact between the two particles.

Diffusional flow is the most important mechanism of material transport. The difference in curvature at the neck with  $\rho$  and the adjacent flat surface causes a difference in stress and chemical potential which produces a gradient in the concentration of the vacancies. Thus, the highly curved neck surface has a high vacancy concentration and the adjacent flat surface, a lower one.

Figure 12. Model for the initial stage of sintering [37].

This difference causes a flux of vacancies from the curved to the flat surface, or, what is the same a flux of material in the contrary direction, that can be done from the volume (path IV), or from the surface (path III). The resulting shrinkage is due to the diffusion of material to the neck from the grain boundary (path II) and from the volume (path I). The path V represents the evaporation and condensation produced from the flat surface (higher vapour pressure) to the neck (lower vapour pressure). Also the presence of liquid phase due to a specific chemical reaction can accelerate the sinterization [38]. Sometimes, hot isostatic pressing (HIP) after blending or cold isostatic pressing (CIP) is required. With this technique net-shape products can be obtained, the particle segregation is avoided [39] and more homogeneity compared to the as cast technique can be acquired [40].

- 2) *Diffusion bonding of foils.* This is a solid-state creep deformation process and is used for consolidating alternate layers of metal foils and fibres or monofilaments to create single or multiple composites [41]. The foils alternate with the reinforcement is held under low pressure (to avoid the damage of the fibres), sometimes at high temperatures, and a necessary time for the consolidation. After creep flow of the matrix between the fibres to make complete metal-to-metal contact, diffusion across the foil interfaces completes the process.
- 3) *Physical vapour deposition.* The reinforcement is covered (normally fibres or monofilaments) with the metal deposited by physical vapour deposition methods. Then, the covered reinforcement is arranged and hot pressed in order to promote the diffusion and



consolidation of the metal phase. This method is quite expensive and slow, and is limited to very specific parts like TiMMC [42].

### 2.2.3 Composite mechanics.

The *Slab Model* developed for continuous and aligned fibres treat the composite as if it is composed of two slabs bonded together, one of matrix and one of reinforcement, where the thickness of the ceramic part is in proportion to the fibre content  $f$ .

For the axial stiffness the two components of the slab composite must have the same strain  $\epsilon_{aC}$  in the direction parallel to the fibre axis, and this results in the linear “Rule of Mixtures”:

$$E_{aC} = (1 - f)E_M + fE_I \quad \text{Equation 1}$$

where  $E$  is the Young’s Modulus,  $I$  refers to the inclusion,  $M$  to the matrix,  $C$  to the composite, and  $a$  to the axial direction.

The prediction of the transverse ( $t$ ) stiffness based on the hypothesis of the equal stress, results in the “Reuss model”:

$$E_{tC} = \left[ \frac{f}{E_I} + \frac{(1-f)}{E_M} \right]^{-1} \quad \text{Equation 2}$$

The “Reuss model” gives a crude approximation and usually a low theoretical limit of the composite’s Young’s modulus not only for transverse fibres, but also for particulate reinforced materials. The semi-empirical approximation suggested by Halpin and Tsai [43] have been widely used, and the expression for transverse stiffness is given by:

$$E_{tC} = \frac{E_M(1 + \xi\eta_f f)}{(1 - \eta_f f)} \quad \text{with } \eta_f = \frac{\left(\frac{E_I}{E_M} - 1\right)}{\left(\frac{E_I}{E_M} + \xi\right)} \quad \text{Equation 3}$$

where  $\xi$  is an empirical parameter that depends of several processing factors, but usually hat the value of the unity, and  $\eta_f$  is the reinforcement efficiency factor.

### 2.2.4 Strengthening mechanisms of the particulate composites

The particles and the reinforcements strengthen the matrices by changing the stress state of the matrix, or by altering the flow properties of the matrix via changes in its microstructure [44].

Ceramics and intermetallic reinforcements have in general smaller coefficient of thermal expansion (CTE) compared to the metals. Since fabrication of MMCs involves consolidation at relatively high temperatures, they often contain significant differential thermal contraction stresses during cooling to ambient temperatures. If  $T_{esf}$  is a temperature in an effectively stress free state, then the misfit strain is simply as  $\Delta\alpha \Delta T$ , where  $\Delta T = T_{esf} - T_{ambient}$ . For an isolated spherical particle, the resultant stress field can be obtained easily by the Eshelby model using the Lamé relation. Figure 13 [44] shows the elastic field caused by cooling 500K an infinite matrix of Ti containing a spherical particle of SiC. The distribution of the stress produced by the local

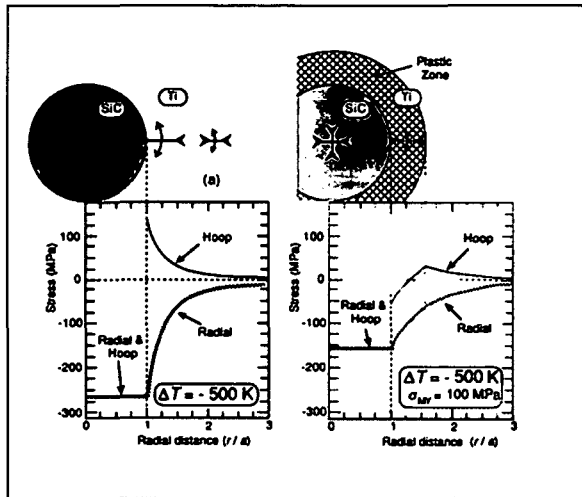


Figure 13. Stresses calculated for a) spherical isolated particle in an elastic state and b) a spherical particle in a 100MPa yielding metal matrix [44]

plastic flow obtained by assuming a yield stress of the matrix of 100MPa shows that the hoop or tangential stress is reduced in such a way that it becomes compressive near the particle.

Some approaches were also done in the numerical calculation field, resulting in a good concordance with the analytical resolutions [45, 46].

The reinforcement brings also changes in the microstructure of the matrix provoked by:

- *Dislocation strengthening.* The dislocations can be formed either as a result of applied straining or through the relaxation of the thermal residual stresses derived from the CTE misfit. There are many relations to predict the dislocation density ( $\Delta\rho$ ). Miller and Humphreys [47] have obtained the following expression assuming cube-shaped particles

$$\Delta\rho = 12 \frac{\Delta\alpha\Delta T f}{bd} \quad \text{Equation 4}$$

where  $\Delta\alpha\Delta T$  is the thermal misfit strain,  $f$  the particle percentage,  $b$  the Burgers vector and  $d$  the particle size. Furthermore, the influence of dislocation density on the variation of the matrix strength  $\Delta\sigma_{YM}$  is predicted by:

$$\Delta\sigma_{YM} \propto Gb\sqrt{\rho} \quad \text{Equation 5}$$

Due to the reinforcement size, they act as some dislocation sources [48].

- *Strengthening from grain size refinement.* The composites present in general smaller grain size than their unreinforced matrices. The contribution to the yield stress of this refinement can be estimated using the Hall-Petch relation:

$$\Delta\sigma_{YM} \approx \beta D^{-1/2} \approx \beta d^{-1/2} \left( \frac{1-f}{f} \right)^{1/6} \quad \text{Equation 6}$$

where  $\beta$  depends of a numbers of factors, and is typically  $0.1 \text{ MPa}\sqrt{\text{m}}$ , and  $D$  is the grain size.

- *Orowan and dispersion strengthening.* Most of the particles of a composite material are coarse and the interparticle spacing is large. But this mechanism is important for aged materials, because the reinforcement can help the nucleation of the precipitates due to the high concentration of dislocations.

### 2.2.5 Titanium Matrix composites

Improvements of the thermo-mechanical and tribological properties by reinforcing titanium with ceramics has been attractive not only for scientific studies, but also for industrial applications.

Continuous monofilaments improve considerably the strength of titanium alloys, especially at high temperatures, in the direction of the monofilaments [2]. Although Si reacts with titanium producing some brittle sub-products, SiC monofilaments are widely used nowadays. The new research studies lead in the direction of finding a way to cover the monofilaments with the optimal protective layer [49, 50, 51]. Figure 14c) shows the SiC monofilaments embedded in a titanium matrix [52]. This material was produced using the diffusion bonding method for matrix-coated monofilaments. The SiC monofilaments, called SCS-6 and manufactured by Textron Specialty Materials, (today Specialty Materials, Inc), consist of a carbon core surrounded with a mid-radius boundary, and then with the  $\beta$ -SiC. The whole monofilament was covered with a protective layer called SCS. The titanium matrix was then sputtered onto the fibres using a magnetron sputter, and after that, packed in a regular array. The consolidation was done by HIP and the final product is ready for heat treatments and machining.

The continuous reinforced materials present high costs of production, no formability, and have anisotropic properties. On the other hand, the particulate reinforced alloys are cheaper, can be forged, cut, formed, and their properties are more or less isotropic. The particles investigated in previous works as reinforcement are ceramics: TiC [53], TiN [54], TiO<sub>2</sub> [55], Si<sub>3</sub>N<sub>4</sub> [3], SiC [56], TiB<sub>2</sub>, TiB [57,58], oxides: Al<sub>3</sub>O<sub>2</sub> (in titanium aluminides [59]) Zr<sub>2</sub>O<sub>3</sub>, R<sub>2</sub>O<sub>3</sub> (with R= rare element) [60, 61], and intermetallic compounds: Ti<sub>3</sub>Al or TiAl [62] Ti<sub>5</sub>Si<sub>3</sub> [63,].

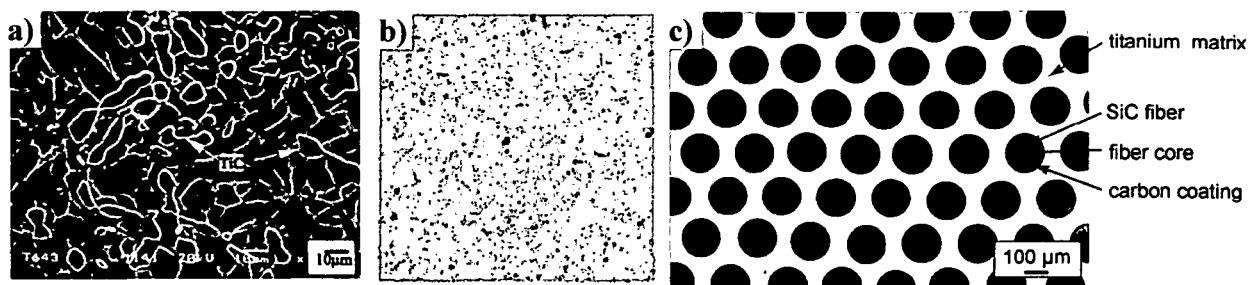


**Figure 14. Titanium Matrix Composites:** a) Ti-6Al-4V/10 wt.% TiC composite after reacting at 700 °C for 30 min and sintering at 1300 °C for 2 h in vacuum. b) Titanium alloy reinforced with TiB<sub>2</sub> and c) Titanium alloy reinforced with SiC monofilaments [52]

Figure 14b) shows the distribution of the TiB<sub>2</sub> particles (in black) in a Ti64 alloy matrix [3]. The material was produced by conventional powder metallurgy. Normally, the TiB<sub>2</sub> is used as a precursor to produce titanium reinforced with TiB [64]. TiB reinforcement is well known as needle like reinforcement due to its thermal stability and to the possibility of producing the composite by an in-situ precipitation of the ceramic phase [65, 66].

The SiC particle reinforced titanium alloys produced by conventionally powder metallurgy tend to be porous and with brittle interface reaction zone, due to the high reactivity of the Si with the titanium matrix [67]. Recent studies show that it is possible to produce high quality SiC reinforced titanium by decreasing the time and or the temperature of consolidation, using new techniques, such as shock wave consolidation [68]. S. Gorsse, and Y. Le Petitcorps did a complete work [69] where they obtained the reaction profile at 900°C of the two brittle phase zone TiC<sub>x</sub> and Ti<sub>5</sub>Si<sub>3</sub>C<sub>x</sub>, as well as the diffusion constant rate of Si. Many other previous works studied the development of such reaction layers and their properties as well as the influence of the alloying elements, the parameters of production, and the possibility of protective coatings on the SiC reinforcement [70, 71, 72]. In the case of AlMgSi/Al<sub>2</sub>O<sub>3</sub>/xp composites spinel reaction occurs at the interface, which does not degrade the MMC properties [73].

Although the mismatch in CTE between titanium matrix (8-11 ppm/K) and TiC (6.6-7.4 ppm/K) particles is not big enough to expect an important improvement in the strength and stiffness by mismatch strains, the composite material has been widely studied. Two different TiC reinforced titanium alloys are nowadays under study: the composites produced by mixing the two ingredients, and the in-situ composite.

The materials produced by mixing the titanium alloy with the titanium carbide particles show high compressive stress even at 1% vol TiC particles addition [74]. The work of Badini et al

reported also that the strength and the stiffness were improved at high temperatures, while the TiC particles remained stable up to at least 700°C [75].

The in-situ materials produced by gas-solid reaction [53] and by a powder metallurgy method called XD<sup>TM</sup> [76] with higher mechanical properties than the matrices present no secondary reaction products, but the diffusion of C into the matrix which strengthen it.

## 2.3 Thermomechanical concepts.

### 2.3.1 Deformation maps

The workability of a material is specified by its flow stress dependence on processing variables, its failure behaviour and the metallurgical transformation of its alloy system. In industry, one of the objectives is to manufacture components with controlled microstructure and properties, without macro or microstructural defects.

The deformation maps delineate safe and risky working conditions, based on the experimental data of flow stress ( $\sigma$ ) as a function of the temperature ( $T$ ), strain rate ( $\dot{\epsilon}$ ) and strain ( $\epsilon$ ) [77].

Gandhi and Ashby [78] were the first to consider the materials response in the form of deformation maps, which were developed from the creep mechanisms applicable to lower strain rates. Raj [79] extended the map concept representing the limiting conditions for two damage mechanisms: (a) cavity formation at hard particles in a soft matrix and (b) wedge cracking at grain boundary triple junctions. While the first phenomenon occurs at lower temperatures and higher strain rates, the second one is delimited to the higher temperatures and lower strain rates; adiabatic heating was identified at very high strain rates. These concepts were also used to study the MMCs [80] deformation behaviour. A correlation of the flow softening with the materials properties was proposed by Semiatin et al [81], where a parameter  $\alpha = (-\gamma/m)$  ( $\gamma$ : flow softening and  $m$ : strain sensitivity) defines the limit of the flow localization during deformation.

Prasad et al [82] developed the processing maps based on the dynamic materials model (DMM).

The DMM is based on the fundamental principles of continuum mechanics of large plastic deformation and describes the patterns of the dynamic response of the material in hot deformation. A parameter of power dissipation plotted against the temperature and the strain rate represent the processing maps, and the superimposed instability maps distinguish the safe from the unsafe zones.

The DMM model was re-analysed by N. Murty and N. Rao [83] and corrected as explained in the following sections.

### 2.3.2 Thermodynamics

The deformation maps are derived from the continuum mechanics as well as from the thermodynamics concepts. The second law of the thermodynamics can be expressed per time unit as [84]:

$$T\dot{S} \geq Q^* \quad \text{Equation 7}$$

where  $T$  is the temperature,  $Q^*$  is the heat supply per unit time and  $\dot{S}$  is the rate of entropy production composed by two terms:

$$\dot{S} = \frac{dS^{(r)}}{dt} + \frac{dS^{(i)}}{dt} \quad \text{Equation 8}$$

where the first term refers to the entropy given from outside to the system, and the second term to the internal production of entropy. Furthermore,

$$\frac{dS^{(r)}}{dt} = \frac{Q^*}{T} \quad \text{and} \quad \frac{dS^{(i)}}{dt} \geq 0 \quad \text{Equation 9}$$

The total power dissipated is related to the rate of entropy production inside the system  $\dot{S}^{(i)}$  as follows:

$$P = T \frac{dS^{(i)}}{dt} \geq 0 \quad \text{Equation 10}$$

and it is always positive for irreversible processes (e.g. plastic deformation) and zero for reversible processes.

Under isothermal conditions, ( $Q^* = 0$ ) the rate of entropy production is totally “internal” and consists of two separable parts. The first part may be called the rate of conduction entropy ( $G$ ), which is due to the conduction of heat generated due to dislocation movement to the colder parts of the body, and the second part ( $J$ ) is due to the rate of change in the microstructure of the material.

### 2.3.3 Dynamic Materials Model (DMM)

In this model, the material is considered to have the following characteristics:

- 1- *Dissipative*: The material essentially dissipates power during hot deformation and does not store energy significantly.

2- *Dynamic*: The constitutive response of the material at a given temperature during hot deformation depends essentially on the strain rate and to a smaller extent on strain.

3- *Non-linear*: The response of the material to the imposed variables like strain, strain rate and temperature is non-linear.

4- *Far from Equilibrium*: The material undergoing large plastic flow at high temperatures is far from equilibrium since the strain is not being applied in infinitesimally small increments.

5- *Irreversible*: The extremum principles of irreversible thermodynamics as applied to large plastic flow [84] are applicable.

According to the DMM model, at any strain and temperature the power  $P$  (per unit volume) absorbed by the work piece material during plastic flow is given by [82]:

$$P = G + J = \int_0^{\dot{\epsilon}} \sigma d\dot{\epsilon} + \int_0^{\sigma} \dot{\epsilon} d\sigma = \sigma \dot{\epsilon} \quad \text{Equation 11}$$

the second integral ( $J$ ) is the co-content, which is a complementary function of  $G$  content. At a constant temperature and strain, the dynamic response of the work-piece material under hot deformation is represented by the power law:

$$\sigma = K \dot{\epsilon}^m \quad \text{Equation 12}$$

where  $K$  is a constant and  $m$  is the strain rate sensitivity of flow stress.

The total derivative of equation 11 is:

$$dP = \frac{\partial P}{\partial G} dG + \frac{\partial P}{\partial J} dJ = \sigma d\dot{\epsilon} + \dot{\epsilon} d\sigma \quad \text{Equation 13}$$

In this model, the factor that partitions power between these two complementary parameters is  $m$ :

$$\left( \frac{\partial J}{\partial G} \right)_{\epsilon, T} = \frac{\partial P}{\partial G} \cdot \frac{\partial J}{\partial P} = \frac{\sigma d\dot{\epsilon}}{\dot{\epsilon} d\sigma} = \left[ \frac{\partial(\ln \sigma)}{\partial(\ln \dot{\epsilon})} \right]_{\epsilon, T} \equiv m \quad \text{Equation 14}$$

From Equation 11, the  $G$  content can be represented by the area under the dynamic constitutive equation curve and  $J$  co-content represents the area above it (Figure 15).

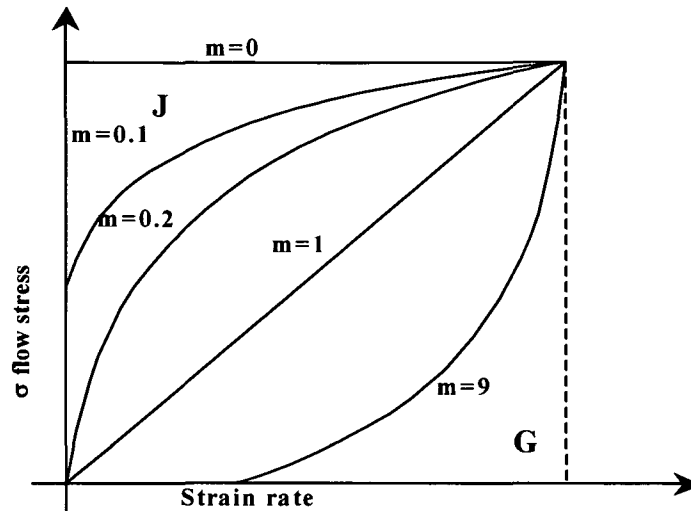


**Figure 15.** Stress as a function of strain rate for a temperature and a strain rate.

For stable flow, the limits for the strain rate sensitivity are between 0 and 1;  $m=0$ : the material does not dissipate power through metallurgical processes and  $m=1$ : the material reaches a situation close to that of a viscous fluid (e.g.: superplastic material). If  $m > 1$ , the power law breaks down. The curvature of the stress strain rate curve is reversed and at a critical strain rate the flow stress increases steeply to become nearly independent of strain and strain rate. If the flow stress obeys the power law (Equation 12), then:

$$G = \frac{P}{1+m} \quad \text{Equation 15}$$

$$J = \frac{mP}{1+m} \quad \text{Equation 16}$$

The value of  $m$  however, could vary non-linearly with temperature and strain rate, the  $J$  co-content variation is also non-linear. The variation may be normalized with respect to a linear dissipator for which  $m = 1$  and  $J$  co-content will assume a maximum value given by:

$$J = J_{\max} = \frac{\sigma \dot{\epsilon}}{2} = \frac{P}{2} \quad \text{Equation 17}$$

The value of  $J$  may be normalized with respect to  $J_{\max}$  to obtain a dimensionless parameter called efficiency of power dissipation defined as:

$$\eta = \frac{J}{J_{\max}} \quad \text{Equation 18}$$

which results in



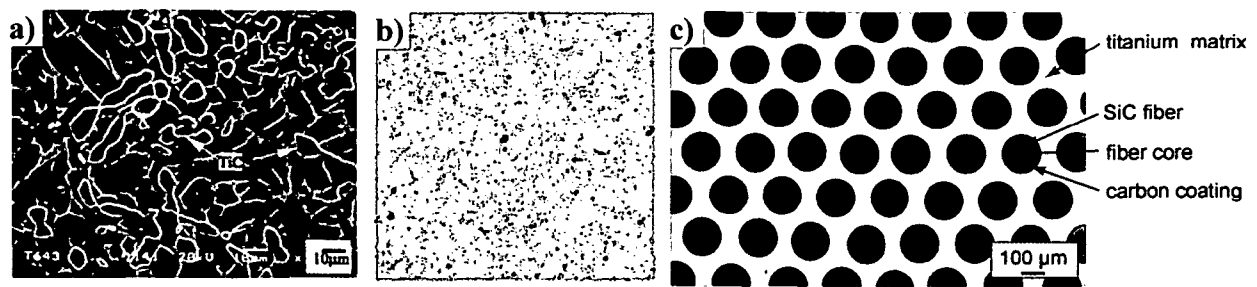


**Figure 14. Titanium Matrix Composites:** a) Ti-6Al-4V/10 wt.% TiC composite after reacting at 700 °C for 30 min and sintering at 1300 °C for 2 h in vacuum. b) Titanium alloy reinforced with  $\text{TiB}_2$  and c) Titanium alloy reinforced with SiC monofilaments [52]

Figure 14b) shows the distribution of the  $\text{TiB}_2$  particles (in black) in a Ti64 alloy matrix [3]. The material was produced by conventional powder metallurgy. Normally, the  $\text{TiB}_2$  is used as a precursor to produce titanium reinforced with TiB [64]. TiB reinforcement is well known as needle like reinforcement due to its thermal stability and to the possibility of producing the composite by an in-situ precipitation of the ceramic phase [65, 66].

The SiC particle reinforced titanium alloys produced by conventionally powder metallurgy tend to be porous and with brittle interface reaction zone, due to the high reactivity of the Si with the titanium matrix [67]. Recent studies show that it is possible to produce high quality SiC reinforced titanium by decreasing the time and or the temperature of consolidation, using new techniques, such as shock wave consolidation [68]. S. Gorsse, and Y. Le Petitcorps did a complete work [69] where they obtained the reaction profile at 900°C of the two brittle phase zone  $\text{TiC}_x$  and  $\text{Ti}_5\text{Si}_3\text{C}_x$ , as well as the diffusion constant rate of Si. Many other previous works studied the development of such reaction layers and their properties as well as the influence of the alloying elements, the parameters of production, and the possibility of protective coatings on the SiC reinforcement [70, 71, 72]. In the case of  $\text{AlMgSi}/\text{Al}_2\text{O}_3/\text{xp}$  composites spinel reaction occurs at the interface, which does not degrade the MMC properties [73].

Although the mismatch in CTE between titanium matrix (8-11 ppm/K) and TiC (6.6-7.4 ppm/K) particles is not big enough to expect an important improvement in the strength and stiffness by mismatch strains, the composite material has been widely studied. Two different TiC reinforced titanium alloys are nowadays under study: the composites produced by mixing the two ingredients, and the in-situ composite.

The materials produced by mixing the titanium alloy with the titanium carbide particles show high compressive stress even at 1% vol TiC particles addition [74]. The work of Badini et al

reported also that the strength and the stiffness were improved at high temperatures, while the TiC particles remained stable up to at least 700°C [75].

The in-situ materials produced by gas-solid reaction [53] and by a powder metallurgy method called XD<sup>TM</sup> [76] with higher mechanical properties than the matrices present no secondary reaction products, but the diffusion of C into the matrix which strengthen it.

## 2.3 Thermomechanical concepts.

### 2.3.1 *Deformation maps*

The workability of a material is specified by its flow stress dependence on processing variables, its failure behaviour and the metallurgical transformation of its alloy system. In industry, one of the objectives is to manufacture components with controlled microstructure and properties, without macro or microstructural defects.

The deformation maps delineate safe and risky working conditions, based on the experimental data of flow stress ( $\sigma$ ) as a function of the temperature ( $T$ ), strain rate ( $\dot{\epsilon}$ ) and strain ( $\epsilon$ ) [77].

Gandhi and Ashby [78] were the first to consider the materials response in the form of deformation maps, which were developed from the creep mechanisms applicable to lower strain rates. Raj [79] extended the map concept representing the limiting conditions for two damage mechanisms: (a) cavity formation at hard particles in a soft matrix and (b) wedge cracking at grain boundary triple junctions. While the first phenomenon occurs at lower temperatures and higher strain rates, the second one is delimited to the higher temperatures and lower strain rates; adiabatic heating was identified at very high strain rates. These concepts were also used to study the MMCs [80] deformation behaviour. A correlation of the flow softening with the materials properties was proposed by Semiatin et al [81], where a parameter  $\alpha = (-\gamma/m)$  ( $\gamma$ : flow softening and  $m$ : strain sensitivity) defines the limit of the flow localization during deformation.

Prasad et al [82] developed the processing maps based on the dynamic materials model (DMM).

The DMM is based on the fundamental principles of continuum mechanics of large plastic deformation and describes the patterns of the dynamic response of the material in hot deformation. A parameter of power dissipation plotted against the temperature and the strain rate represent the processing maps, and the superimposed instability maps distinguish the safe from the unsafe zones.

The DMM model was re-analysed by N. Murty and N. Rao [83] and corrected as explained in the following sections.

### 2.3.2 Thermodynamics

The deformation maps are derived from the continuum mechanics as well as from the thermodynamics concepts. The second law of the thermodynamics can be expressed per time unit as [84]:

$$T\dot{S} \geq Q^* \quad \text{Equation 7}$$

where  $T$  is the temperature,  $Q^*$  is the heat supply per unit time and  $\dot{S}$  is the rate of entropy production composed by two terms:

$$\dot{S} = \frac{dS^{(r)}}{dt} + \frac{dS^{(i)}}{dt} \quad \text{Equation 8}$$

where the first term refers to the entropy given from outside to the system, and the second term to the internal production of entropy. Furthermore,

$$\frac{dS^{(r)}}{dt} = \frac{Q^*}{T} \quad \text{and} \quad \frac{dS^{(i)}}{dt} \geq 0 \quad \text{Equation 9}$$

The total power dissipated is related to the rate of entropy production inside the system  $\dot{S}^{(i)}$  as follows:

$$P = T \frac{dS^{(i)}}{dt} \geq 0 \quad \text{Equation 10}$$

and it is always positive for irreversible processes (e.g. plastic deformation) and zero for reversible processes.

Under isothermal conditions, ( $Q^* = 0$ ) the rate of entropy production is totally “internal” and consists of two separable parts. The first part may be called the rate of conduction entropy ( $G$ ), which is due to the conduction of heat generated due to dislocation movement to the colder parts of the body, and the second part ( $J$ ) is due to the rate of change in the microstructure of the material.

### 2.3.3 Dynamic Materials Model (DMM)

In this model, the material is considered to have the following characteristics:

- 1- *Dissipative*: The material essentially dissipates power during hot deformation and does not store energy significantly.

2- *Dynamic*: The constitutive response of the material at a given temperature during hot deformation depends essentially on the strain rate and to a smaller extent on strain.

3- *Non-linear*: The response of the material to the imposed variables like strain, strain rate and temperature is non-linear.

4- *Far from Equilibrium*: The material undergoing large plastic flow at high temperatures is far from equilibrium since the strain is not being applied in infinitesimally small increments.

5- *Irreversible*: The extremum principles of irreversible thermodynamics as applied to large plastic flow [84] are applicable.

According to the DMM model, at any strain and temperature the power  $P$  (per unit volume) absorbed by the work piece material during plastic flow is given by [82]:

$$P = G + J = \int_0^{\dot{\epsilon}} \sigma d\dot{\epsilon} + \int_0^{\sigma} \dot{\epsilon} d\sigma = \sigma \dot{\epsilon} \quad \text{Equation 11}$$

the second integral ( $J$ ) is the co-content, which is a complementary function of  $G$  content. At a constant temperature and strain, the dynamic response of the work-piece material under hot deformation is represented by the power law:

$$\sigma = K \dot{\epsilon}^m \quad \text{Equation 12}$$

where  $K$  is a constant and  $m$  is the strain rate sensitivity of flow stress.

The total derivative of equation 11 is:

$$dP = \frac{\partial P}{\partial G} dG + \frac{\partial P}{\partial J} dJ = \sigma d\dot{\epsilon} + \dot{\epsilon} d\sigma \quad \text{Equation 13}$$

In this model, the factor that partitions power between these two complementary parameters is  $m$ :

$$\left( \frac{\partial J}{\partial G} \right)_{\epsilon, T} = \frac{\partial P}{\partial G} \cdot \frac{\partial J}{\partial P} = \frac{\sigma d\dot{\epsilon}}{\dot{\epsilon} d\sigma} = \left[ \frac{\partial(\ln \sigma)}{\partial(\ln \dot{\epsilon})} \right]_{\epsilon, T} \equiv m \quad \text{Equation 14}$$

From Equation 11, the  $G$  content can be represented by the area under the dynamic constitutive equation curve and  $J$  co-content represents the area above it (Figure 15).

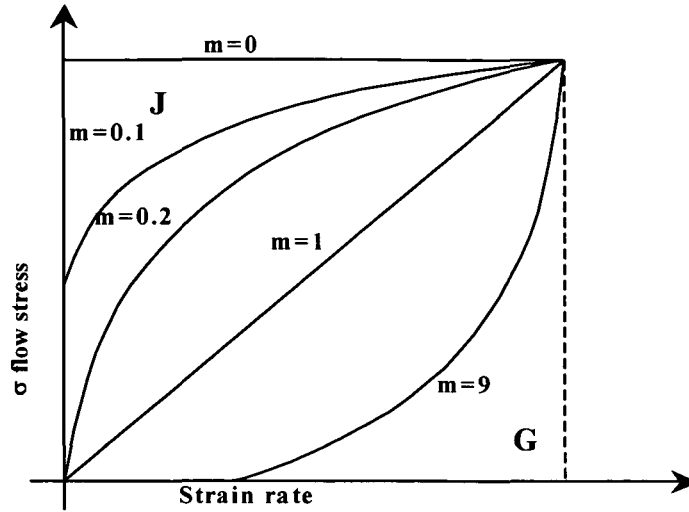


**Figure 15. Stress as a function of strain rate for a temperature and a strain rate.**

For stable flow, the limits for the strain rate sensitivity are between 0 and 1;  $m=0$ : the material does not dissipate power through metallurgical processes and  $m=1$ : the material reaches a situation close to that of a viscous fluid (e.g.: superplastic material). If  $m > 1$ , the power law breaks down. The curvature of the stress strain rate curve is reversed and at a critical strain rate the flow stress increases steeply to become nearly independent of strain and strain rate. If the flow stress obeys the power law (Equation 12), then:

$$G = \frac{P}{1+m} \quad \text{Equation 15}$$

$$J = \frac{mP}{1+m} \quad \text{Equation 16}$$

The value of  $m$  however, could vary non-linearly with temperature and strain rate, the  $J$  co-content variation is also non-linear. The variation may be normalized with respect to a linear dissipator for which  $m=1$  and  $J$  co-content will assume a maximum value given by:

$$J = J_{\max} = \frac{\sigma \dot{\epsilon}}{2} = \frac{P}{2} \quad \text{Equation 17}$$

The value of  $J$  may be normalized with respect to  $J_{\max}$  to obtain a dimensionless parameter called efficiency of power dissipation defined as:

$$\eta = \frac{J}{J_{\max}} \quad \text{Equation 18}$$

which results in

$$\eta = \frac{2m}{m+1} \quad \text{Equation 19}$$

The efficiency parameter is not the process efficiency or overall efficiency of energy for the process since it only refers to that with respect to a linear dissipator. Since efficiency is obtained by normalizing  $J$  with  $J_{\max}$ , it represents relative rate of entropy production due to microstructural dissipation, i.e. the metallurgical transformations within the material, such as recovery, recrystallisation, phase transformations and material damage [85].

Ziegler [86] has shown that the condition for the plastic flow to become unstable is given by:

$$\frac{dD}{d\dot{\epsilon}} < \frac{D}{\dot{\epsilon}} \quad \text{Equation 20}$$

where  $D$  is the dissipative function that is characteristic of the constitutive behaviour of the material. Thus,  $J$  may replace  $D$  and we get a condition for flow instabilities:

$$\xi(\dot{\epsilon}) = \frac{\partial \ln \left[ \frac{m}{m+1} \right]}{\partial \ln \dot{\epsilon}} + m < 0 \quad \text{Equation 21}$$

When the parameter  $\xi(\dot{\epsilon})$  is plotted, as a function of temperature and strain rate, the regime where it is negative will give flow instabilities, and this plot is called *instability map*. The above instability criterion has the physical meaning that if the system is not able to generate entropy at a rate that at least matches with the imposed rate, the system will localize the flow and cause flow instability in the form as shear bands and flow localization.

### 2.3.4 Modified DMM.

The Dynamic Material Model was analysed by S.V.S. Narayana Murty and Nageswara Rao by studying first the criterion of stability flow [87], and they demonstrated that the equation of the linear dissipator (Equation 17) is contradictory with the instability and power dissipation definitions. If  $m$  varies with  $\dot{\epsilon}$  and  $T$  as in many engineering alloys, the flow stress does not obey the power law, and hence, the evaluation of  $J$  using Equation 17 is erroneous [88].

The concepts are clearly developed in [77] and are exposed below.

If  $P$  is differentiated with respect to  $\dot{\epsilon}$ , then:

$$\frac{\partial P}{\partial \dot{\epsilon}} = \frac{\partial}{\partial \dot{\epsilon}}(\sigma \dot{\epsilon}) = \dot{\epsilon} \frac{\partial \sigma}{\partial \dot{\epsilon}} + \sigma = \sigma \left( \frac{\dot{\epsilon}}{\sigma} \frac{\partial \sigma}{\partial \dot{\epsilon}} + 1 \right) = \sigma \left( \frac{\partial \ln \sigma}{\partial \ln \dot{\epsilon}} + 1 \right) = \sigma(m+1) \quad \text{Equation 22}$$

which implies that:

$$\sigma = \frac{1}{(m+1)} \frac{\partial P}{\partial \dot{\epsilon}} = \frac{\partial}{\partial \dot{\epsilon}} \left( \frac{P}{m+1} \right) - P \frac{\partial}{\partial \dot{\epsilon}} \left( \frac{1}{m+1} \right) \frac{\partial}{\partial \dot{\epsilon}} \left( \frac{P}{m+1} \right) + P \frac{\partial}{\partial \dot{\epsilon}} \left( \frac{m}{m+1} \right) \quad \text{Equation 23}$$

Using the definition of G (Equation 15):

$$G = \int_0^{\dot{\epsilon}} \sigma \dot{\epsilon} = \frac{P}{m+1} + \int_0^{\dot{\epsilon}} \sigma \dot{\epsilon} \frac{\partial}{\partial \dot{\epsilon}} \left[ \frac{m}{1+m} \right] d\dot{\epsilon} \quad \text{Equation 24}$$

If J is expressed as a function of G and P, then:

$$J = G - P = \frac{mP}{1+m} - \int_0^{\dot{\epsilon}} \sigma \dot{\epsilon} \frac{\partial}{\partial \dot{\epsilon}} \left[ \frac{m}{1+m} \right] d\dot{\epsilon} \quad \text{Equation 25}$$

In the two equations of above, it can be observed that if m is independent of the strain rate, then Equation 24 and 25 are identical to Equations 15 and 16. Furthermore, if the material obeys the power law (m independent of  $\dot{\epsilon}$ ), the flow instability condition given by Equation 21 reduces to  $m < 0$ . For complicated alloy systems, the computation of  $\eta$  in terms of m from Equation 19 and the flow instability condition given in Equation 21 become erroneous.

The differential form of J is (from the definition)

$$dJ = \dot{\epsilon} d\sigma = \dot{\epsilon} \frac{\partial \sigma}{\partial \dot{\epsilon}} d\dot{\epsilon} = \frac{\dot{\epsilon}}{\sigma} \frac{\partial \sigma}{\partial \dot{\epsilon}} \sigma d\dot{\epsilon} = m \sigma d\dot{\epsilon} \Rightarrow J = \int_0^{\dot{\epsilon}} m \sigma d\dot{\epsilon} \quad \text{Equation 26}$$

Integrating by parts, it is possible to define F as the second term in the following equation:

$$J = m \sigma \dot{\epsilon} - \int_0^{\dot{\epsilon}} \dot{\epsilon} \frac{\partial (m \sigma)}{\partial \dot{\epsilon}} d\dot{\epsilon} = mP - F \quad \text{Equation 27}$$

And now using the criteria of instability from Equation 20, the instability condition can be written as:

$$F < 0 \Rightarrow m < \frac{J}{P} \leq 0 \quad \text{Equation 28}$$

Using the definition of power dissipation (Equation 18), the instability condition is expressed as:

$$\kappa = \frac{2m}{\eta} - 1 < 0 \quad \text{Equation 29}$$

The parameter of power dissipation shall be calculated using the definition that can be re-written as  $2J/P = \eta$ . J is calculated using

$$J = P - G = \sigma \dot{\epsilon} - \int_0^{\dot{\epsilon}} \sigma d\dot{\epsilon} \quad \text{Equation 30}$$

As the experimental data are not available up to a minimum strain rate, then the integral to evaluate G can be expressed as:

$$G = \int_0^{\dot{\epsilon}_{\min}} \sigma d\dot{\epsilon} + \int_{\dot{\epsilon}_{\min}}^{\dot{\epsilon}} \sigma d\dot{\epsilon} = \left[ \frac{\sigma \dot{\epsilon}}{m+1} \right]_{\dot{\epsilon}=\dot{\epsilon}_{\min}} + \int_{\dot{\epsilon}_{\min}}^{\dot{\epsilon}} \sigma d\dot{\epsilon} \quad \text{Equation 31}$$

The value of m for the first integral is estimated as the slope of the curve  $\log \sigma$  vs.  $\log \dot{\epsilon}$  near the  $\dot{\epsilon}_{\min}$ . Important discrepancies between  $\eta$  and  $2m/(m+1)$  were reported by Narayana Murty and Nageswara Rao for titanium aluminides [89]. Spigarelli et al have concluded that this method appears to be the most promising approach to the behaviour of a metal matrix composite (6061+20%  $\text{Al}_2\text{O}_3$ ) [90].

## 2.4 Behaviour at high temperatures.

### 2.4.1 Deformation at high temperatures

The behaviour of titanium alloys at high temperatures during deformation depends basically on the alpha-beta ratio and on the grain distribution and orientation. The most widely studied alpha-beta titanium alloy is the Ti64. Three main mechanisms of hot deformation during compression were described depending on the temperatures and the strain rates [91]:

- 1) At strain rates  $< 0.1 \text{ s}^{-1}$  and temperatures 750-1100°C, steady-state behaviour was observed due to superplasticity at strain rates  $< 0.002 \text{ s}^{-1}$ , to dynamic recrystallisation in the beta zone and to dynamic recovery in the alpha- beta region [92]
- 2) At strain rates  $> 0.1 \text{ s}^{-1}$  in the  $\alpha+\beta$  range, flow softening behaviour was observed due to globularization process of lamellar structures [93,94], flow instability due to flow localization (shear bands), or micro-cracking during deformation. The softening in lamellar microstructures was also attribute the to the kinking mechanism in previous works [95,96].
- 3) At strain rates  $> 1 \text{ s}^{-1}$  in the  $\beta$  range oscillatory flow curves were observed due to dynamic flow instabilities [97].

In previous works it was observed that titanium alloys reinforced with TiC particles present values of ultimate tensile strength [53, 75], and compressive strength [74] up to 27% higher than for the unreinforced matrices. At high temperatures, the results are much better, achieving values



of strength up to 74% higher than the matrix [98]. On the other hand, the addition of 20-40% of TiB particles at high temperatures produces no important improvements of the tensile strength [99]. Furthermore, compared with titanium matrix, the tensile strength of titanium reinforced with TiB and  $\text{Nd}_2\text{O}_3$  at elevated temperature is significantly improved according to [100].

The studies for TiC particle reinforced titanium and titanium alloys proposed the diffusion of the C from the TiC into the matrix during the high temperatures processing steps [76] that can strengthen the matrix by interstitial alloying. As a consequence, some  $\text{Ti}_2\text{C}$  instead TiC was found by X-Ray [101]. C. Ouchi et al [102] demonstrated that the addition of 0.02-0.03%wt O, N or C to ultrahigh purity titanium improves the 0.2% proof strength at room temperature up to 40, 57 and 20% respectively.

#### **2.4.2 Hot compression tests.**

In the study of the workability of the materials, the hot compression tests are the most reliable method to obtain the flow data, because it is easy to obtain a constant strain rate as well as isothermal conditions. Physical simulation of materials hot forming using a Gleeble machine involves the exact reproduction of the thermal and mechanical processes in the laboratory using a small sample. The Gleeble machine in its different models have been used to get accurate flow data to generate the processing maps for more than 3 decades. The computer controlled servo-hydraulic Gleeble®1500 can be used for compression testing, and it can be programmed to simulate both the thermal and mechanical industrial process variables for a wide range of deformation conditions. The specimen is resistance heated by thermo-couple feedback controlled A-C current, and the heating rate can reach up to  $10,000^\circ\text{K/s}$  [103]. On the other hand, a thermal gradient existing along the specimen's axis because of the heat transfer to the water-cooled jaws was reported for different materials, especially for those with bad thermal conductivity [104, 105]. This effect was decreased in some cases by using different interfaces between the anvils and the specimen, such as nickel compound and graphite foil [106], or by using special anvils materials [103]. This heating mechanism has another disadvantage, which is the friction during compression at high temperatures that is normally decreased in the industry by using glasses, but they are electrical isolators. It is possible to reduce the friction between the specimen and the anvils up to  $600^\circ\text{C}$  using graphite [107], for higher temperatures normally Ta foils [104] or A5 glass lubricant, from Baoji Non-ferrous Metal Works [108, 109] are used.

## 2.5 Objectives of this work

The most well known titanium alloy Ti64 was widely studied. But less is known about the thermomechanical properties of the Ti-6Al-6V-2Sn (Ti662) alloy for high strength applications at high temperatures. On the other hand, the performance of the reinforced alloy with TiC particles produced by Dynamet was deeply studied here in order to find potential applications of the new material.

In this work the forgeability of Ti662 Ingot (as used nowadays in the industry) and Ti662 produced by powder metallurgy were studied and compared with that of the well-known Ti64 alloy. Furthermore, the deformation at high temperatures of the composite of Ti662 alloy reinforced with TiC was compared with that of the matrix. Compression tests, metallography, and deformation maps were used in order to find out the best parameters for forging, the mechanisms of deformation and the damage of the materials.

As during heat treatments the Ti662 transforms its alpha-beta ratio, some changes in the volume are expected, and this was the reason why dilatometry experiments were carried out for the matrices, but also for the composite; in the last case to see if there is some influence of the particles.

At the beginning of this work, a question was inevitable: Why reinforce titanium alloys with TiC instead of SiC that should bring a higher strengthening? Looking for this answer, some trials to produce Ti64 reinforced with SiC were carried out.

As in light weight design one of the most important parameters is the stiffness, measurements of the Young's modulus were carried out and compared with some theoretical models in order to find if there is some special bonding between the matrix and the particles.

The wear mechanisms were also studied to see if the ceramic particles bring some improvement of the poor tribological behaviour of the titanium alloys.

The questions dealt with are:

- What are the performance advantages of particulate reinforced Ti, considering stiffness, strength and wear resistance?
- Where is the "forging window" to manufacture components of Ti-PRM?

### 3 Experimental.

#### 3.1 Materials

##### 3.1.1 Materials description.

In this work, the titanium alloys Ti-6Al-4V (Ti64) and Ti-6Al-6V-2Sn (Ti662) and their composites were studied. Ti-Grade 2 was tested only in the dilatometer to compare the beta transus transformations with the other materials. Table 1 shows the nomenclature and the production method of the materials.

Table 1. Nomenclature of the materials used in this work.

Name	Material	Production method
<i>Ti662 ingot</i>	Ti-6Al-6V-2Sn	as cast and cogging
<i>CermeTi<sup>®</sup>-C-662</i>	Ti-6Al-6V-2Sn	powder metallurgy (Dynamet)
<i>CermeTi<sup>®</sup>-C-20-662</i>	Ti-6Al-6V-2Sn reinforced with 20vol% of TiC particles	powder metallurgy (Dynamet)
<i>CermeTi<sup>®</sup>-C-12-662</i>	Ti-6Al-6V-2Sn reinforced with 12vol% of TiC particles	powder metallurgy (Dynamet)
<i>Ti64 (PM)</i>	Ti-6Al-4V	powder metallurgy (Dynamet)
<i>Ti64/TiC/12p (PM):</i>	Ti-6Al-4V reinforced with 12vol% TiC particles	powder metallurgy (Dynamet)
<i>Ti64/SiC/15p</i>	Ti-6Al-4V reinforced with 15vol% of SiC particles	powder metallurgy by IFAM (Dresden) <sup>1</sup>
<i>Ti Grade2</i>	Ti 99.4%	as cast and forged

<sup>1</sup>Prototype material

Some mechanical and physical properties of the alloys and of the ceramic reinforcements taken from the literature [2, 24, 110,] are listed in Table 2.

Table 2. Properties of Ti662 and Ti64 alloys, and SiC and TiC reinforcements from literature.

	Density (kg/m <sup>3</sup> )	Strength RT (MPa)	E-Modulus RT (GPa)	CTE (ppm/K)	Hardness (Vickers)	Structure
<b>Ti662</b>	4537	960-1190 (Tensile)	110-117	9.5 (RT-538 °C)	267-346	hcp< 945°C<bcc
<b>Ti64</b>	4470	862-1200 (Tensile)	110-119	8.7-9.1	380-420	hcp< 995°C<bcc
<b>TiC</b>	4930	3750 (Comp.)	270-460	6.6-7.4 (RT-538 °C)	2500- 3200	Cubic (NaCl structure)
<b>SiC</b>	3100	1000-5250 (Comp.)	350-461	2.7-5.1 (RT-538 °C)	1900-3500	Cubic (ZnS structure)

### 3.1.2 Production methods.

The titanium alloys as well as the composites used in this work were primarily produced using two different processing techniques: powder metallurgy and casting followed by cogging. The cogging process is used to convert coarse-grained cast ingot into fine-grained wrought billet by forming at high temperatures.

- *Powder Metallurgy: Dynamet method.* The CermeTi<sup>®</sup>s and the Ti64 (PM) unreinforced and reinforced with TiC particles were produced by Cold-Hot Isostatic Pressing (CHIP). Figure 16 shows this method schematically. The processing steps include:

- 1) Blending: Raw material powders in proper weight percents are blended to achieve a desired final chemical composition for the alloy to be produced. Ceramic particles are added if the desired final product shall be a composite.
- 2) Cold Isostatic Pressing (CIP): The mixed powders are transferred to reusable pre-shaped elastomeric tooling and sealed. Then it is placed in an isostatic pressure vessel, and pressed at room temperature using hydrostatic pressure (often at pressures exceeding 340 MPa). Finally, the compacted powder is removed from the tooling resulting in a “green” preform.
- 3) Sintering: The “green” preform is transferred into a vacuum furnace and processed at a prescribed time and temperature (below the melting point), with controlled heat-up and cool-

down rates. During sintering, the material is further densified and alloying of the raw material ingredients is accomplished through solid-state diffusion.

- 4) Hot Isostatic Pressing (HIP): The HIP process is used to produce full density, closing small residual porosity and improving mechanical properties of the finished material.

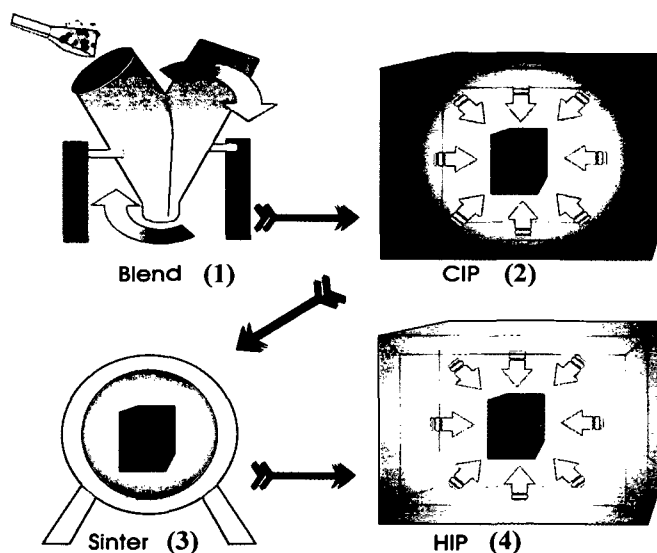


Figure 16. Dynamet CHIP method: (1) after blending the powders, (2) they are pressed at low temperatures, (3) then sintered in vacuum and (4) finally isostatically pressed at high temperatures.

- *Ingot material.* Ti662 ingot was first produced by casting. Posterior thermo-mechanical treatments were applied, to achieve the AMS 4979 specifications shown in Table 3.

Table 3 AMS 4979 specification for the Ti662 ingot material.

Specification	AMS 4979			
Form	Bar and forging			
Condition	Solution treated and aged			
Thickness or diam., in	≤ 1.000	1.001-2.000	2.001-3.000	3.001-4.000
Mechanical properties				
Ultimate Stress, MPa	1206	1172	1069	1034
Yield Stress, MPa	1103	1069	1000	965
e, percent	8	8	8	8
RA, percent	20	20	20	20
E, GPa	110			
G, GPa	43			
Physical properties				
Density, g/cm <sup>3</sup>	4.54			

The solution treat refers to the heat treatment at 885°C during 30 min -1 hour, and quenched in water. Aging was done at  $538 \pm 14^\circ\text{C}$  for 4 to 8 hours, and then the material was air-cooled.

The cogging consists on the reduction of the as cast ingot of at least 50 percent at temperatures just below the beta transus temperature (i.e.,  $<945^\circ\text{C}$ ). In this way, a grain orientation in the direction perpendicular to the deformation, called direction of cogging is obtained (Figure 17).

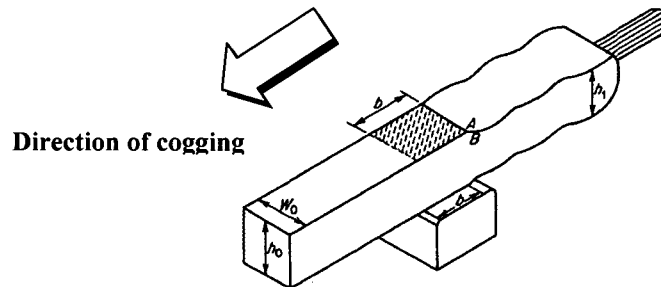


Figure 17. Cogging of a slab to obtain a pre-deformed ingot.

The materials produced by Dynamet or by casting plus cogging without further thermomechanical treatments are called *as received* in the present work.

Secondary thermomechanical treatments were carried out by Böhler Schmiedetechnik in a screw press as follows:

- SiC reinforced Ti64: forged in an open die at  $850^\circ\text{C}$  and approximately  $1\text{ s}^{-1}$  strain rate.
- SiC reinforced Ti64: forged inside a titanium alloy ring in an open die at 750, 850 and  $950^\circ\text{C}$  and approximately  $1\text{ s}^{-1}$  strain rate.

### 3.1.3 Density measurements

The density ( $\rho$ ) of different materials at room temperature were measured using the Archimedes's Principle by means of an analytical balance (accuracy of  $\pm 0.0005\text{g}$ ), and was calculated as:

$$\rho = \frac{W(a) * [\rho(\text{fl}) - \rho(a)]}{W(a) - W(\text{fl})} + \rho(a) \quad \text{Equation 32}$$

where  $W(a)$  is the weight of the sample in air,  $W(\text{fl})$  the weight of the sample distilled water,  $\rho(\text{fl})$  the density of the water, and  $\rho(a)$  density of the air.

### **3.1.4 Reinforcing titanium alloys with SiC particles**

The most important obstacle to produce this material is the reaction between titanium and SiC. Therefore, the goal is to obtain a non-porous material avoiding or reducing the production of brittle reaction products.

The samples were produced in cooperation with IFAM Dresden by HIP, in vacuum and varying the production parameters with the following criteria:

- *Powder size.* To obtain a good distribution of the particles, the Ti64 powders should be bigger than the SiC powders or equal. If the size of the powder of the matrix is too big, the result is a non-homogenous material. On the other hand, the finer the powders, the larger the surface of reaction and the higher the costs.
- *Mixture method.* The blending of the powders is the first step of the whole process. If the mixture is not good enough, the resulting distribution of the particles in the material will be non-homogeneous. Dry mixing and mixing with glycerine were tested in this work. The shape of the powder grains interferes in this process as well.
- *Temperature of consolidation.* The higher the temperature needed to close the pores (see sintering mechanisms), the faster the reaction between Si and titanium.
- *Pressure of consolidation.* The higher pressures are possible using some special die materials, and then the temperature and the time of consolidation can be decreased, decreasing the reaction zone thickness.
- *Time of consolidation.* The sintering process needs time for the solid diffusion of the metal atoms to close the pores. On the other hand, the longer the time, the larger the reaction zone.
- *Protective layer.* In the present work, it was tried to cover the particles with C using a PVD technique, which could act as sacrificial layer forming TiC instead of silicides.

## **3.2 Metallography**

### **3.2.1 Sample preparation.**

The samples for DMA (2x4x55mm), for compression tests (10 mm diameter x 15 mm long) and dilatometry (4x4x15mm) were cut by eroding. Additional cuttings were done by means of an Accutom-5 machine provided by Struers, using CBN discs (355CA) for the unreinforced titanium alloys, and diamond (352CA) discs for the composites.

The samples for metallography were embedded in a three-component resin with filler for hard mounts called TrioFix and produced by Struers.

The method used for grinding and polishing by means of an Abraim machine (Struers) and a Multidoser provided by Struers is described in Table 4.

**Table 4** Description of the grinding and polishing steps by means of the automatic grinder and polisher Abraim machine (Struers)

<i>Step</i>	<i>Cloth</i>	<i>Suspension</i>	<i>Pressure</i>	<i>Time</i>
Grinding	80 piano		5	Up to a planar surface
Grinding	220 piano		5	5-15 min
Fine grinding	MD-Largo	9µm Diamond	7	15 min
Polishing	DP-MOL	3 µm Diamond	5	10 min
Polishing	OP-Chem	OPS	3	30 min

### 3.2.2 Microscopy

Light optical microscope was used to observe the particles distribution, cracks and pores. Some samples were etched using Kroll's reagent (94 ml water, 2 ml hydrofluoric acid –Merck 98%– and 4ml nitric acid –Merck 35%–) to reveal the grain size and shape before and after deformation. The two phases of the reinforced and unreinforced Ti alloys were distinguished using the Back Scattered Electron mode in a Philips 30XL Scanning Electron Microscope (SEM). When the electron beam strikes the sample some of the electrons will interact with the nucleus of the atom. The electron with negative charge will be attracted to the positive nucleus but if the angle is just right instead of being captured by the "gravitational pull" of the nucleus it will circle the nucleus and come back out of the sample without slowing down. These electrons are called backscattered electrons (BSE) because they come back out of the sample without significant loss in energy. As the size of the atom nucleus increases, the number of BSE increases. Thus, BSE can be used to get an image that shows the different elements present in a sample. In this work, the contrast observed is due to the distribution of the alloying elements: Al-rich  $\alpha$ -phase dark, and V-rich  $\beta$ -phase, denser than the  $\alpha$  phase, appears bright. The TiC particles are darker than the  $\alpha$  phase. The worn surfaces were observed using SEM in the secondary electron (SE) and BSE mode. Energy Dispersive X-Ray (EDX) analysis were carried out to identify the elements of the phases of the as received materials, as well as of the samples after the wear experiments, the heat



treatments, the deformation tests, etc. Furthermore, line-scans were performed to analyse the gradient of some elements of interest.

### **3.2.3 Ion Beam Etching (IBE)**

Ion etching is a process applied to a sample under vacuum whereby a selected area of the surface can be bombarded by an energetic beam of ions. The bombardment of a material with ions with high kinetic energies erodes its surface, and rotation and angle of attack are important parameters to prevent the ion implantation.

The ions that impact the surface produce the following topographic effects that can reveal the microstructure [111]:

- Intergranular effects. The grain boundaries are dislocation networks, with lower surface binding energy than the grains, resulting in an increase of the sputtering yield value and finally, in larger erosion.
- Intragranular effects. Etch pits, faceting and ripples can be formed at the surface of the samples, depending on the grain orientation.
- Two phase system. The two phases of a system usually erode at different rates, giving a contrast visible under SEM and/or LOM.

The IBE with non-reactive atmosphere can be used to decrease the roughness and /or to etch surface of material [112]. Compared to the chemical etching, some advantages can be seen: the etching can be done without oxidising the sample and without dissolving some particular precipitates, and the parameters can be controlled very precisely.

### **3.2.4 Microhardness.**

Vickers micro-hardness (HV 0.2N) was measured in the matrix for the reinforced and the unreinforced materials by means of an universal hardness tester model M1C010 Emcotest, to find out about hardening effects of the particles in the matrices.

The micro-hardness was measured in the Ti662 reinforced with 20%TiC (CermeTi®-C-20-662) and unreinforced Ti662 (CermeTi®-C-662) samples after heat treatments under an atmosphere of air at low pressure where the diamond point hit any TiC particle were excluded.



### 3.4 EBSD

Electron Backscatter Diffraction (EBSD) gives crystallographic information from samples in the scanning electron microscope (SEM). In EBSD a stationary electron beam strikes a tilted crystalline sample and the diffracted electrons form a pattern characteristic of the crystal structure and orientation of the sample region from which it was generated. When the beam is scanned in a grid across a polycrystalline sample and the crystal orientation measured at each point, the resulting map will reveal the constituent grain morphology, orientations, and boundaries.

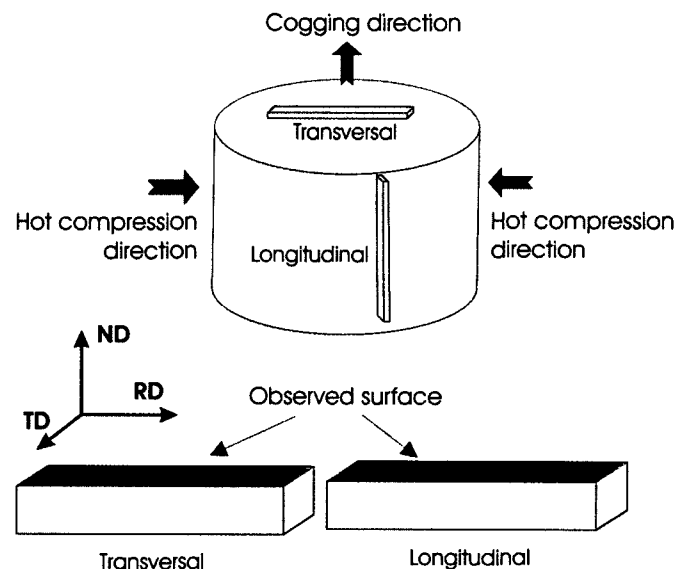


Figure 19 Transversal and longitudinal samples cut to observe the texture using EBSD (ND, TD, RD indicate axis of samples)

Two samples were cut from the Ti662 ingot as shown in Figure 19 to observe the grade of texture after the cogging.

### 3.5 Diffractometry

X-ray diffractometry experiments were carried out in the Institut für Chemische Technologien und Analytik, in the University of Technology of Vienna by Professor Frank Kubel. The phase distribution was also compared with the SigmaScan Pro estimations.

One sample of CermeTi®-C-12-662 as received was also X-Ray diffracted, looking for some evidence of Carbon diffusion into the matrix, as done in previous works [76]. The lattices parameters of the composite were compared to those of the unreinforced material.

### 3.6 Dilatometry

#### 3.6.1 Equipment.

The thermal expansion was measured by means of a dilatometer provided by BÄHR-Thermoanalyse GmbH model DIL 805A/D. Figure 20a) shows the heating (A) and the measurement (B) chambers, thermal and electronically isolated (C) one from the other.

The constituent parts of the heating chamber are (Figure 20b)): fixed holder of the sample (1), mobile holder of the sample (2), inductive oven (3), circulation of gas (4), thermocouple's interface (5).

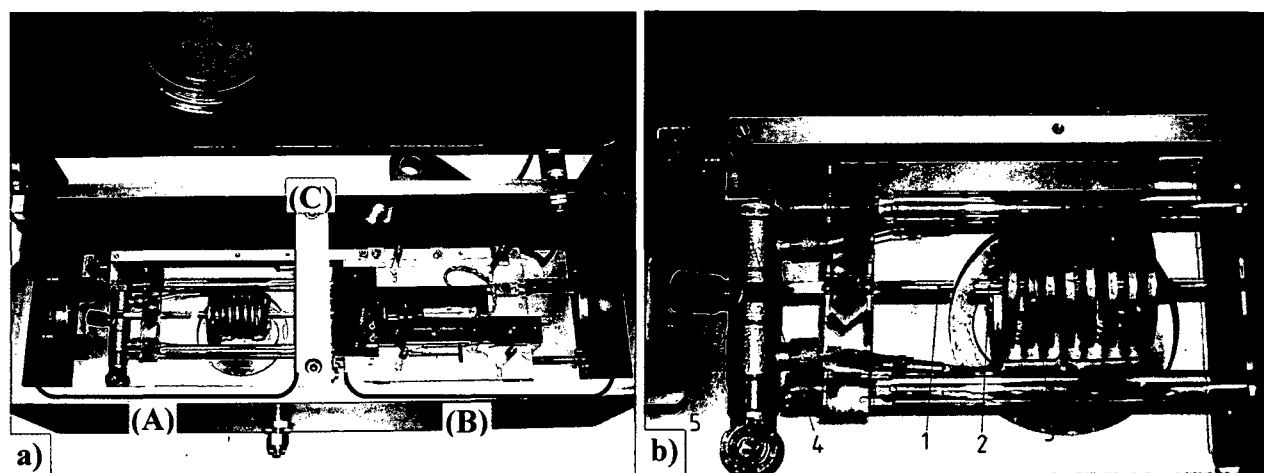


Figure 20. a) View inside of the Dilatometer DIL 805A/D. b) details of the heating chamber.

The temperature range permitted in the dilatometer is between  $20^{\circ}\text{C} - 1500^{\circ}\text{C}$  and  $-90^{\circ}\text{C} - 1000^{\circ}\text{C}$ ; up to  $1100^{\circ}\text{C}$  using the quartz holder, and up to  $1400^{\circ}\text{C}$  using the alumina holder. The maximum heating rate achieved by this equipment is  $4000\text{ K/s}$ . Different atmospheres (air, vacuum, Ar, etc) are allowed, as well as cooling gas with a maximum cooling rate of  $2500\text{ K/s}$ .

The calibrations were carried out for each temperature program, using the same parameters than for the tests from Platinum reference sample provided also by BÄHR-Thermoanalyse GmbH.

#### 3.6.2 Tests.

Due to the changes in volume during the alpha- beta transformation, it is possible to observe the behaviour of the titanium alloy in the range of temperature where the beta transformation occurs, and compare these results with the expansion of the pure titanium at the beta transus temperature. Diverse tests and heat treatments were carried out in order to study the temperature of the alpha-beta transformation, and the influence of the alloying elements. Figure 21 shows these tests; the

holding times were varied at high temperatures in order to find out the minimum time required for a complete transformation of alpha in beta. As explained in “limitations of the technique”, this phenomenon was hidden by the secondary reactions.

Table 5 shows the tested materials. A thermocouple type S (Platinum –Rhodium) was welded at the middle of the titanium or of the reference Pt sample to control the temperature.

**Table 5. Tests carried out with the Dilatometer.**

Test	Temp_01	Temp_04	Temp_05	Temp_02
Material tested	Ti662 Ingot	Ti64 PM	CermeTi®-C-662	Ti64 PM
		CermeTi®-C-20-662	Ti Grade 2	

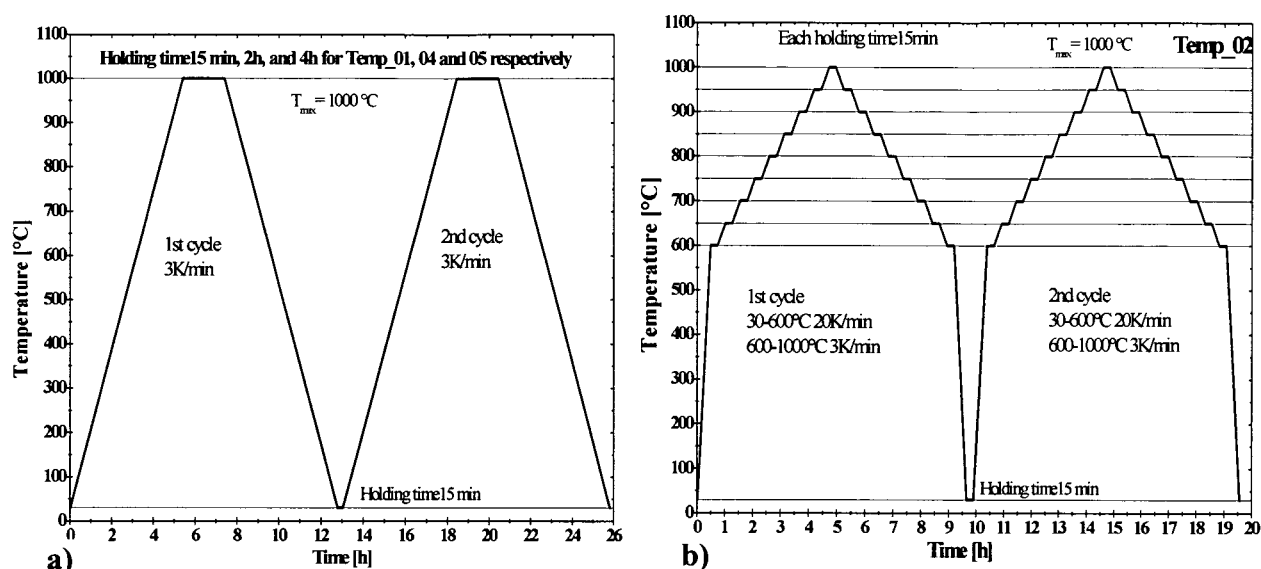


**Figure 21 Heat treatments.** a) two cycles heating up to 1000°C at 3K/min and cooling down to room temperature at 3K/min, with a holding time at 1000°C of 15 minutes. (Temp01), 2 hours (Temp04) and 4 hours (Temp05). b) Two steps cycles from 600°C up to 1000°C holding each 50°C for 15 minutes.

Test 1 was carried out for the CermeTi®-C-20-662 to compare with the unreinforced material and reveal some influences of the particles on the beta transus temperature.

### 3.6.3 Limitations of the technique.

Although the dilatometry is a good technique to measure the changes in length with the temperature, some limitations were found when titanium is the material to test.

- *Secondary reactions.* Due to the high temperatures required to reveal the beta transus range, some undesired secondary reactions occur between the holders and the samples. Figure 22 a) shows some reaction products expected in equilibrium, between Si and Ti at 849°C [113], as well as some previous studies [69] demonstrated the high reactivity of Si with titanium alloys.

Thus, the results in the changes of length measurements show a considerable constant contraction of the samples (Figure 22b)) for each cycle (1 and 2). What's more in the first heating cycle it is possible to observe an anomalous first large decrement of the length of the titanium sample (3) at approximately 800°C. The sputtering of the sample with gold results in worse results due to the reaction of Au with Si at only 360°C [114]. The reactions between aluminium and titanium are important even at low temperatures (Figure 23a) [115]) and the effect in the length changes is stronger for the alumina holder than for the quartz holder, as shown in Figure 23 b) (1), yielding CTE values up to 30 at 850°C for Ti64.

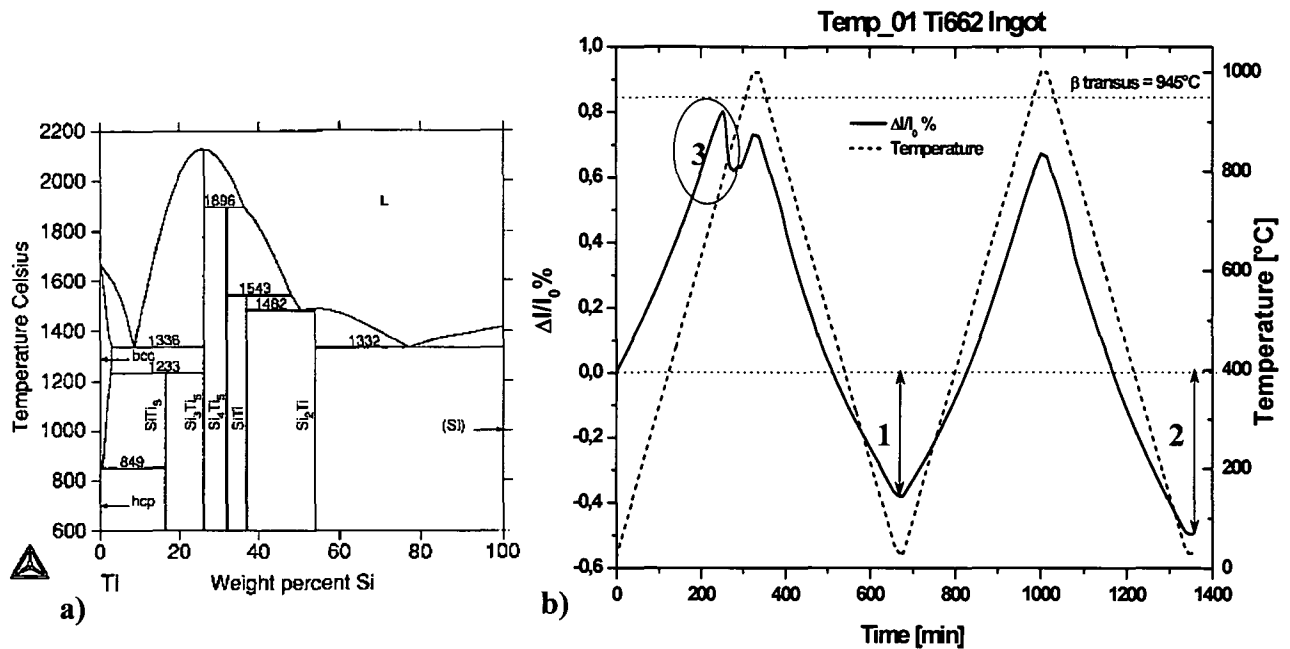


Figure 22. a) Si-Ti phase diagram [113] and b) measurement using  $\text{SiO}_2$  (quartz) holder.

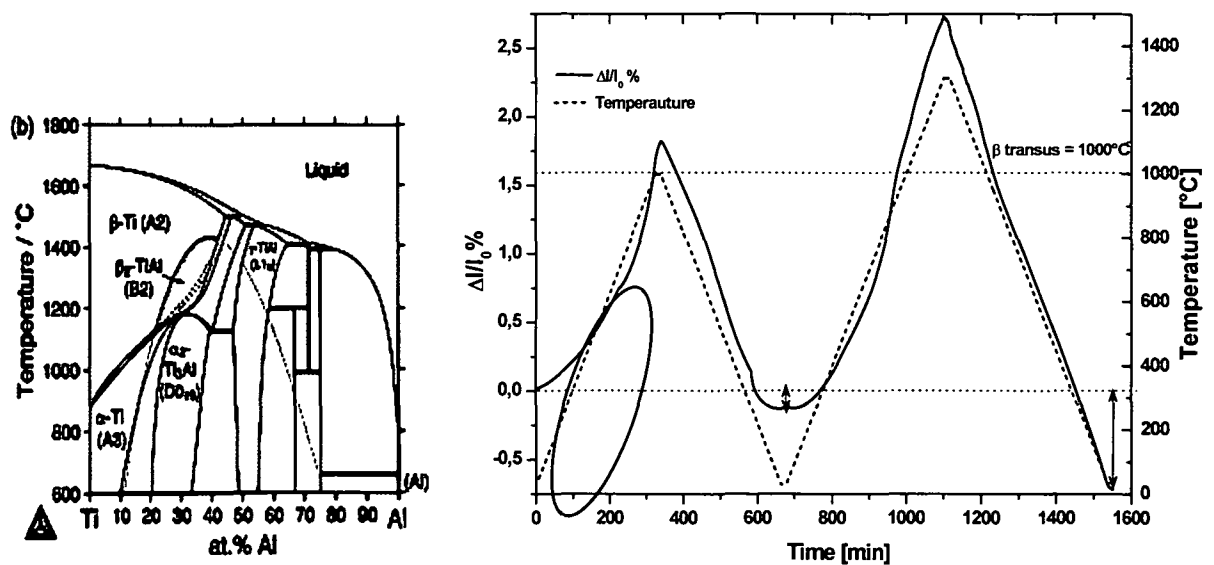


Figure 23 a) Al-Ti phase diagram [115] and b) measurement using  $\text{Al}_2\text{O}_3$  (alumina) holder.

The reaction products were analysed using SEM and EDX, and intermediate compounds found were  $Ti_xAl_y$  and  $Ti_xSi_y$ , respectively.

Figure 24 shows how the reaction products using a Quartz holder (a)) as well as an Alumina holder (b)) adhered to the surface, affecting the length measurement.

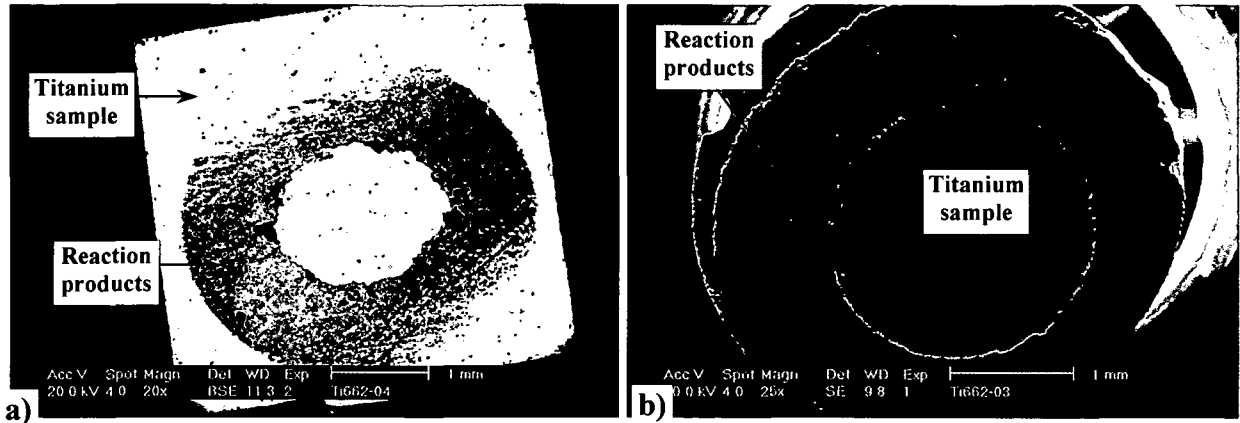


Figure 24. Pictures of the titanium samples after tests showing the reaction products adhered to the surfaces after using a) a quartz holder and b) an alumina holder

- *Cooling rate.* Although it is possible to reach high cooling rates using some inert gases, these should be pure enough not to contaminate the titanium alloys with N, C, O and/or other interstitial elements.

### 3.6.4 Calculation of the CTE.

The Coefficient of Thermal Expansion (CTE)  $\alpha$  was calculated following the equation:

$$\alpha = \frac{dl}{ldT} \quad \text{Equation 33}$$

where  $l$  is the length of the sample at the time  $t$  and  $dl/dT$  is the variation of the length with the temperature. The original data of change in length plotted against the temperature were interpolated every  $10^\circ\text{C}$  to reduce the number of data. This interpolated curve was smoothed using the FFT filter that consists in removing Fourier components with frequencies higher than:

$$\frac{1}{n\Delta t}$$

where  $n$  is the number of data points considered at a time, and  $\Delta t$  is the time (or more generally the abscissa) spacing between two adjacent data points. The resulting data were used to calculate the numerical derivative, and finally the coefficient of thermal expansion  $\alpha$  in ppm [25].

### 3.7 Dynamical Mechanical Analysis.

#### 3.7.1 Equipment and Young's Modulus

Dynamical Mechanical Analysis (DMA) delivers information on the visco-elastic behaviour of a material under small, sinusoidally modulated dynamic loads in dependence of temperature, time and frequency. The equipment utilized here was a DMA 2980 provided by TA Instruments.

In Figure 25 (a) the used clamp for the 3-point bending test is shown. The principle of the DMA test is represented in Figure 25 (b). A sinusoidal load  $\sigma$  is applied, and a sinusoidal strain response  $\epsilon$  is obtained. During the elastic mode, the strain response is in phase with the applied load, and the Young's modulus can be related to the resulting storage modulus. The difference of phase is represented with the  $\delta$  angle, where  $\tan(\delta) = \text{Loss modulus} / \text{Storage modulus}$ . For a completely elastic behaviour,  $\delta = 0^\circ$ , while for an ideal plastic material,  $\delta$  will be  $90^\circ$ .

Titanium alloys and their composites exhibit damping ( $0^\circ < \delta$ ). If the angle is bigger than a certain value, the Storage modulus cannot be related to the Young's modulus anymore. The criterion used here was that the elastic behaviour develops at  $\delta < 0.02$ , i.e. a deformation less than 0.035%.

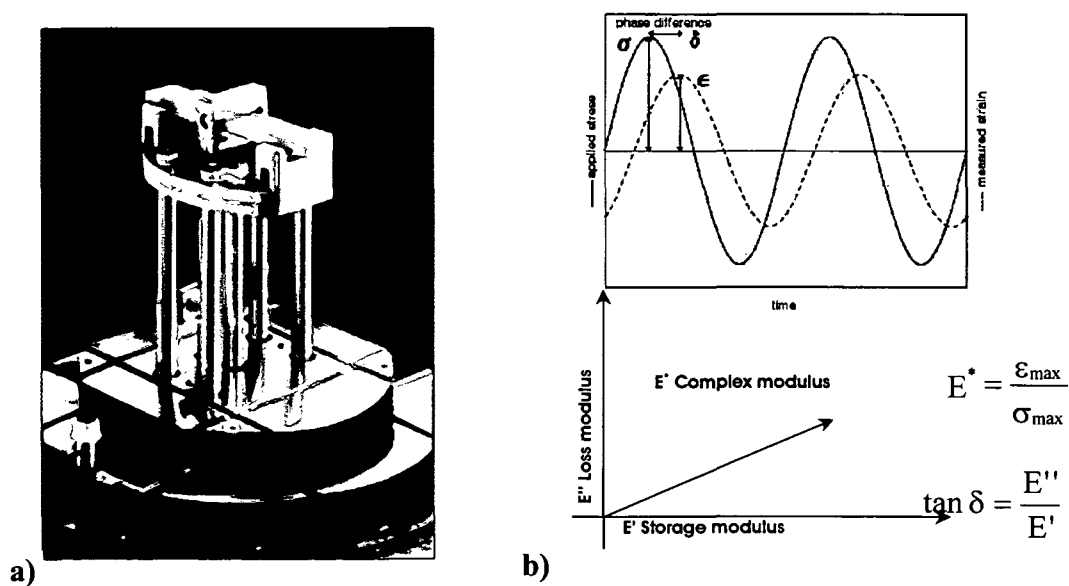


Figure 25. DMA tests to obtain the Young's Modulus, (a) 3 point bending clamp, (b) a sinusoidal load  $\sigma$  is applied, a sinusoidal strain response  $\epsilon$  is obtained, and the Young's modulus can be related to the storage modulus.

For an ideal elastic behaviour, the Storage Modulus  $E'$  is calculated as follows:

$$E' = K_S \frac{L^3}{6I} \left[ 1 + \frac{12}{5} (1 + \nu) \left( \frac{t}{L} \right)^2 \right] \quad \text{Equation 34}$$



where  $L$  is the sample length,  $t$  the sample thickness,  $I$  the moment of inertia of the sample,  $\nu$  the Poisson number, and  $K_S$  is the stiffness measured by the equipment.

### 3.7.2 DMA Tests

The tests for the Ti662 ingot, CermeTi<sup>®</sup>-C-662, CermeTi<sup>®</sup>-C-12-662, CermeTi<sup>®</sup>-C-20-662, Ti64 (PM), Ti64/TiC/12p and Ti64/SiC/15p were carried out up to 350°C at a heating rate of 2K/min. The specimen dimensions ( $L \times W \times H = 55 \times 4 \times 2 \text{ mm}^3$ ) for the 3-point bending tests had to be adjusted to the measurable stiffness range. The frequency used was 1 Hz, and the optimum amplitudes found were between 25  $\mu\text{m}$  and 40  $\mu\text{m}$  depending on the stiffness of the materials.

Furthermore, a measurement of a sample of Ti662 Ingot oriented in the direction of the cogging (transversal) was compared with that of a Ti662 Ingot sample oriented in perpendicular to the cogging (transversal), to see some influence of the grain orientation in the Young's modulus.

## 3.8 Hot compression tests.

### 3.8.1 Gleeble<sup>®</sup> 1500

The slower compression tests (up to  $1,5 \text{ s}^{-1}$  strain rate) of cylindrical specimens (10 mm diameter, 15 mm length) were carried out in a Gleeble<sup>®</sup> 1500 machine (Figure 26). The argon atmosphere was used to avoid the oxidation of the device and each sample was covered with delta glass except contact faces to avoid its corrosion. Because the Gleeble chamber is not gas tight, the Ar was contaminated with air. The specimens were heated by alternating current passing through the sample, and the temperature was controlled by a centrally spot welded K-type thermocouple. The stainless steel jaws were cooled continuously with a water-cooling system.

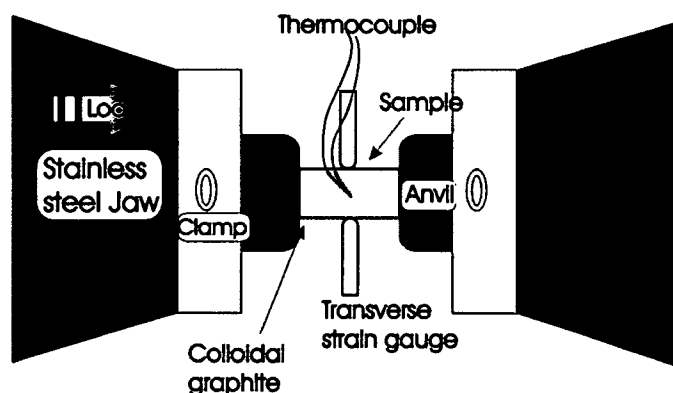


Figure 26. Compression tests: arrangement of Gleeble<sup>®</sup> 1500 with transverse strain gauge at the controlled temperature point.

Due to the non-uniform deformation and the barrelling caused by the high friction and the temperature gradient up to 80°C between the centre of the sample and the faces in contact with the colder Anvil, as

seen in the state of the art, the deformation was measured transversely at the central diameter using an Alumina and Quartz C-Gauge. As the load was applied only from one side, the C-Gauge moved freely accompanying the movement of the centre of the sample.

The true strain  $\varepsilon$  and the true stress  $\sigma$  of the flow curves were obtained as follows:

$$\text{True strain: } \varepsilon = 2 \ln \left( \frac{d}{d_0} \right) \quad \text{Equation 35}$$

$$\text{True stress: } \sigma = \frac{4F}{\pi d^2} \quad \text{Equation 36}$$

where F is the load, d the diameter of the sample at time t and  $d_0$  the initial diameter of the sample (at time=0).

### 3.8.2 SERVOTEST TMTS Test System

The highest strain rate  $15 \text{ s}^{-1}$  tests (Test series 1) were carried out at the Institut für Bildsame Formgebung (RWTH Aachen), in a SERVOTEST TMS Test System. The samples were lubricated with glass to decrease the friction and to obtain an uniform deformation. The flow curves were calculated using the following equations:

$$\text{True strain: } \varepsilon = \ln \left( \frac{l}{l_0} \right) \quad \text{Equation 37}$$

$$\text{True stress: } \sigma = \frac{4Fl}{\pi d_0^2 l_0} \quad \text{Equation 38}$$

Where F is the load, l the length of the sample at time t,  $l_0$  the initial length of the sample and  $d_0$  the initial diameter of the sample

### 3.8.3 Parameters and tests.

Four different compression tests were carried out:

- **Test series 1.** Standard tests carried out at 650, 750, 850 and 950°C and at 0.015, 0.08, 0.15, 1.4 and  $15 \text{ s}^{-1}$  strain rates (Figure 27a)) to obtain the flow data for the processing maps.
- **Test series 2.** Tests carried out at 650°C at  $0.15 \text{ s}^{-1}$  after a holding time of 40 minutes at the compression temperature (Figure 27b)). It was intended to observe a relaxation effect.
- **Test series 3.** Tests carried out at  $0.15 \text{ s}^{-1}$  and 650 and 750°C after holding at 900°C/1hour as shown in Figure 27c). This experiment can reveal some interstitial strengthening due to C, O, N, and or H that can diffuse from the air into the sample.

- **Test series 4.** Tests carried out at  $0.15\text{s}^{-1}$   $750^\circ\text{C}$  after a heat treatment consisting of: heating the sample at  $10\text{K/s}$  up to  $1000^\circ\text{C}$ , soaking time of 20 minutes, cooling down at  $1\text{K/s}$  to  $900^\circ\text{C}$ , soaking time of 1 hour and cooling down to the deformation temperature.

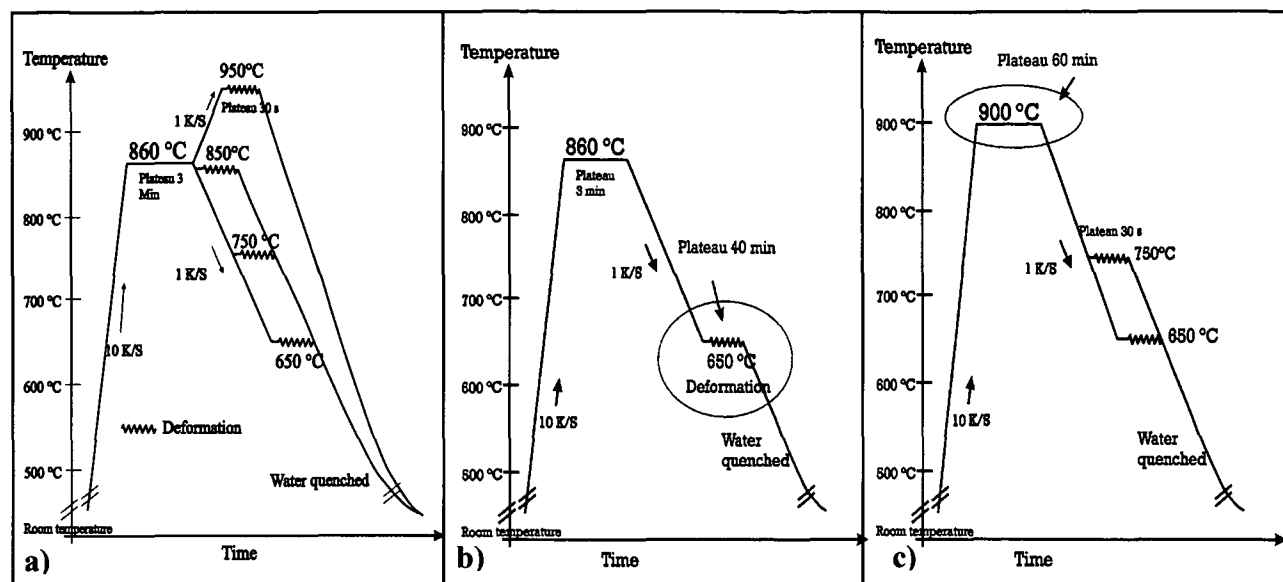


Figure 27. Thermo-mechanical history at the centre of the specimens. (a) Temperature and strain rate influence. (b) Holding time influence at  $650^\circ\text{C}$  (c) Influence of preceding heat treatment ( $\alpha/\beta$  portion)

Table 6. Compression tests

Test	Strain rate ( $\text{s}^{-1}$ )	Temp. of def. ( $^\circ\text{C}$ )	Materials
Series 1	0.015 – 0.08 – 0.15 – 1.4 – 15	650 – 750 – 850 – 950	Ti662 ingot CermeTi <sup>®</sup> -C-662 CermeTi <sup>®</sup> -C-12-662
Series 1	0.015 – 0.08 – 0.15 – 1.4	650 – 750 – 850 – 950	CermeTi <sup>®</sup> -C-20-662
Series 1	0.015 – 0.15 – 1.4	650 – 750 – 850 – 950	Ti64 PM Ti64/TiC/12p
Series 2	0.15	650	CermeTi <sup>®</sup> -C-662 CermeTi <sup>®</sup> -C-20-662
Series 3	0.15	650 – 750	CermeTi <sup>®</sup> -C-662 CermeTi <sup>®</sup> -C-20-662
Series 4	0.15	750	CermeTi <sup>®</sup> -C-662 CermeTi <sup>®</sup> -C-20-662

Table 6 gives a summary of the compression tests carried out in this work.

### 3.9 Wear tests.

#### 3.9.1 Description of the equipment.

Pin on disc and pin on ring wear tests were carried out at the Austrian Research Centre Seibersdorf (ARCS), in the Aerospace Technology OrgUnit by Dr. A. Merstallinger in air at room temperature. Humidity was only recorded, but not controlled. Cylindrical pin samples of 4 mm diameter were used for the pin on ring tests, and cylindrical pin samples with 4 mm diameter and conical shape (2mm diameter, 30° angle) for the pin on disc tests. Rings and discs made of 100Cr6 steel (AISI52100) were used as counter-parts (Figure 28).

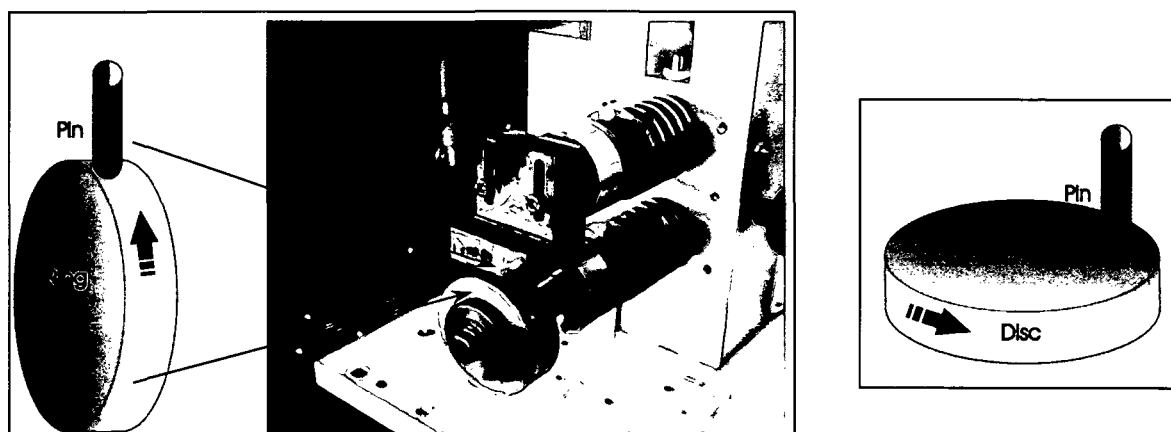


Figure 28. a) Pin on ring machine: pin of Ti alloys and ring of steel at ARC-Seibersdorf. b) Pin on disc array

The range for the pin on disc tests of normal pressure was 0.6 to 4.8 MPa, the relative velocity from 0.1 to 0.9 m/s. For the pin on ring tests, the range was 2 to 9.3 MPa and 0.1 to 1.5 m/s.

#### 3.9.2 Surface and subsurface studies.

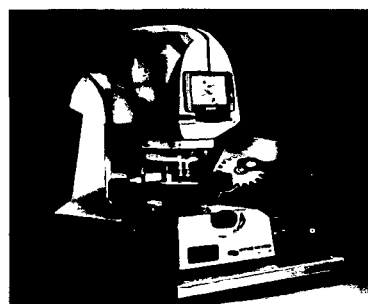


Figure 29. Optical Profiler provided by Veeco.

The topography of the pins and rings before and after test was studied using the NT1100 optical profiler provided by Veeco (Figure 29) at the ARCS. The device has a high resolution in 3D surface measurement, from sub-nanometre roughness to millimetre high steps. It is possible also to obtain the profile in 2D (depth vs. distance) by drawing a line in the 3D graphic.

The subsurfaces were studied by cutting the samples transversally in the direction of sliding and then observed with SEM in the BSE mode.

### **3.9.3 *Wear rate and friction coefficient.***

The friction force (F) is the tangential force that must be overcome in order for contacting bodies to slide over another, and the normal force (N) is measured. The friction coefficient is defined as:

$$\mu = \frac{F}{N} \quad \text{Equation 39}$$

The wear rate k is the loss of volume (W), divided by the normal force (N) and the total sliding distance (D).

$$k = \frac{W}{ND} \quad \text{Equation 40}$$

the loss of volume was calculated by measuring the change in length during the test and the change in the initial diameter for the conical sample.

## 4 Results.

### 4.1 Microstructure features.

#### 4.1.1 As received

Figure 30a), b) and c) show the phase distribution of the  $\alpha$ -grains embedded in  $\beta$ -phase of all the unreinforced alloys. The ingot material presents a fine globular microstructure, consisting of alpha phase (darker) embedded in a beta field (brighter). The alloys produced by powder metallurgy show a microstructure called Widmanstätten consisting of three micro-constituents: lamellar  $\alpha+\beta$  colonies, grain boundary  $\alpha$  and a thin  $\beta$  layer in-between the colony side-plates and the  $\alpha$  grain boundaries. The amount of alpha phase at room temperature is higher for Ti64 alloy than for the Ti662 alloy.



Figure 30. Ti662 with dark  $\alpha$ -phase within the bright  $\beta$ -phase (a) ingot Ti662: globular microstructure, (b) CermeTi®-C-662: Widmanstätten microstructure, and (c) Ti64 (PM): Widmanstätten microstructure with more alpha phase than in the Ti662 alloys (SEM).

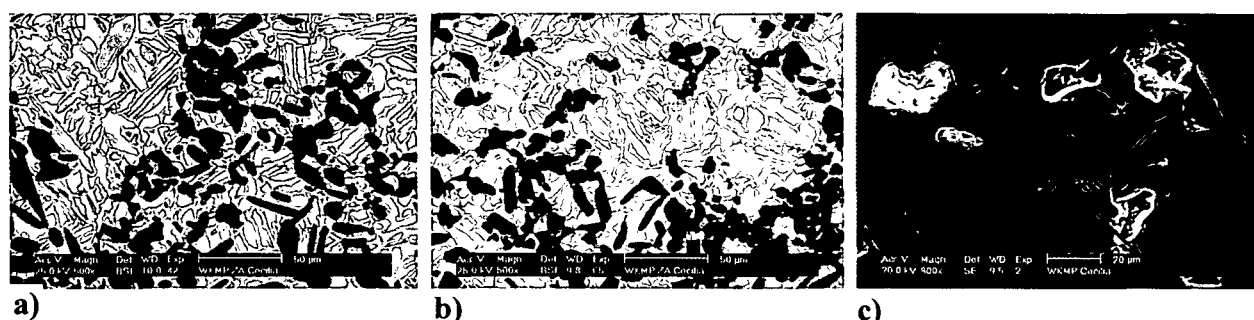
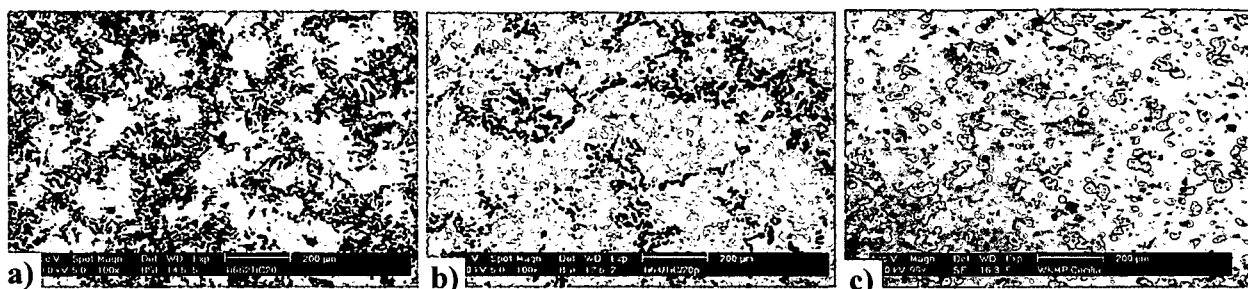


Figure 31. Reinforced materials showing smaller and more disordered  $\alpha$  phase in the unreinforced zones than near the TiC particles: a) CermeTi®-C-20-662 and b) CermeTi®-C-12-662. c) Ti64/SiC/15p showing porosity and secondary reaction products of the interfaces (SEM).

Figure 31a), b) and c) show the Particulate Reinforced Ti alloys (PRTi). The  $\alpha$ -phase is roughly twice as big in the unreinforced zones than close to the TiC particles. Ti64/SiC/15p shows porosity and secondary reaction products of the interfaces.

The distributions of the ceramic reinforcements in the PRTi are observed in Figure 32. TiC particles decorate the grain boundaries at the former borders of the Ti662 and Ti64 powder grains, as observed in Figure 32a) and b) respectively. Figure 32c) shows a much better distribution of the SiC particles in the Ti64 matrix but also high porosity.



**Figure 32. Ceramic-particle distribution:** a) and b) CermeTi®-C-20-662 and CermeTi®-C-12-662 respectively showing TiC particles decorating the grain boundaries, and c) Ti64/SiC/15p with a good SiC distribution and pores (white) (SEM).

Titanium alloys and composites produced by Dynamet using the CHIP powder metallurgy method show pores (Figure 33a)). In the reinforced material the TiC particles are agglomerated, and pores are also in these ceramic clusters (approximately 0.1% vol), as shown in Figure 33b).

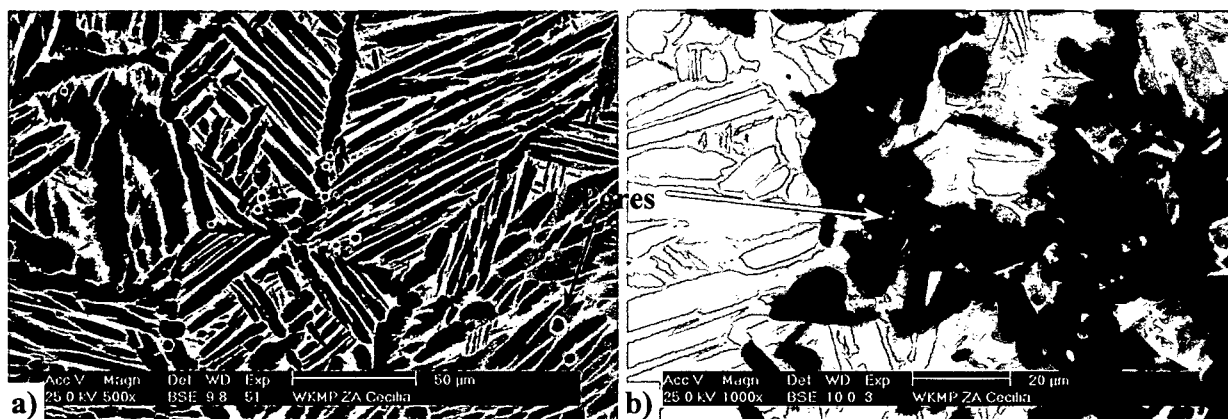


**Figure 33. Porosity in the materials produced by powder metallurgy** a) CermeTi®-C-662 and b) CermeTi®-C-20-662, showing pores between the ceramics (SEM).

Figure 34 shows the distribution of the alloying elements (Al, V and Sn) in a Ti662 Ingot alloy obtained with an EDX Line –scan test. V is present mostly in the beta phase, Al in the alpha phase, and Sn is distributed homogeneously in both phases. In Figure 35 can be observed that there is no carbon gradient. The signal of the EDX line scan was smoothed, i.e. that the CPS values are not really the obtained with the test, but represent the tendency (arbitrary units).

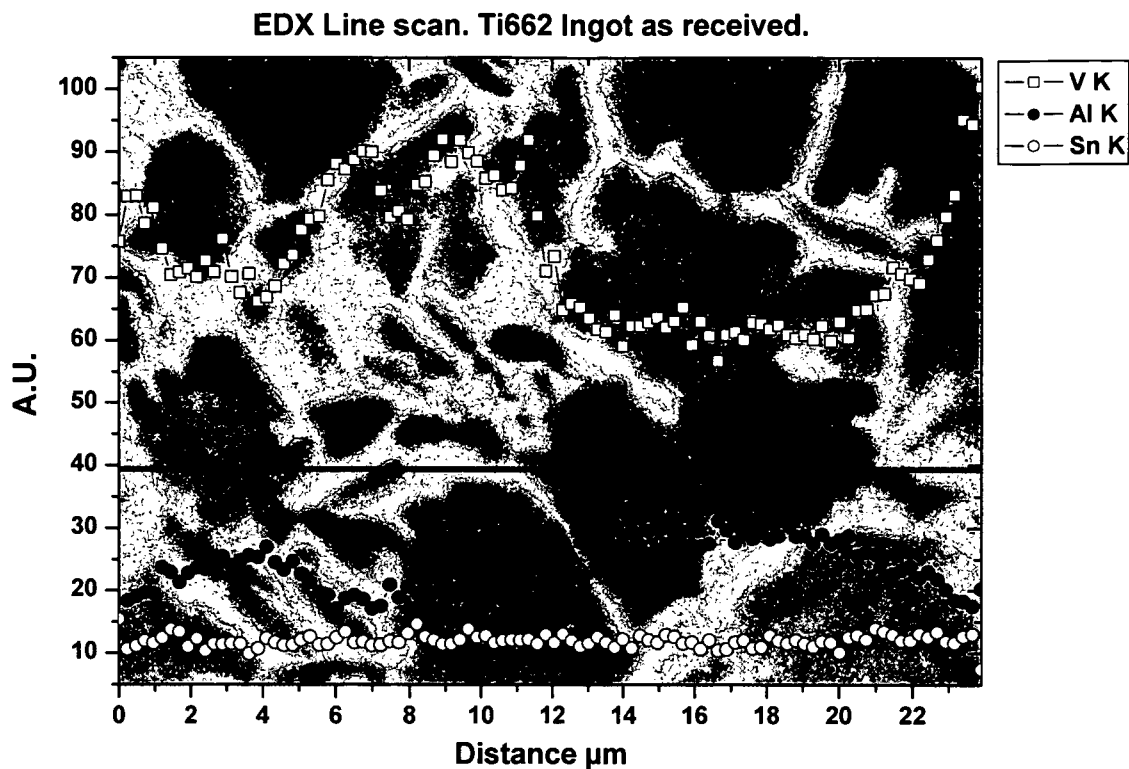


Figure 34. EDX Line-Scan along the horizontal line of Ti662 Ingot as received showing the enrichment of the alloying elements: V in the  $\beta$  phase, Al in the  $\alpha$  phase, and Sn homogeneously in both phases (SEM-BSE)

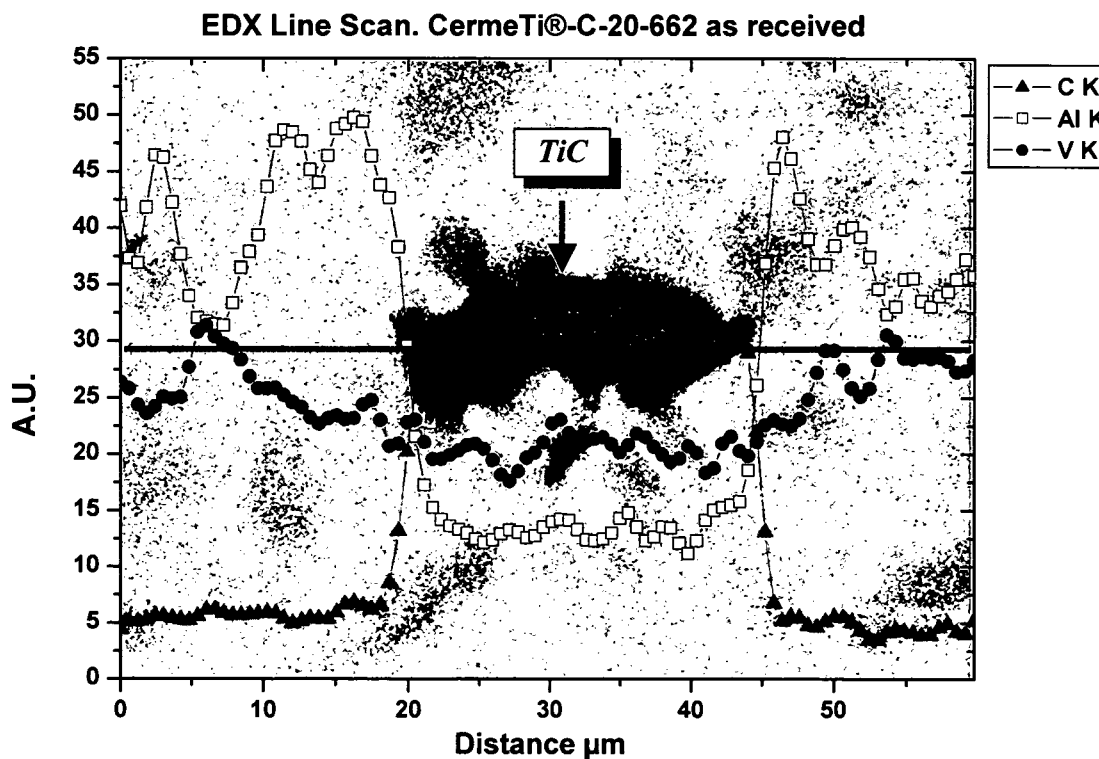
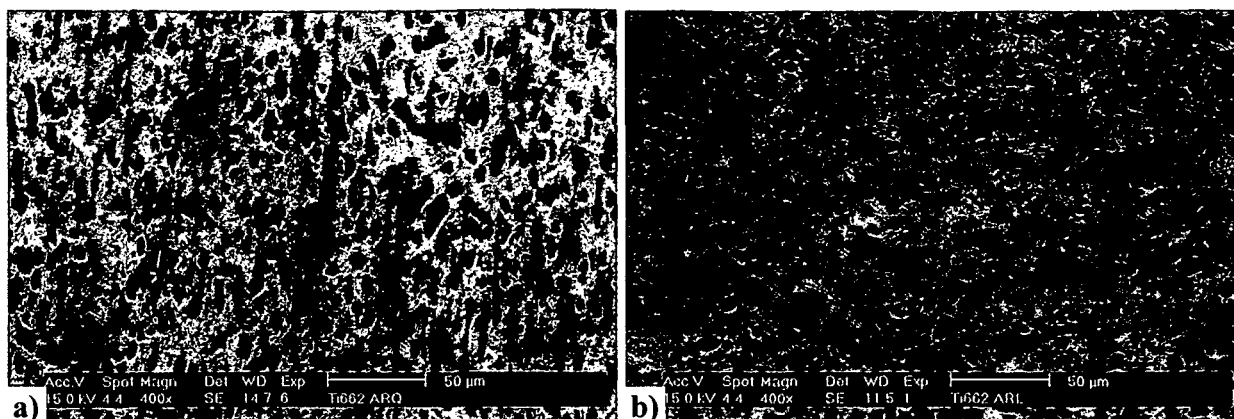


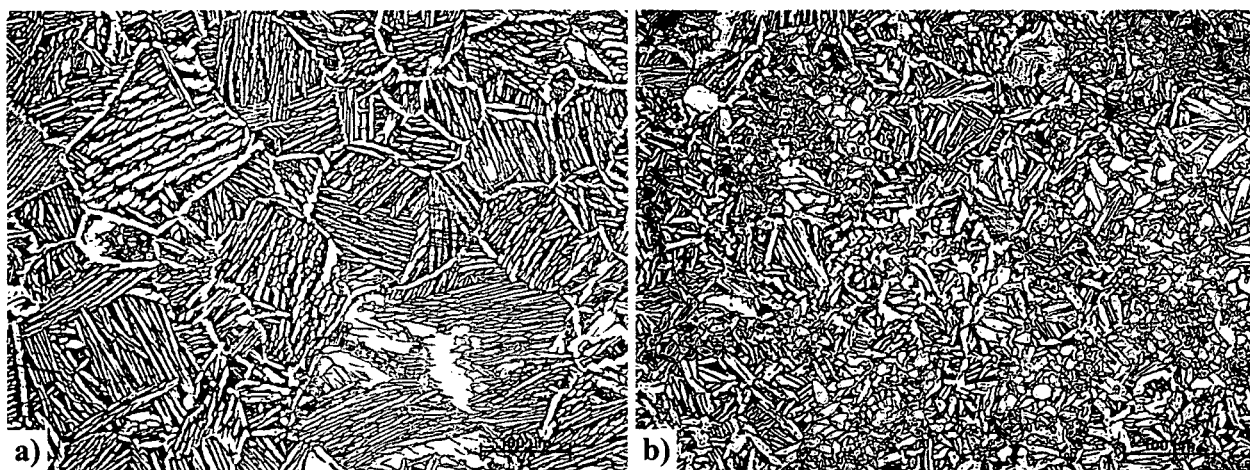
Figure 35 EDX Line-Scan along the horizontal line for a CermeTi®-C-20-662 as received sample, showing the enrichment of V in the beta phase, Al in the alpha phase, and C is confined to the TiC particles (SEM-BSE).





**Figure 36** Ti662 ingot cut in the a) longitudinal direction showing alpha elongated grains oriented in the cogging direction b) transversal direction showing no preferred orientation of the alpha grains (SEM-Kroll).

Due to the deformed characteristic of the Ti662 Ingot material, the alpha grains appear oriented in the direction of the cogging (Figure 36).



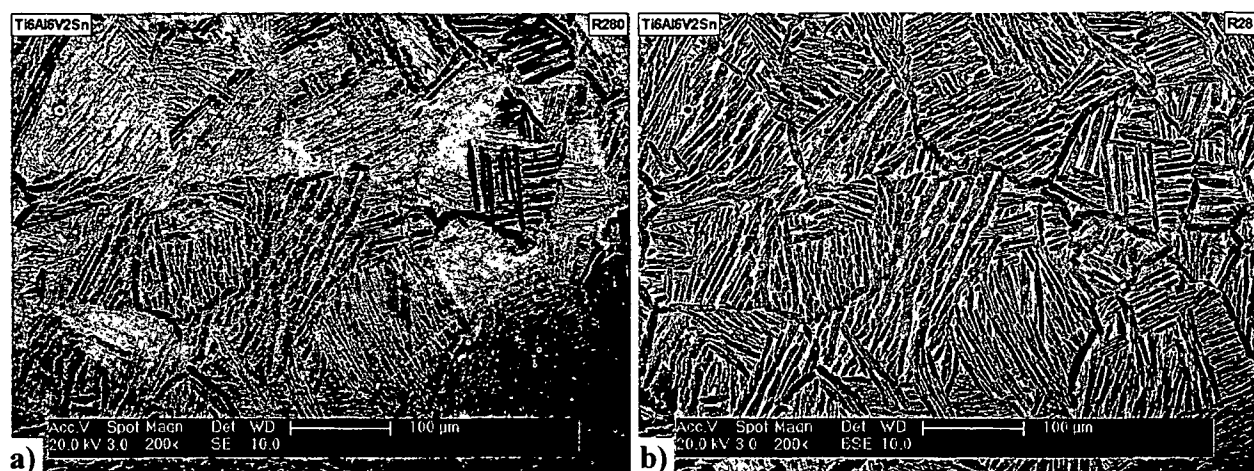
**Figure 37** LOM pictures after etching with Kroll a) alpha lamellar with a grain size between 50 and 300µm. b) grain refinement and disordered alpha as a result of the presence of TiC particles (grey).

Figure 37 shows the effect of the TiC particles in the grain size and in the alpha distribution. In a), the original  $\beta$  grain of about 50-400µm can be seen, and also some sub-grains can be distinguished (alpha colonies oriented in the same direction). In Figure 37b), the Ti662 original  $\beta$  grains are smaller (up to  $\approx 100\mu\text{m}$ ), and the alpha phase appears less oriented than in a).

#### 4.1.2 Ion Beam Etching pictures.

After etching the unreinforced samples with the IBE, it is possible to distinguish not only the alpha beta distribution, but also the sub-grains due to the different orientations. Figure 38 shows the contrasts of the sub-grains inside the grains (a) using the SE, in comparison with the BSE method, which does not provide orientation contrast within the alpha – beta distribution.

At higher magnifications it is possible to see that the IBE erodes the surface according to the grain (or sub-grain) orientation, and that the contrast in SE is the result of the roughness of the surface; i.e., the brighter zones correspond to the rougher surfaces (more electrons reflected), and the darker zones to the smoother ones.



**Figure 38.** Ti662 PM after Ion Beam Etching showing the lamellae alpha in the beta field a) in the SE mode, the grains and sub-grains orientations can be distinguished, while b) in the BSE mode there is only a contrast between the alpha phase from the beta field

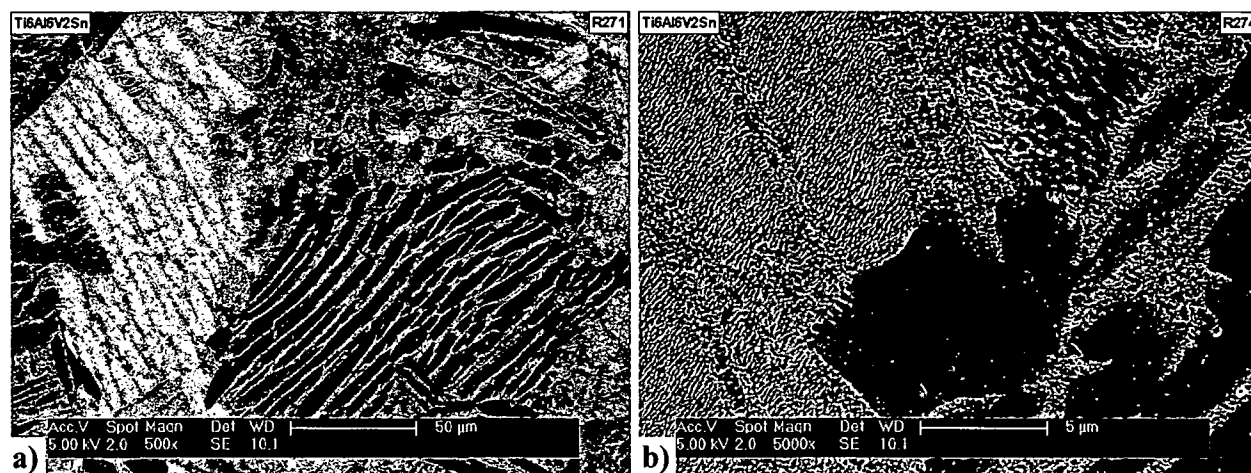


**Figure 39.** Ti662 PM after Ion Beam Etching observed using Field Electron Gun (FEG) showing a) the contrast between the grains due to b) the different roughness provoked on the surfaces.

Figure 40 shows the microstructure of the titanium Grade 2. The whole material is composed by alpha phase, and the different contrasts observed in a) distinguish one grain from the other generated by the ion-etched roughness generated on the surface (Figure 40b)). The grain size is about 20-100µm, and the material present an equiaxed microstructure.

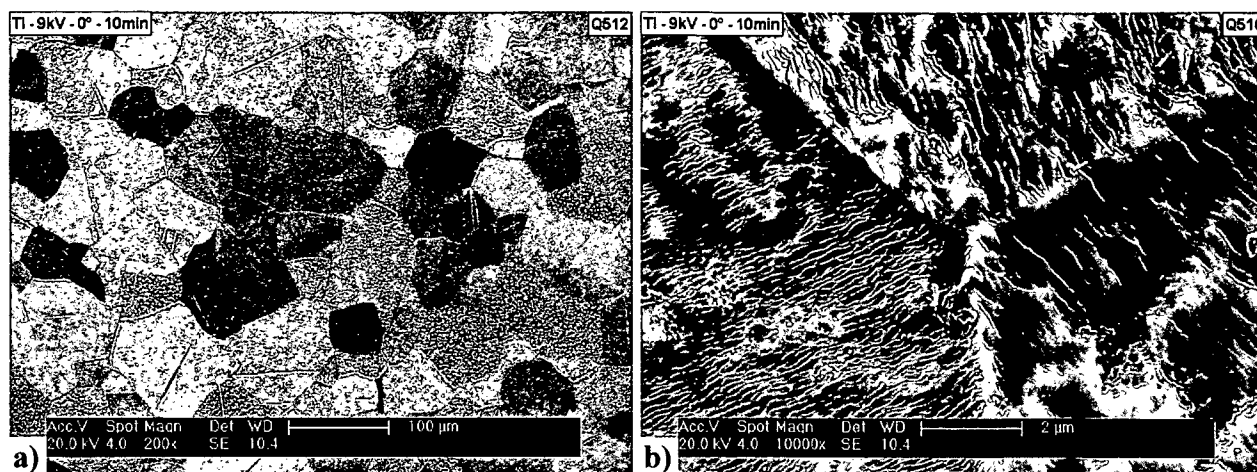


**Figure 40** Titanium Grade 2 (CP) after Ion Beam Etching showing a) the contrast between the grains due to b) the different roughness provoked on the surfaces (SEM).

#### 4.1.3 *SiC reinforced Ti64*

The composite Ti64/SiC/15p was developed at IFAM (Institut für Fertigungstechnik und Materialforschung) Fraunhofer Ges. in Dresden, by Dr. Thomas Schubert. Several trials were carried out in order to obtain a material with little porosity and small reaction zone by sintering and hot pressing. Table 7 shows all the trials and the comments about the results using a heating rate of 10K/min in Argon atmosphere. Two microstructural phenomena were observed: the thickness of the reaction zone, and the distribution and size of the pores.

**Table 7.** Trials to produce the SiC reinforced titanium alloy

N°	% SiC	Powders Ti64	SiC size	holding time	temp of HIP	rate of compact.	Porosity	reaction zone
S101	20	rounded dry mixed	Ti64 F600	30 min	1000°C	8kN/min	high	consumes most of the particles
S102	20	rounded dry mixed	Ti64 F600	5 min	1000°C	8kN/min	high	consumes most of the particles
S103	20	rounded dry mixed	Ti64 F400	15 min	900°C	4kN/min	low (between the ceramic particles)	smaller than 2µm
S104	20	rounded dry mixed	Ti64 F400	5 min	850°C	8kN/min	high	smaller than 2µm
S105	20	rounded dry mixed	Ti64 F400	5 min	880°C	4kN/min	intermediate (between the ceramic particles)	smaller than 2µm
S106	20	rounded dry mixed	Ti64 F400	60 min	880°C	4kN/min	low (between the ceramic particles)	smaller than 4µm

		dry mixed						ceramic particles)	
S107	15	rounded dry mixed	Ti64	F400	60 min	910°C	4kN/min	low (between the ceramic particles)	smaller than 7µm
S108	15	edged mixed	Ti64 dry	F400	15 min	900 °C	4kN/min	low (between the ceramic particles)	smaller than 2µm
S109	15	edged mixed	Ti64 wet	F400	15 min	900 °C	4kN/min	low (between the ceramic particles)	Big pores and particles agglomeration

It can be observed that 1000°C is a extremely high temperature at which the reaction between the Ti and the SiC accelerates considerably. All the trials are shown from Figure 41 to Figure 48 .

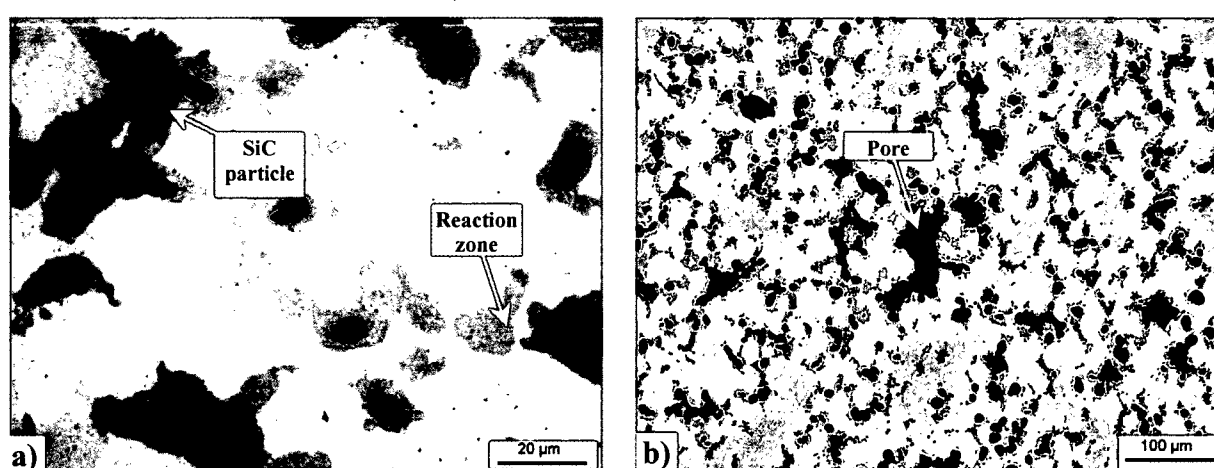


Figure 41. Sample S101 (LOM). Consumption of the particles through a) the reaction between particle and matrix and b) presence of big pores can be observed.

As observed in the Figure 42, the porosity comes also from the round shape of the Ti64 powders.

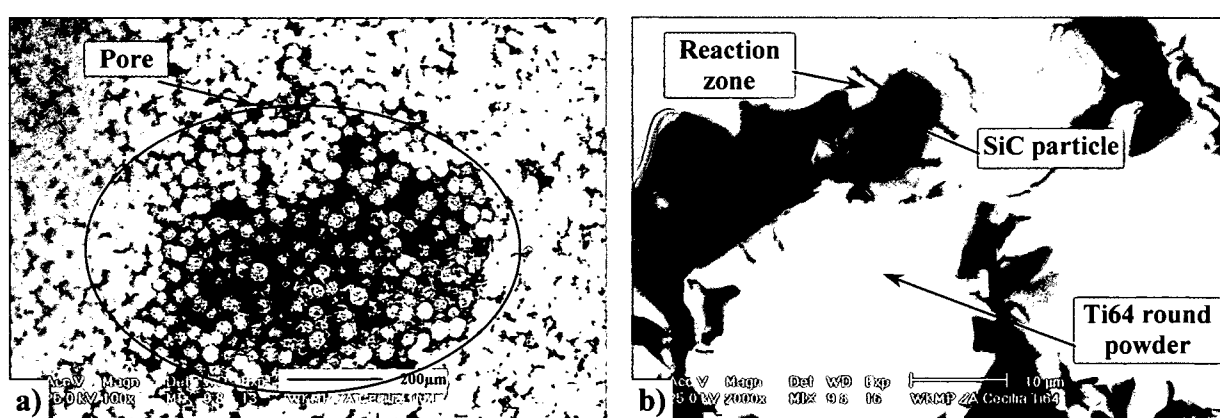


Figure 42. Sample 102 (SEM). Porosity due to the round powder titanium, as shown in (a), and due to the formation of a large brittle ceramic reaction zone, as shown in picture (b)

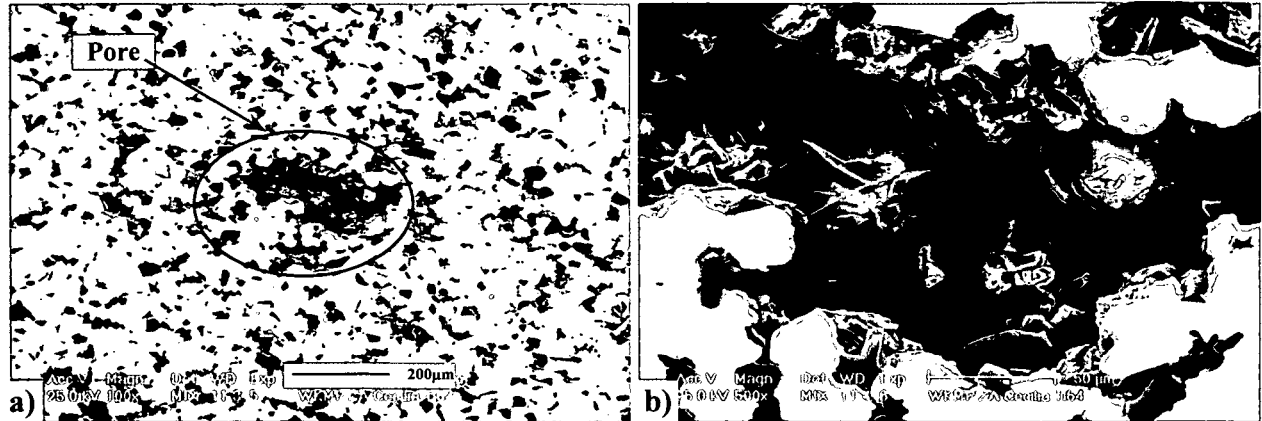


Figure 43. Sample 103 (SEM). Larger SiC particles, longer times and lower temperatures than in sample 102 results in a) less porosity and b) smaller reaction layer.

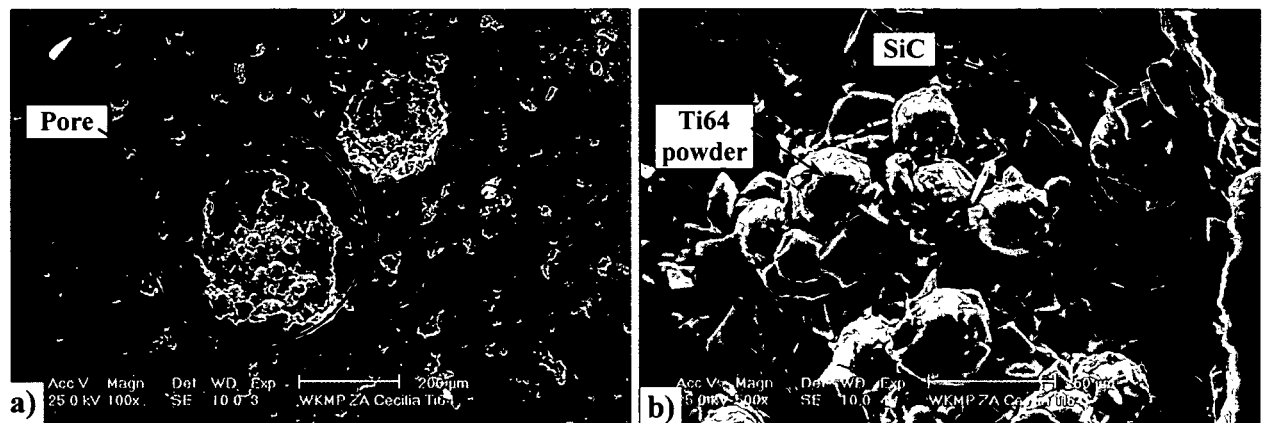


Figure 44. Sample 104 (SEM). 850°C shows to be a too low temperature for sintering, even by increasing the pressure of compression resulting in a) high porosity and b) big amounts of non sintered Ti powders.

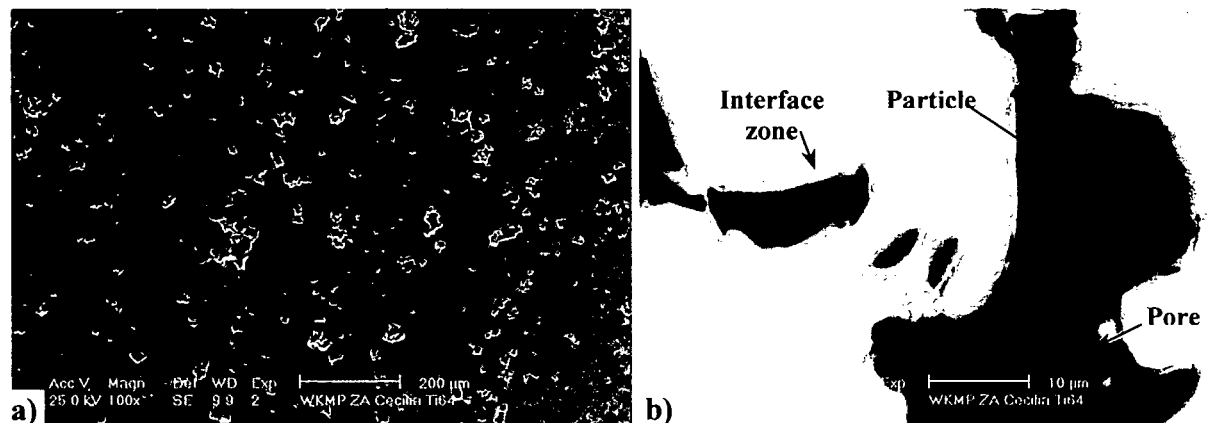


Figure 45. Sample 105 (SEM). Porosity between the ceramic particles a) overview: pores and an homogeneous particle distribution b) BSE Image showing the particles, the pores and the interface zone

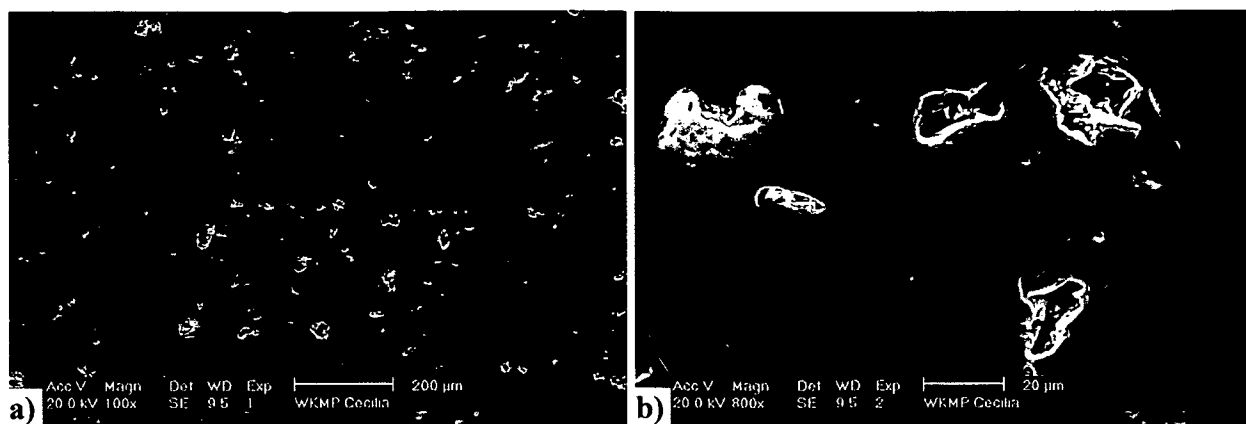


Figure 46. Sample 107. a) Low porosity and good distribution of the ceramic particles b) Pores between the particles and large reaction zones (SEM).

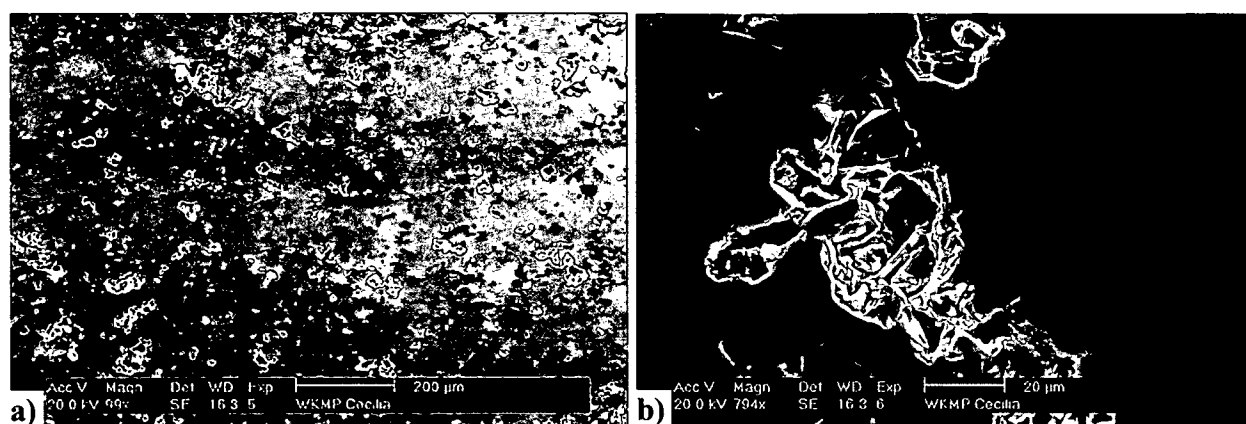


Figure 47. Sample 108 showing the porosity and the particle distribution (SEM).

The mixture of the matrix powders and the TiC particles with glycerine results in the agglomeration of the particles. Thus, the material got a bad particle distribution and big pores within particles clusters (Figure 48).

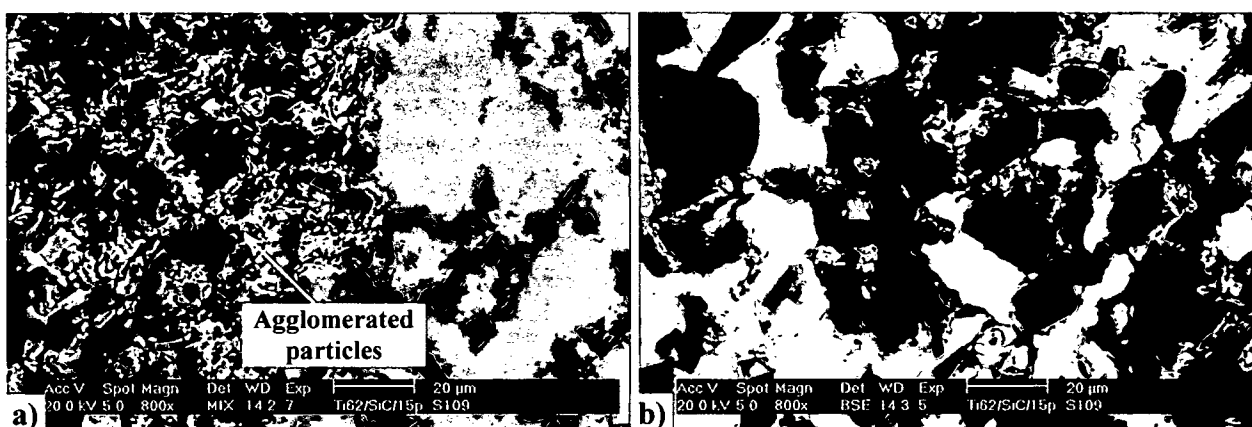


Figure 48. Sample 109. a) Large amount of agglomerated SiC particles b) Pores between the particles (SEM)

X- Ray line scan tests were performed in order to see the distribution of the elements in samples produced using different parameters. Figure 49 and Figure 50 show the Si, Ti, Al and V gradient through the horizontal lines.

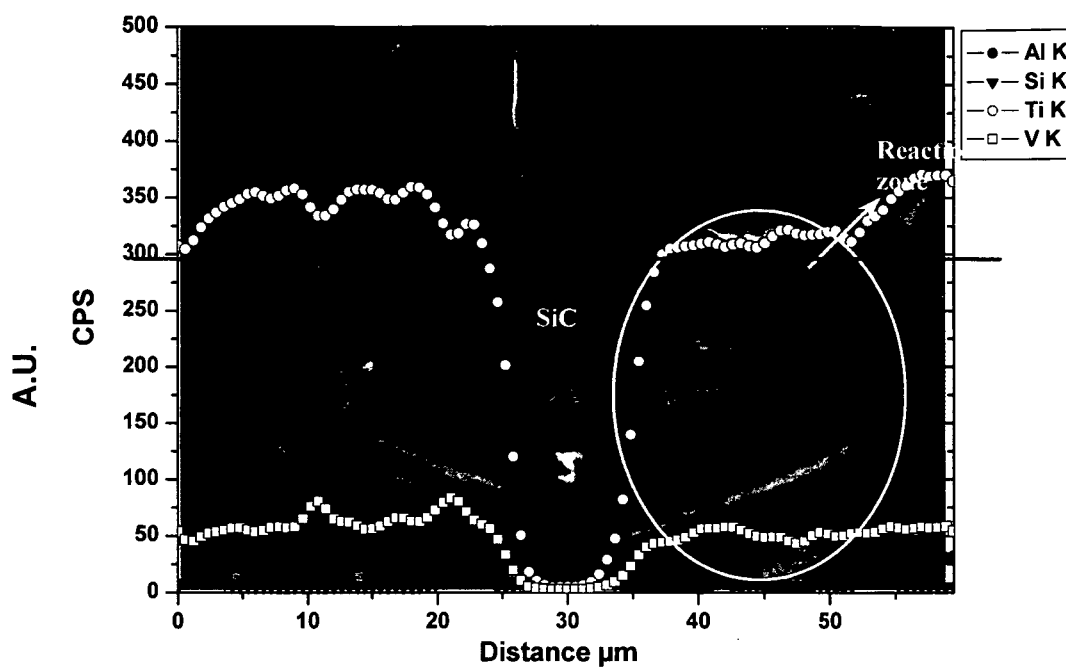


Figure 49. Line scan showing the presence of increased Si content along Ti, and V in the reaction zone sample S102.

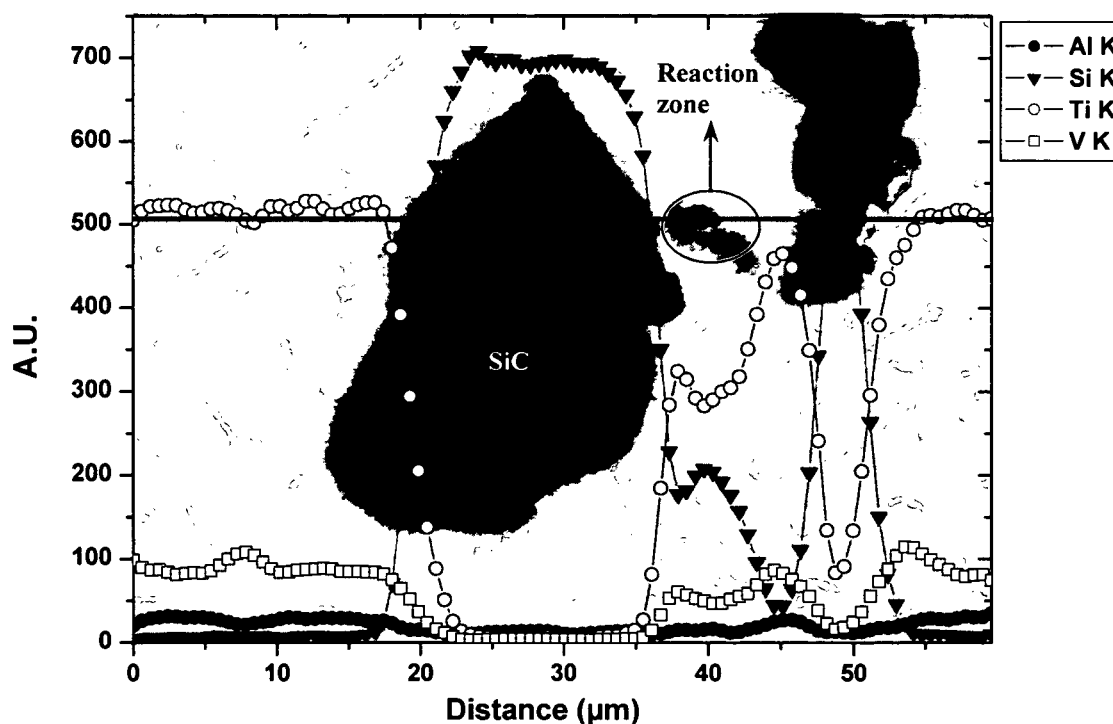


Figure 50. Smaller reaction zone by decreasing the sintering temperature sample S105 (SEM-BSE).

Comparing sample 102 with sample 105 (Figure 50) less Si penetration into the matrix is observed for the second sample; i.e. Si is almost limited to the insides of the particles, and the Ti to the matrix. Nevertheless, there is a small reaction zone around the particles.

#### 4.1.4 Microstructures after heat treatments.

Figure 51 shows the alpha-beta evolution with the temperature. These samples were heated in an induction oven and then water quenched.

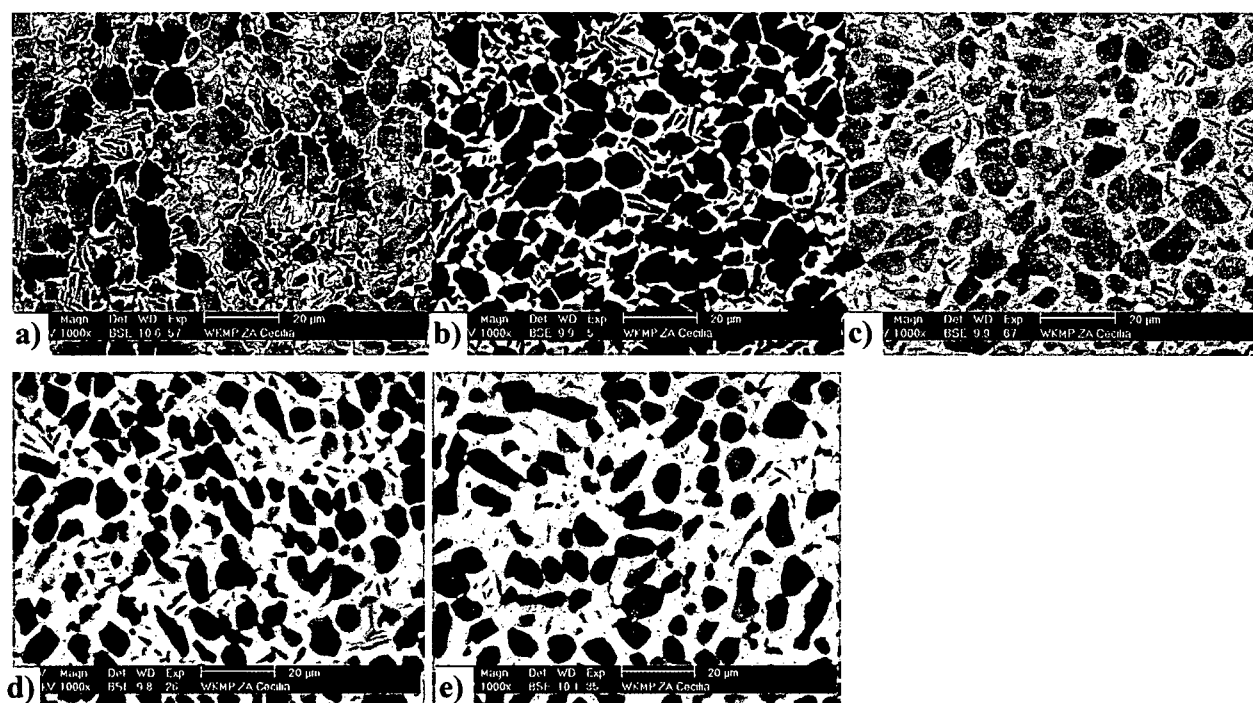


Figure 51. SEM-BSE micrographs of Ti662 ingot material: a) as received, and heat treated (from below) for 15 min and water quenched from b) 780°C, c) 820°C, d) 840°C, e) 860 °C.

It can be observed that the smaller alpha phase transforms first in beta phase, and that the alpha phases tend to be rounded, probably decreasing the surface energy. No influence of time on the isothermal phase relation in Ti662 was detected within the tested period of 15-45 min.

Figure 52 a) shows the acicular microstructure of the Ti662 Ingot after heating the sample at 10K/s up to 960 °C (above the beta transus temperature), holding time of 15 minutes, cooling down to 600°C, holding time of 15 minutes, and water quenched. On the other hand, the original globular microstructure of the ingot Ti662 was not really changed by a heat treatment consisting in heating the sample up to 600°C, holding time of 15 minutes and water quenched (Figure 52b)). A similar phenomenon was observed in Figure 53a) and b) for 800 °C and 820°C respectively.



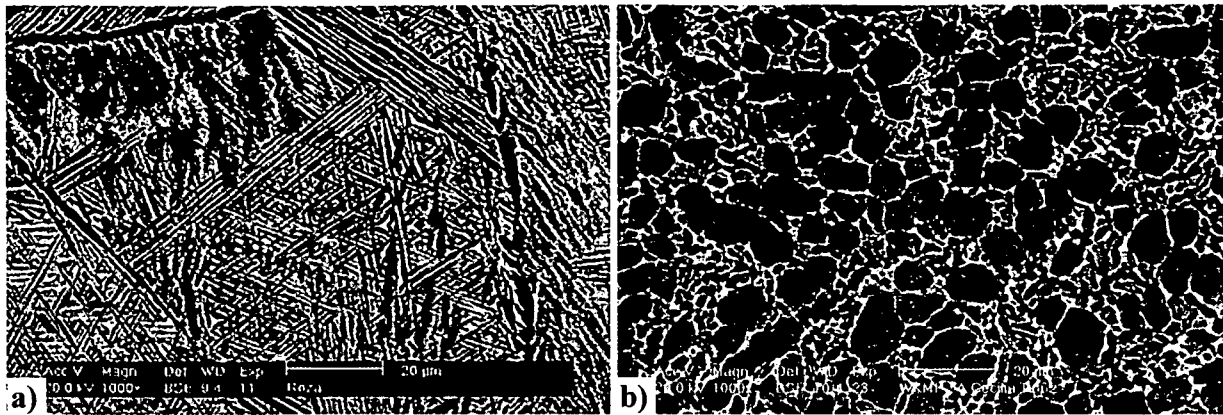


Figure 52. Ti662 Ingot quenched from 650°C with different previous heat treatments (a) cooled down from beta transus temperature, acicular microstructure (b) heated from room temperature, globular microstructure (no changes in shape from original) (SEM).

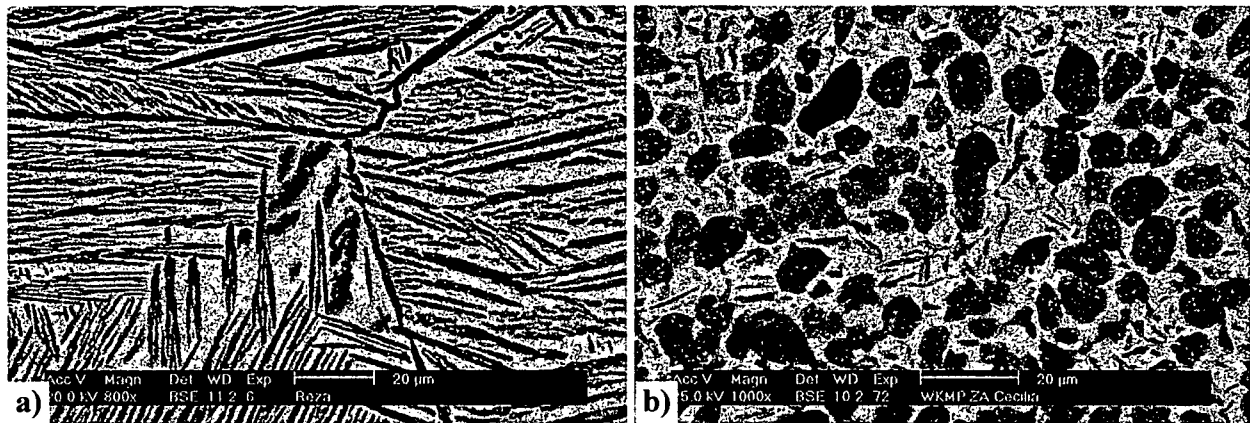


Figure 53. Ti662 Ingot after heat treatment and water quenching a) Acicular microstructure by heating above the beta transus temperature, cooled down to 800°C and held 15 minutes b) Globular microstructure after heating up to 820°C and held for 15 minutes (SEM).

#### 4.1.5 Microstructures after deformation

The following pictures show the samples after deformation in the direction of the arrow.

- **SiC reinforced samples after forging (open die).** Because the distribution of the particles is quite homogeneous, it was tried to close the pores by forging the samples S103 and S105 in an open die. Figure 54 and Figure 55 show no satisfactory results due to the propagation of cracks and microcracks into the matrix.

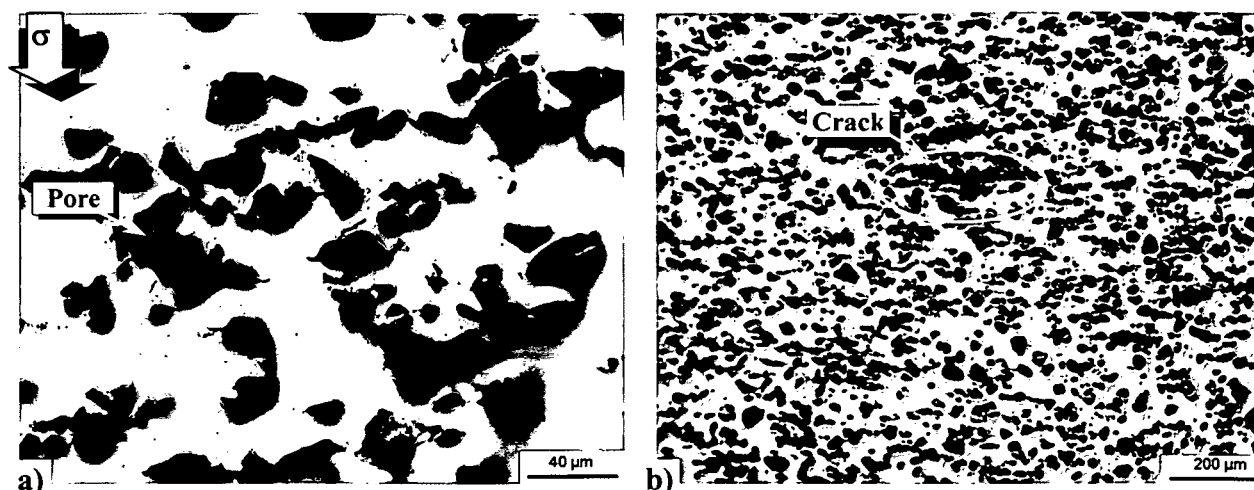


Figure 54. Sample S103 after forging at 850°C a) the pores between the particles remain, and b) cracks in the matrix are also observed. No growing of the reaction zone was observed (LOM).

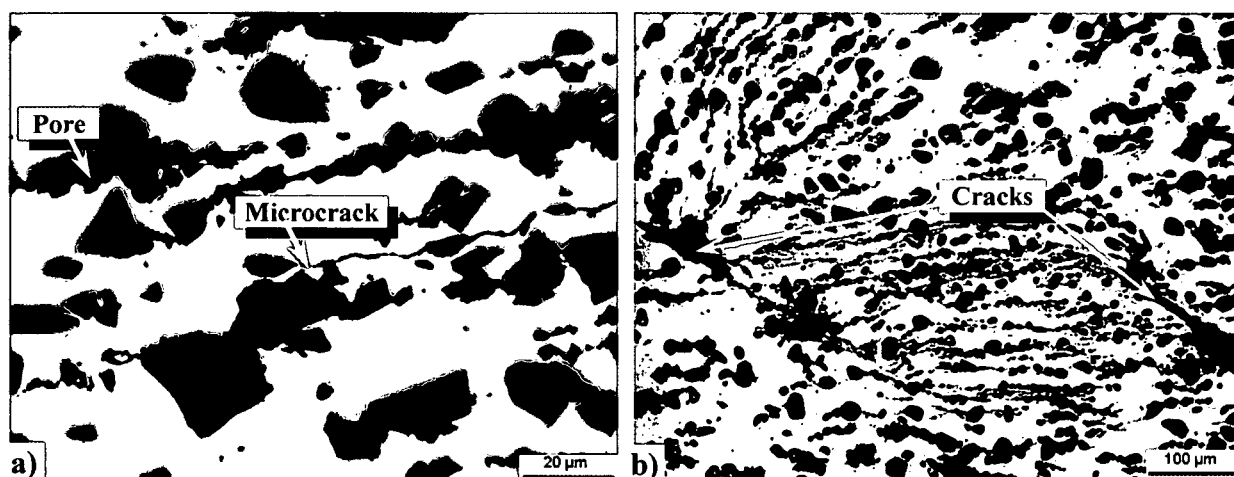


Figure 55. Sample 105 after forging at 850°C. a) the pores between the particles remain and some cracks in the matrix appear, and b) macro-cracks in the matrix (LOM).

-SiC reinforced materials after forging inside a titanium ring. As the samples forged in an open die present large amount of cracks, some trials of forgings were carried out inside a titanium alloy (Ti64) ring.

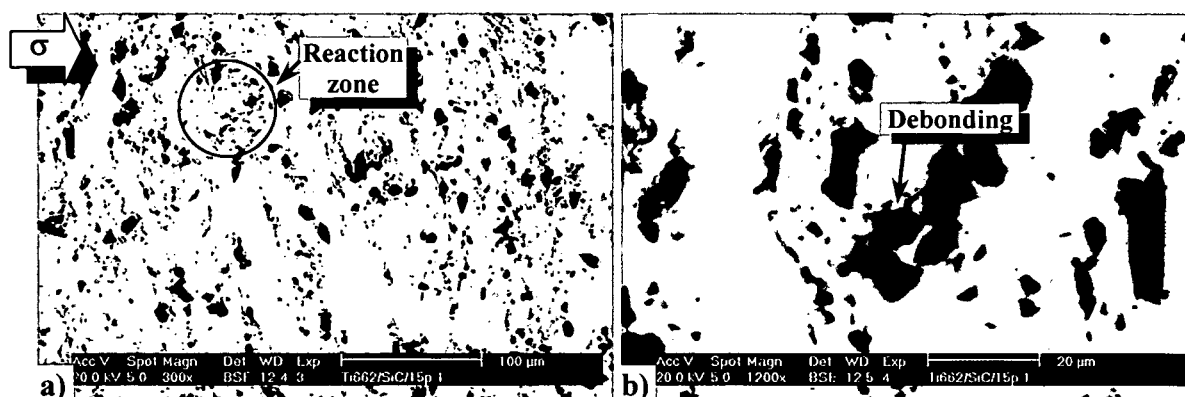


Figure 56. Ti64 reinforced with 15% SiC particles after forging at 950°C. a) reaction zone and b) debonding of the particles can be observed (SEM).

The sample S108 was tested, and the results are shown in Figure 56 for 950°C, Figure 57 for 850°C and Figure 58 for 750°C forging temperature.

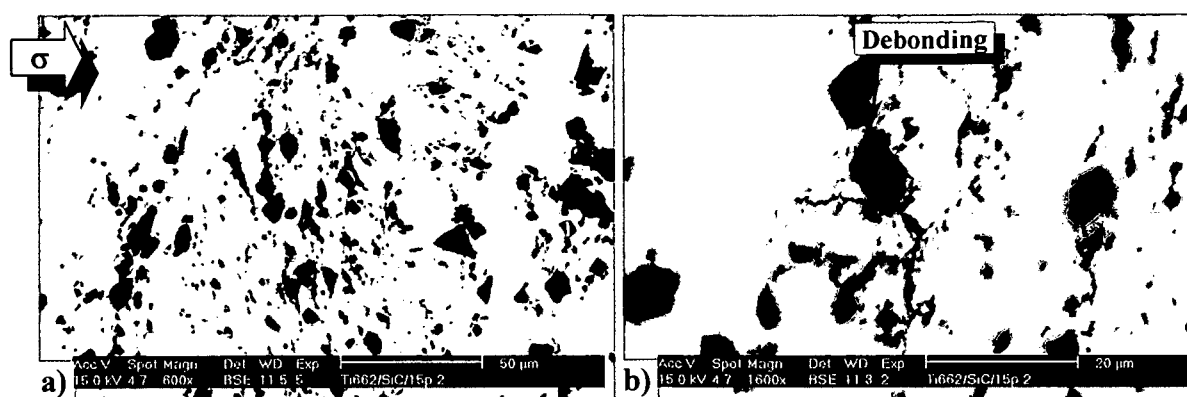


Figure 57. Ti64 reinforced with 15% SiC particles after forging at 850°C. a) reaction zone and b) debonding of the particles can be observed (SEM).

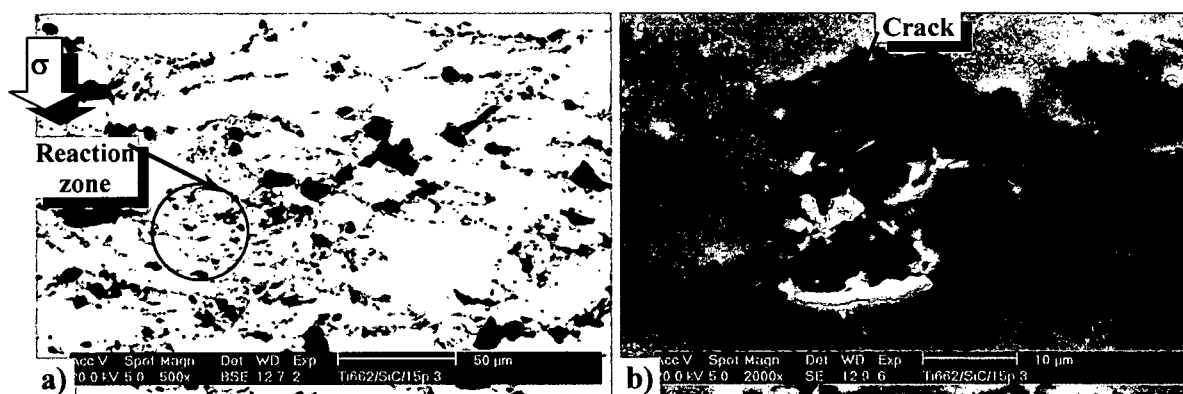


Figure 58. Ti64 reinforced with 15% SiC particles after forging at 750°C. a) reaction zone and b) cracking of the particles can be observed (SEM).

Some cracks in the matrix as well as broken particles at 750°C and debonding of the particles at higher temperatures can be observed. Nevertheless, the damage of the whole material is markedly less compared to the samples forged in the open die.

#### - After compression Test 1.

- *CermeTi®-C-662*: The initial lamellar microstructure after compression shows in general porosity at the grain boundary of prior beta grain. The pores are larger by increasing the temperature. At the lowest strain rate ( $0.015s^{-1}$ ) (Figure 59 to Figure 61) shows deformation of the alpha phase by kinking (Figure 60b) while the grains get rounded at higher temperatures (Figure 61a)). The behaviour at  $0.15s^{-1}$  is similar as at the lowest strain rate, showing higher porosity while increasing the temperature (Figure 62).

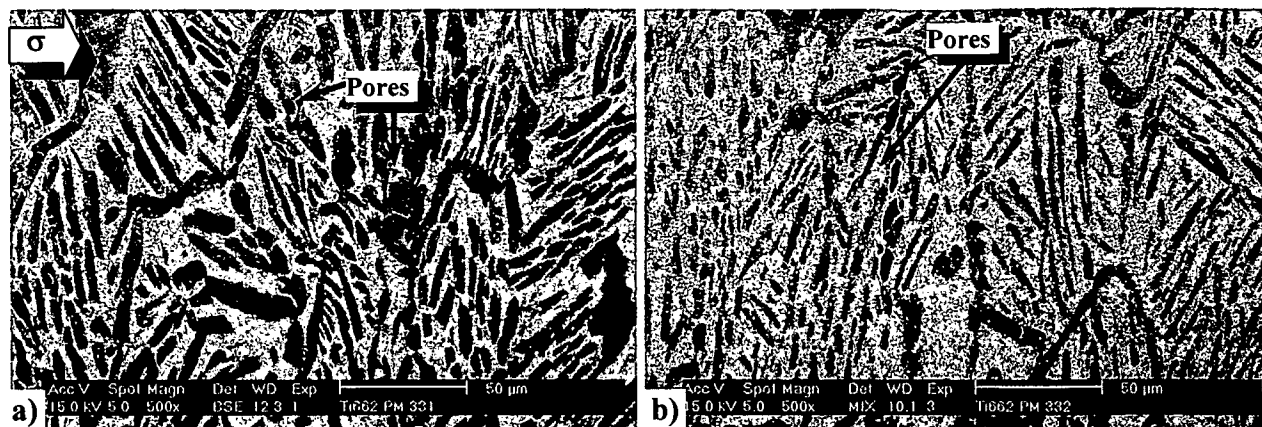


Figure 59. CermeTi®-C-662 showing deformed initial lamellar microstructure and pores produced during the deformation at a)  $0.015 \text{ s}^{-1}$  strain rate and  $650^\circ\text{C}$ , b)  $0.015 \text{ s}^{-1}$  strain rate and  $750^\circ\text{C}$  (SEM).

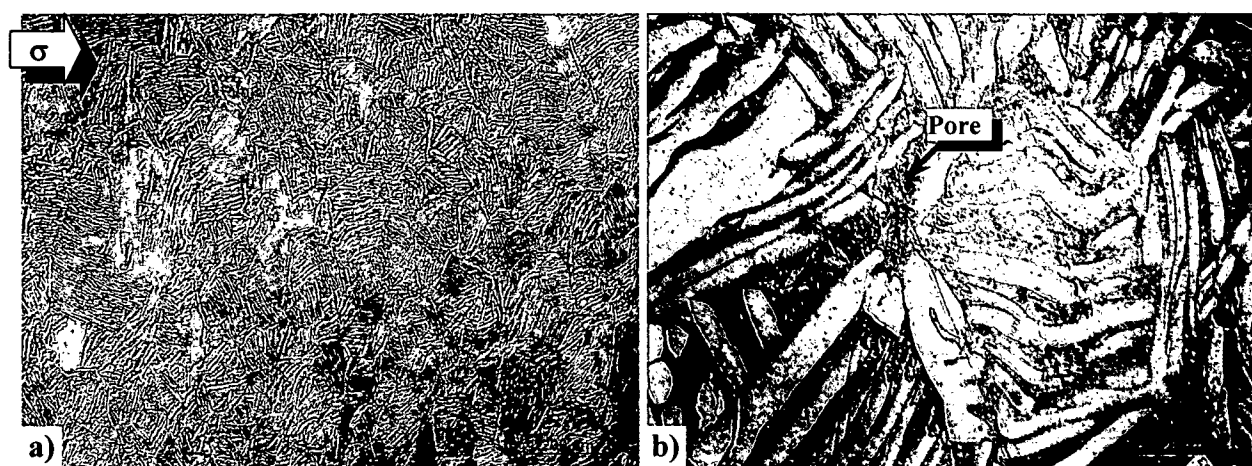


Figure 60. CermeTi®-C-662 during the deformation at  $0.015 \text{ s}^{-1}$  strain rate and  $650^\circ\text{C}$  showing a) the deformation of the initially bright lamellar microstructure and b) porosity produced at the grain boundary of the prior beta grains (LOM).

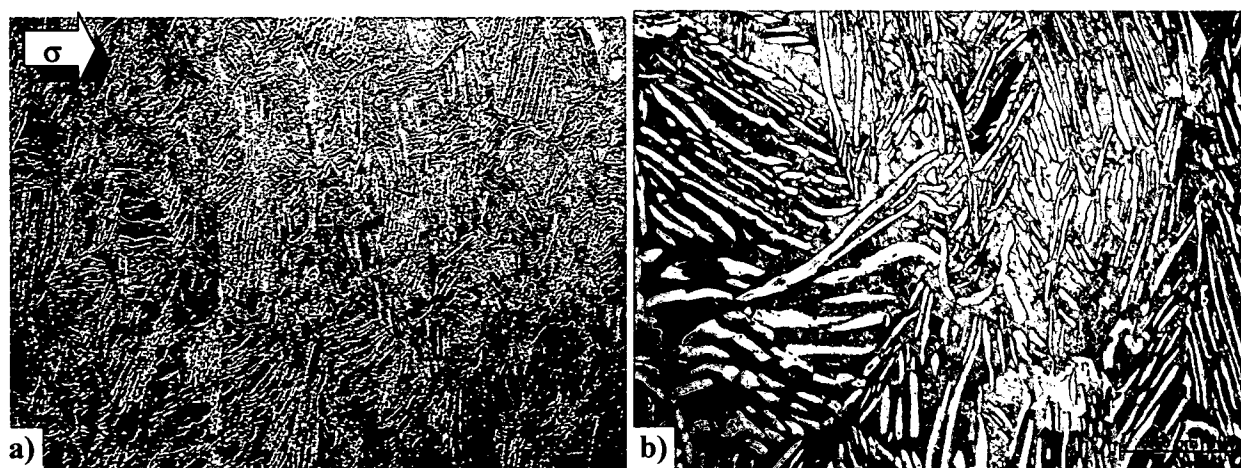


Figure 61. CermeTi®-C-662 during  $0.015 \text{ s}^{-1}$  strain rate and  $750^\circ\text{C}$ . showing a) the deformation of the prior beta grains and alpha lamellae b) the alpha phase deformation in detail (LOM).

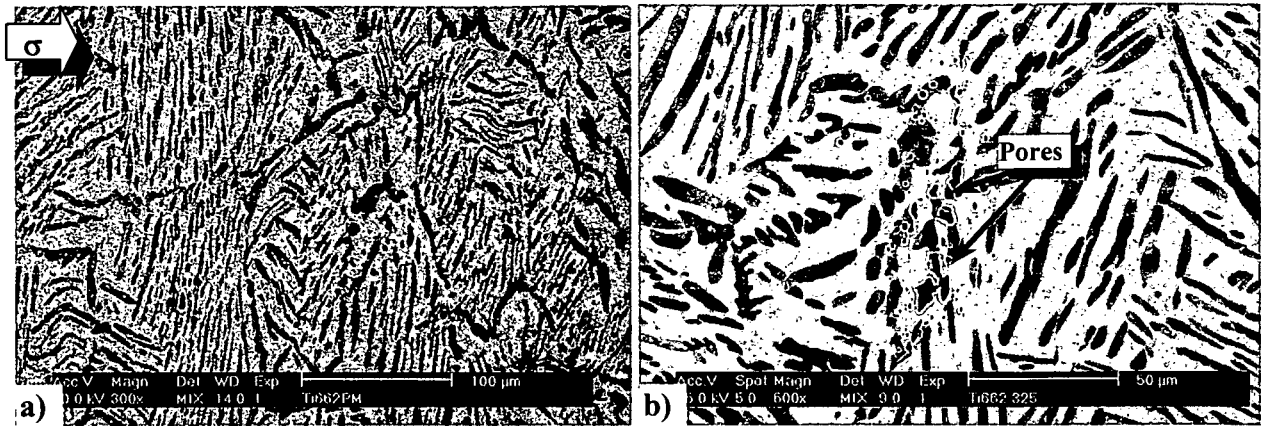


Figure 62. CermeTi®-C-662 at  $0.15 \text{ s}^{-1}$  strain rate and  $850^\circ\text{C}$  showing the deformed initial lamellar microstructure and the pores produced during the deformation (SEM).

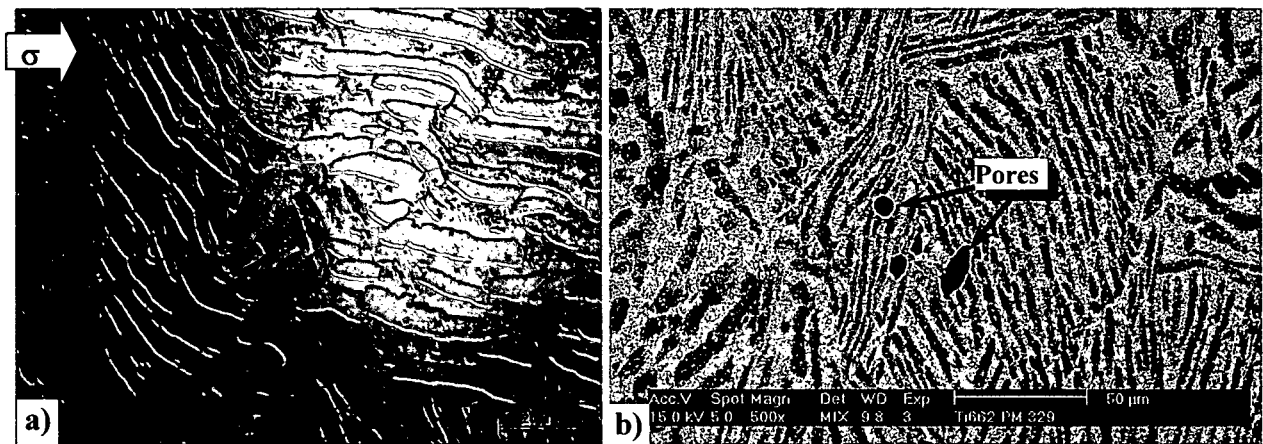


Figure 63. CermeTi®-C-662 at  $1.4 \text{ s}^{-1}$  strain rate and  $750^\circ\text{C}$  showing a) the deformed prior beta grains and the alpha lamellae (LOM) and b) the porosity produced during deformation (SEM).

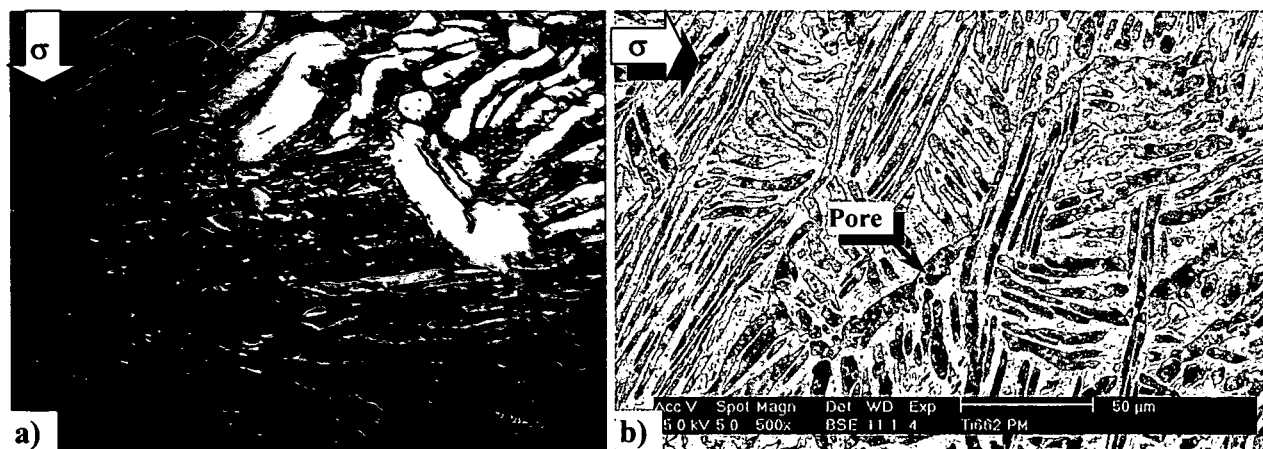
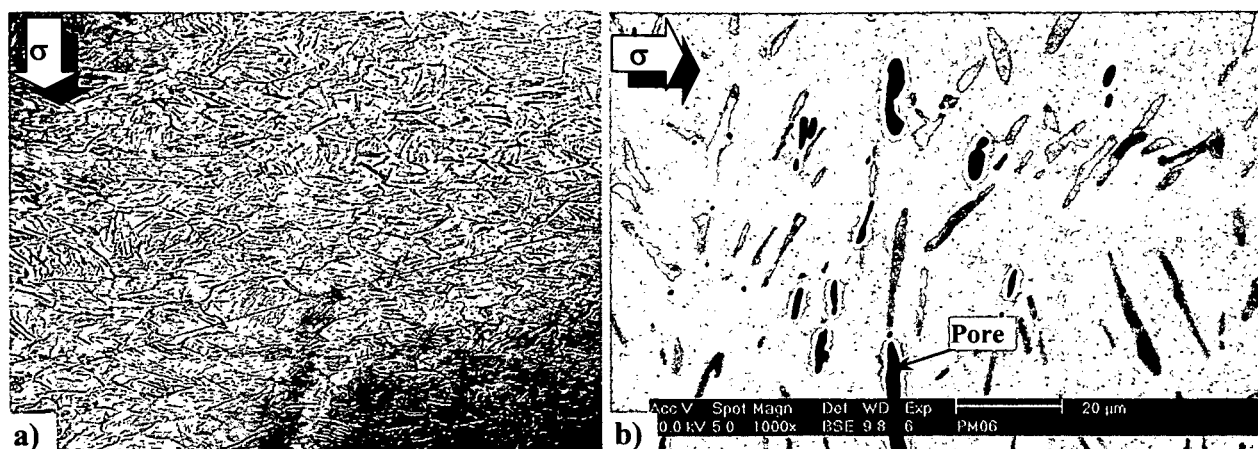


Figure 64. CermeTi®-C-662 at  $15 \text{ s}^{-1}$  strain rate up to 0.8 strain and  $650^\circ\text{C}$  showing a) deformation of the lamellae alpha phase and small globular alpha of prior beta grain boundary (LOM) b) pores in a high local stress zones differently oriented lamellae (SEM).

Figure 63 shows inhomogeneities in the deformation of the material, with some bands of deformation and large pores.



**Figure 65** CermeTi®-C-662 compressed at  $15 \text{ s}^{-1}$  strain rate up to 0.8 strain and  $950^\circ\text{C}$  showing a) deformed and rounded grains (LOM) b) porosity produced during deformation (SEM).

At high strain rate ( $15 \text{ s}^{-1}$ ) and strain (0.8) recrystallisation of the beta phase (Figure 64a)) and shear bands and pores (Figure 64b)) can be observed at  $650^\circ\text{C}$ . On the other hand, at  $950^\circ\text{C}$  no shear bands were observed, while the grains are deformed in an elliptic shape and the pores are larger (Figure 65).

- *Ti662 ingot*: Cracks were not observed in any Ti662 ingot sample after compression.

At  $0.15 \text{ s}^{-1}$  strain rate, zones of alpha growth were observed, and alpha phase with wavy grain boundaries deformed at  $650^\circ\text{C}$  (Figure 66) and  $750^\circ\text{C}$  (Figure 67) and polygonisation of the alpha and beta grains at  $950^\circ\text{C}$  (Figure 68).

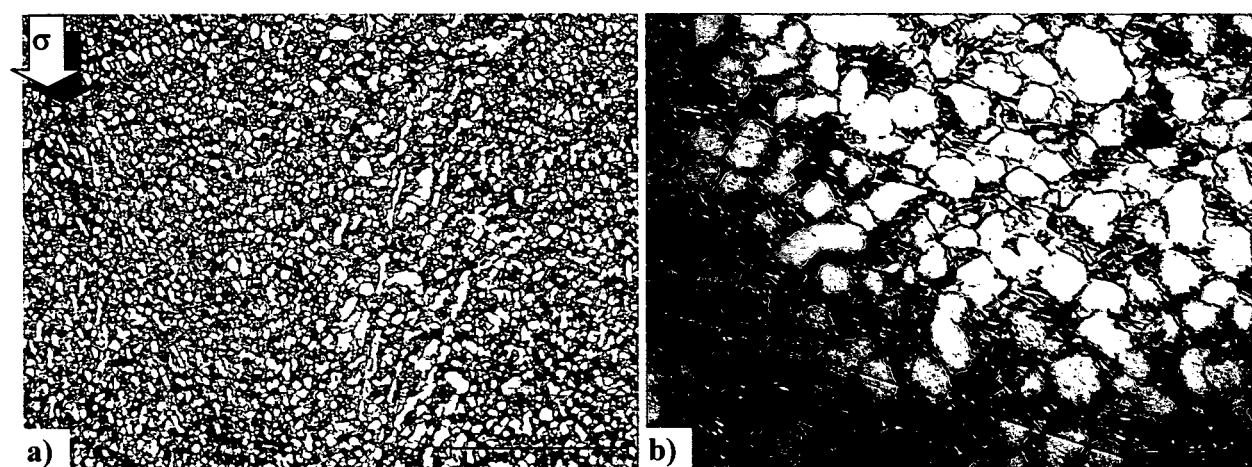


**Figure 66.** Compression of Ti662 Ingot at  $650^\circ\text{C}$  and  $0.15 \text{ s}^{-1}$  up to 0.3 strain showing a) lines of deformation and growth of the alpha phase b) alpha grains with wavy grain boundaries (LOM).



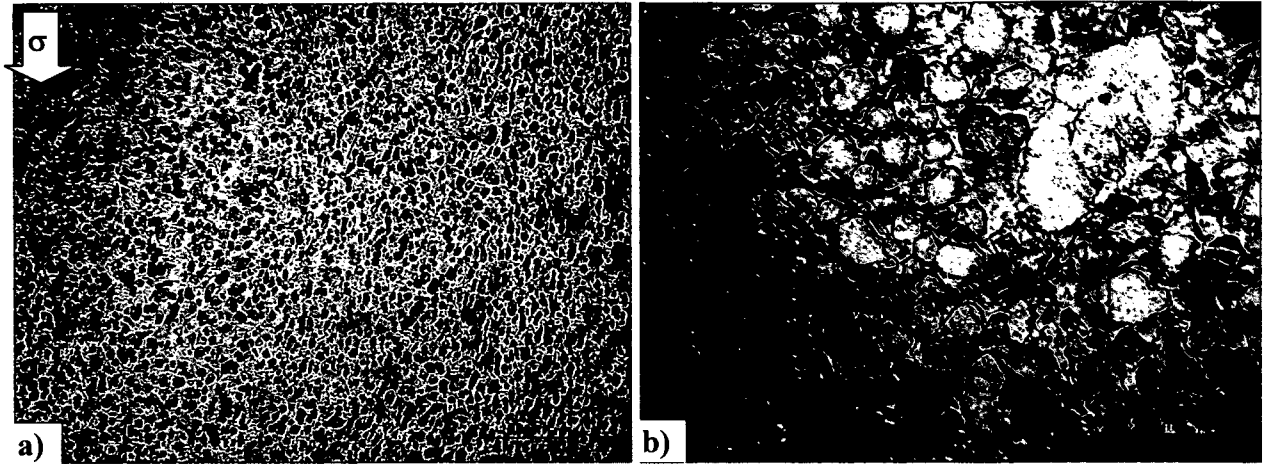


Figure 67 Compression of Ti662 Ingot at 750°C and  $0.15 \text{ s}^{-1}$  up to 0.3 strain a) zones of growth of the alpha phase b) alpha grains with wavy grain boundaries (LOM).

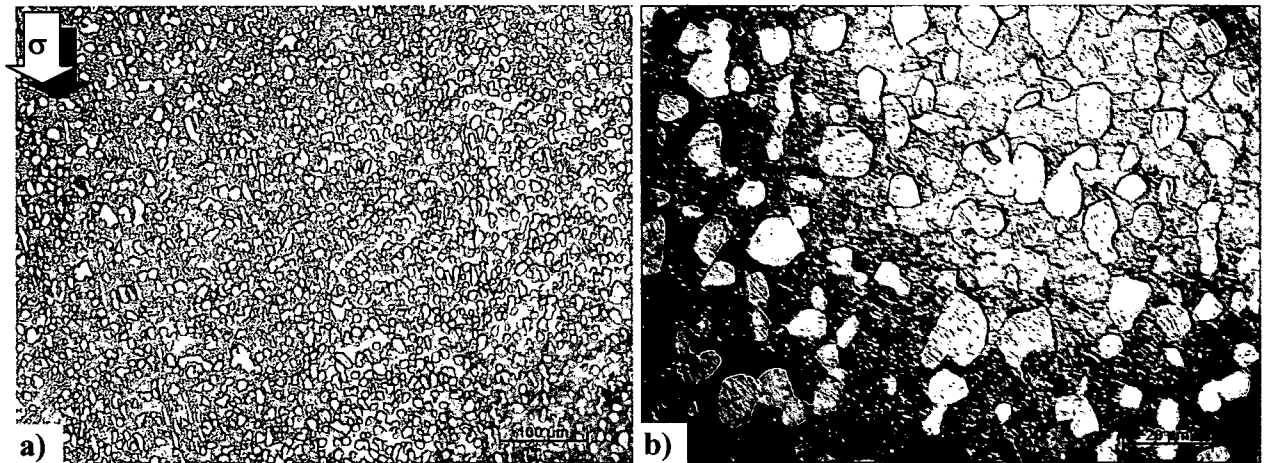


Figure 68 Compression of Ti662 Ingot at 850°C and  $0.15 \text{ s}^{-1}$  up to 0.3 strain showing a) zones of growth of the alpha phase b) alpha grains with polygonal alpha and beta grains (LOM).

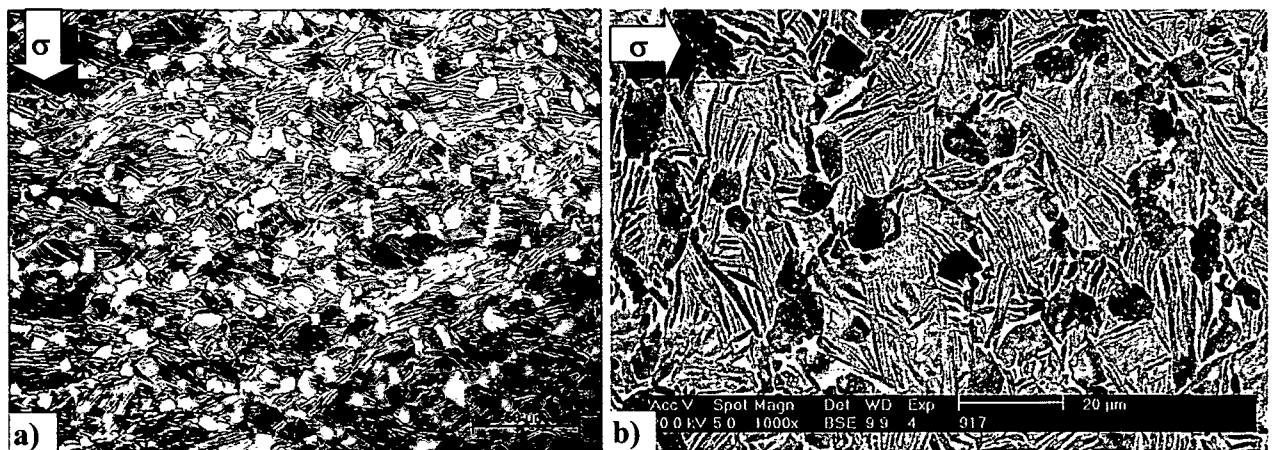


Figure 69. Deformation of Ti662 Ingot at  $1.3 \text{ s}^{-1}$  and 650°C and up to 0.3 strain showing (a) the growing of the secondary lamella alpha phase (LOM) (b) and the deformed grains (SEM).

Some recrystallisation occurs at medium strain rates ( $1.3 \text{ s}^{-1}$ ) and low temperatures (650°C), as seen in Figure 69.

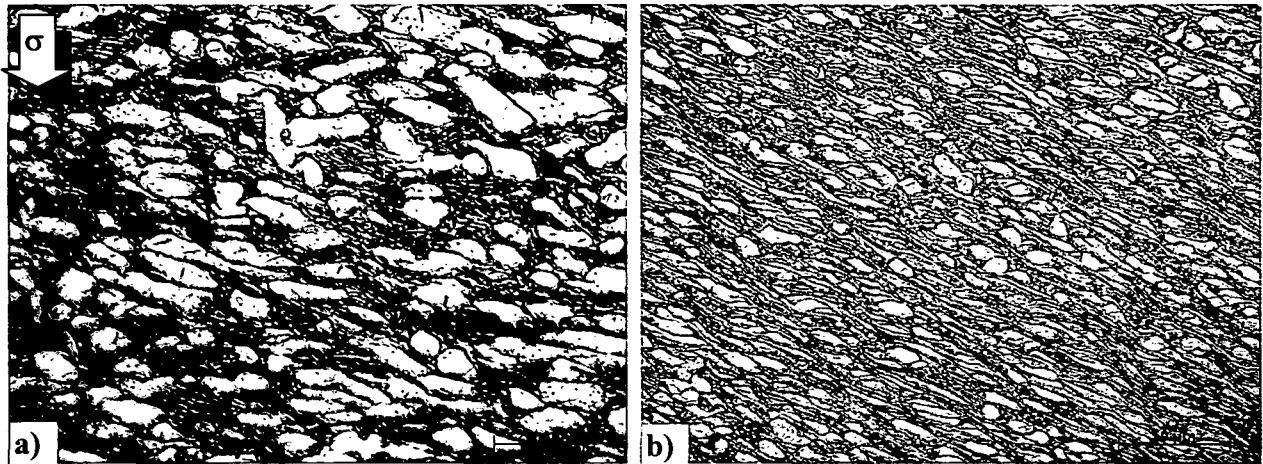


Figure 70 Ti662 Ingot after compression at 650°C and  $15 \text{ s}^{-1}$  up to 0.8 strain showing a) the deformed alpha phase and b) shear bands zones (LOM).

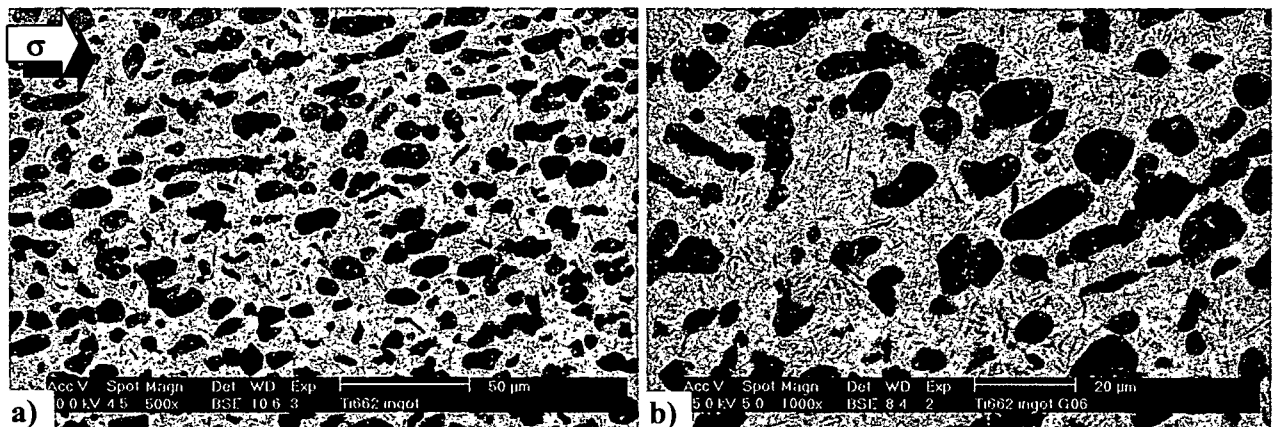


Figure 71 Ti662 Ingot after compression at 850°C and  $15 \text{ s}^{-1}$  up to 0.8 strain showing a) the deformed alpha phase and b) the deformation of the secondary alpha phase lamellae (SEM)

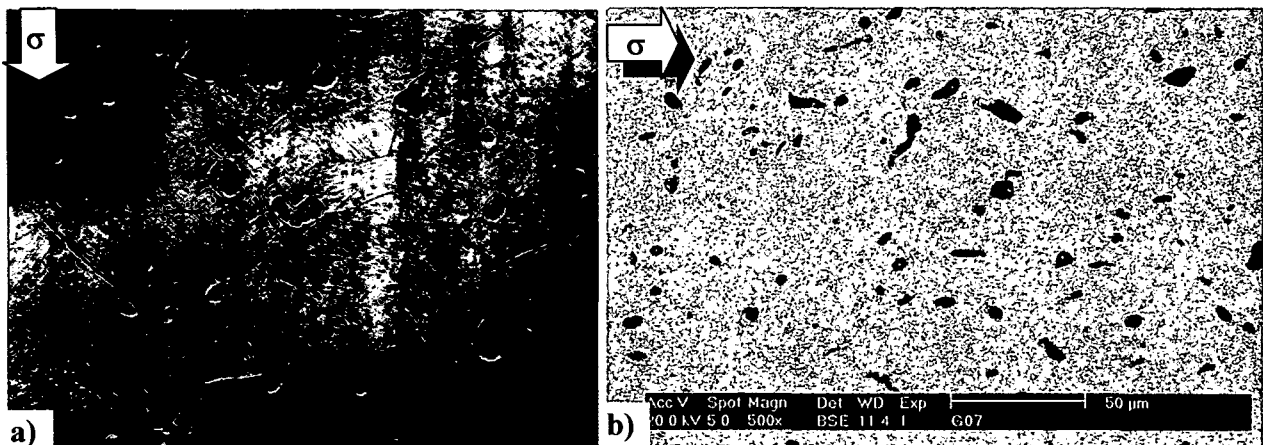


Figure 72 Deformation of Ti662 Ingot at  $15 \text{ s}^{-1}$  at 950°C and up to 0.8 strain (a) showing the grains (LOM) (b) and the deformed alpha phase (SEM)

At the highest strain rate ( $15 \text{ s}^{-1}$ ) and strain of 0.8, shear bands were observed at 650°C (Figure 70), while slightly deformed alpha phase was observed at 850 and 950°C (Figure 71 and Figure 72, respectively).



- *Ti64*. The after deformed *Ti64* micrographs show also the deformation of the alpha lamellae and the cracks at the grain boundaries at 750°C (Figure 73) and high porosity at the lowest test temperature (Figure 74).

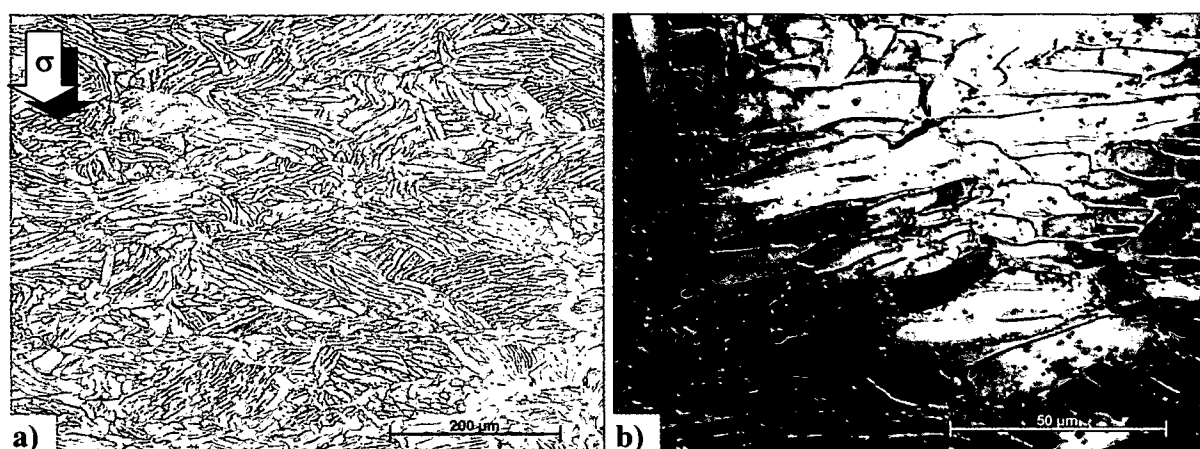


Figure 73 *Ti64* deformed at 750 °C and  $0.015s^{-1}$  showing a) the deformed prior grains b) cracks production at the grain boundaries

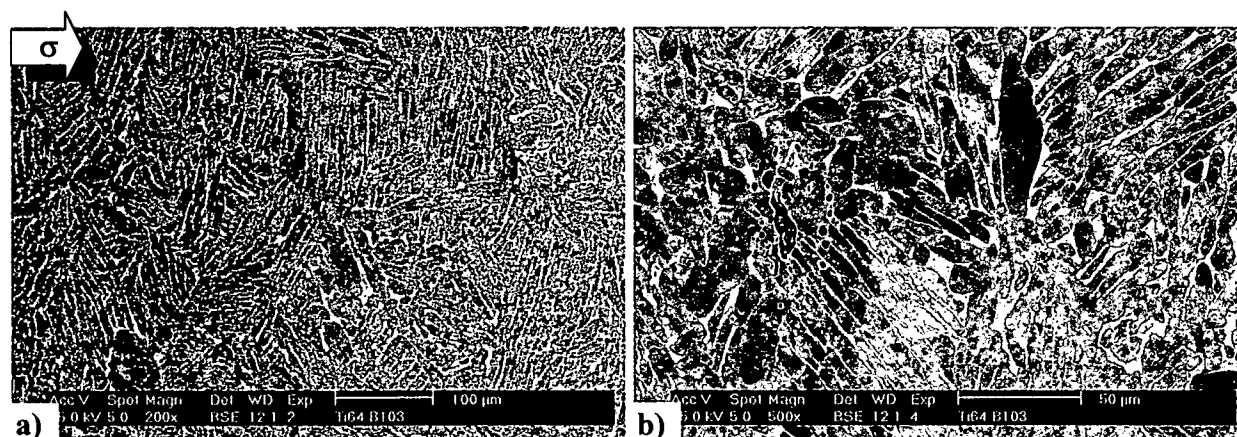


Figure 74 *Ti64* PM deformed at 650°C and  $1.4s^{-1}$  showing a) deformed alpha lamellae and b) porosity produced during the deformation (SEM)

- *CermeTi®-C-12-662* and *CermeTi®-C-20-662* composites: For all the strain rates, of the particles was observed debonding at high temperatures (850-950°C) and cracking of the particles at low temperatures (650-750°C). Furthermore, the composite reinforced with 20% of TiC showed more frequent particle fracture than the material reinforced with 12% of TiC.

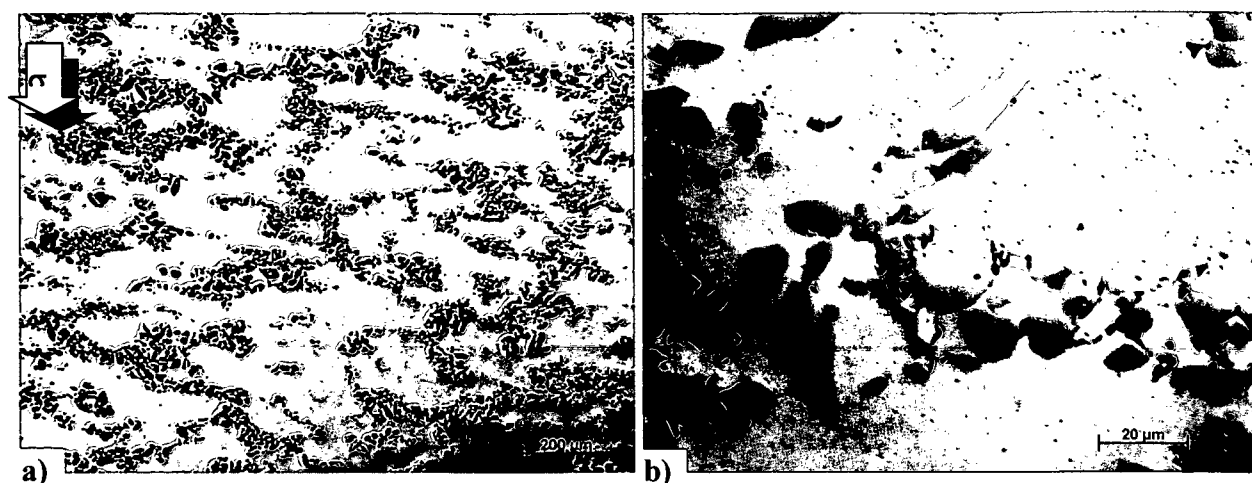


Figure 75 Ti662 reinforced with 12%TiC particles deformed up to  $\epsilon \sim 0.3$  at  $0.015s^{-1}$  and  $650^{\circ}C$  showing a) the orientation of the particles b) cracking and debonding of the TiC particles.

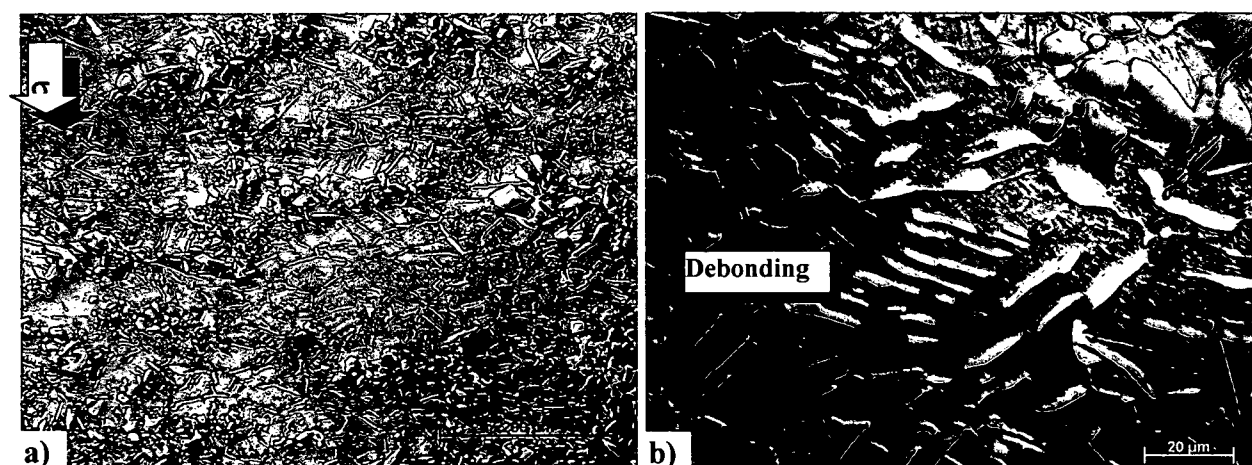


Figure 76 Ti662 reinforced with 12%TiC particles deformed up to  $\epsilon \sim 0.3$  at  $0.015s^{-1}$  and  $950^{\circ}C$  showing a) rounding of the grains and b) debonding of the particles



Figure 77. Ti662 reinforced with 12%TiC particles deformed up to  $\epsilon \sim 0.3$  at  $650^{\circ}C$ , strain rate  $0.15s^{-1}$  a) and b) showing TiC-particle fracture

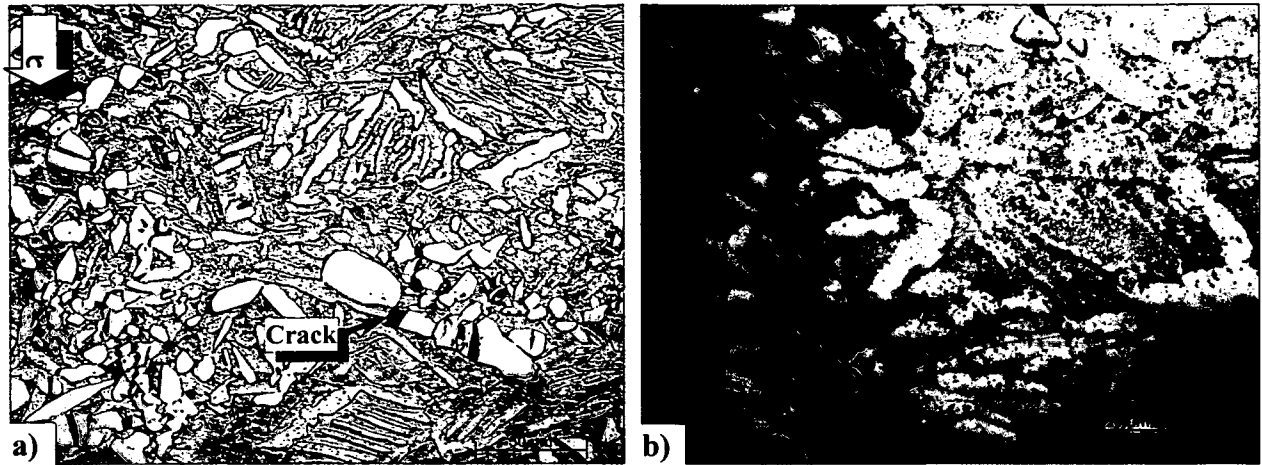


Figure 78 Ti662 reinforced with 12%TiC particles deformed up to  $\epsilon \sim 0.3$  at  $750^\circ\text{C}$ , strain rate  $0.15\text{s}^{-1}$  a) and b) showing deformation of the alpha phase and cracks of the particles

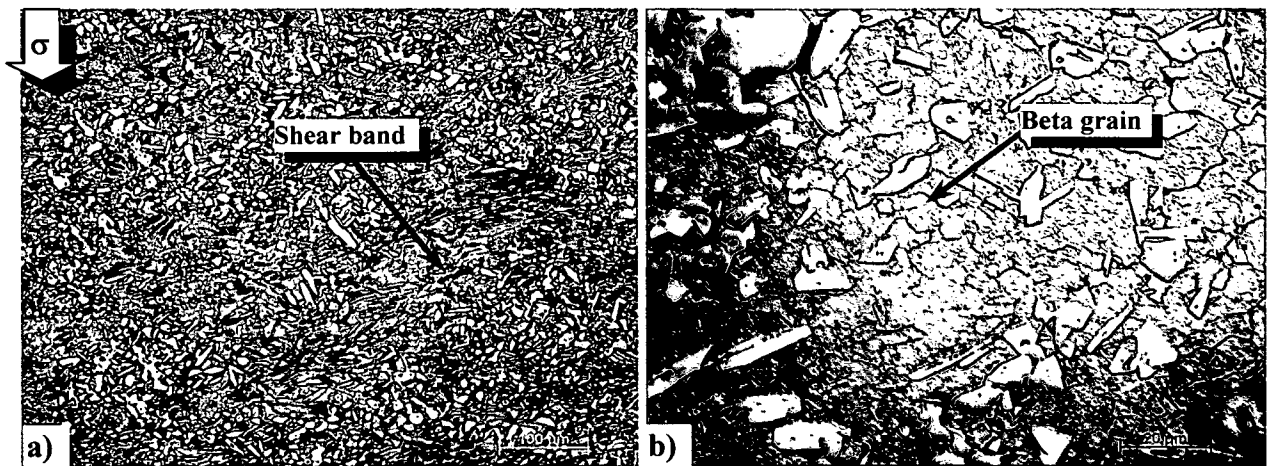


Figure 79 Ti662 reinforced with 12%TiC particles deformed up to  $\epsilon \sim 0.3$  at  $0.15\text{s}^{-1}$  and  $850^\circ\text{C}$  showing a) highly deformed grains (shear bands?) and b) polygonisation of the beta grains of the particles

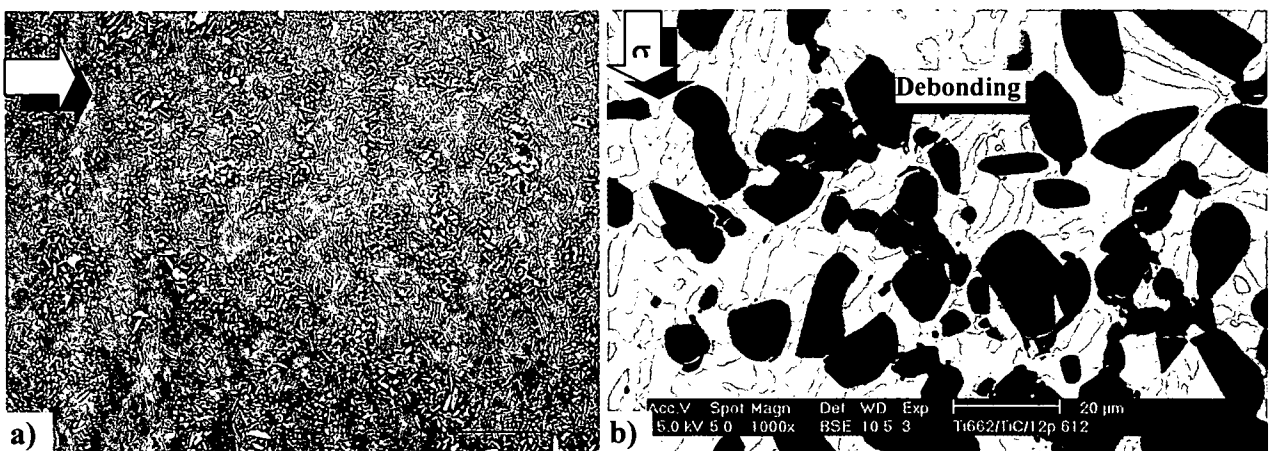


Figure 80 Ti662 reinforced with 12%TiC particles deformed up to  $\epsilon \sim 0.3$  and  $1.4\text{s}^{-1}$  and  $850^\circ\text{C}$  showing a) high deformed grains and debonding of the particles

At  $15\text{s}^{-1}$  and 0.8 strain, polygonisation of the prior beta grains was observed at high temperatures (Figure 82 and Figure 83).

Shear bands and macrocracks were observed at low temperatures (Figure 81) and high strain rates ( $15\text{s}^{-1}$ ) and strain (0.8).

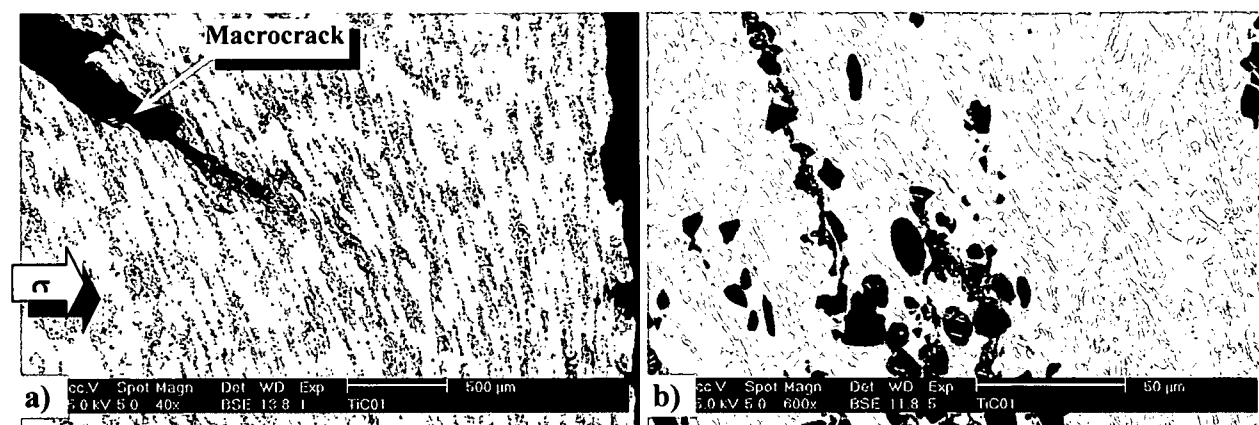


Figure 81 Ti662 reinforced with 12% TiC up to  $\epsilon \sim 0.8$  at  $15\text{s}^{-1}$  and at  $650^\circ\text{C}$  showing a) macrocrack and piled up TiC particles and b) microcracks between the TiC particles and shear bands in the unreinforced zones

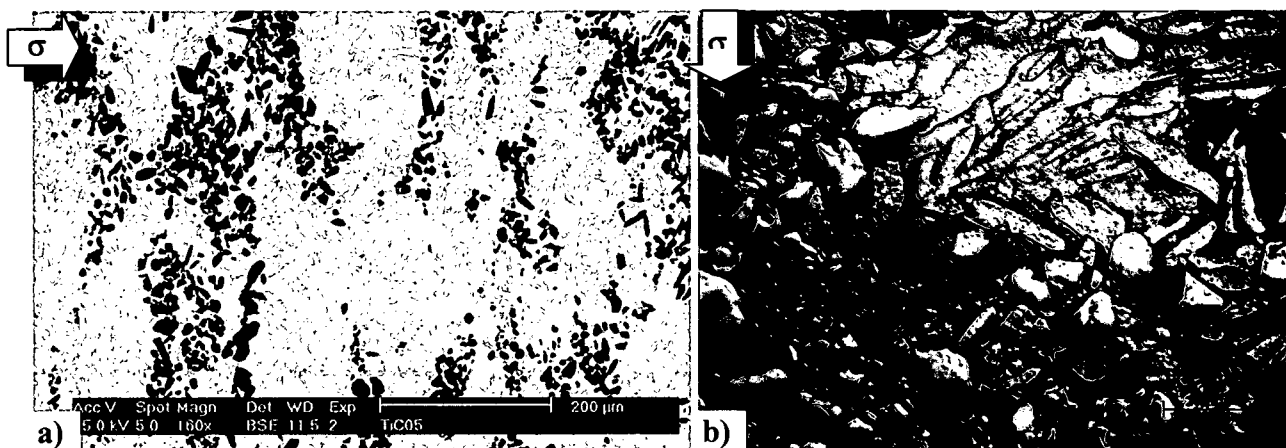


Figure 82 Ti662 reinforced with 12% TiC up to  $\epsilon \sim 0.8$  at  $15\text{s}^{-1}$  strain rate and  $850^\circ\text{C}$  showing a) chains of TiC particles and b) the debonding of the particles and the alpha orientation

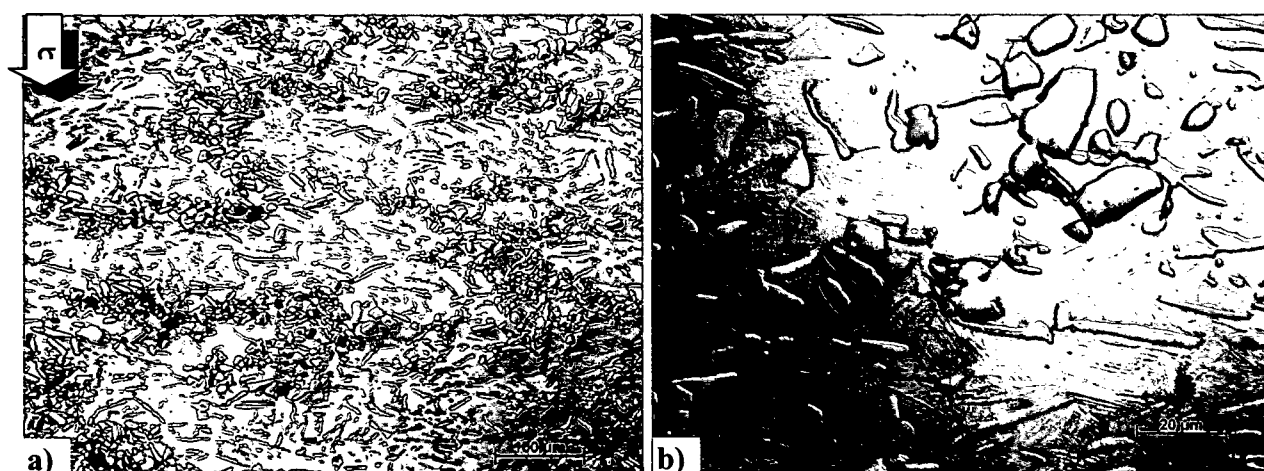


Figure 83 CermeTi<sup>®</sup>-C-12-662 deformed at  $950^\circ\text{C}$ ,  $15\text{s}^{-1}$  strain rate and 0.8 strain showing a) the production of high porosity and b) recrystallisation of the prior beta grains (grain size smaller than  $20\text{ }\mu\text{m}$ )

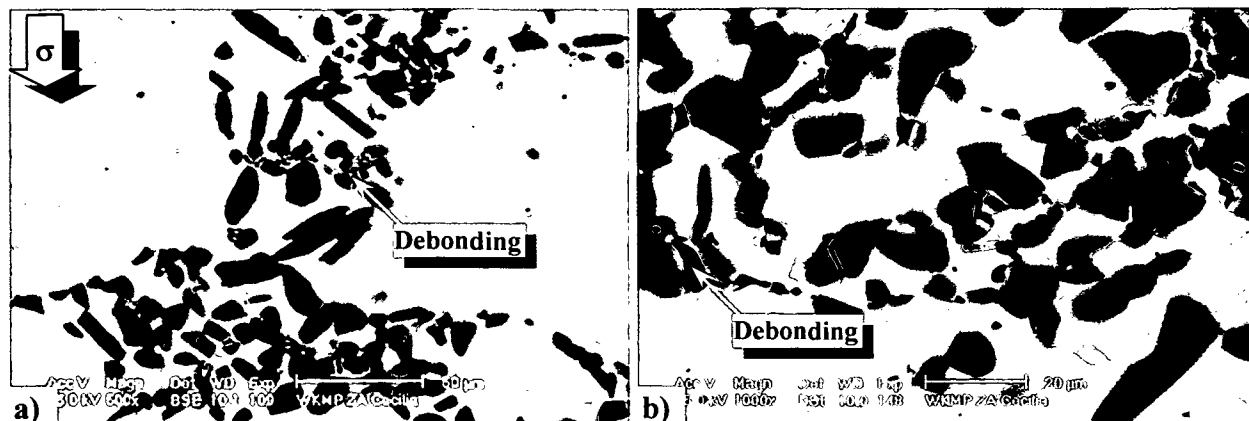


Figure 84 CermeTi®-C-20-662 after compression up to  $\epsilon \sim 0.3$  (a) at 950°C 1.3s<sup>-1</sup> showing debonding of the TiC particles and polygonisation of the grains and (b) at 850°C 0.015s<sup>-1</sup> showing debonding of the TiC particles

- After compression Test 2 CermeTi®-C-662 and CermeTi®-C-20-662 were deformed at 650°C after a holding time of 1 hour at test temperature.

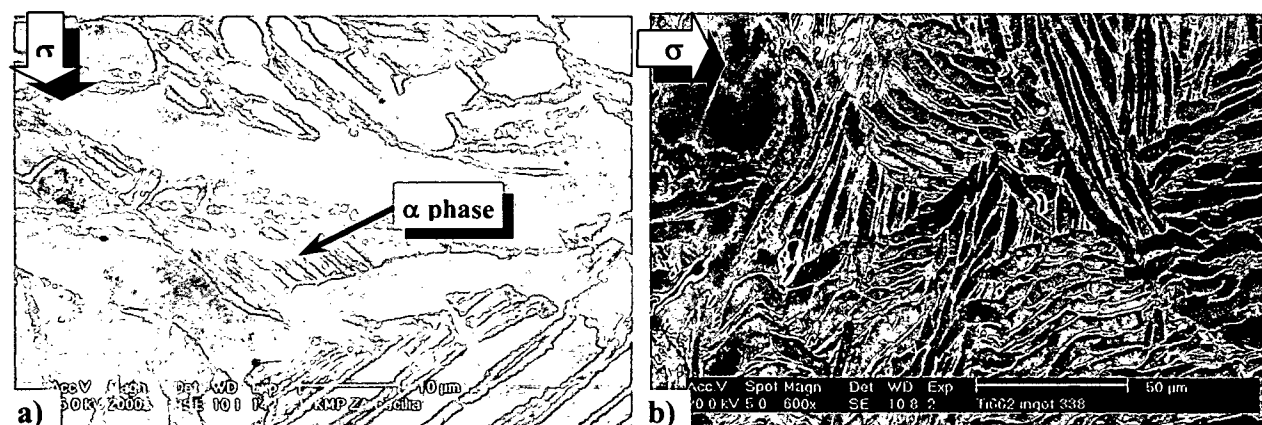


Figure 85. CermeTi®-C-662 deformed at 650°C after 40 min. held at 650°C a) growing of fine secondary  $\alpha$ -phase with time b) deformation of the lamellae and damage of the material after deformation (SEM-Kroll).

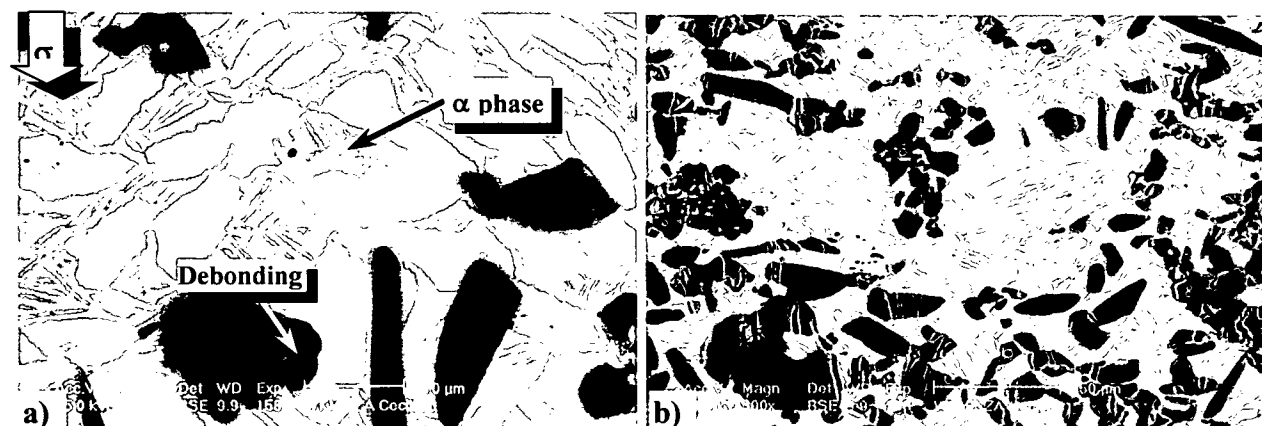


Figure 86 CermeTi®-C-20-662 deformed at 650°C after 40 minutes held at 650°C a) Growing of the  $\alpha$  phase b) broken particles

A fine secondary lamellar alpha phase grows up in the beta field with the time up to reach the phase equilibrium.

- **Compression Test 3.** CermeTi<sup>®</sup>-C-662 and CermeTi<sup>®</sup>-C-20-662 deformed at 750 or 650°C after a holding time of 1 hour at 900°C. Figure 87 shows also the growth of secondary fine alpha lamellae.

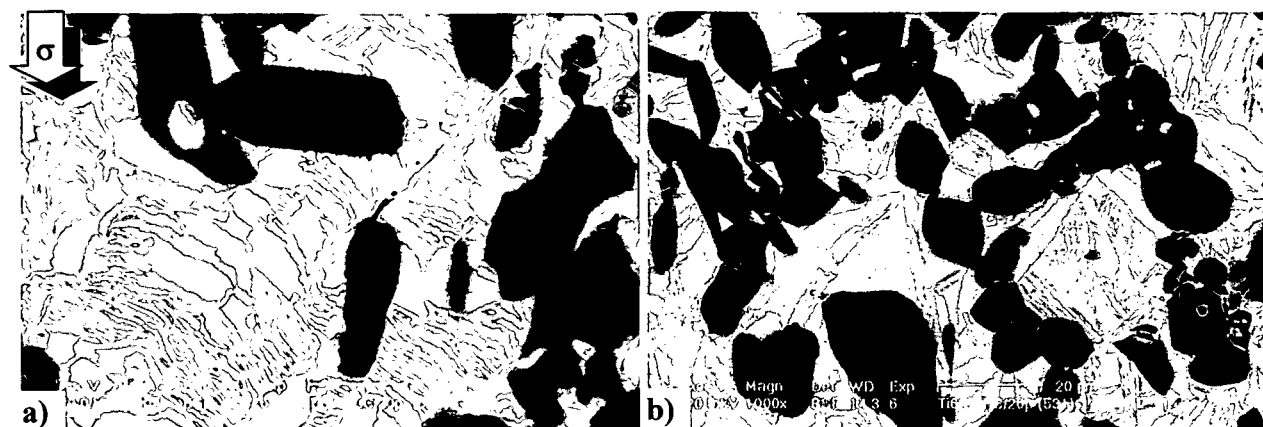


Figure 87. Microstructure of the CermeTi<sup>®</sup>-C-20-662 samples after deformation showing the fine sheared alpha lamella a) 750°C, and b) 650°C.

- **After compression Test 4.** CermeTi<sup>®</sup>-C-662 and CermeTi<sup>®</sup>-C-20-662 deformed at 750°C after a holding time of 1 hour at 1000°C and 20 minutes at 900°C.

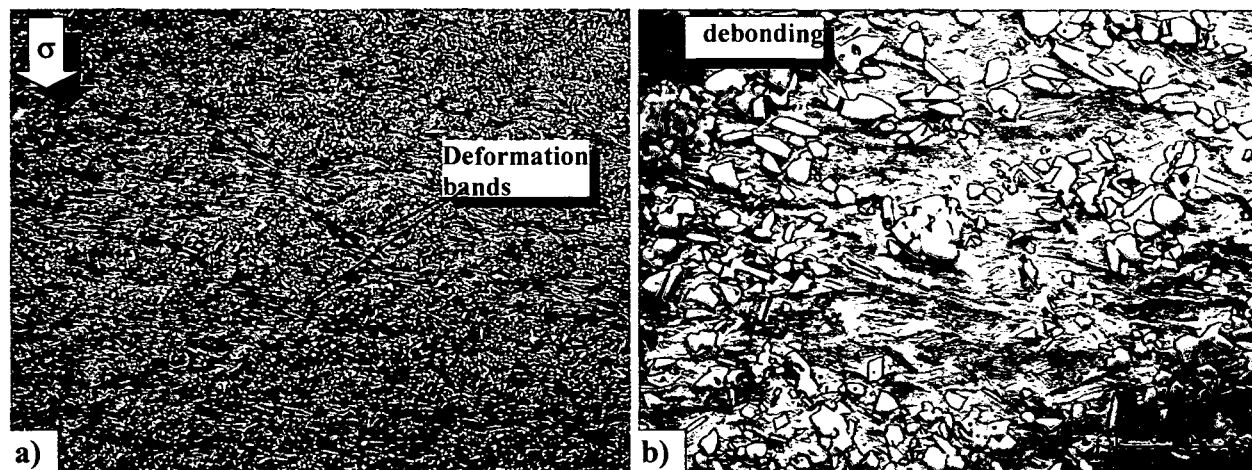
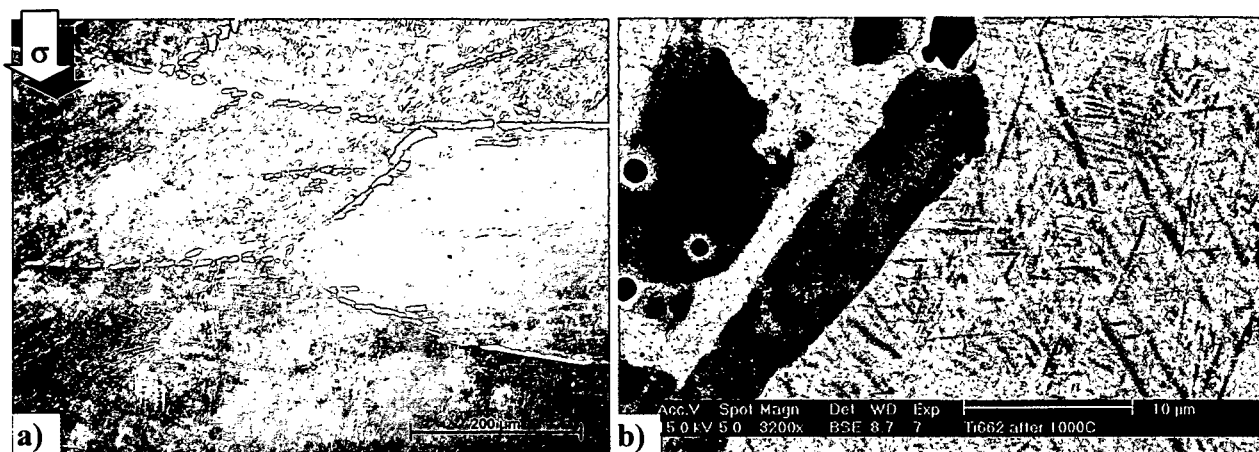


Figure 88. CermeTi<sup>®</sup>-C-20-662 sample after a heat treatment and deformation at 750°C showing a) deformation bands and damage of the matrix (debonding and cracks) and b) orientation of the alpha phase.

Figure 88a) shows the deformation bands crossing the sample in the free spaces without particles, while b) shows the orientation of the alpha phase in the tested composite. Furthermore, debonding of the particles provoked large pores.



Ti662 PM deformed at 750°C after a heat treatment at 1000°C during 1 hour shows grain growth of the beta prior grains up to values higher than 1000μm (Figure 89a). The alpha phase grows in two steps: during cooling from 1000-900°C holding 3 minutes at 900°C and further cooling to test temperature of 750°C, lamellae at the grain boundaries are formed



**Figure 89.** Hot compression of Ti662 PM at 750°C after a heat treatment at 1000°C during 1 hour showing a) prior beta grain boundaries b) alpha growth as needles during cooling and porosity formed at the alpha prior grain boundaries during hot deformation.

The hot compression at 750°C up to 0.3 displaces the original beta grain boundaries and the decorating alpha lamellae, where pores are produced. During quenching from 750°C plate-like (observed as needles) alpha phase is formed.

#### 4.1.6 Microstructure during dilatometry.

During the dilatometric tests, the microstructure of the ingot sample was specially studied using metallography. The microstructures studied were taken by stopping the test with the holding time of 15 minutes, as shown in Figure 90.

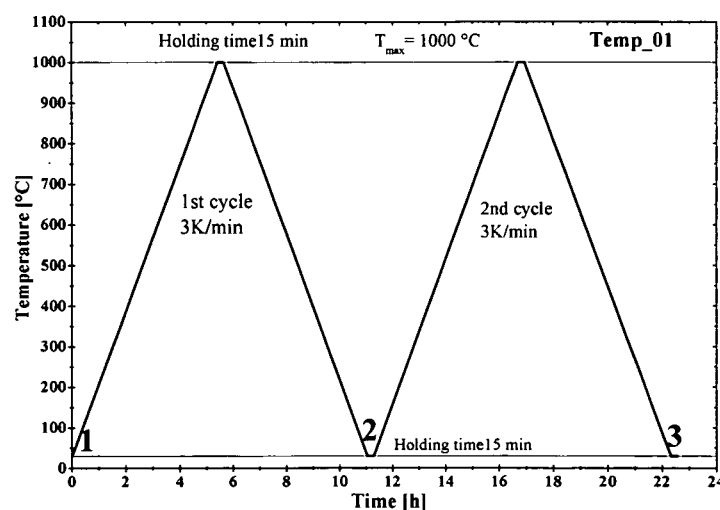


**Figure 90** Points where the microstructure was studied for the Ti662 Ingot material after 15 min holding time.

Figure 91 shows the as received globular microstructure (a), and the grain growth in a lamellar microstructure after the whole test (b) where grains became approximately 600 $\mu\text{m}$  large.

Figure 92 showing the microstructure of the Ti662 Ingot after the first and the second cycle (after beta transformation) (a) and b), respectively showing the new grain boundaries and the fine alpha lamellar microstructure.

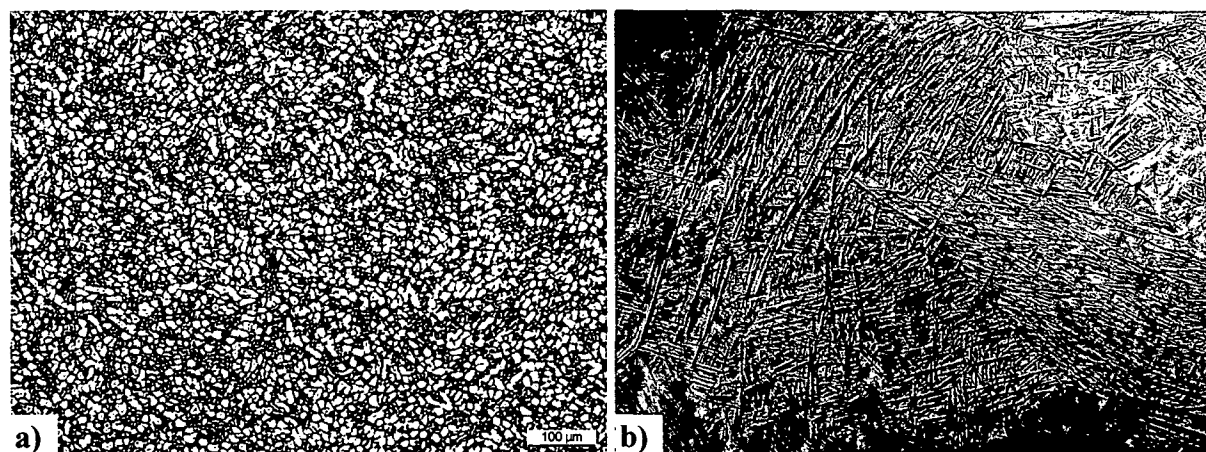


Figure 91 a) sample (1) as received, showing a globular microstructure, and b) at the end of the dilatometry test, showing grain sizes of about 600 $\mu\text{m}$  after 2 cycles (3). (LOM-Kroll).

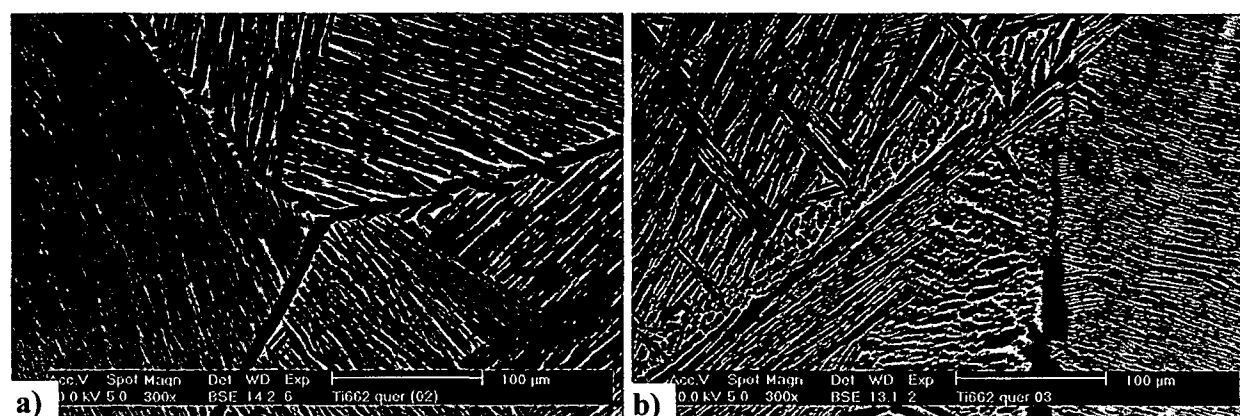


Figure 92 Ti662 Ingot showing a lamellar microstructure and a) grain growth after the first cycle (2) and b) after the second cycle (3). (SEM-BSE).

## 4.2 Microhardness

Figure 93 shows the results of the microhardness measurements and the percentage of change in comparison to the unreinforced alloy produced by Dynamet. An increment of about 18% in hardness is observed for both, the CermeTi®-C-662 and the composite reinforced with 20% of TiC after a heat treatment of 5 h at 900°C. For a heat treatment consisting on 28 hours at 900°C for the TiC particle reinforced Ti662 alloy the increase of the hardness is about the 26%.



As the heat treatments were not carried out in high vacuum, the samples could be contaminated with oxygen and/or nitrogen from the air that increase the hardness by alloying interstitially the Ti cell.

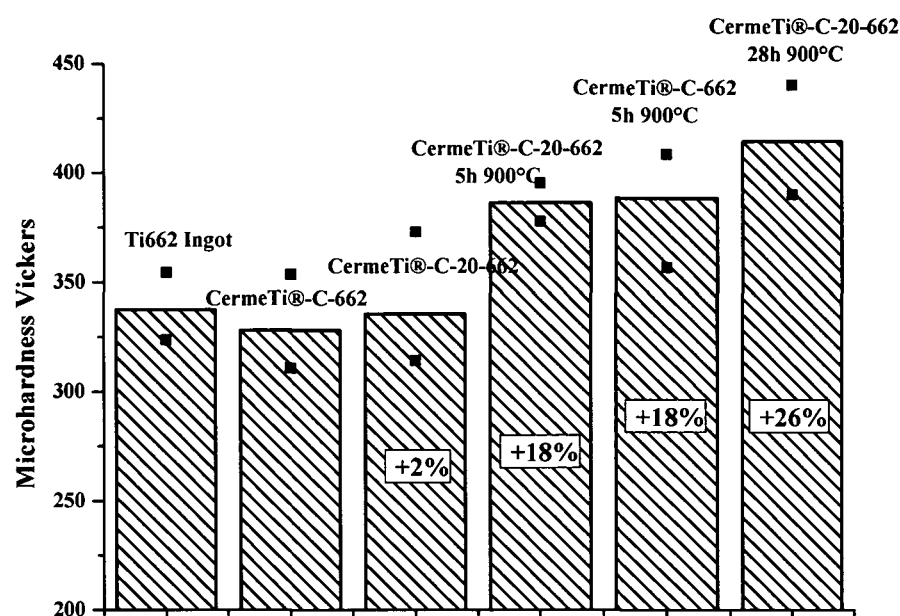


Figure 93. Vickers micro-hardness variation due to the different heat treatments.

### 4.3 Image Analysis.

The samples, the heat treatments and the percentages of beta phase calculated with Sigma Scan Pro are listed in Table 8.

Table 8. Percentage of Beta content calculated with Sigma Scan Pro.

Sample	Heat treatment	β- Content vol %
Ti662 Ingot	As received	23
	15 min 600°C	24
	15 min 780°C	35
	15min 800°C	43
	15 min 820°C	44
	15 min 840°C	53
	15 min 860°C	58

	3min 860°C/ 15min 850°C	70
	10min 960°C/15min 600°C	21
	10min 630°C/ 15min 600°C	52
	3min 860°C/ 40min 650°C	28
	10min 720°C/15min 700°C	32
	3min 860°C/ 15min 750°C	53
	3min 860°C/15min 780°C	42
	10min 960°C/15min 800°C	29
	As received	27
CermeTi®-C-662	3min 860°C	58
	15min 650°C	30
	45min 860°C	58
	15min 860°C	58

The percentages of beta phase that result from the tests “from above” do not fit with the results obtained from the tests “from below”. This indicates that there is some microstructural hysteresis of more or less 10%, that the equilibrium was not reached, and/or that the quenching with water can bring some changes to the microstructure.

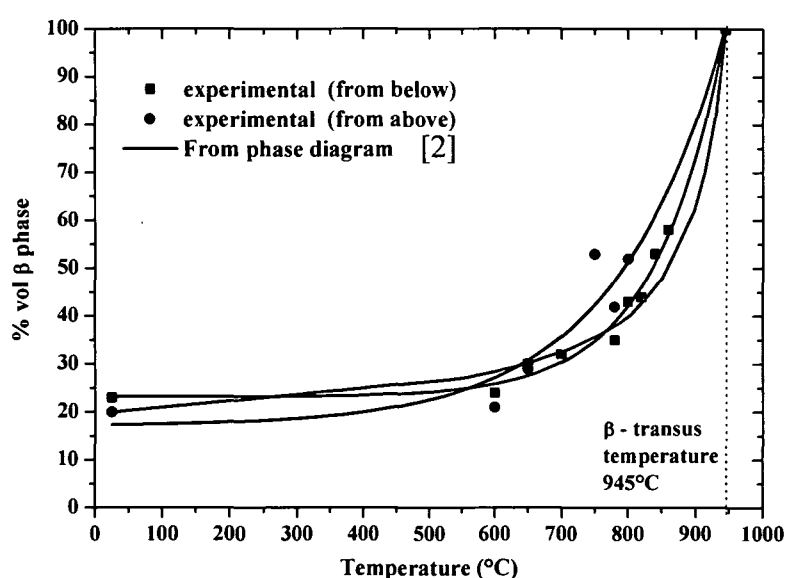


Figure 94. Plot of the measured values of β% after cooling or heating and compared with the data from the phase diagram.

## 4.4 EBSD

The EBSD tests were done in an area of  $25200\ \mu\text{m}^2$  for the transversal direction (Figure 95) and  $58800\ \mu\text{m}^2$  for the direction of the cogging (Figure 96) shows a mean grain size of  $9.23\ \mu\text{m}$  and  $16.79\ \mu\text{m}$  respectively (measured with SigmaScan Pro).

Furthermore, the grains are mainly oriented in the direction of cogging, and the c-axis of the hcp alpha phase are oriented in the direction perpendicular to the cogging.

### - Transversal specimen

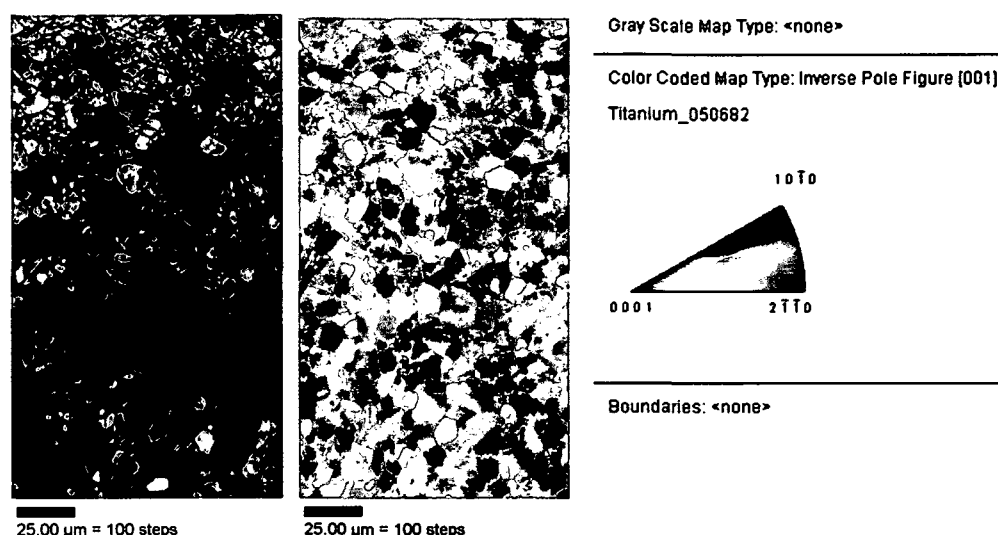


Figure 95 Alpha grain orientations in Ti662 Ingot in the plane transversal to the cogging direction

### - Longitudinal specimen

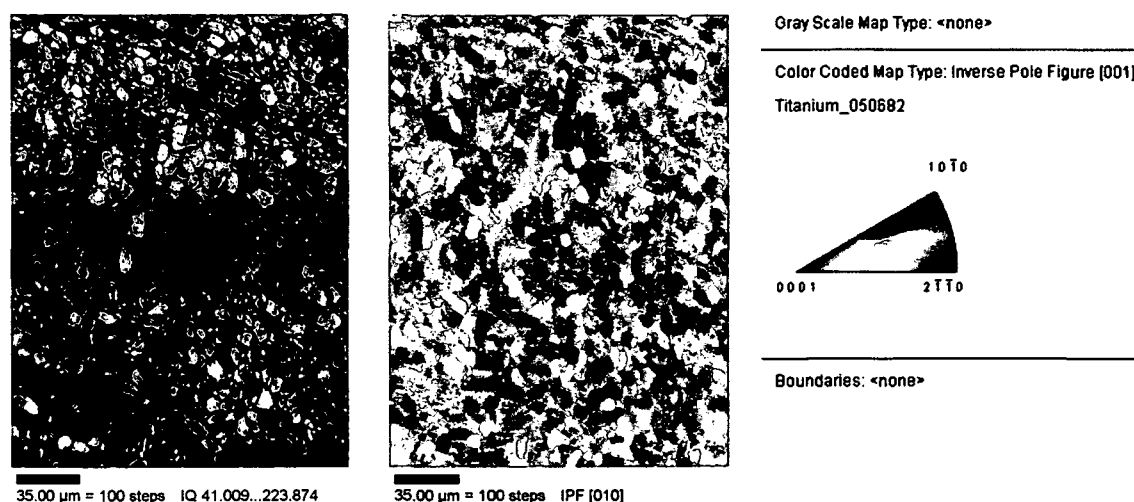


Figure 96 Alpha grain orientations in Ti662 Ingot in the cogging direction (vertical)

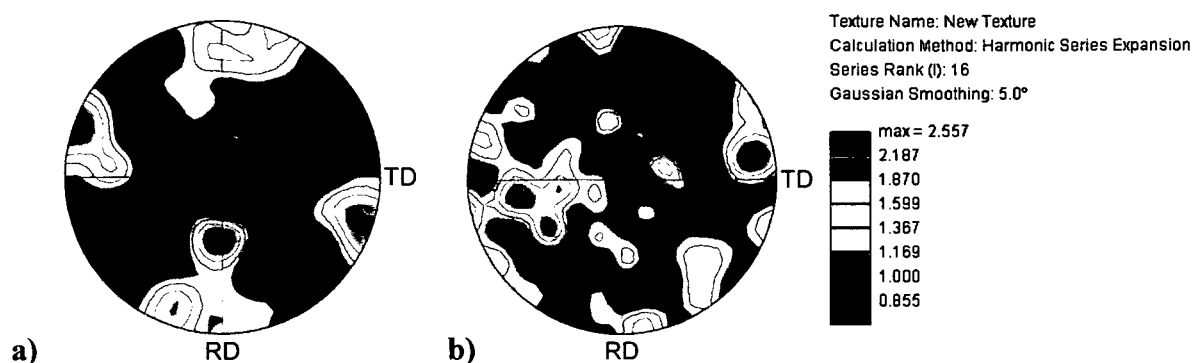


Figure 97 Pole figure showing texture of the 0001 planes of a) a longitudinal sample and b) a transversal sample showing dominant orientation of the basal planes perpendicular to TD, that means perpendicular to the cogging direction.

## 4.5 Diffractometry

Table 9 summarises the lattice parameters, the crystal size and the percentage of the present phases for each sample.

Table 9 Lattice parameters, crystal size and percentage of the phases

Sample	Phase	Lattice parameters Å	Crystal domain size (nm) Lorentzian	Percentage (wt%)
<i>CermeTi<sup>®</sup>-C-662</i>	alpha	$a = 2.925251(6)$ $c = 4.67560(1)$	296	85.0
	beta	$a = 3.214434(9)$	51	15.0
<i>CermeTi<sup>®</sup>-C-662 after a heat treatment at 600°C and water quenched</i>	alpha	$a = 2.925720(8)$ $c = 4.67532(2)$	358	83.0
	beta	$a = 3.22168(2)$	170	17.0
<i>Ti662 Ingot as received</i>	alpha	$a = 2.92566$ $c = 4.67434$	164.6	85.5
	beta	$a = 3.21520$	71.9	14.5
<i>CermeTi<sup>®</sup>-C-12-662</i>	alpha	$a = 2.92544(1)$ $c = 4.67944(2)$	231	62.1
	beta	$a = 3.22056(2)$	48	18.2
	TiC <sub>x</sub> (*)	$a = 4.30334$	2400	19.7

(\*) x estimated = 0.7 ; from literature = 0.6 [116]

It should be noted, that the diffractometry was done on the polished surfaces, and that the high texture of the samples after the first cycle of dilatometry (2) and after the second one (3) (see above) did not allow us to measure their cell parameters.

Comparing CermeTi<sup>®</sup>-C-662 samples before and after the heat treatment, it can be seen that there is a slight increase in the crystal size for the second one, in alpha and especially in beta phase. There is also an increment of the  $a$  parameter of the beta phase and the percentage of beta phase in the heat-treated sample. Furthermore, the Ti662 Ingot and the CermeTi<sup>®</sup>-C-662 samples show the same cell parameters and phase percentage, but half of the alpha crystal size in the ingot version.

After quenching from 600°C, the value of  $a$  parameter of the beta phase of Ti662 is higher than that of the as received material, suggesting higher content of V in the beta face in the as received sample [22].

For the reinforced material, it was found that the ratio Ti: C in the TiC particles is 1.4 approximately. This phenomenon is deduced from the small cell parameter  $a$  obtained by X- Ray and compared with the literature. The addition of TiC in the powder metallurgical material provokes an enlargement of the alpha phase in the  $c$  direction and of the beta phase cell parameter. The TiC crystal  $a$  value is lower than that from literature as a result of the poor content of carbon in the titanium carbide particles. On the other hand, the relatively high value of the carbide crystal size affects the estimation of the different phases.

The diffractometry patterns of Figure 98 show the signals of alpha and beta phases of the unreinforced Ti662, while Figure 99 shows the peaks of the TiC<sub>x</sub>, and no peak of the ordered phase TiC<sub>0.5</sub>.

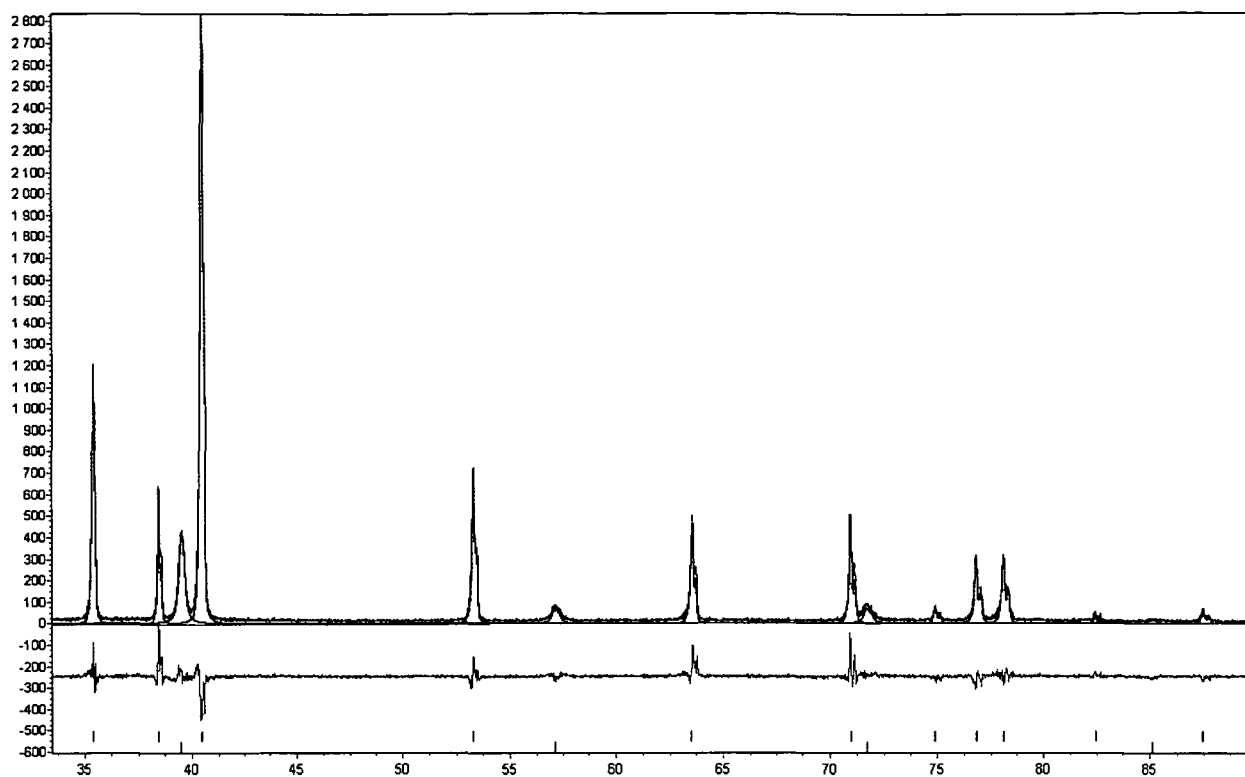


Figure 98. X-Ray diffraction pattern of the as received CermeTi®-C-662.

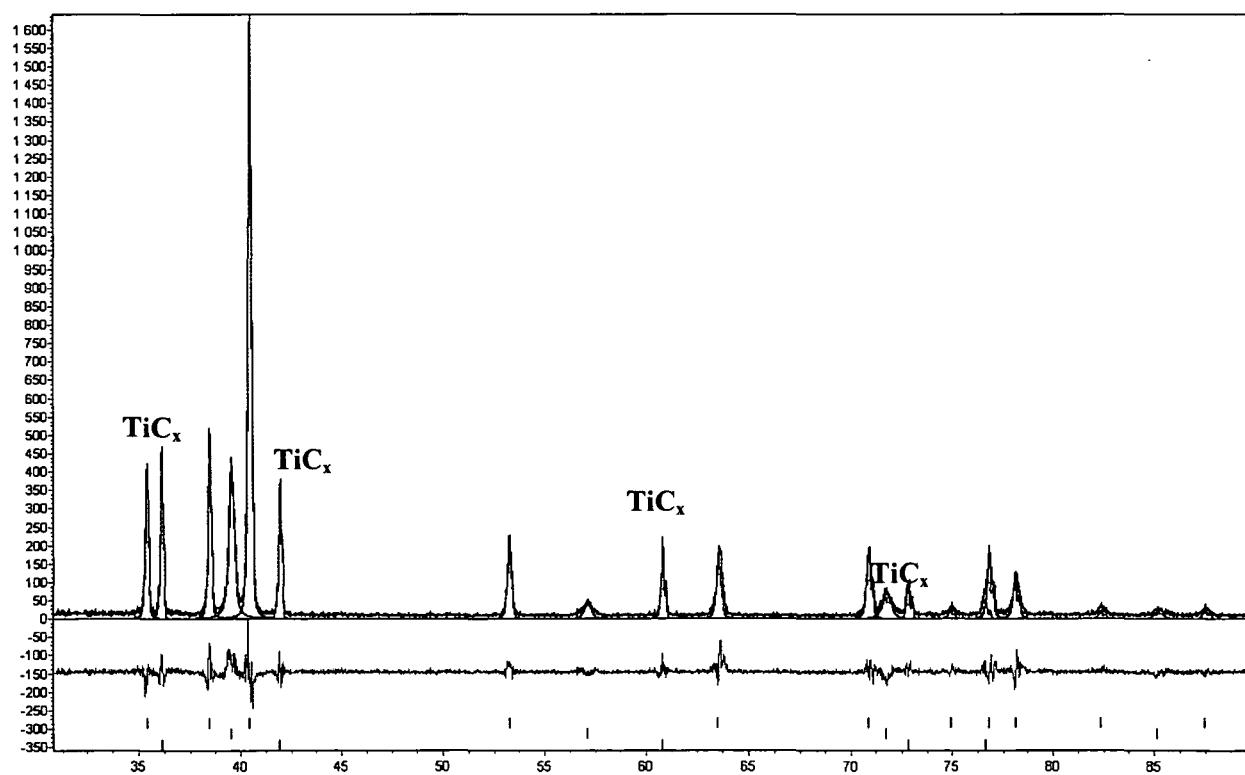


Figure 99 X-Ray diffraction pattern of the as received CermeTi®-C-20-662

## 4.6 Dilatometry Results

### 4.6.1 Change in length

The percentage change in length for the second cycle was drawn for all the temperature programs, normalized to begin at 0% change in length. The experiments were repeated, and the comparison shows a good reproducibility except some experimental

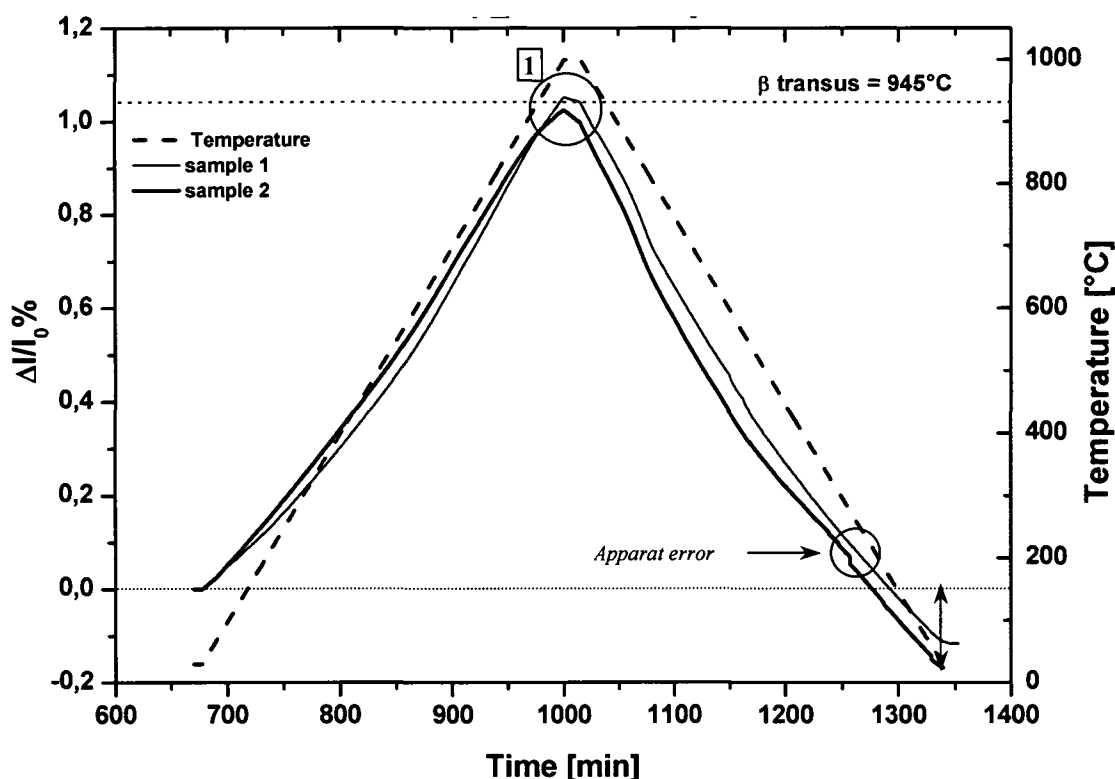


Figure 100 Temp\_01 Ti662 Ingot showing a contraction of the sample with the holding time.

The Ti662 alloy (Ingot in Figure 100 and produced by powder metallurgy in Figure 103) and the Ti64 (Figure 101) show non-linearity of the change in length in the range between 600°C and beta transus temperature. A significant contraction in the length can be observed for titanium Grade 2 in Figure 102 at the beta transus temperature.

Comparing for the same Ti64 alloy two different heat treatments (Temp\_04 and Temp\_02), it was observed at 1000°C that  $\Delta l/l$  % maximum is 1% in the first case, but only 0.4% in the second case.

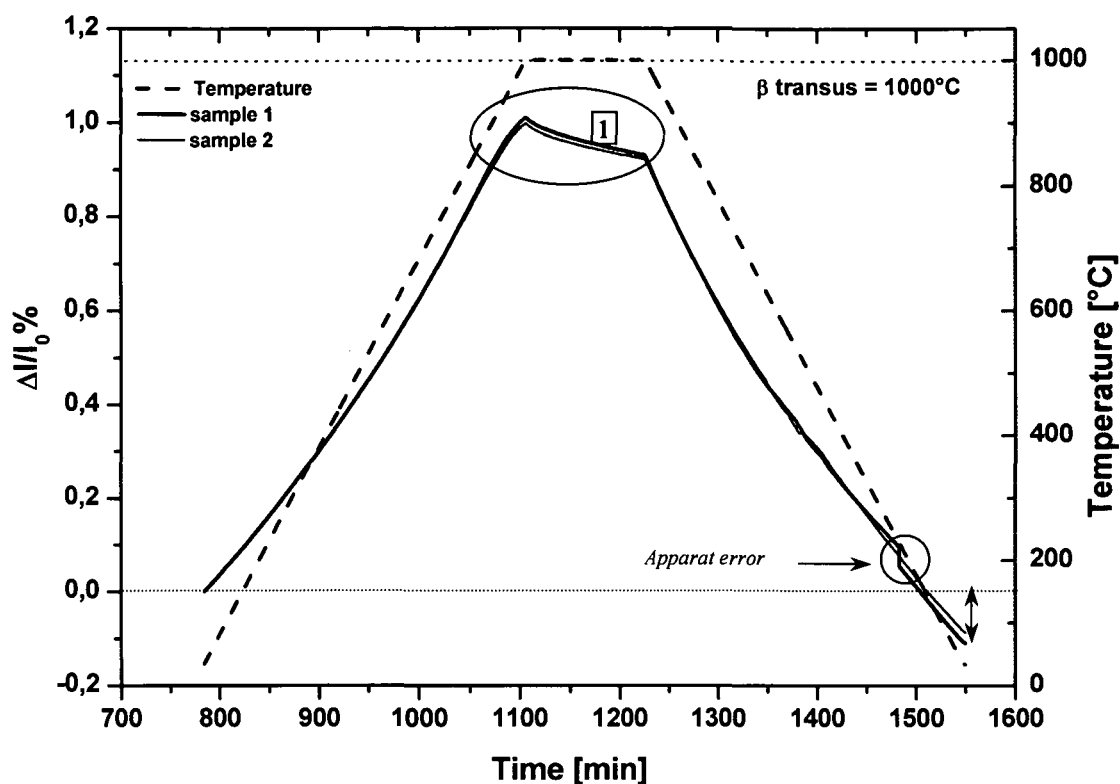


Figure 101 Temp\_04. Ti64 produced by Dynamet, showing a significant contraction of the sample at the transus temperature.

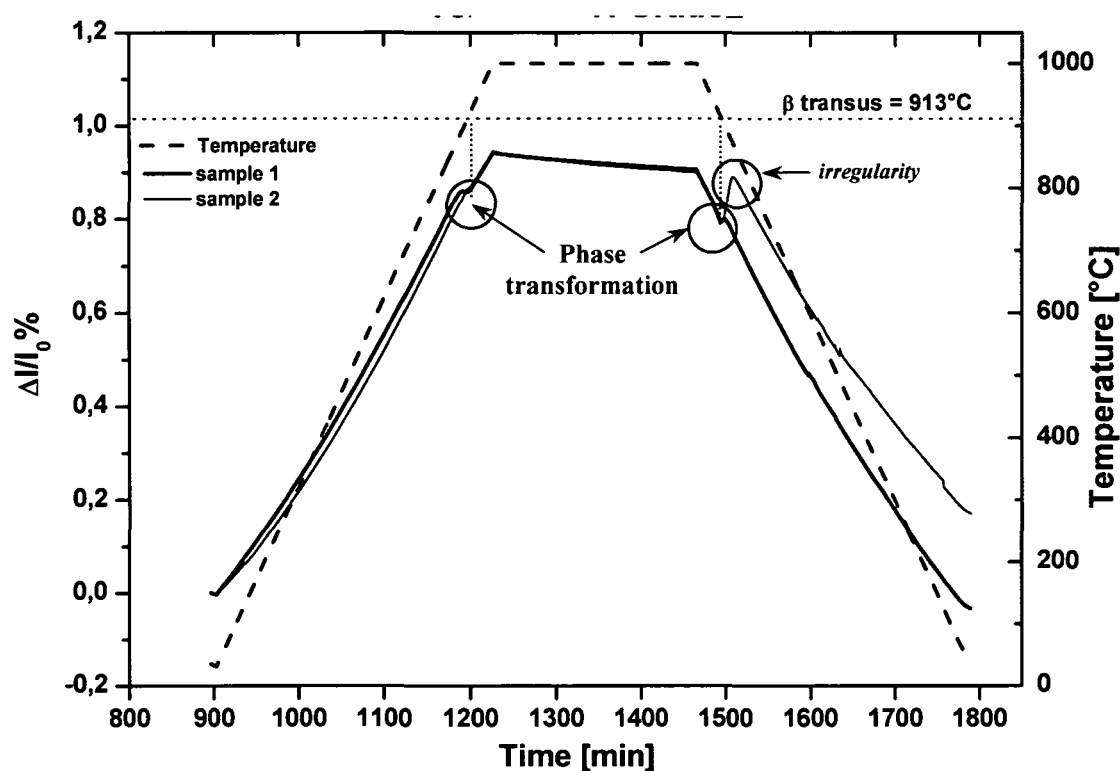


Figure 102. Temp\_05. Titanium commercial purity Grade 2, showing a significant contraction of the sample at the beta transus temperature.



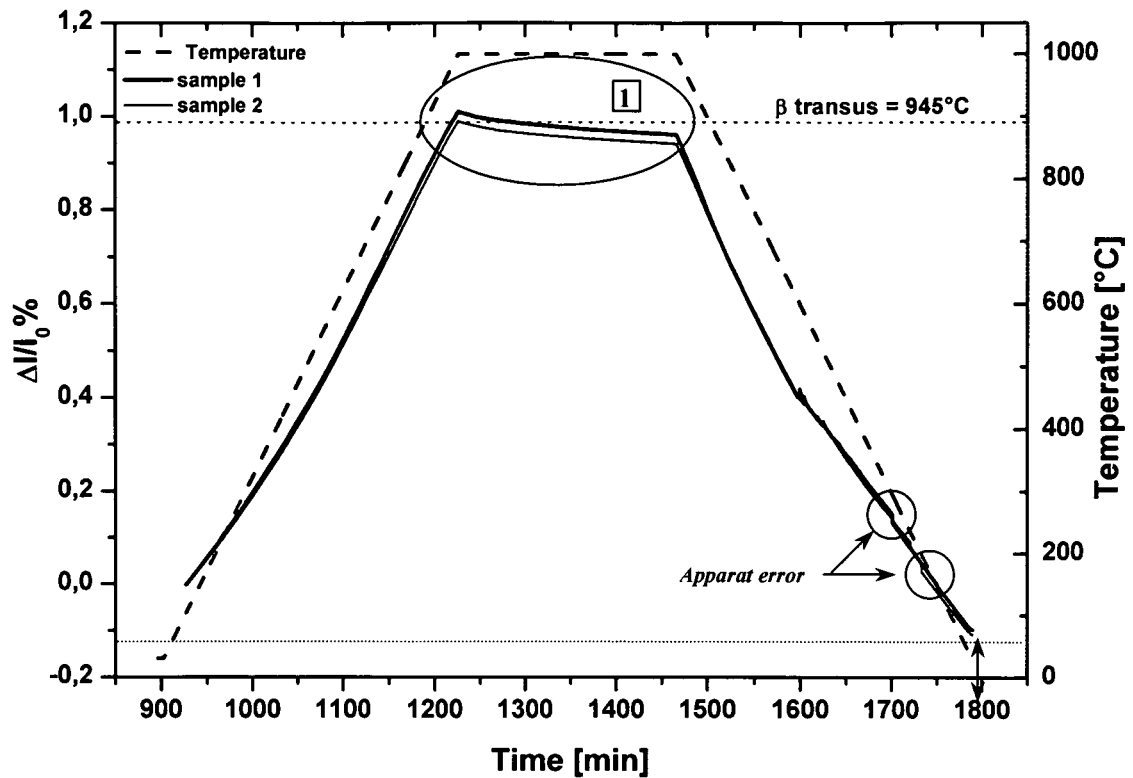


Figure 103. Temp\_02. Ti662 alloy showing the change in length with the time and the temperature

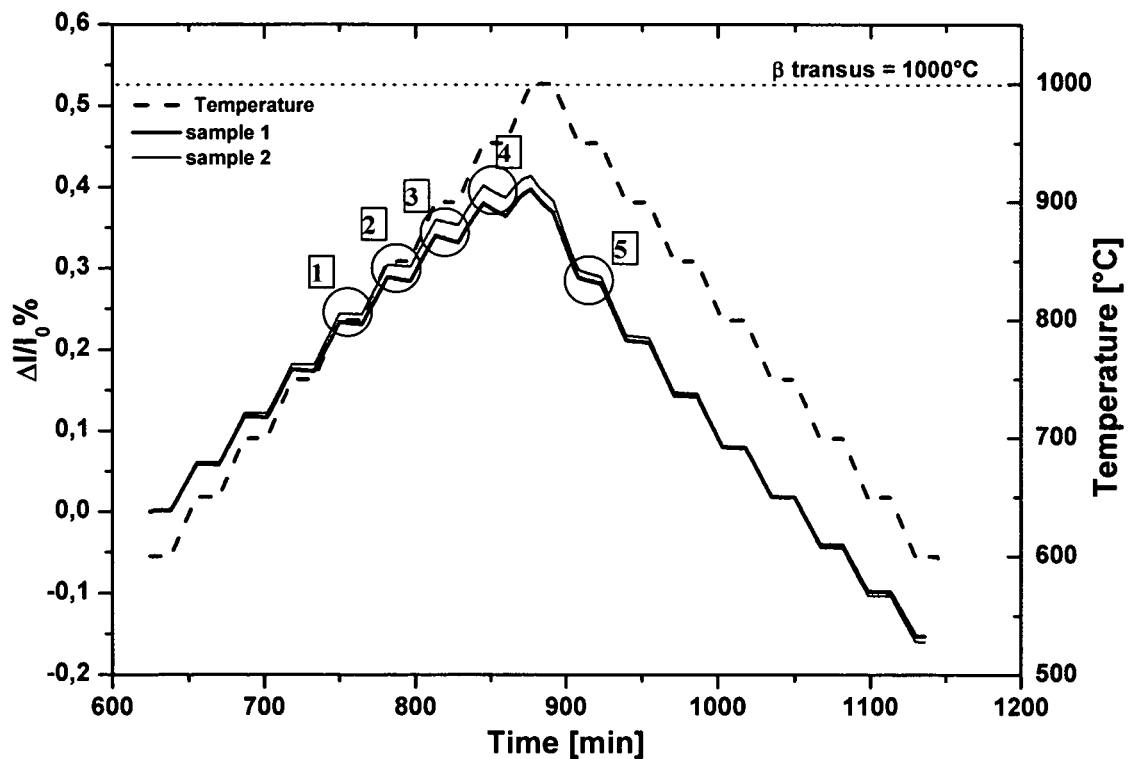


Figure 104. Step temperature programme for Ti64 alloy produced by powder metallurgy, showing the contraction of the sample at constant temperature above 750°C. Not the higher expansion in the second cycle.

As explained in “limitations of the method” in the experimental part, the measurements show a constant decreasing in the length of the sample, which can be caused by the reaction of the titanium with the  $\text{SiO}_2$  holder. This phenomenon is pronounced at temperatures above  $750^\circ\text{C}$ , as shown in the zone 1 of Figure 100. If we compare the change in length at the holding time of Ti662 with that of the Ti64 at the beta transus temperature (Figure 101), we can see that the second one is more raised than the first one, due to a non-equilibrium state. In this way it is also possible to explain the decreasing slopes 1, 2, 3, 4 in the Figure 104. The slope 5 is clearly more flat than that of 4, even though they are at the same temperature, indicating that in 5 the reaction with the holder is decreasing and superimposed by the transformation into alpha.

Coefficient of thermal expansion.

Figure 105 shows the CTE ( $\alpha$  ppm/K) as a function of the temperature for Ti662 Ingot (a), and Ti64 (b). It can be seen an increment of the coefficient of thermal expansion at  $600^\circ\text{C}$ , more evident for the Ti662 alloy (1). The closer the temperature to the beta transus, the smaller the CTE (2). Once the beta transus has been passed, the CTE seems to reach a minimum (3) and should begin to increase, but this is not possible to measure due to the high temperatures and the secondary reactions explained in “limitations of the technique”. During cooling, below beta transus a maximum in CTE is produced (4).

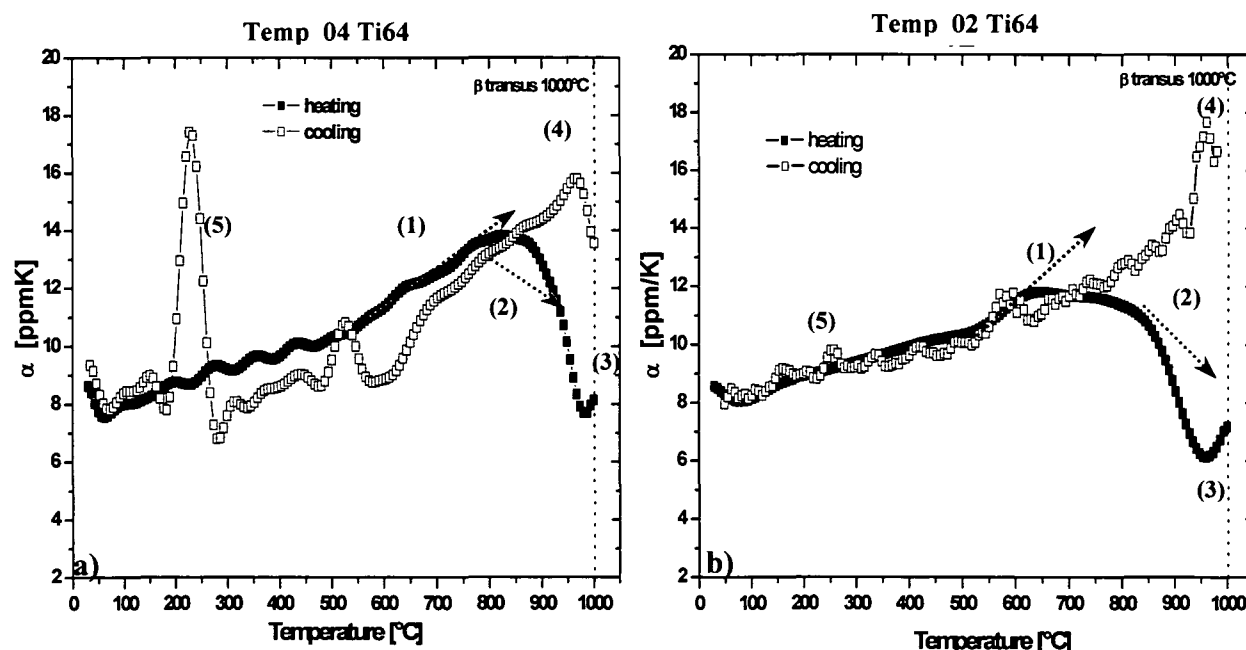


Figure 105. Coefficient of thermal expansion for Ti64 alloy a) and b), showing the increment in the CTE at  $600^\circ\text{C}$  (1), the CTE decrement near the beta transus (2), the minimum near the beta transus (3), a peak when cooling starts (4) and irregularities during cooling (5)

Sometimes non-reproducible peaks appear like in (5) at different temperatures, depending on the sample

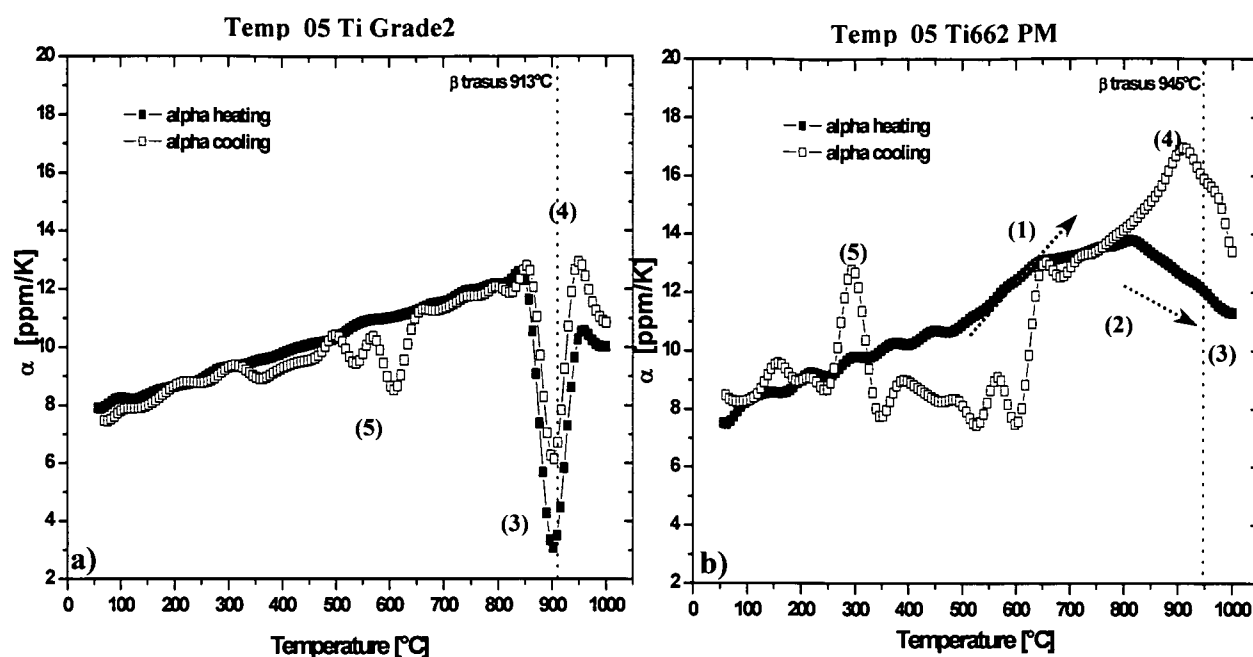


Figure 106 Coefficient of thermal expansion for the a) Ti Grade2 showing a large decrement of the CTE close to the beta transus temperature and b) Ti662 alloy, showing the increment in the CTE at 600°C (1), the CTE decrement near the beta transus (2), the minimum the beta transus (3), a peak when cooling starts (4) and irregularities during cooling (5)

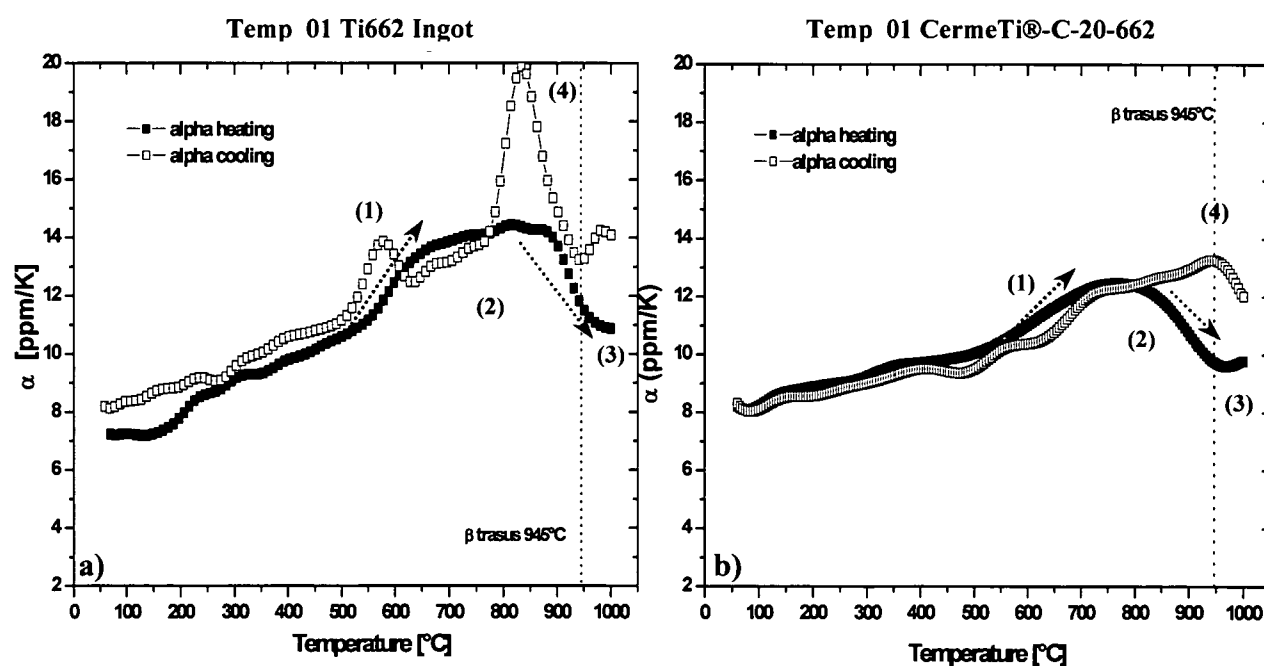


Figure 107 Coefficient of thermal expansion for a) Ti662 Ingot and b) Ti662 alloy reinforced with 20% TiC particles showing the increment in the CTE at 600°C (1), the CTE decrement near the beta transus (2), the minimum near the beta transus (3), a peak when cooling starts (4) and irregularities during cooling (5).

The Figure 107 was calculated extracting the steps of heating and cooling, and it can be seen that the CTE values are continuous and coincident to the values of Figure 105b).

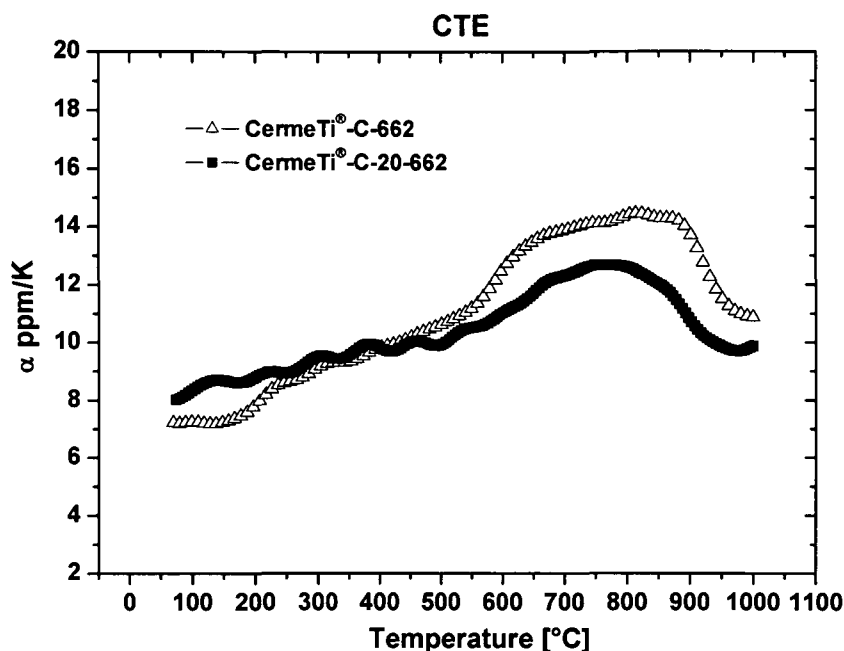


Figure 108 Comparison between the CTE values of the unreinforced alloy (CermeTi®-C-662) with these of the composite (CermeTi®-C-20-662).

Figure 106 shows the same 3 zones than before for the Ti662 alloy b), but not for the Ti Grade 2 a), for which only a marked CTE decrease is observed in a small temperature range close to the beta transus temperature.

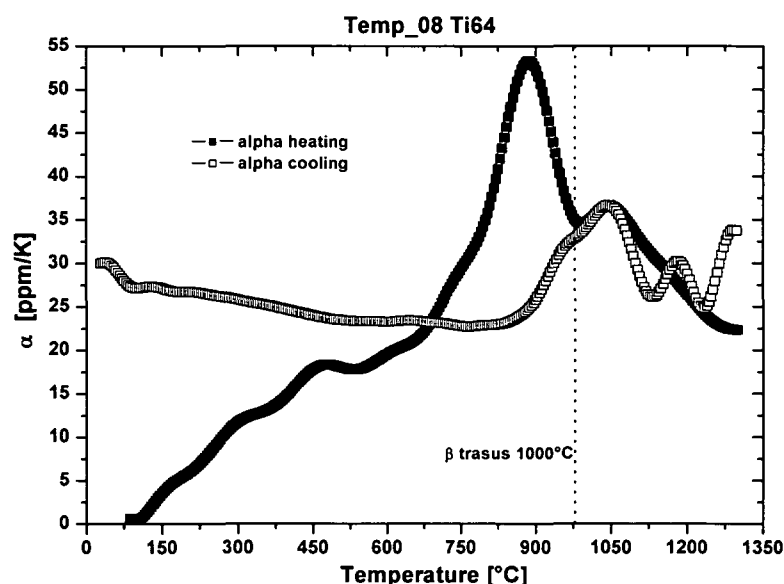


Figure 109. Extremely high values of thermal expansion for Ti64 alloy using the alumina holder, showing the error in the measurement due to reactions at high temperatures in comparison with Figure 104b)

The material reinforced with 20% of TiC particles shows lower CTE compared with the unreinforced alloy at temperatures higher than 500°C, and maximal difference of 15% lower near the beta transus temperature (Figure 108).

Figure 109 shows the calculated values of instantaneous thermal expansion by heating and cooling for Ti64 using the alumina holder, and it can be seen that the CTE becomes extremely high at 800°C compared to those show before due to interface reaction with the holder.

#### 4.7 Young's modulus.

Figure 110 compares the Young's modulus of all the materials produced by powder metallurgy with Ti662 alloy in the temperature range between room temperature and 350°C. The reinforcement increases the stiffness over the whole temperature range. The TiC particles increase the E modulus by about 30% for the 20%vol of particles, and 15% for 12% of reinforcement. Due to the high content of pores and bad mechanical properties of the interface reaction zone, the addition of 15%vol SiC reinforcement in the Ti64 matrix increases its Young's modulus by not more than the 5%. The kink in the curves between 240°C and 300°C seems to be an experimental effect, which is reproducible.

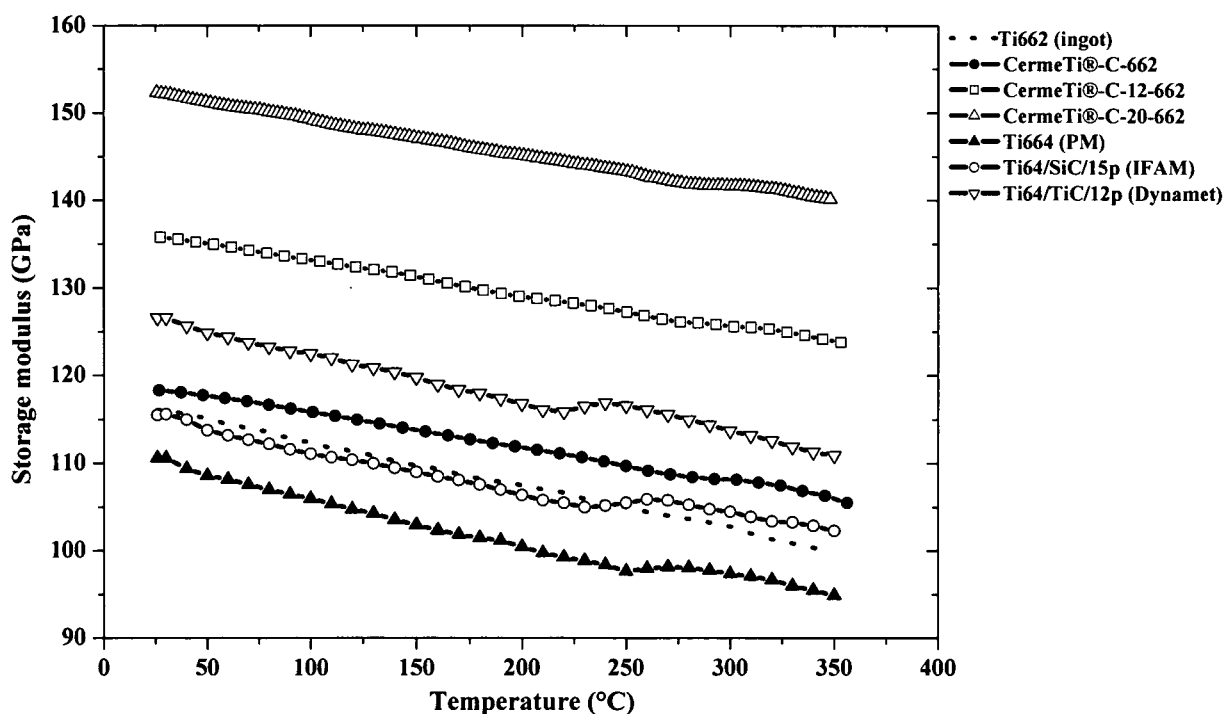


Figure 110. Young's modulus comparison for the titanium alloys unreinforced and reinforced with ceramic particles.

Figure 111 shows a comparison of the specific stiffness for the reinforced and unreinforced titanium alloys. The specific modulus  $E_{\text{spc}}$  expressed in km were calculated as follows:

$$E_{\text{spc}} = \frac{E_{\text{exp}}(T)}{\rho_{\text{RT}} \cdot g} (1 + 3\alpha) \quad \text{Equation 41}$$

where  $\rho$  is the density of the material in  $\text{kg/m}^3$ ,  $E_{\text{exp}}$  is the experimental Young's modulus in GPa and  $g$  is the gravity constant ( $9.81 \text{ m/s}^2$ ).

The thermal expansions between room temperature and  $350^\circ\text{C}$  for Ti662 Ingot, Ti662 PM, Ti64 PM and Ti662/TiC/20p were taken from the experimental values. The thermal expansion used for the materials Ti662/TiC/12p and Ti64/TiC/12p was taken from Ti662/TiC/20p. As the Ti64/SiC/15p has high porosity, the thermal expansion was not measured, but taken from the literature as  $7.7 \text{ ppm/K}$  [5].

The density results are shown in Table 10, and the  $\Delta\%$  for the MMC were calculated applying the ROM using values from the literature: density of Ti662:  $4590 \text{ kg/m}^3$  and of Ti64:  $4425 \text{ kg/m}^3$ . The difference for the MMC might be due to porosity and under-stoichiometric TiC particle.

**Table 10 Density results**

	Ti662 ingot	CermeTi®-C- 662	CermeTi®-C- C-20-662	CermeTi®-C- 12-662	Ti64 (PM)	Ti64/TiC/12p	Ti64/SiC/15p	Ti Grade2
<b>Density (<math>\text{g/cm}^3</math>)</b>	4.590 [24]	4.528	4.557	4.552	4.424	4.436	4.198	4.51 [24]
<b><math>\Delta\%</math></b>	0	-1,4	-2,2	-1,7	-0,02	-1.1	-0.7	0

Figure 111 shows that the addition of 12%vol of TiC particles increases the specific modulus in about 14%, and for the addition of 20%vol of TiC particles, the increase in specific modulus is about the 28%. Due to the lower density of the SiC reinforced material, the specific modulus is now comparatively higher, but still lower than that of the TiC reinforced Ti64 alloy. The addition of 15%vol SiC particles results in an improvement of the specific Young's modulus of about the 10%, while the addition of only 12%vol of TiC particles results in an improvement of about 13%.

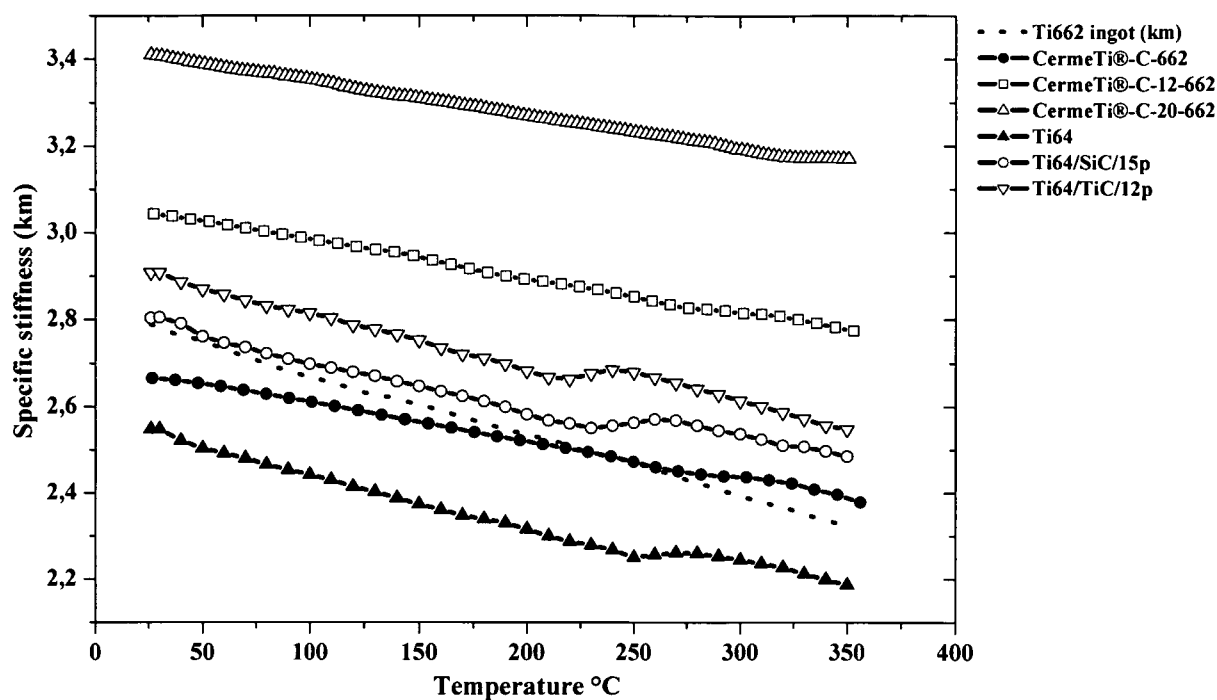


Figure 111. Specific modulus for the reinforced and unreinforced Ti662 and Ti64 produced by powder metallurgy compared to the Ti662 Ingot.

#### 4.7.1 Dependence of the Young's modulus with the orientation

Figure 112 shows a discrepancy up to 4% in the values of the storage modulus between two samples with different grain orientation.

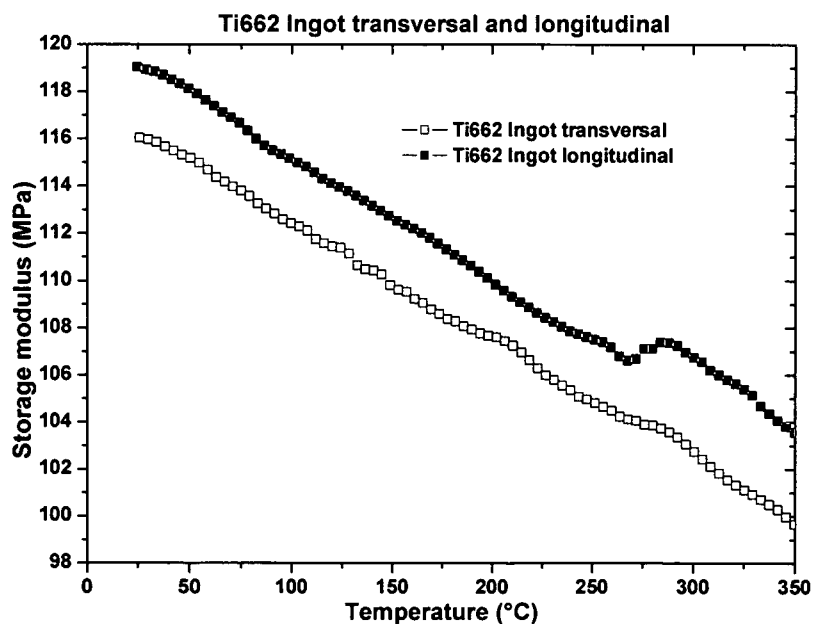


Figure 112 Discrepancies between the measurements of the Storage modulus for two Ti662 ingot samples taken at two different directions of cogging.

## 4.8 Compression tests.

### 4.8.1 Flow curves.

Figure 113-to Figure 117 show all the flow curves at 0.015, 0.08, 0.15, 1.4, and 15s<sup>-1</sup> strain rates and at temperatures of 650, 750, 850 and 950°C for all the materials. In the curves, the true stress as a function of the true plastic strain is plotted, as explained above.

In general, it can be observed that the higher the temperature and the lower the strain rate, the lower the compressive stress values.

The flow behaviour can be described for all the materials defining two main regions of strain rate:

- *Ti662 Ingot.*
  - 1) strain rates up to 0.15 s<sup>-1</sup>. Steady state can be observed at temperatures between 750-950°C, while softening occurs at 650°C.
  - 2) strain rates higher than 0.15 s<sup>-1</sup>. Flow softening occurs not only at 650°C, but also at 750°C, while the steady state lays between 850°C and 950°C. At 15s<sup>-1</sup> strain rate and temperatures lower and equal than 850°C, oscillations in the flow can be observed.
- *CermeTi<sup>®</sup>-C-662*
  - 1) strain rates up to 1.4 s<sup>-1</sup>. Steady state at 950°C, while softening occurs in the range of 650-850°C. At 1.4s<sup>-1</sup> strain rate and temperatures higher than 750°C, oscillations in the flow can be observed.
  - 2) strain rate of 15 s<sup>-1</sup>. Flow softening as well as oscillations in the flow occurs in the whole range of temperatures.
- *CermeTi<sup>®</sup>-C-12-662 and CermeTi<sup>®</sup>-C-20-662*
  - 1) strain rates up to 1.4 s<sup>-1</sup>. Steady state occurs only at 950°C (except for CermeTi<sup>®</sup>-C-20-662 at 0.08s<sup>-1</sup>), while softening is observed in the range of 650-850°C. At 1.4s<sup>-1</sup> strain rate and temperatures higher than 750°C, oscillations in the flow can be observed.
  - 2) strain rate of 15 s<sup>-1</sup>. Flow softening as well as oscillations in the flow occurs in the whole range of temperatures.
- *Ti64 PM*
  - 1) strain rates up to 1.4 s<sup>-1</sup>. Steady state is observed in the whole range of temperature. At strain rate of 1.4 s<sup>-1</sup> oscillations in the flow occur between 850 and 950°C.



---

- *Ti64/TiC/12p PM*

- 1) strain rates up to  $0.15 \text{ s}^{-1}$ . The steady state flow is observed only at  $950^{\circ}\text{C}$ , while slight softening can be seen between  $650^{\circ}\text{C}$  and  $850^{\circ}\text{C}$ . At strain rate of  $1.4 \text{ s}^{-1}$  oscillations in the flow occur between  $850$  and  $950^{\circ}\text{C}$ .
- 2) strain rate of  $1.4 \text{ s}^{-1}$ . Low ductility and softening is observed in the range of  $650$ - $950^{\circ}\text{C}$ .

Some other parameters, such as grain size, particle content and alpha percentage have also influences in the compressive stress values. The Ti662 ingot, with a grain size of about  $10 \mu\text{m}$  (Figure 96 and Figure 98) shows higher compressive strength than the Ti662 produced by powder metallurgy, with a grain size up to  $400 \mu\text{m}$ . The comparison between the two alloys produced by powder metallurgy shows higher compressive strength for the Ti64, with higher alpha content than for the Ti662 alloy. The ceramic particles increase markedly the compressive strength values of the matrices. Although the maximum stress values of CermeTi<sup>®</sup>-C-20-662 are slightly higher than those of the CermeTi<sup>®</sup>-C-12-662, the strong softening of the first composite result in similar and also lower strength values than the second one up to 0.2 of deformation.

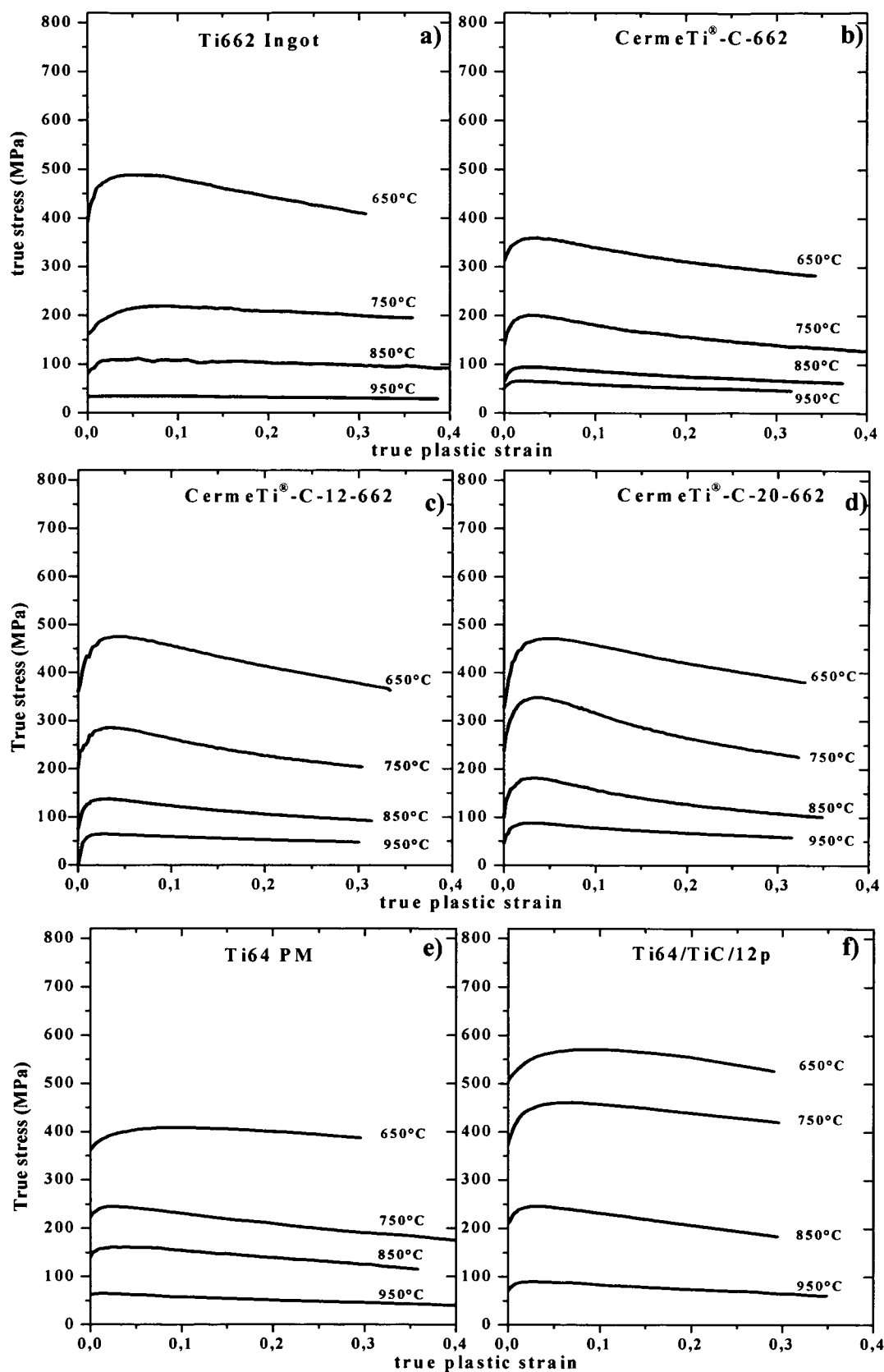


Figure 113. Flow curves at  $0.015 \text{ s}^{-1}$  strain rate a) Ti662 Ingot shows slightly higher strength than Ti662 produced by Dynamet b). The composites of Ti662 reinforced with 12%vol TiC particles c) 20%vol TiC particles d) show higher stress values than the matrix, but also a stronger softening. The higher content of alpha phase results in higher stress values for the Ti64 matrix d) and reinforced with 12%vol TiC e).

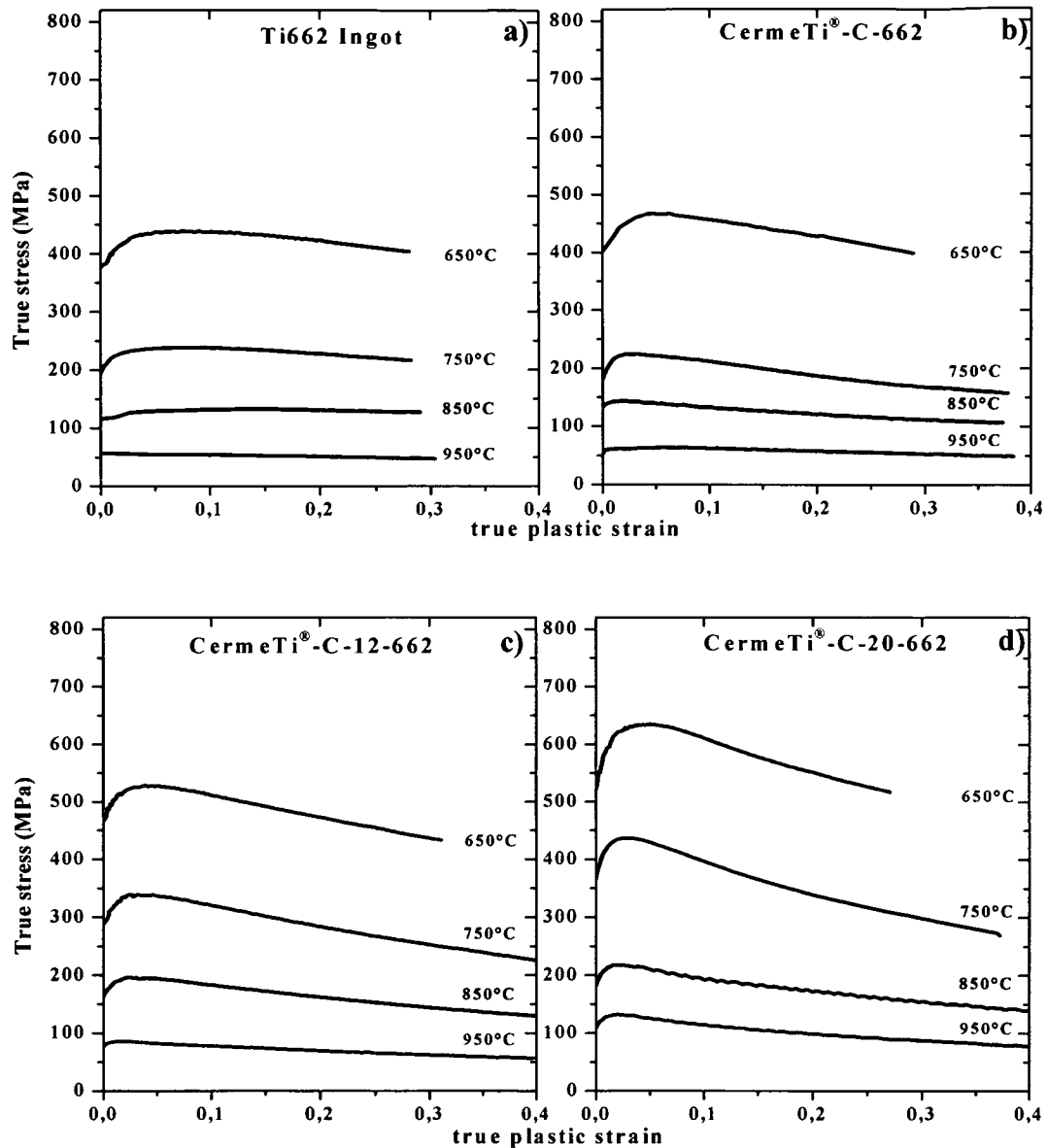


Figure 114 Flow curves at  $0.08\text{s}^{-1}$  strain rate. a) Ti662 Ingot shows similar strength than b) Ti662 produced by Dynamet. c) The composites of Ti662 reinforced with 12%vol TiC particles and d) 20%vol TiC particles show higher stress values than the matrix, but also a stronger softening.

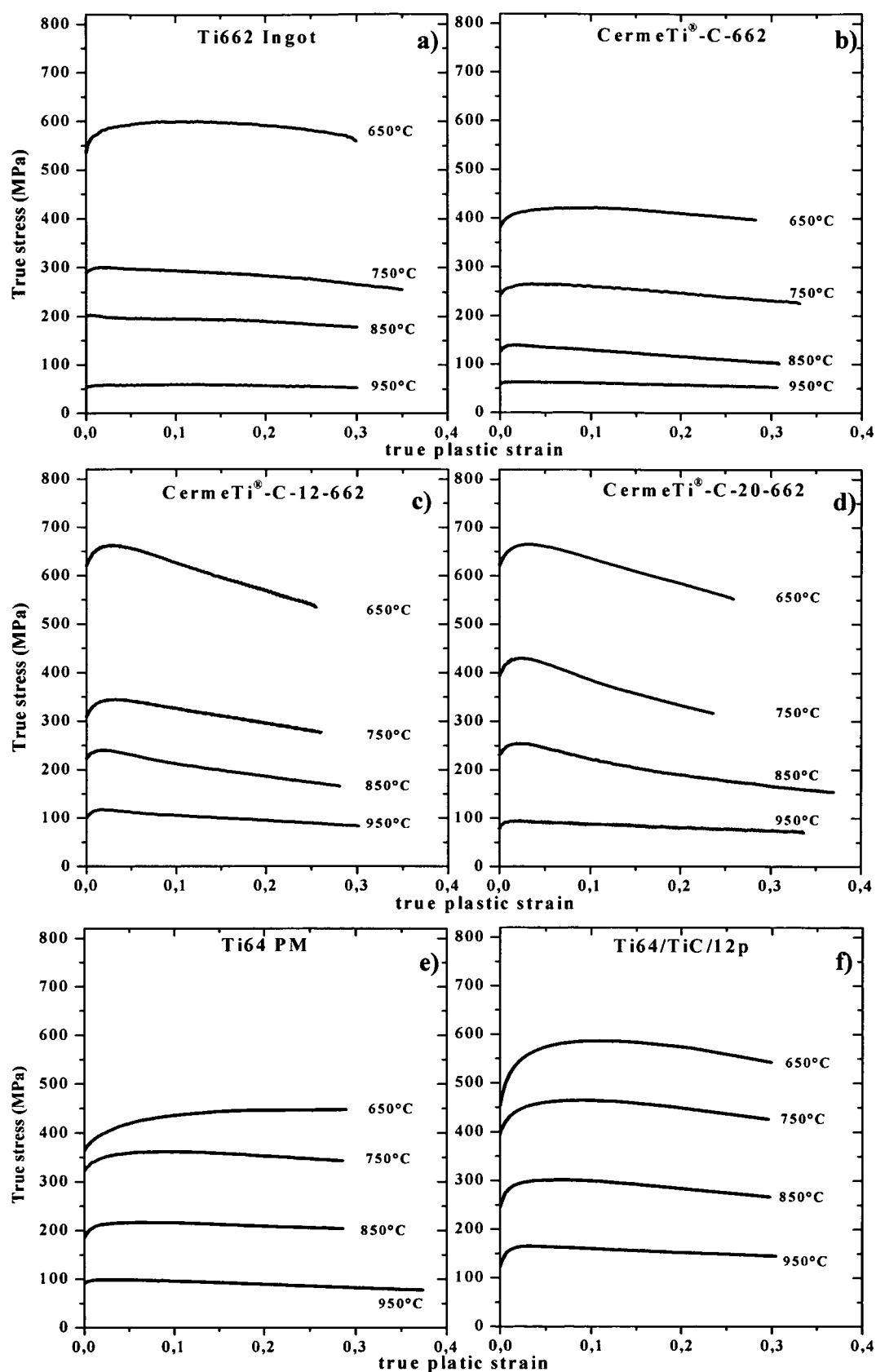


Figure 115 Flow curves at  $0.15\text{s}^{-1}$  strain rate a) Ti662 Ingot shows slightly higher strength than b) Ti662 PM. Composites of c) Ti662 with 12%vol TiC particles and with d) 20%vol TiC particles produce higher strength than the matrix, but also a stronger softening. Higher stress values were observed for e) the Ti64 matrix and f) the composite with 12%vol TiC.

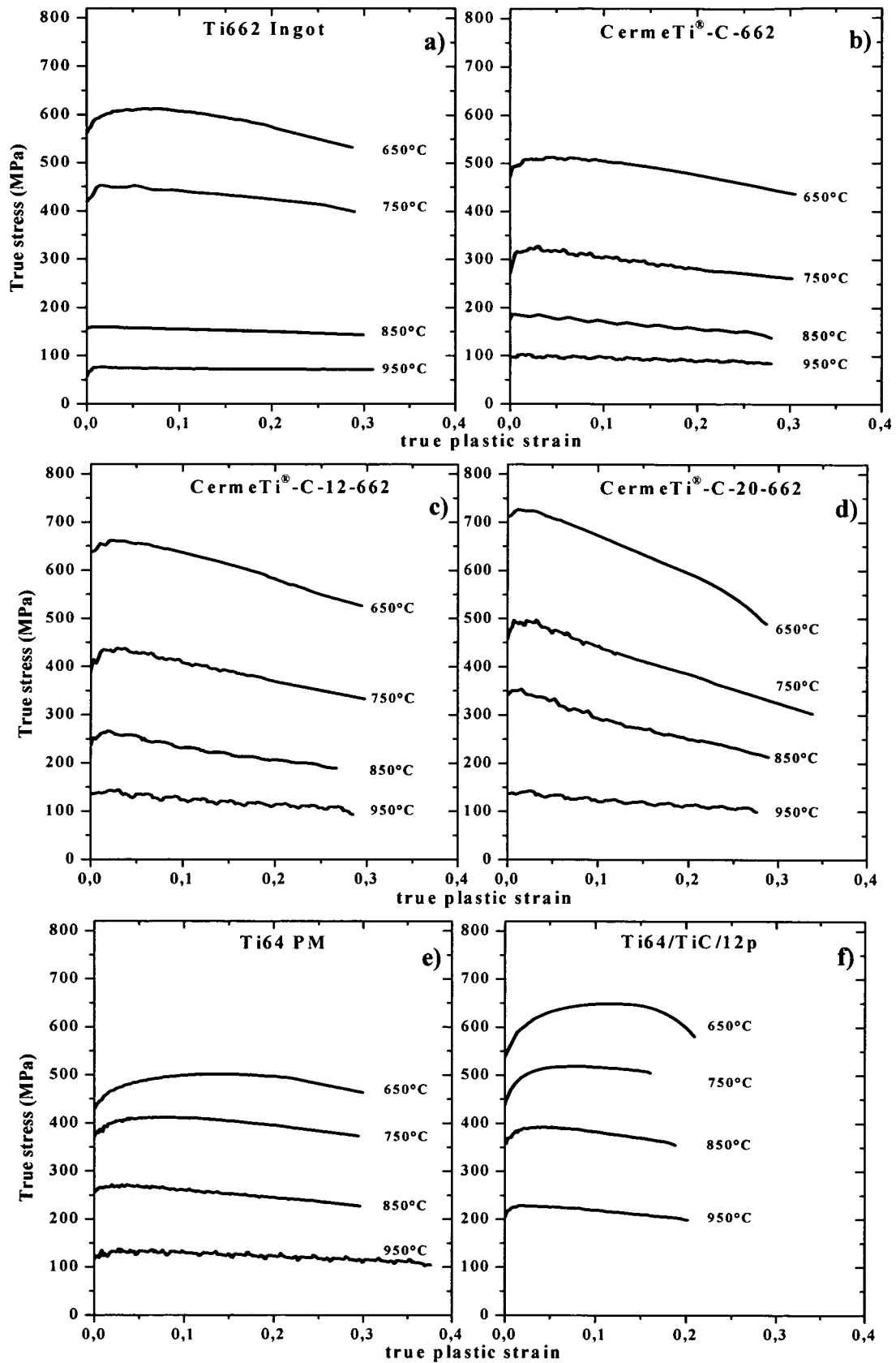


Figure 116 Flow curves at  $1.4s^{-1}$  strain rate a) Ti662 Ingot shows slightly higher strength values than b) Ti662 PM Ti662. The composites reinforced with c) 12%vol TiC particles and d) 20%vol TiC particles show higher stress values and stronger softening than the matrix. The strength values for e) Ti64 matrix and f) reinforced

with 12%vol TiC are slightly lower than that of the Ti622 materials. Some flow instability can be observed at high temperatures.

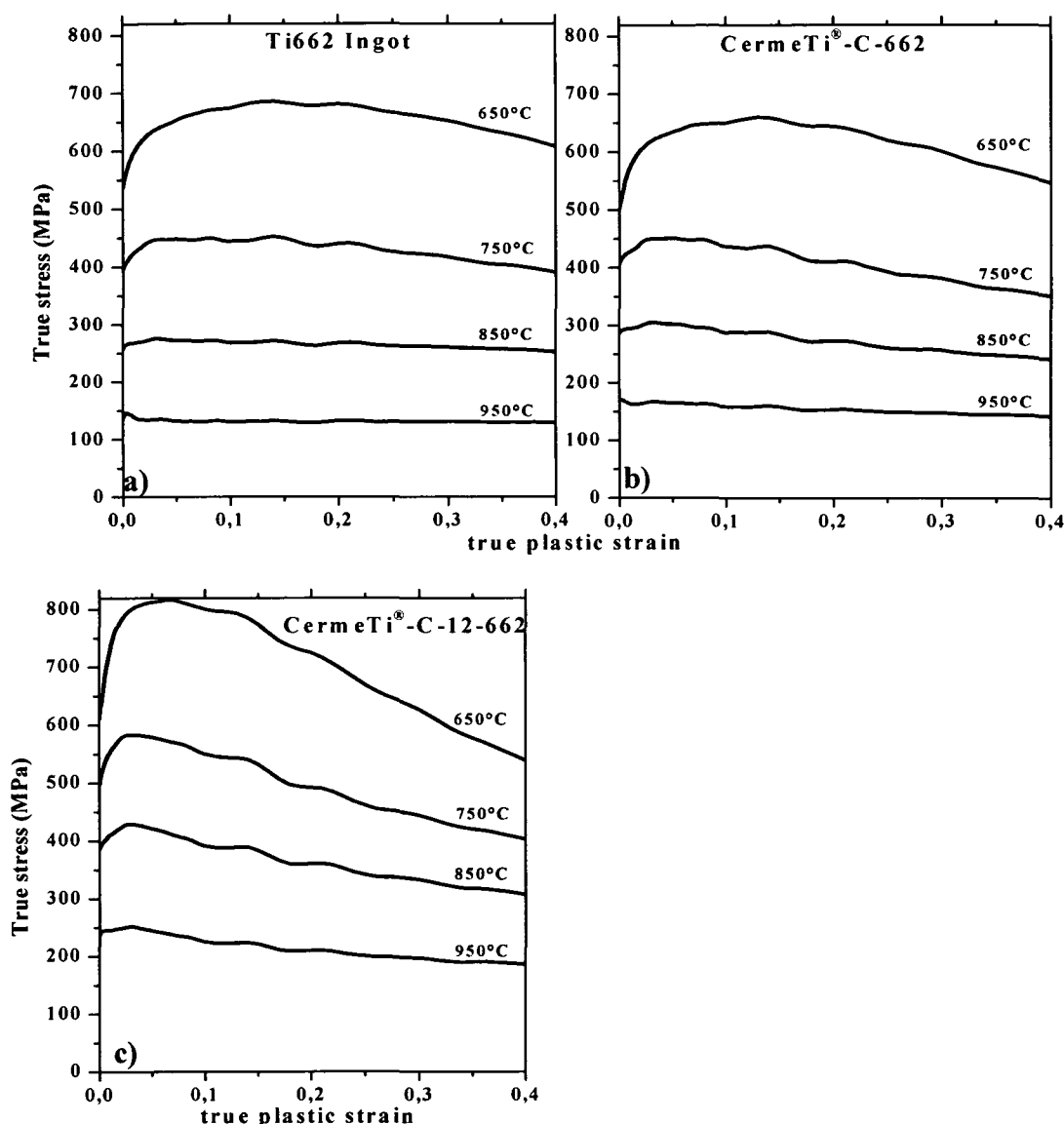


Figure 117. Flow curves at  $15\text{ s}^{-1}$  strain rate. a) Ti662 Ingot shows similar stress values than Ti662 produced by Dynamet b). The Ti662 reinforced with 12%vol TiC particles c) and shows higher stress values and stronger softening than the matrix. Some flow instability can be observe.

#### 4.8.2 Maximum Strength

The maximum strength values were taken from the flow curves and plotted vs. the temperature and the strain rate in a 3D diagram.

Figure 118 shows the variation of the maximum compressive stress with the temperature and the strain rate for the reinforced and unreinforced Ti662. The maximum strength values increase with

increasing temperature and decreasing the strain rate. The highest values are those of the CermeTi®-C-20-662, followed by the composite reinforced with 12% of TiC particles.

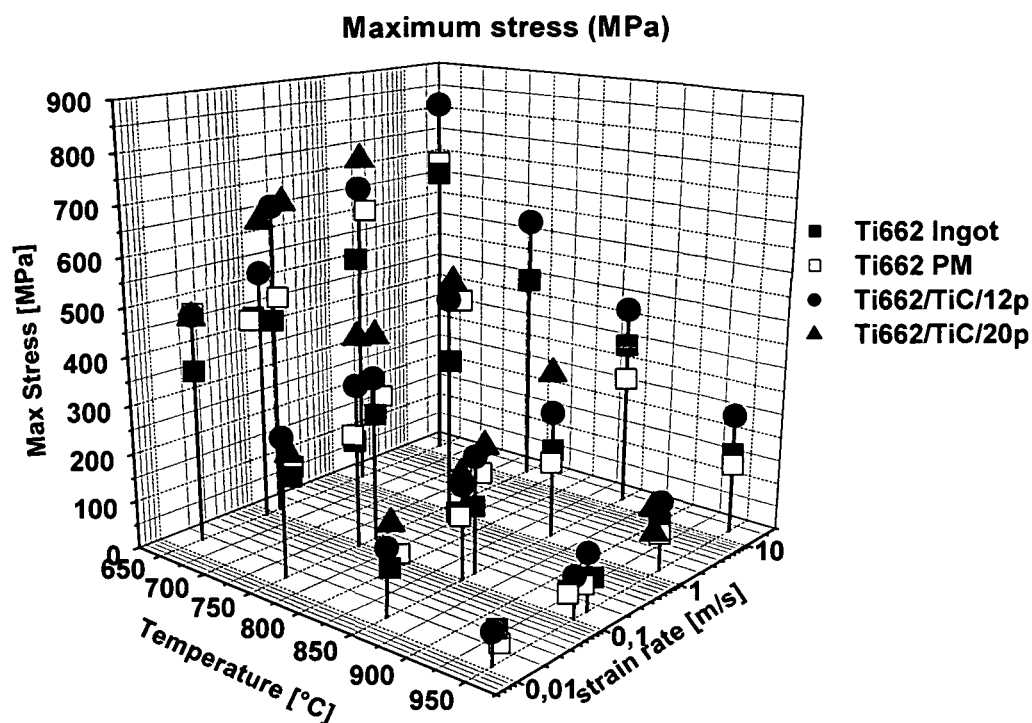


Figure 118. Maximum Stress (MPa) for the unreinforced materials Ti662 Ingot and CermeTi®-C-662, and for the composites CermeTi®-C-12-662 and CermeTi®-C-20-662.

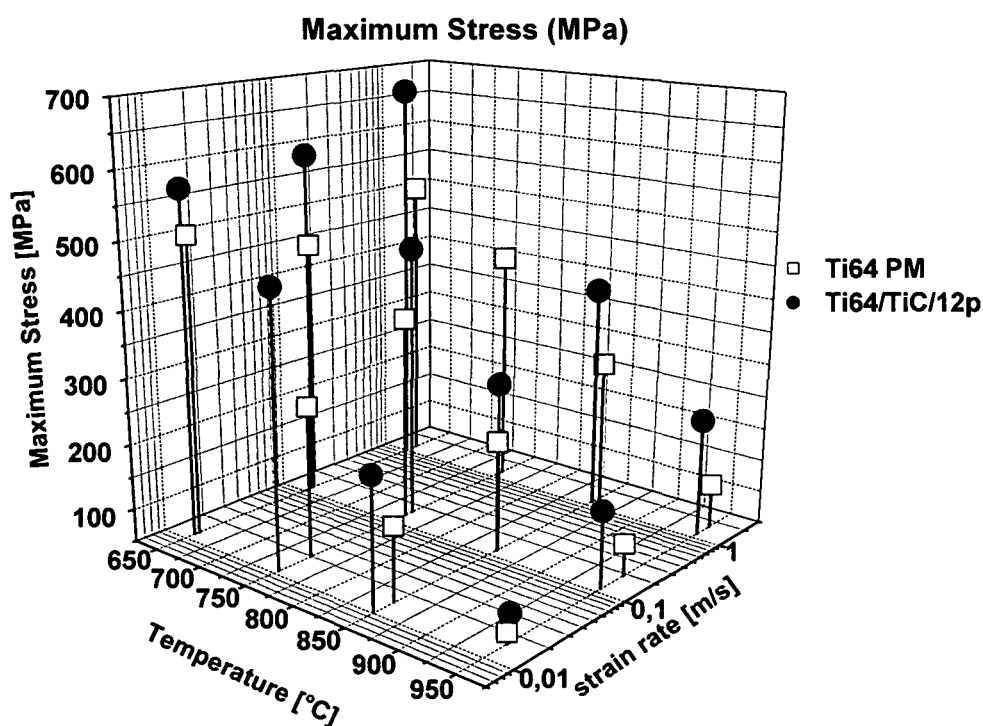


Figure 119. Maximum Stress (MPa) for the unreinforced Ti64 and the composite Ti64/TiC/12p.

The values of the maximum compressive stresses of the reinforced and unreinforced Ti64 also increases with the strain rate and with the decreasing temperatures, as shown in Figure 119. Furthermore, the addition of ceramic particles results in higher strength values.

#### 4.8.3 Temperature changes.

At high strain rate ( $1.4s^{-1}$ ), changes in the temperature in the centre of the specimen were registered during the tests with the Gleeble® 1500.

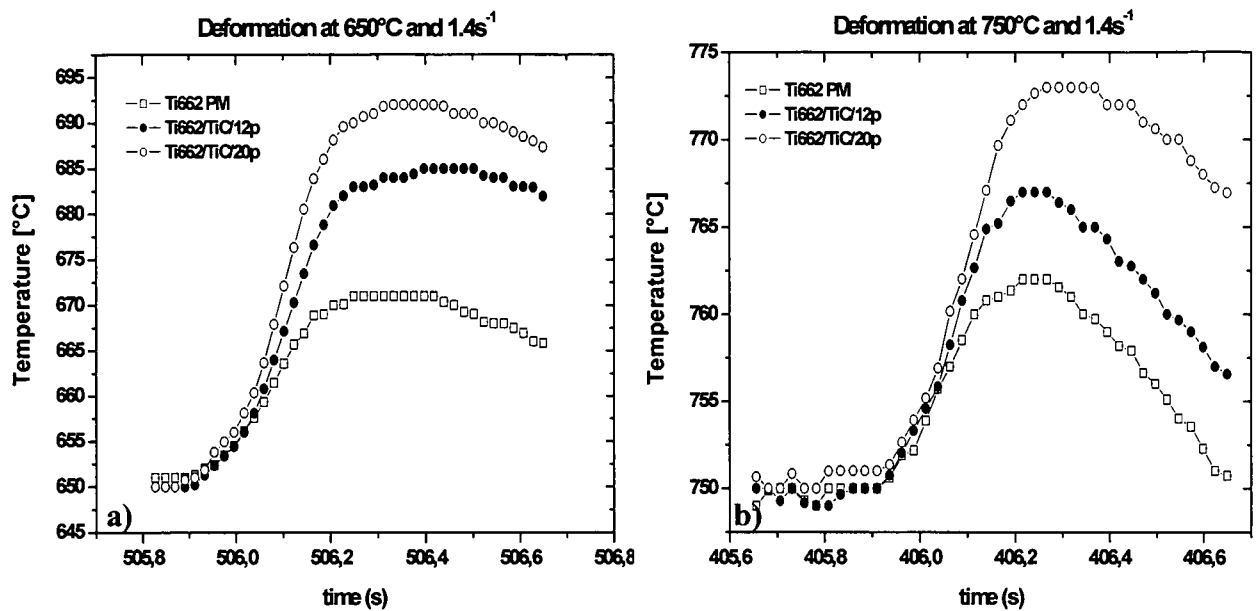


Figure 120. Increase of the temperature during deformation at  $1.4s^{-1}$  a) 650°C and at b) 750°C

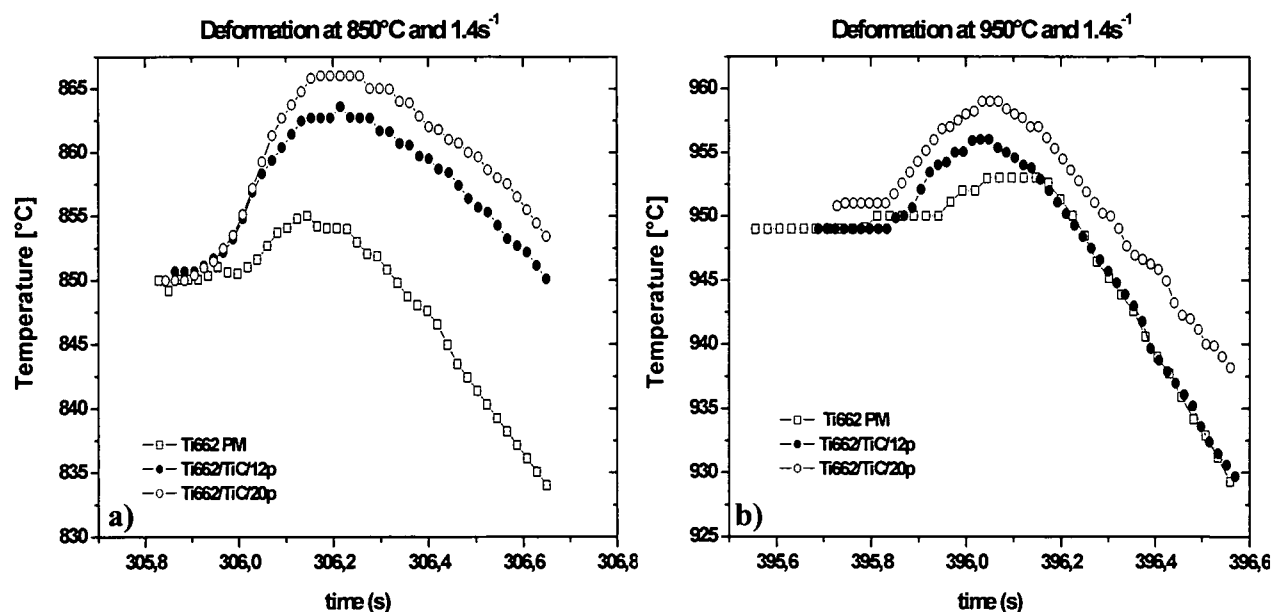


Figure 121. Increase of the temperature during deformation at  $1.4s^{-1}$  a) 850°C and at b) 950°C



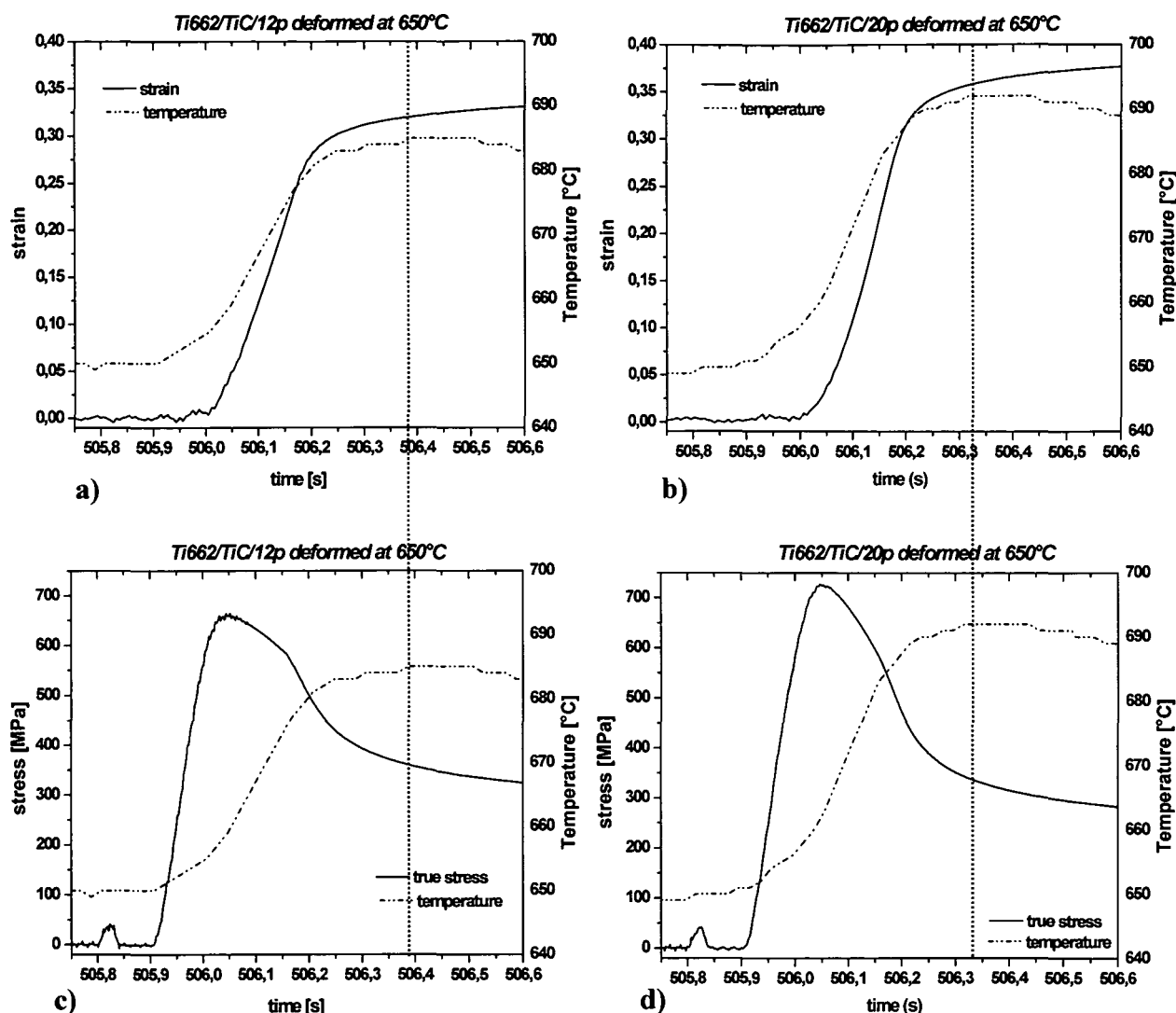


Figure 122. change of temperature during the deformation at 650°C of a) and c) Ti662 reinforced with 12% vol of particles and of b) and d) Ti662 reinforced with 20% vol of particles.

Figure 120 and Figure 121 show that the increment of the temperature during the deformation at 650, 750, 850 and 950°C is higher for higher particles content, while the Ti662 produced by powder metallurgy shows lower increment of the temperature than the other materials, except at 650°C. Furthermore, the changes in the temperature are more pronounced by decreasing the temperature of the compression test. The decay is due to the Gleeble control of the temperature that reduces the current when adiabatic heating increases the specimens' temperature.

The maximum of temperature corresponds to the end of the deformation (Figure 122 a) and b)). Furthermore, the increment of the temperature during the deformation results in the softening of the samples as shown in Figure 122 c) and d).

Figure 123 shows the maximum heating rate during compression at  $1.4 \text{ s}^{-1}$ . the heating rate increases by increasing the percentage of TiC particles and by decreasing the temperature of the compression test.

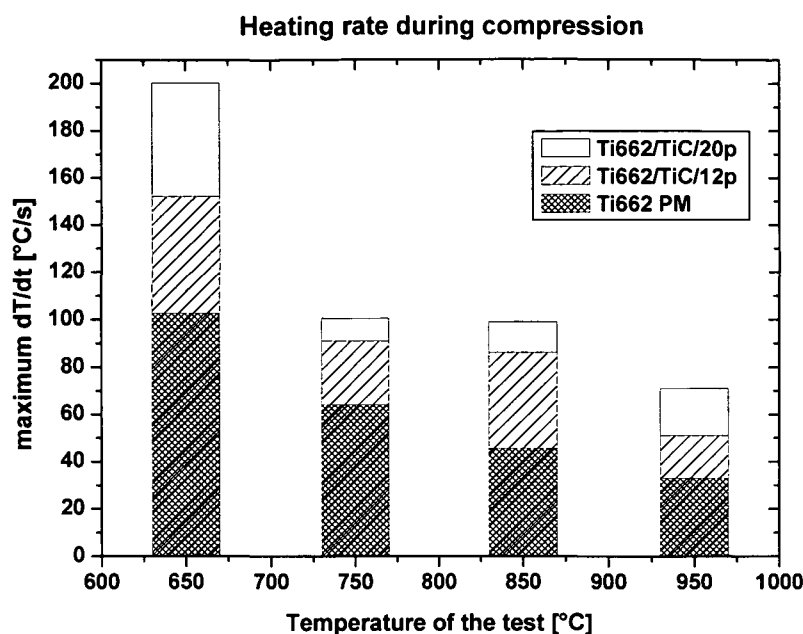


Figure 123. Maximum heating rate during deformation at the test temperature for the different materials.

#### 4.8.4 Effect of holding time at 650°C.

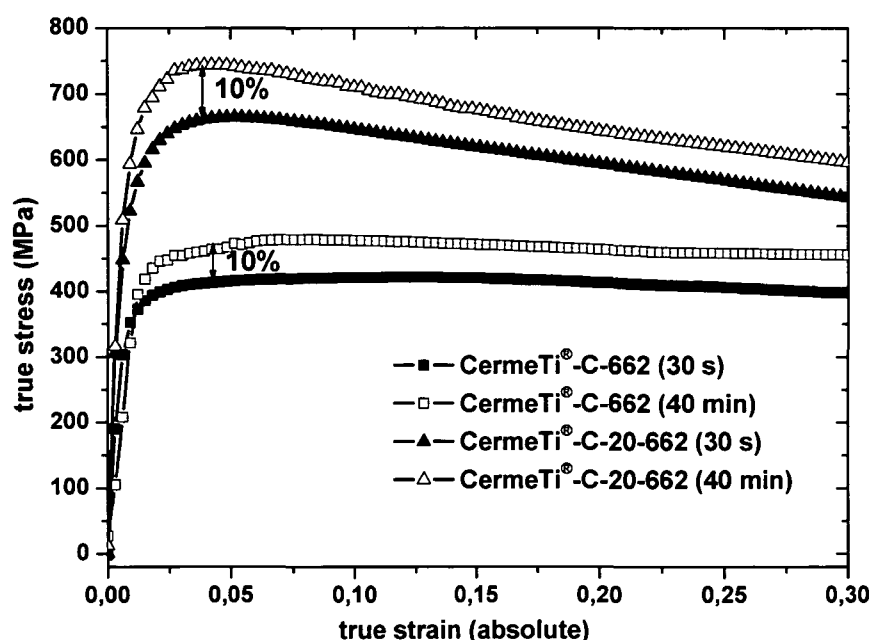


Figure 124. Compression test 2 at 650°C and  $0.15 \text{ s}^{-1}$  strain rate (soaking time is indicated). Increment of 10% in the strength of the Ti662 as well as of the reinforced material at 650°C.

These tests were carried out at 650°C after the heat treatment described before (Figure 27b)). Figure 124 shows the influence of the holding time at 650°C for the unreinforced and the 20% TiC reinforced materials. An increase of the compressive strength about 10% is observed. Furthermore, at this temperature the reinforcement effect in the strength does not disappear with a holding time of 40 min, unlike particulate reinforced Al-alloys at elevated temperatures.

#### 4.8.5 Effect of holding time at 900°C.

This tests were carried out at 650 and 750°C after the heat treatment described in the experimental part (Figure 27c)). Figure 125 shows the influence of the holding time at 900°C for both, the CermeTi®-C-662 and the CermeTi®-C-20-662. An increase of the compressive strength between 26 and 30% was observed for the unreinforced and the reinforced materials respectively.

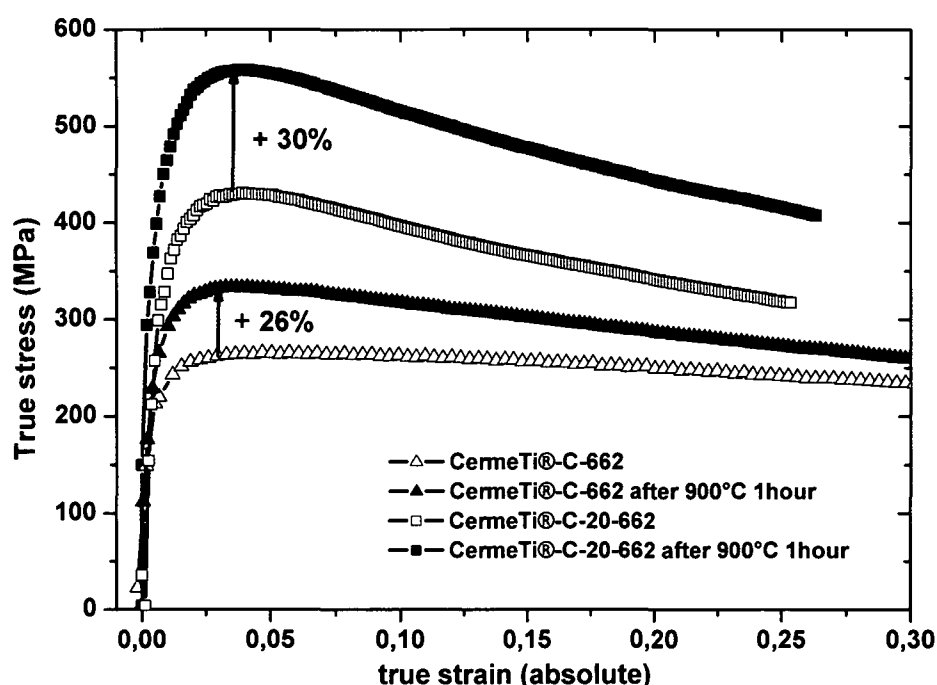


Figure 125. Increasing of the strength at 750°C after a heat treatment at 900°C for the reinforced and the unreinforced Ti662 alloy.

#### 4.8.6 Effect of holding time at 1000°C

CermeTi®-C-662 and CermeTi®-C-20-662 were deformed as described in the experimental part (series test 4). The composite show values of strength more than 55% higher than the matrix, but 20% less than without 1000°C heat treatment. The 1000°C heating reduces the strength of the matrix by 30%. Furthermore, both materials present softening.

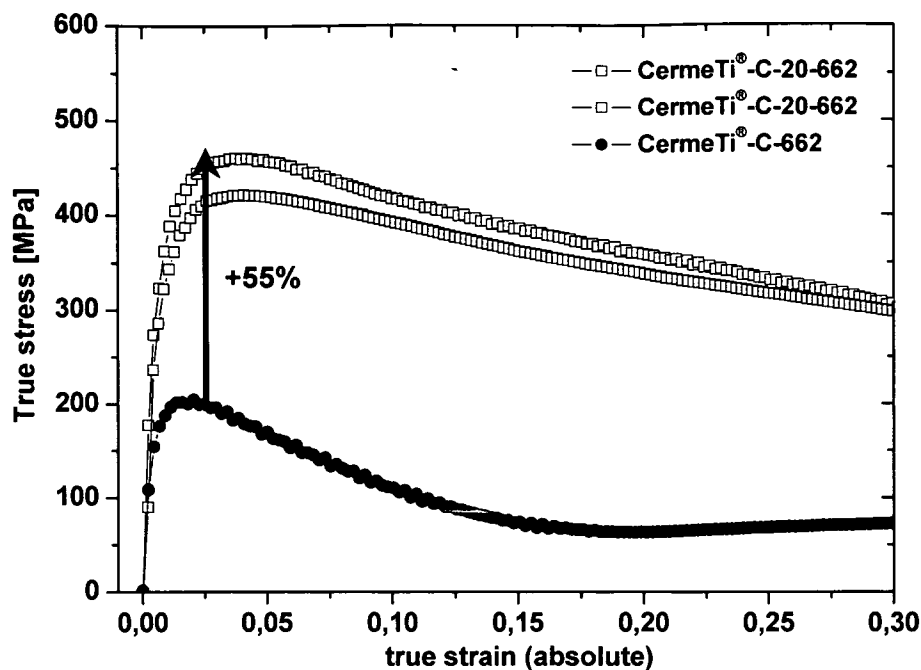


Figure 126. Comparison of two materials, Ti662 reinforced with 20%vol of TiC particles and unreinforced, showing an increment of more than 55% of strength of the composite than of the matrix held at 750°C after 1000°C during 20 minutes followed by 900°C during 1 hour.

## 4.9 Wear rate and friction.

### 4.9.1 Wear rate and friction coefficient results.

Wear rates expressed in  $\text{mm}^3$  volume of lost material per m of sliding distance divided by the normal force (Newton) are shown in Table 11 for CermeTi®-C-662, CermeTi®-C-12-662, CermeTi®-C-20-662, Ti64 and Ti64/SiC/15p.

Negative values are related to the increase in weight of the pin due to the accumulation of iron oxides.

Figure 127 shows the wear rate as a function of the sliding speed and the normal pressure. Comparing CermeTi®-C-662 and CermeTi®-C-20-662, it can be observed that the wear rate is in general higher for the unreinforced alloy than for the composite. The wear rate increases by increasing the normal pressure and by decreasing the sliding speed for both materials. At high values of normal pressure, and for sliding speed  $> 0.6$  m/s, the wear rate increases abruptly. Where comparable, the Ti64/SiC/15p has less wear resistance than the other two materials.

Table 11. Wear rate values as a function of the normal pressure and the sliding speed. [ $\text{mm}^3/\text{km}$ ]

Pressure (MPa)	sliding speed (m/s)	CermeTi®-C-20-662	CermeTi®-C-662	CermeTi®-C-12-662	Ti64	Ti64/SiC/15p
0.637	0.1	-0.0077	-0.014	--	--	--
0.637	0.9	0.00092	0.017	--	--	--
2.021	1.2	0.14	0.1	--	--	--
2.021	0.2	0.091	--	0.21	0.1	0
2.021	1.2	--	--	0.2	0.16	0.91
2.021	0.1	--	--	--	--	0.015
3.183	1.2	-0.14	0.088	--	--	--
3.756	1.5	0.0088	0.071	--	--	--
4.631	0.1	0.39	1	--	--	1.8
4.631	0.6	0.06	0.036	--	--	--
4.775	0.9	0.19	0.14	--	--	--
9.326	1.2	4.5	2.3	--	--	--
9.549	0.2	0.16	0.27	--	--	--

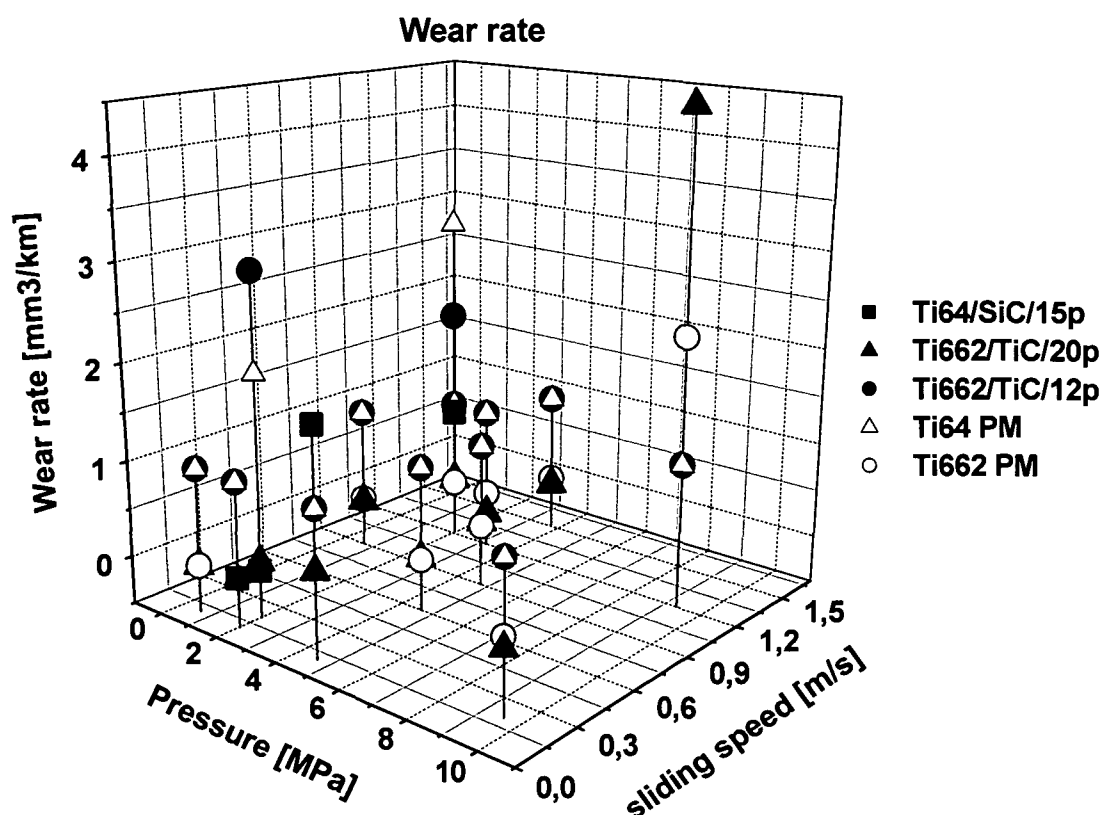


Figure 127. Wear rate as a function of sliding speed and normal pressure for the tested materials.

Table 12. Comparison of the friction coefficient ( $\mu$ ) in the steady state.

Pressure (MPa)	sliding speed (m/s)	CermeTi®-C-20-662	CermeTi®-C-662	CermeTi®-C-12-662	Ti64/SiC/15p	Ti64
0.637	0.1	0.74	0.19	--	--	--
0.637	0.9	0.60	0.54	--	--	--
2.021	1.2	1.06	1.06	--	--	--
2.021	0.2	1.18	--	0.91	--	0.8
2.021	1.2	--	--	0.86	1.08	0.98
2.021	0.1	--	--	--	1.82	--
3.183	0.1	0.93	0.54	--	--	--
3.183	1.2	0.67	0.44	--	--	--
3.756	1.5	1.04	1.03	--	--	--
4.631	0.1	1.25	0.97	--	1.08	--
4.631	0.6	0.81	0.85	--	--	--
4.775	0.9	0.91	1	--	--	--
4.775	0.9	0.47	0.52	--	--	--
9.55	0.2	1.25	0.93	--	--	--
9.55	1.2	1.67	1.59	--	--	--

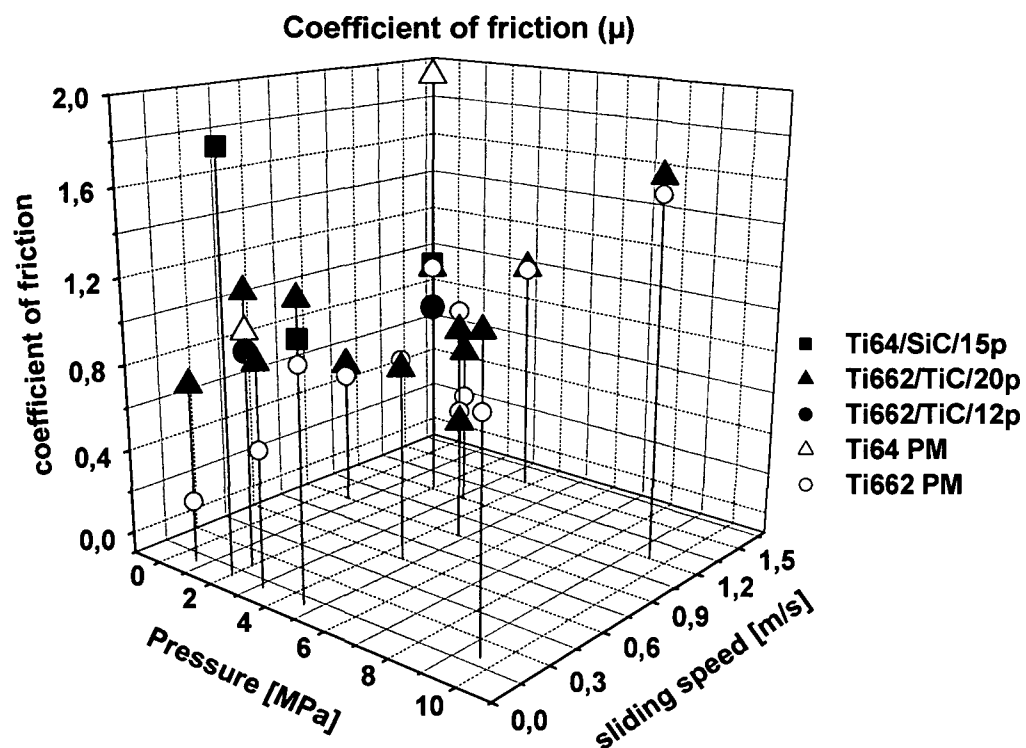


Figure 128. Coefficient of friction as a function of sliding speed and normal pressure for the tested materials.

Table 12 shows the friction coefficient  $\mu$  in the steady state for all the materials. In general, the  $\mu$  coefficient is higher for the TiC reinforced Ti662 than for the pure alloy, and that for both materials, the friction increases by increasing the pressure and the sliding speed. The friction values remain more constant with the sliding speed and the pressure for the alloy reinforced with 20%vol TiC particles than for the unreinforced Ti662, as shown in Figure 128.

#### 4.9.2 Worn surfaces

The microstructures after the wear tests of the composites and the titanium alloys are shown in Figure 129 to Figure 131.

There are some iron oxide and titanium alloy particles on the CermeTi®-C-662 pins along the sliding direction Figure 129a). Cracks can be observed perpendicular to the sliding direction (Figure 129b)). A big amount of iron oxide is present on the surfaces of the composite pins in Figure 130. Figure 131 a) and b) show that for higher loads (15N) there are no visible iron oxides. Also cracks in the matrix surface are observed Figure 131 a). The debonding of the particles at high loads is clearly visible in Figure 131b). Figure 132 a) show some hidden TiC particles, while in b) can be observed the surface that was not in contact with the steel disc on the left and on the right a mixture of broken particles and darker matrix zones.

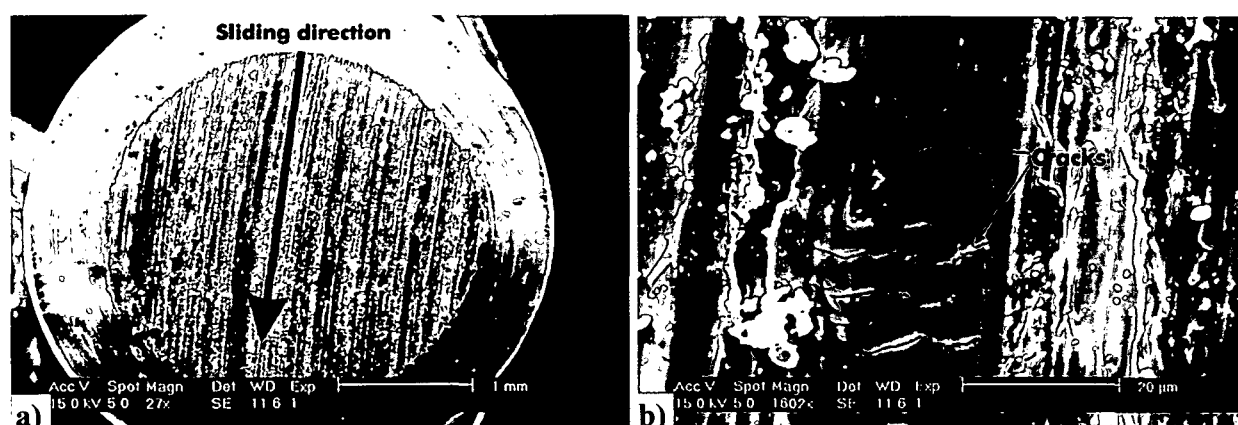


Figure 129. CermeTi®-C-662 pin tested at 3.18 MPa and 0.1 m/s a) wear in the sliding direction, b) transverse cracking of the material. (SEM).

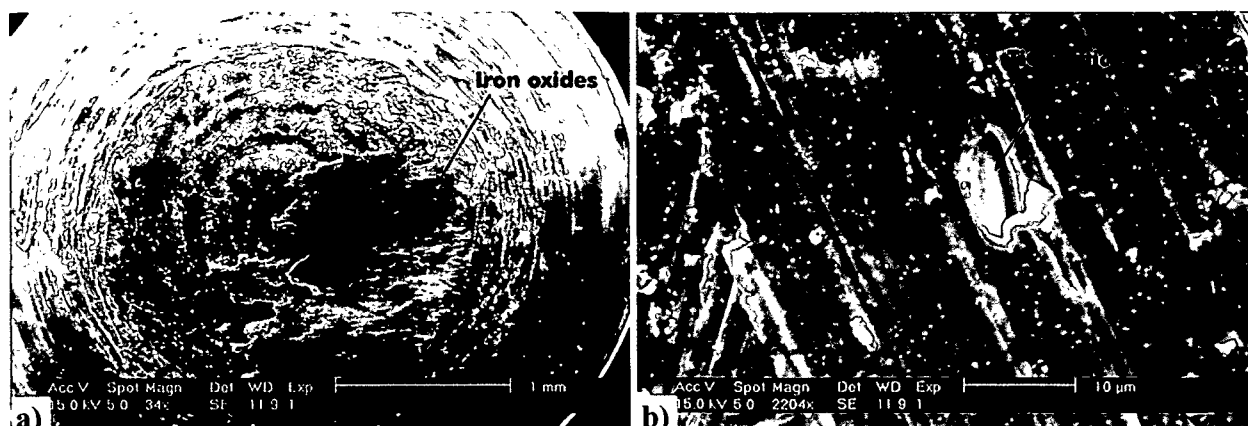


Figure 130. CermeTi®-C-20-662 pin tested at 3.18 MPa and 0.1 m/s a) iron oxides accumulation in the sliding direction, b) TiC particle partially uncovered by the matrix. (SEM).

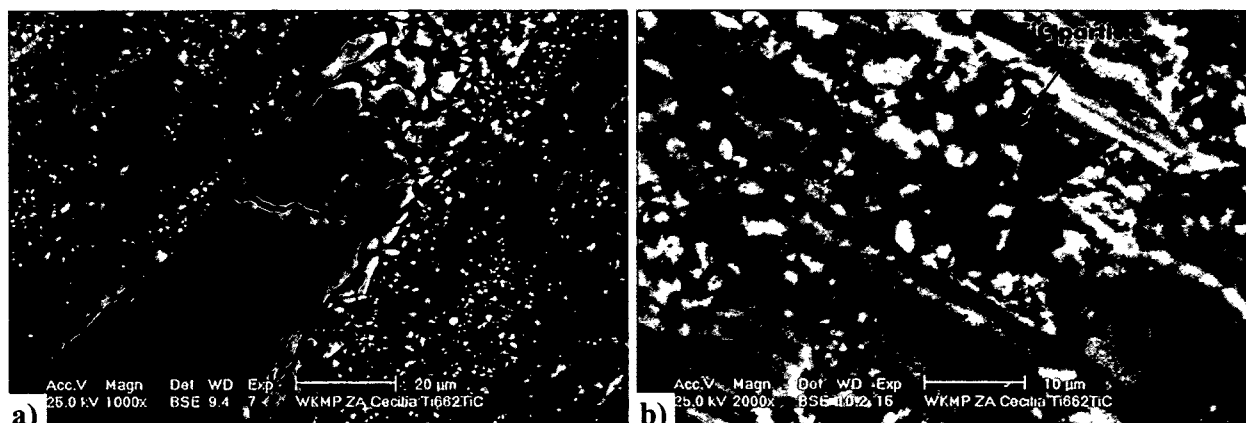


Figure 131. Images of pins tested at 4.78 MPa and 0.9 m/s, showing a) CermeTi®-C-662 cracks perpendicular to the sliding direction b) TiC particle almost de-bonded from the matrix, CermeTi®-C-20-662. (SEM - SE/BSE-)

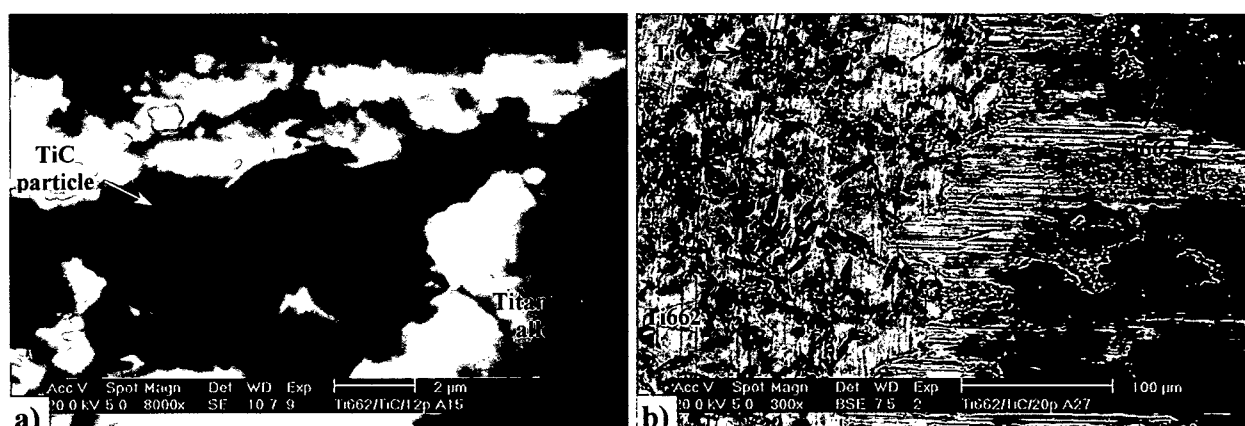
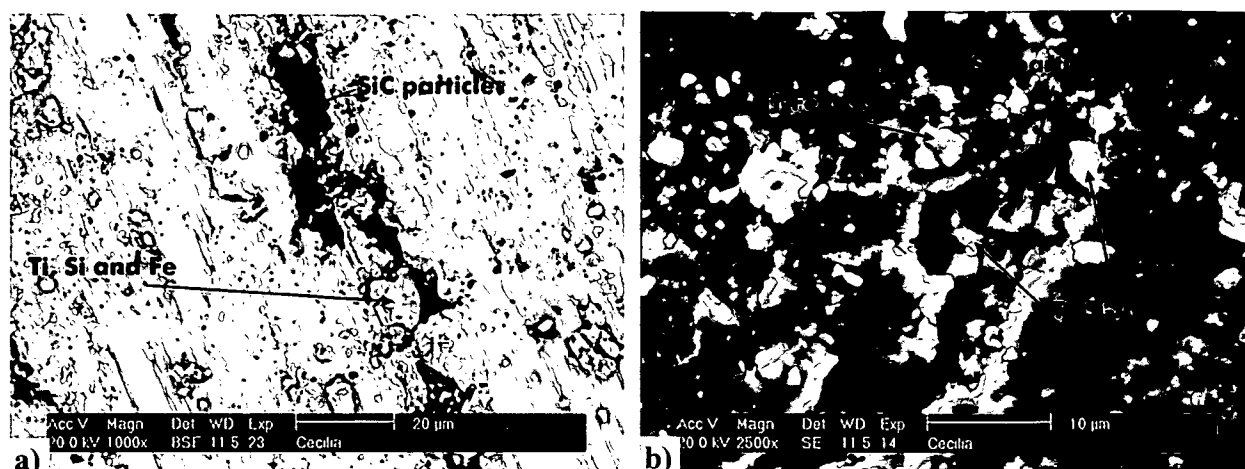


Figure 132 Composites a) CermeTi®-C-12-662 tested at 2 MPa and 0.2 m/s showing the TiC particles partially covered by the matrix, and b) CermeTi®-C-20-662 tested at 2 MPa and 1.2 m/s showing on the left a not worn surface, where the particles are visible, and on the right a worn surface with destroyed particles.(SEM-BSE)





**Figure 133.** Ti64/SiC/15p pins a) tested at 2.02 MPa and 1.2 m/s: SiC particles in black, brittle zones in dark grey, b) tested at 4.6 MPa and 0.1 m/s: SiC particles and the oxides. (SEM -SE/BSE-).

Figure 133 shows the Ti64/SiC/15p pins after the tests. The brittle zones shown in Figure 133 (a) as grey zones, darker than the matrix, crack very easily and this is part of the reaction layer (Si, Ti and C) with some iron from the steel disc.

SEM micrographs of the discs are shown in Figure 134. The discs used for the matrix pins show large amounts of adhered titanium alloy, and a negligible amount of iron oxide in Figure 134a). The steel discs used with the composite pins show some iron oxides in the surface, but no titanium (Figure 134b)). A scratch done by a TiC particle can be observed in the steel surface.

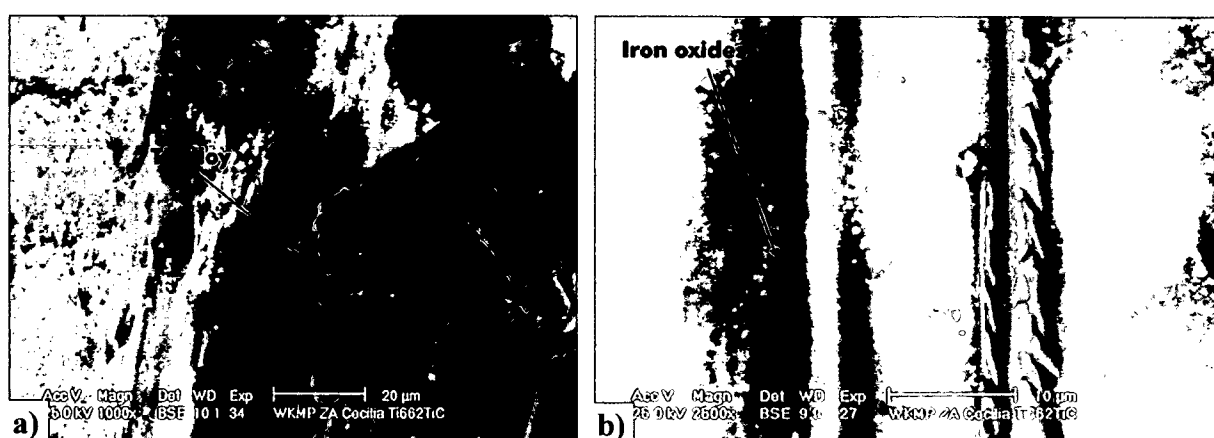


**Figure 134.** Steel discs a) disc tested against CermeTi®-C-662: titanium alloy adhered to the surface, b) disc tested against CermeTi®-C-20-662: a TiC particle scratched the steel surface. (SEM -SE/BSE-)

The micrographs of the sub-surfaces show a plastic deformation zone of about 50  $\mu\text{m}$  for the Ti662 alloy produced by Dynamet at intermediate pressure and high sliding speed. Furthermore, a layer of about 20  $\mu\text{m}$  of a mixture of alpha phase, beta phase and iron from the steel disc, as shown in Figure 135. On the other hand, for the same parameters of wear, the composites show less deformation in the matrix, but cracks in the particles (Figure 136). If the pressure and the

sliding speed are decreased down to 2.02 MPa and 1.2 m/s respectively, a layer of titanium alloy, TiC broken particles and iron can be observed (Figure 137).

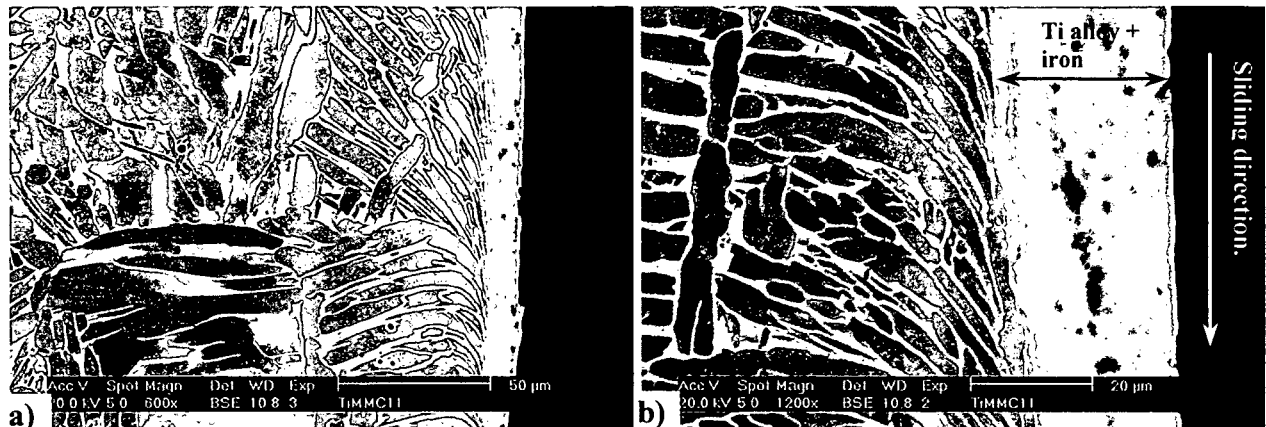


Figure 135. CermeTi®-C-662. Pressure: 3.8 MPa, sliding speed: 1.5 m/s. a) plastic deformation of the grains in a range of about 50 µm a) layer of titanium alloy and iron of about 20 µm formed during the wear test. (SEM-BSE)

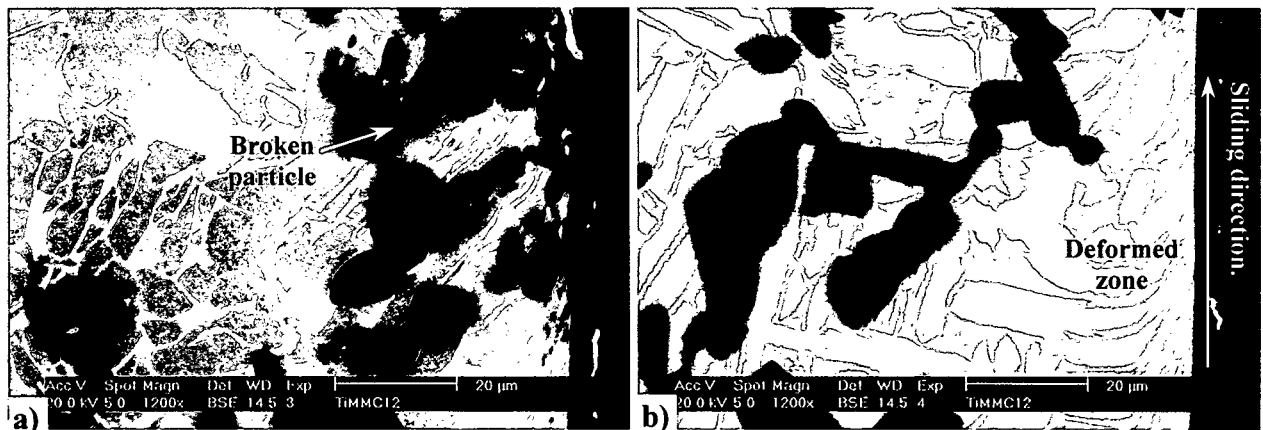


Figure 136. CermeTi®-C-20-662. Pressure: 3.8 MPa, sliding speed: 1.5 m/s. a) plastic deformation of the matrix breaks the TiC particles b) plastic deformation zone is smaller than that of the unreinforced CermeTi®-C-662. (SEM-BSE).

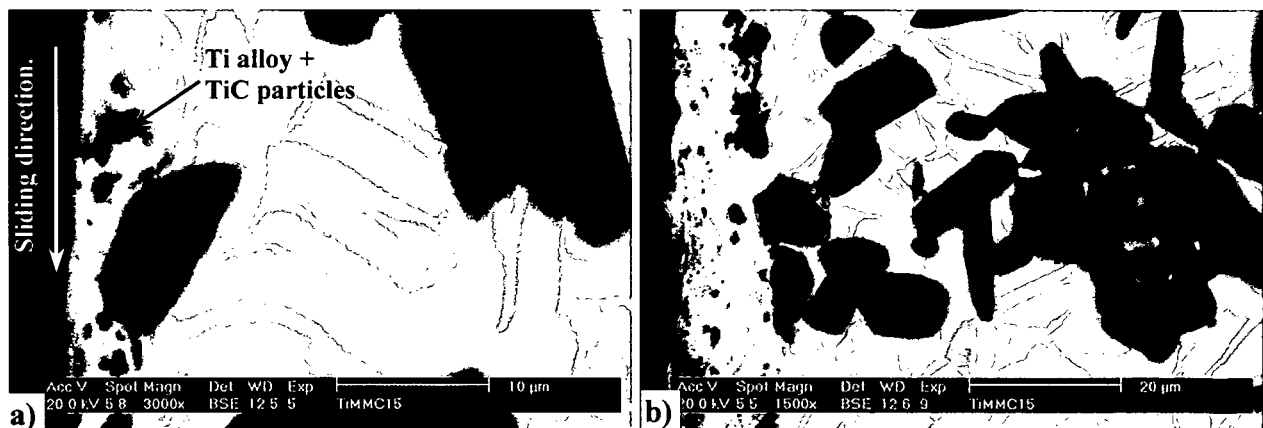
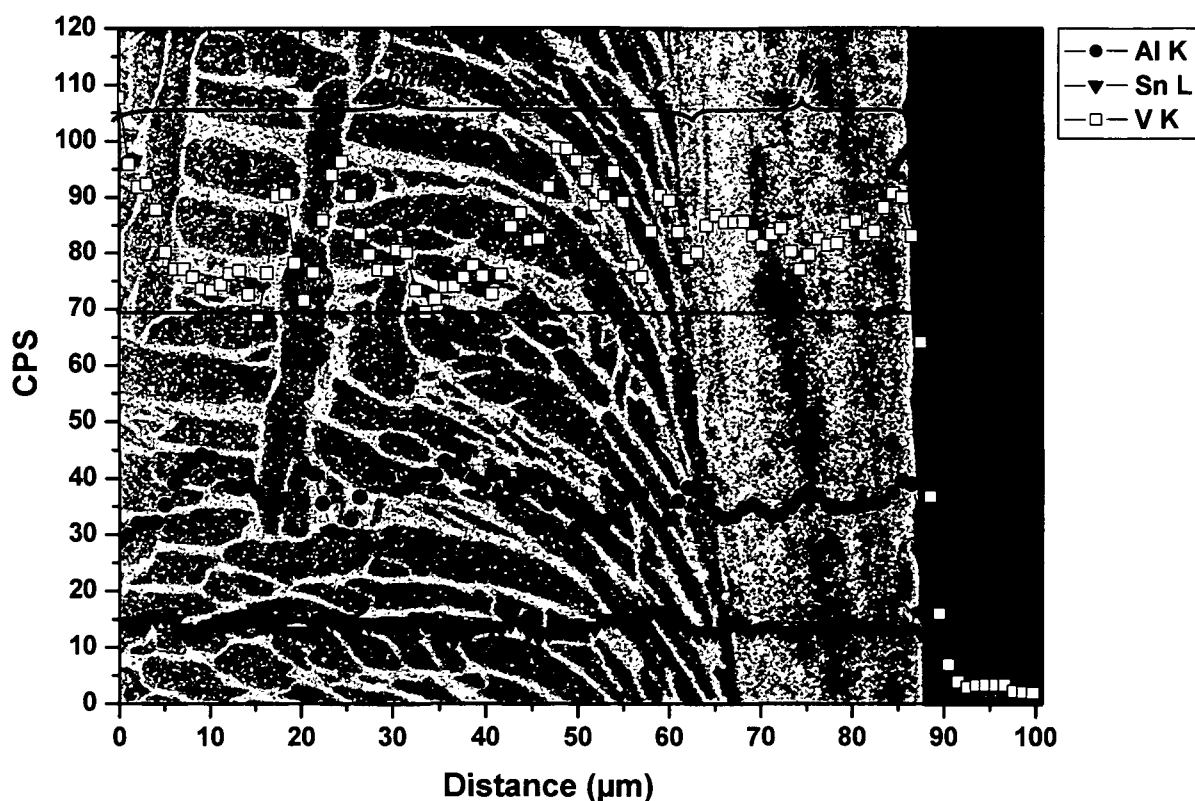


Figure 137. CermeTi®-C-20-662. Pressure: 2.02 MPa, sliding speed: 1.2 m/s. a) less plastic deformation than in Figure 136. b) layer of Ti alloy + TiC broken particles of about 10 µm. (SEM-SE/BSE-).

EDX-line-scan shows the distribution of the elements along the horizontal line. Aluminium (Al), vanadium (V) and tin (Sn) distributions are shown in Figure 138 for CermeTi<sup>®</sup>-C-662. In the bulk, the phases are distinguished by the distribution of the alloying elements: V in the beta phase, and Al in the alpha phase. In the surface up to 20  $\mu\text{m}$  deep the alloying elements are distributed homogeneously, as a result of a mixture of the phases.



**Figure 138.** CermeTi<sup>®</sup>-C-662. Pressure: 3.8 MPa, sliding speed: 1.5 m/s. The distribution of the elements shows: In the bulk, V in  $\beta$ -phase, Al in  $\alpha$ -phase, and Sn in both phases. In the surface, layer the elements are more homogeneously distributed. (SEM –BSE)

Figure 139 shows the distribution of the alloying elements and the C in the Ti662 alloy reinforced with 20% vol of TiC particles. A mixture of the alloy and the TiC particles occurs in the surface layer to 5  $\mu\text{m}$  depth.

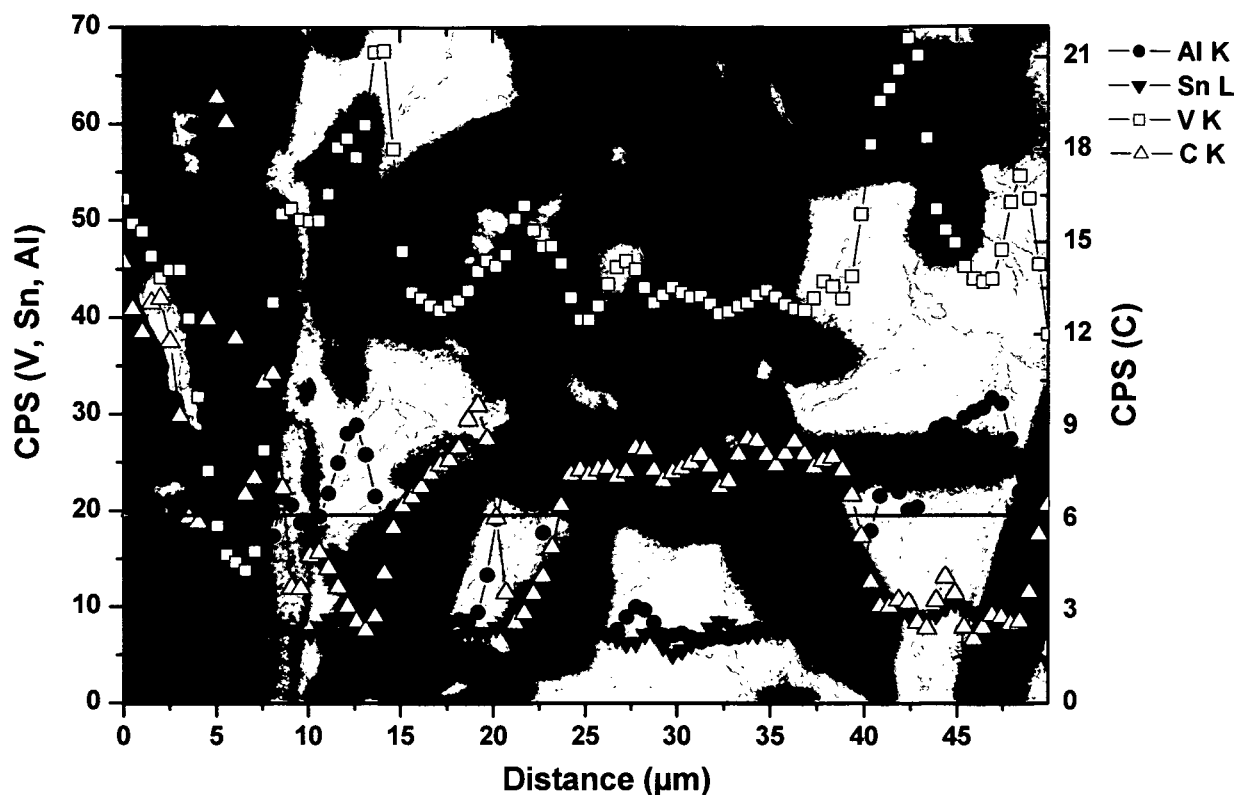


Figure 139. CermeTi®-C-20-662. Pressure: 2.02 MPa, sliding speed: 1.2 m/s. The distribution of the elements shows: In the bulk, V in  $\beta$ -phase, Al in  $\alpha$ -phase, and Sn in both phases and C in the particles. (SEM –BSE)

#### 4.9.3 Topography

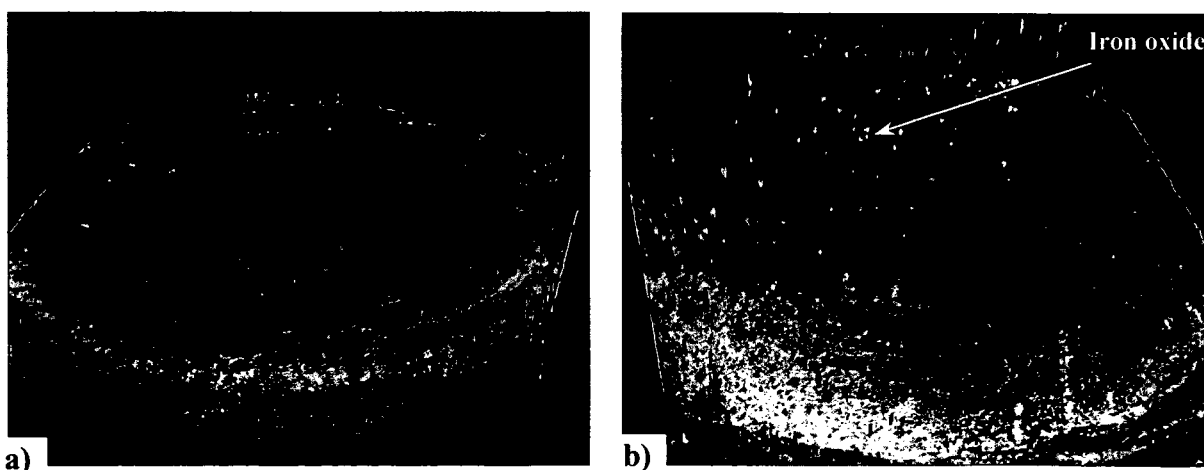
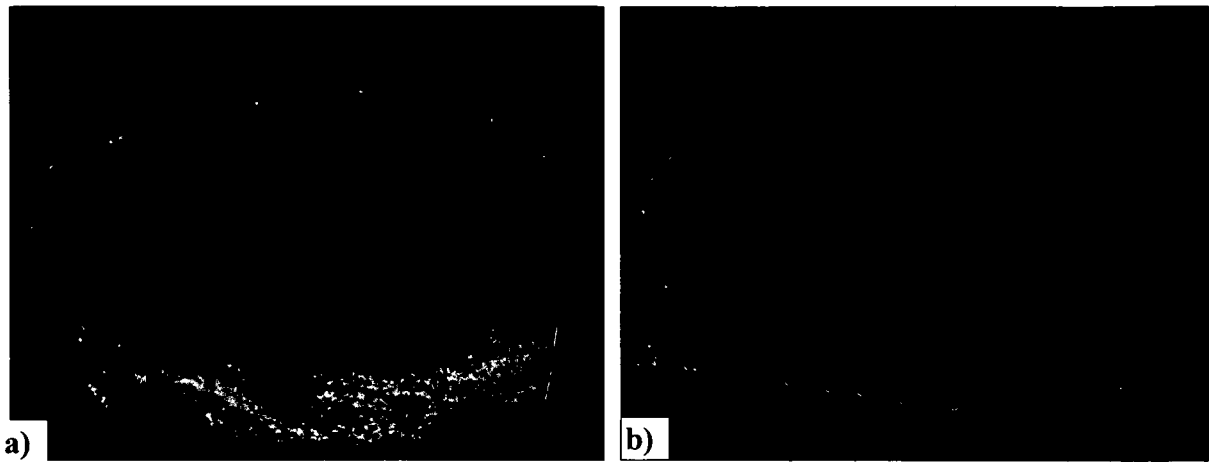


Figure 140. CermeTi®-C-20-662 topography a) before the test and b) after the test, showing the mass increment due to the oxide formation

Figure 140 shows a case where there is an increment of the mass in the CermeTi®-C-20-662 pin due to the material transfer from the disc and /or the oxide formation.

In Figure 141 it is possible to observe the lines of the sliding counterpart after the test for a pin of unreinforced Ti662.



**Figure 141. CermeTi<sup>®</sup>-C-662 topography a) before the test and b) after the test, showing the lines of sliding**

## 5 Interpretation of the results.

### 5.1 Microstructure features.

#### 5.1.1 *SiC reinforced material*

The rounded Ti64 powders chosen at the beginning were more difficult to sinter than the edged powders, and the first trials resulted in a porous material. The edged powder offers a larger surface of contact and the sinterization, based on the diffusion of the material is more intense than in the rounded powders.

The observed reaction layer is brittle and the system SiC – Ti seems to be instable above 600°C. The carbon protective layer tried for the sample S108 did not bring important improvements, but the in-homogeneity of this layer should be taken account.

Agglomeration of the SiC particles provoked during the wet mixture of the powder was also observed, with catastrophic consequences for the produced material.

#### 5.1.2 *Globular and lamellar microstructures*

Powder metallurgical materials show a lamellar microstructure, with grain sizes up to 400µm in the case of Ti662 and Ti64. Furthermore, some alpha colonies inside the grain oriented in different directions form the called sub-grains. To improve some mechanical properties such as strength and ductility, in the industry are used a thermomechanical treatments, after which the material presents a fine globular microstructure, such as the one observed in the Ti662 ingot.

Both microstructures show also a so-called “secondary alpha phase”, a thin phase. Furthermore, while heating the lamellar microstructure as well as the globular one, the finer alpha phase with large specific interface transform into beta faster than the larger alpha grains (Figure 53b)).

By heating the samples with globular or lamellar microstructure above the beta transus, the beta grains coarse, and new grain boundaries form. If the sample is cooling down from the beta transus temperature, a new lamellar microstructures appears as shown in Figure 52a) and Figure 53b). If the cooling is done in water, then it is fast enough to provoke a fine lamellar microstructure, but if the cooling is slow enough (by dilatometry the rate is of 3K/min), then the grains grow (Figure 92 b) and c)).

### 5.1.3 Alpha beta changes

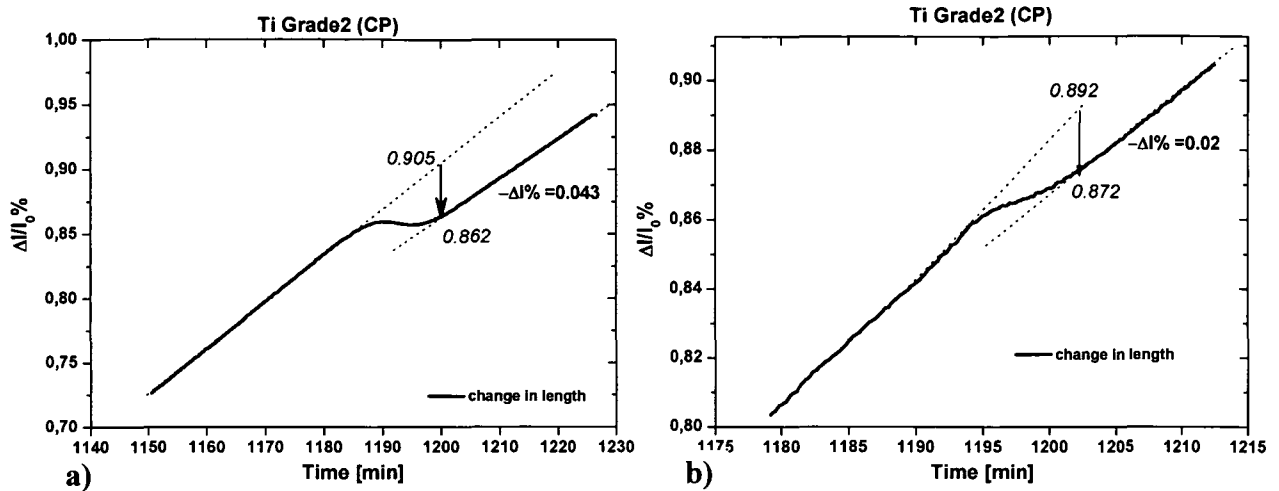


Figure 142. Change in length in the Ti Grade 2 due to the phase transformation for two different samples a) and b).

The transformation of the alpha into the beta phase implies a shrinkage, as observed in the change in length in Figure 142 for pure titanium. That means a change in volume of about 0.08%. As the dilatometric test is a dynamic test, it is not possible to define a temperature of transformation, but a small range. Furthermore, as the phase transformation is a diffusional phenomena (governed by time and temperature), it can be seen that the transformation during cooling occurs in a shorter range, due to the high temperatures, that means in a shorter time.

Concerning to the alloys, Figure 143 shows a comparison between a thermal expansion for an ideal material (line (1)) with the Ti662 ingot. It is possible to see an increment in the expansion rate around 600°C, where the diffusion of V begins (2). Immediately after (actually it occurs at the same time, but this is a dynamic tests), the transformation into beta occurs, and there is a decrement in the expansion rate (3), until the material begins to shrink (4) to complete the transformation.

The analysis of the microstructure also shows that up to 600°C, no considerable changes in the alpha /beta ratio occurs.

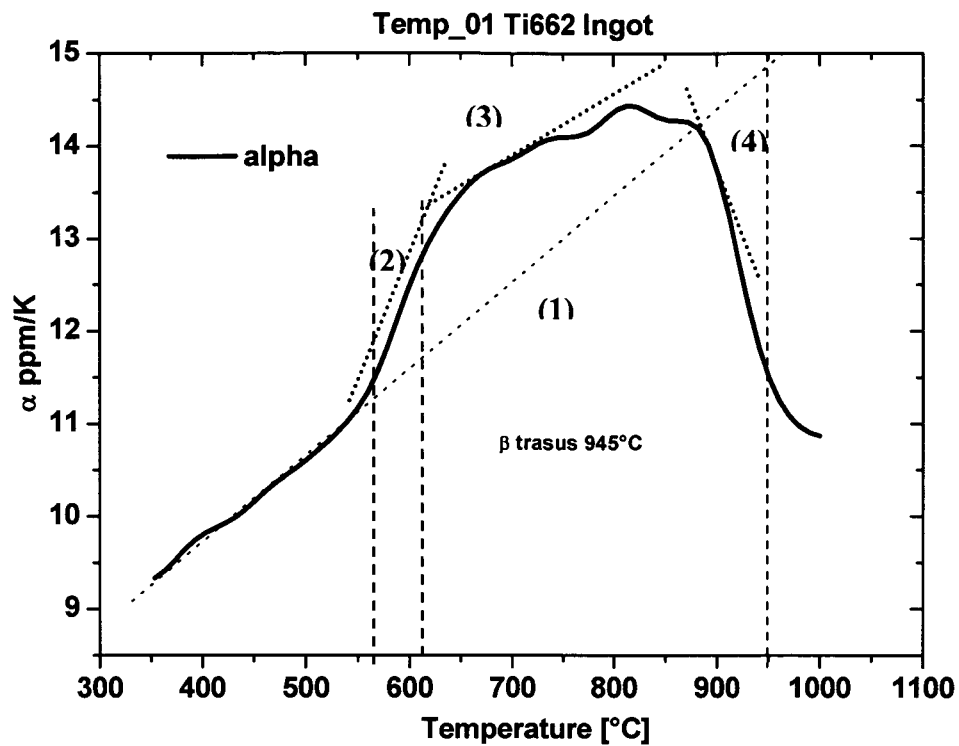


Figure 143. Instantaneous thermal expansion of the Ti662 Ingot, second cycle.

## 5.2 Trials of a new material

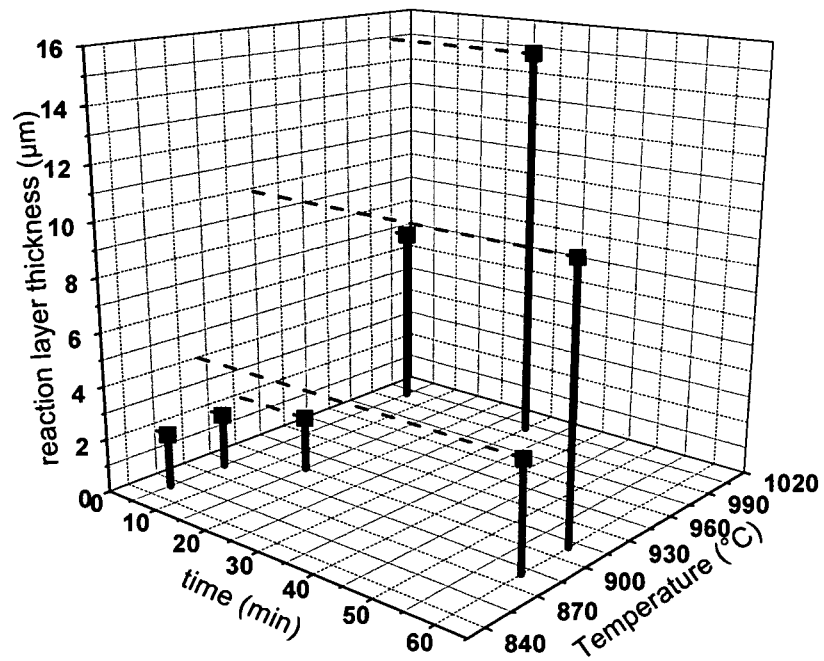


Figure 144. Dependence of the reaction layer thickness with the temperature and the HIP time.



The production of the SiC reinforced Ti64 material means to find a balance between the reaction layer and the porosity. By increasing the parameters temperature and holding time, the reaction layer increases exponentially with temperature and theoretically with the square root of time (as shown in Figure 144), but the porosity of the sintering system tends to decrease.

### 5.3 Young's modulus

Figure 145 shows the comparison of the Ti662 reinforced and unreinforced materials with the Reuss and Halpin and Tsai models. The values used for the matrix were those measured with DMA, while for the TiC particle, the highest Young's modulus value found in the literature of 460 GPa was used [5], and taken as non temperature dependent. The Reuss model (low limit) lays quite below the experimental data; more than 10% for the material reinforced with 20% of TiC particles, and more than 5% for that reinforced with 12% of TiC particle. Furthermore, the  $\xi$  values found for the Halpin and Tsai model were 1 and 1.25 for CermeTi<sup>®</sup>-C-12-662 and CermeTi<sup>®</sup>-C-20-662 respectively.

Concerning to the Ti64 materials, the values used in the models for calculation are: for the matrix those measured with DMA and for the SiC particle, the highest Young's modulus value found in the literature of 461 GPa [5], independent of the temperature. Figure 146 shows for the TiC reinforced alloy the same tendency of the Young's modulus respect to the Reuss model.

If the Reuss model is compared with the experimental values of the SiC reinforced alloy, it is observed that the first values are up to 5% higher than the experimental ones. This put in evidence the bad mechanical properties of the SiC reinforced Ti64 alloy due to the pores and the brittle reaction layer.

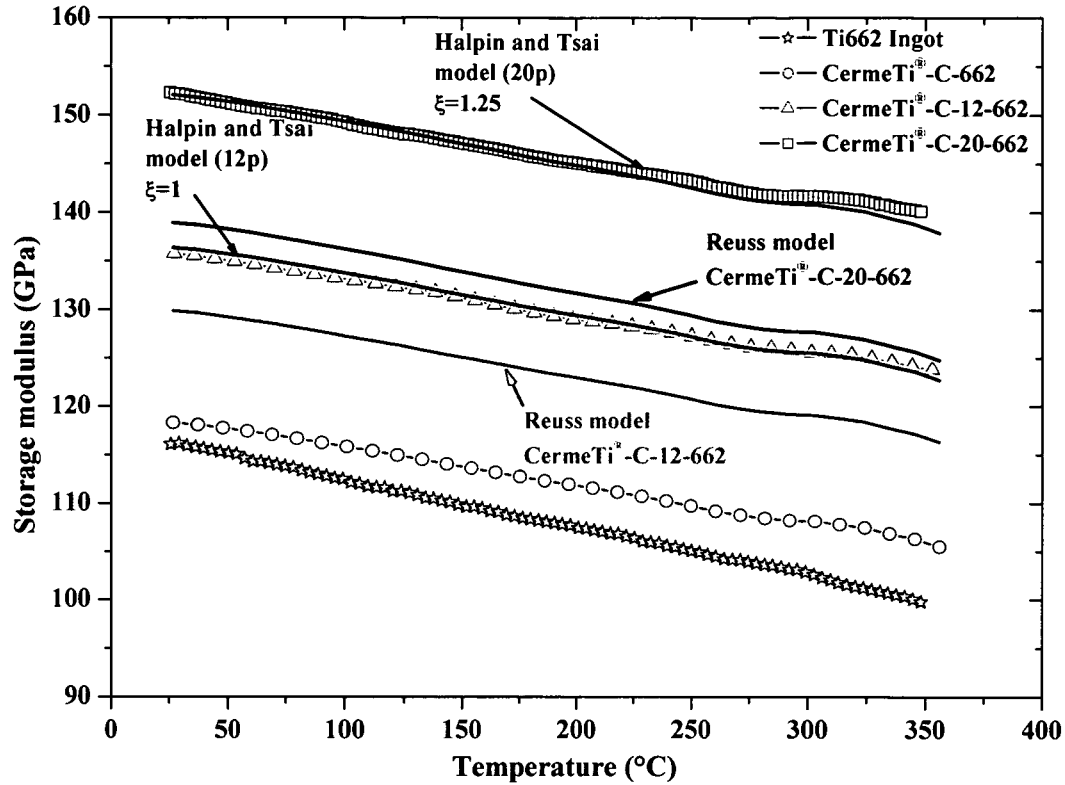


Figure 145. Young's modulus of Ti662 cast, CermeTi<sup>®</sup>-C-662 and CermeTi<sup>®</sup>-C-12/20-662 in function of temperature compared with the Reuss model and the Halpin and Tsai model.

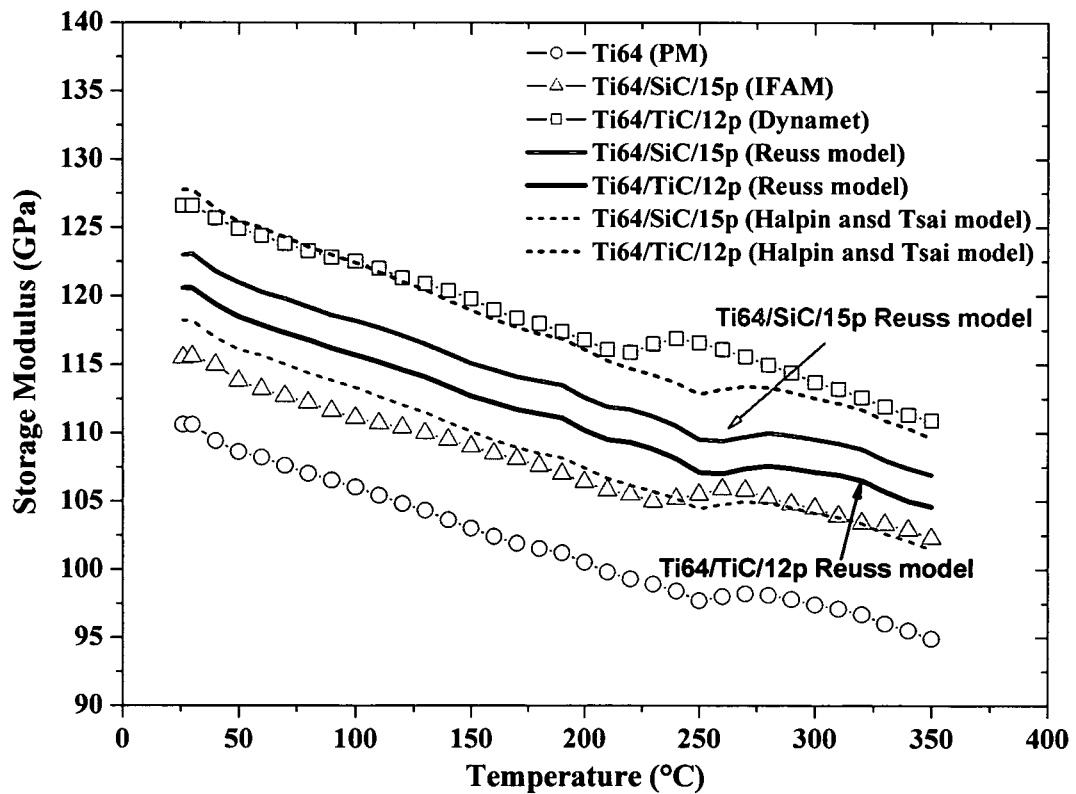


Figure 146. Young's modulus of Ti64 unreinforced, reinforced with 15%vol SiC particles and reinforced with 12%vol TiC particles in function of temperature compared with the Reuss model.

## 5.4 Deformation mechanisms.

### 5.4.1 *Dynamic Materials Model and modified Dynamic Materials Model.*

To get a better understanding of the deformation mechanisms of the Ti662 materials, the processing and the instability maps were calculated and plotted using the models proposed by Prasad et al and by N. Rao and Murty.

- **DDM.** The values of flow stress at 0.3 strain ( $\sigma_{0.3}$ ) were taken from the flow curves at constant temperature and strain rate. The  $\log(\sigma_{0.3})$  was plotted against the  $\log(\dot{\epsilon})$ , and fitted with a cubic spline for all the materials. The derivative of the plot (Equation 14) gives the  $m$  factor as a second order function of the strain rate for each temperature.

Then, the  $\eta$  factor ( $\eta = 2m/(m+1)$ ) was calculated as a function of the strain rate. The matrices for the isolines of  $100\eta$  values of the processing maps were generated using the Origin 6.0 Software. The  $\ln(\eta/2)$  is plotted against  $\ln \dot{\epsilon}$ , then the derivative at each temperature plus  $m$  (Equation 21) gives the value of the instability parameter  $\xi$ , which, when negative, shows the zones of instability flow. Again, the maps were generated using Origin 6.0 Software.

-**Modified DMM.** The values of flow stress at 0.3 strain ( $\sigma_{0.3}$ ) were taken from the flow curves at constant temperature and strain rate. The integral  $J$  was evaluated combining the Equations 30 and 31. The  $m$  at  $\dot{\epsilon}_{\min}$  was evaluated as the derivative of  $\log(\sigma_{0.3})$  vs.  $\log(\dot{\epsilon})$  fitted with a cubic spline at  $\dot{\epsilon}_{\min}$  ( $0.015s^{-1}$ ). The second integral (that is zero at  $\dot{\epsilon}_{\min}$ ) was evaluated calculating the area below the experimental points connected linearly, as shown in Figure 147. Then, the coefficient  $\eta$  was calculated as  $J/(\sigma \dot{\epsilon})$  and plotted but multiplied by 100.

The instability coefficient was calculated as  $\kappa = (2m/\eta - 1)$  using the values of  $m$  calculated as before. For negative values of  $\kappa$ , the flow of the material is instable.

The instability as well as the processing maps were also generated using Origin 6.0 Software.

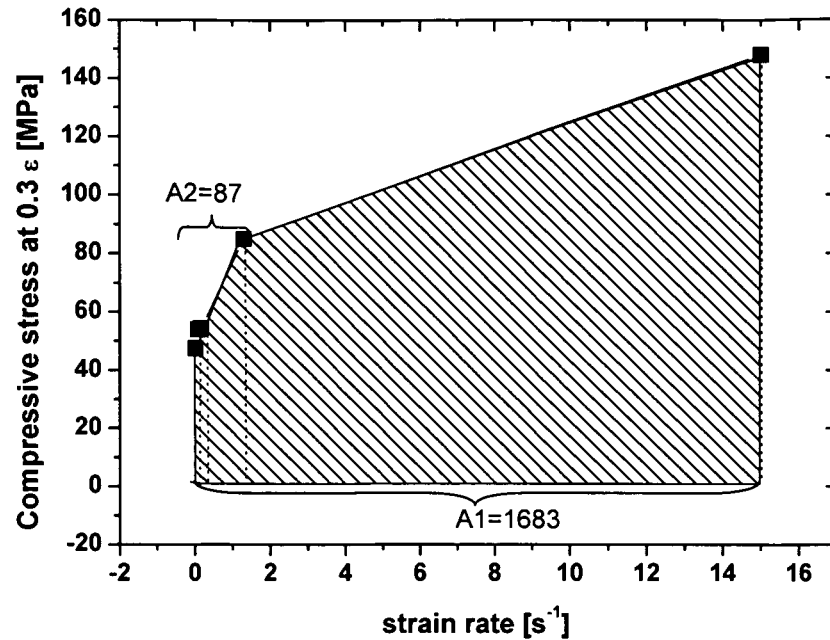


Figure 147 Second integral to evaluate  $G$  following the modified DMM.

#### 5.4.2 Processing and instability maps.

Figure 148 to Figure 155 show the processing and the stability maps calculated according to the Dynamic Materials Model (DMM) proposed by Prasad et al. The values of  $\eta$  were multiplied by 100 and drawn in the processing maps as isolines as a function of the temperature and the strain rate, and only the negative values of  $\xi$  were drawn in the instability maps.

The combination of stable flow and high power dissipation values were enclosed in a dashed area, suggesting the parameters of forging for 0.3 strain.

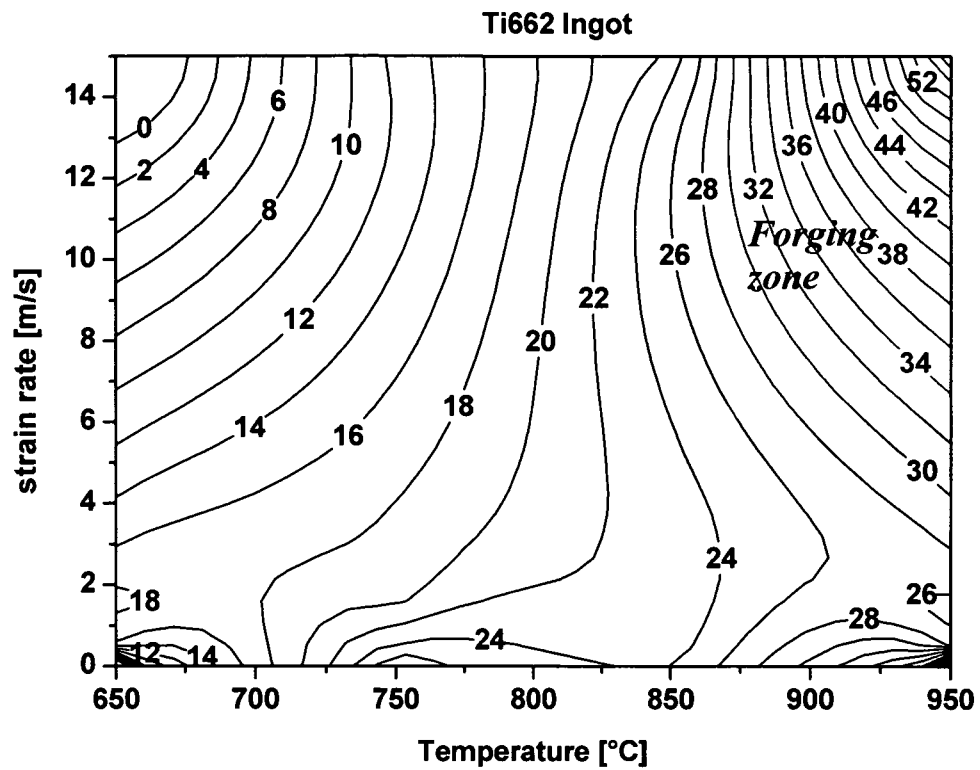


Figure 148. Power dissipation map ( $100\eta$ ) for Ti662 Ingot calculated using the DMM at  $\epsilon = 0.3$

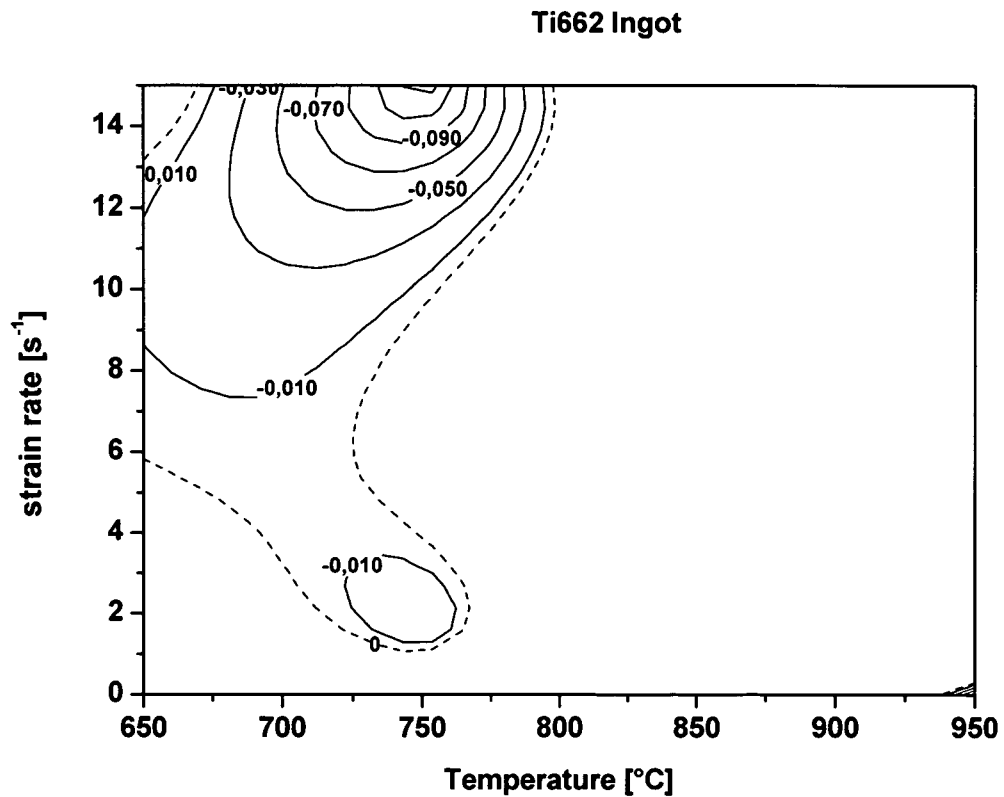


Figure 149. Instability map for Ti662 Ingot calculated using the DMM at  $\epsilon = 0.3$ .

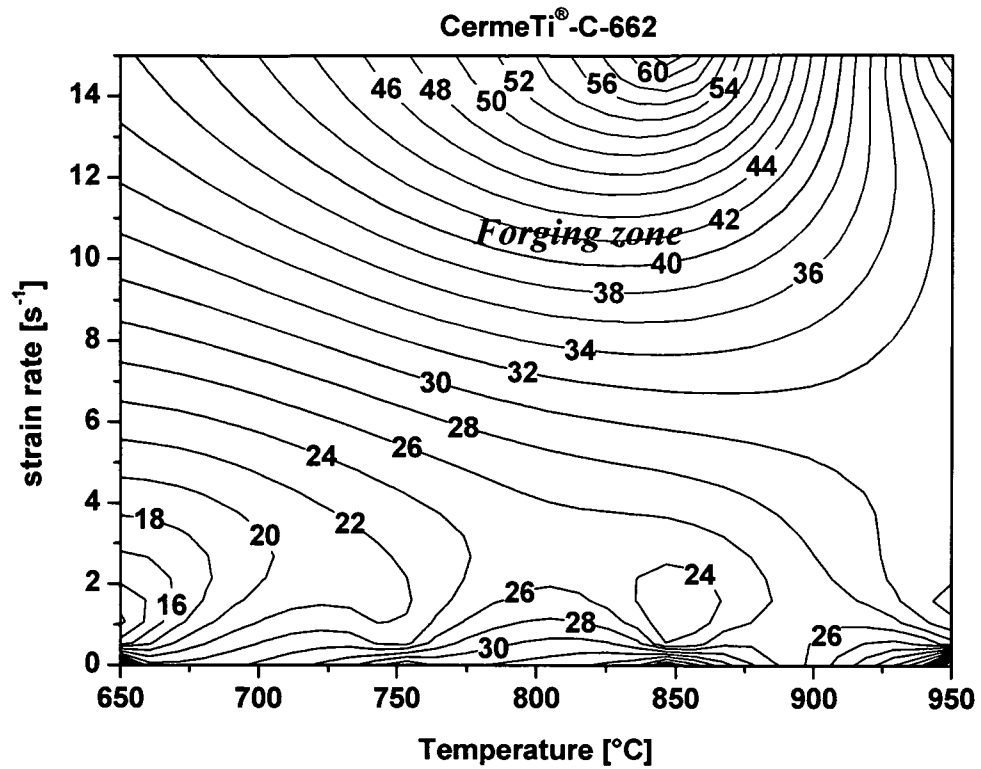


Figure 150. Power dissipation map for the for CermeTi®-C-662 calculated  $\alpha\tau\epsilon = 0.3$  using the DMM.

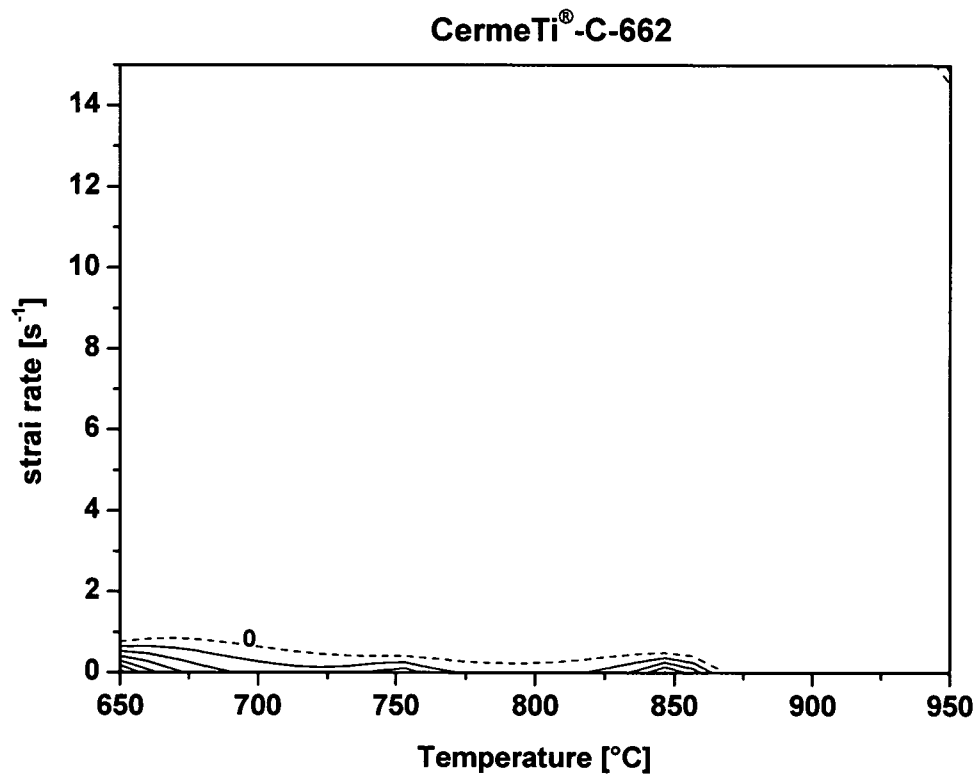


Figure 151. Instability map for the for CermeTi®-C-662 calculated  $\epsilon = 0.3$  using the DMM.

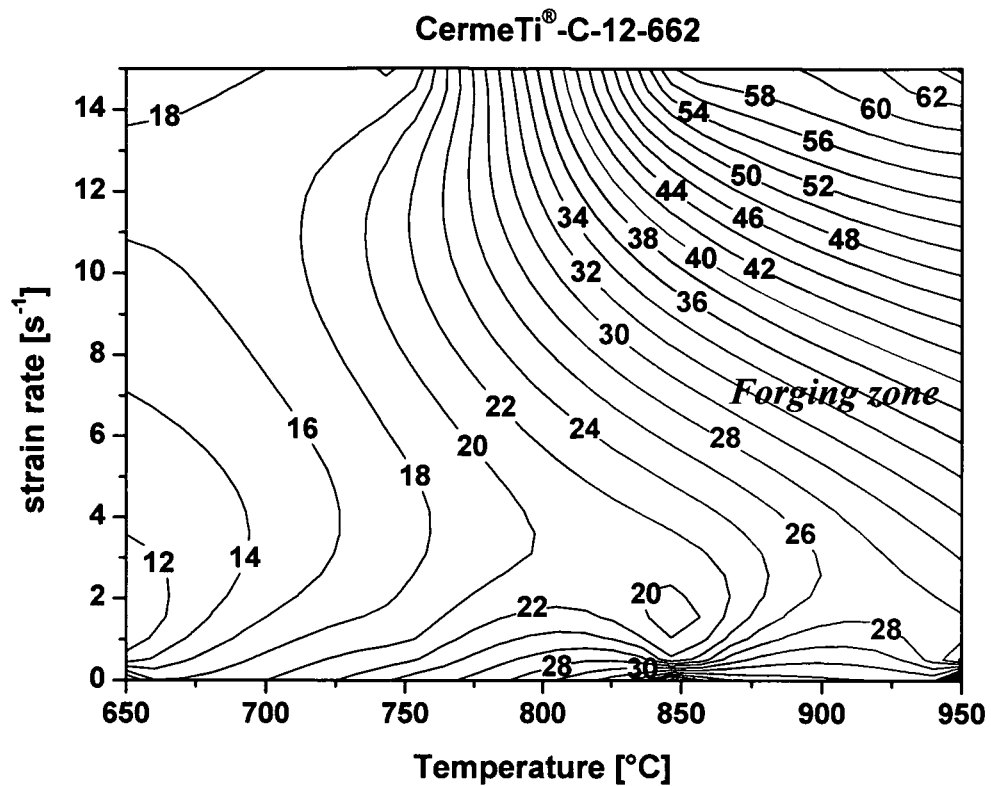


Figure 152. Power dissipation map for CermeTi®-C-12-662 calculated at  $\varepsilon = 0.3$  using the DMM.

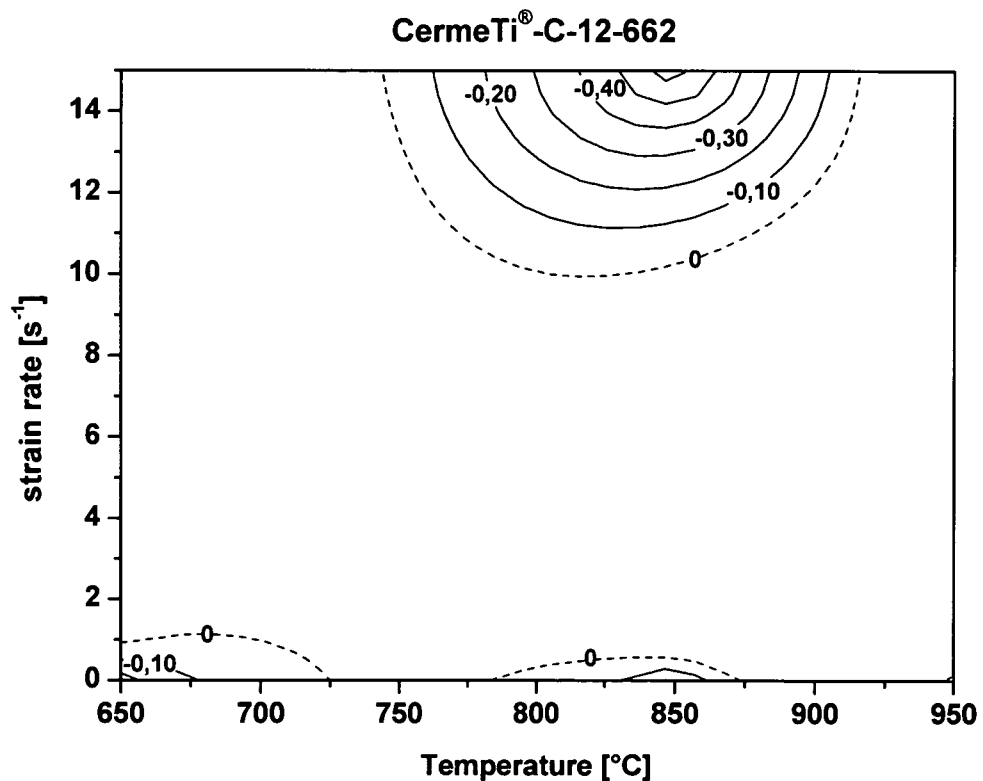


Figure 153. Instability map for the CermeTi®-C-12-662 calculated at  $\varepsilon = 0.3$  using the DMM.

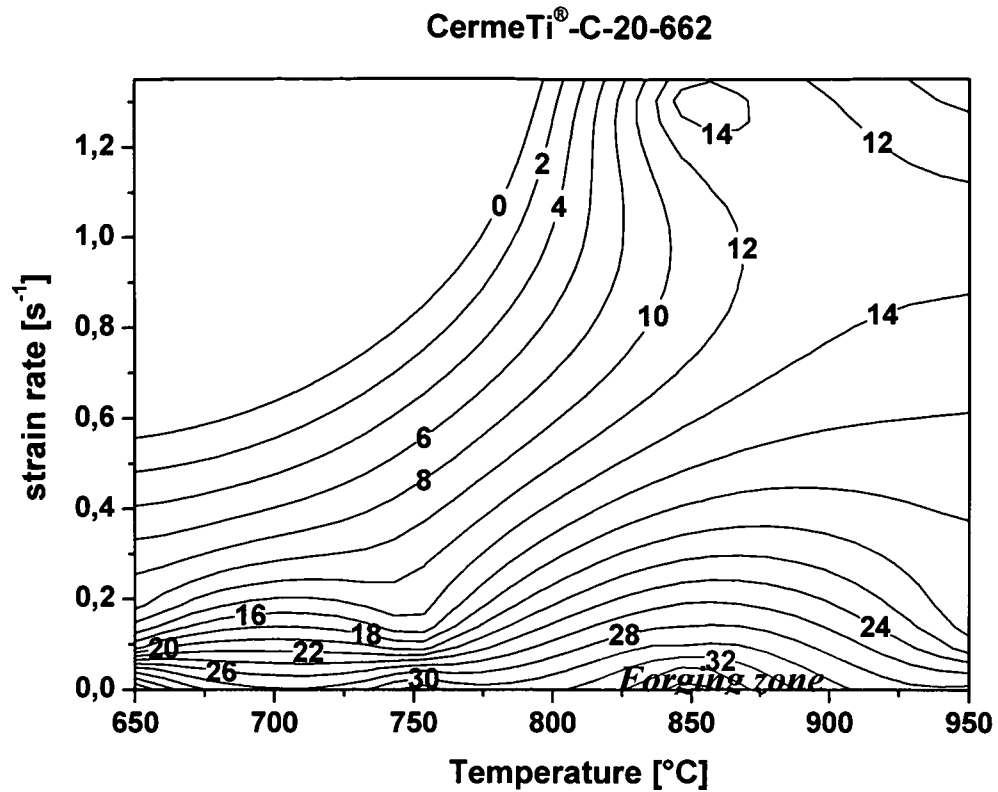


Figure 154. Power dissipation map for CermeTi<sup>®</sup>-C-20-662 calculated at  $\epsilon = 0.3$  using the DMM.

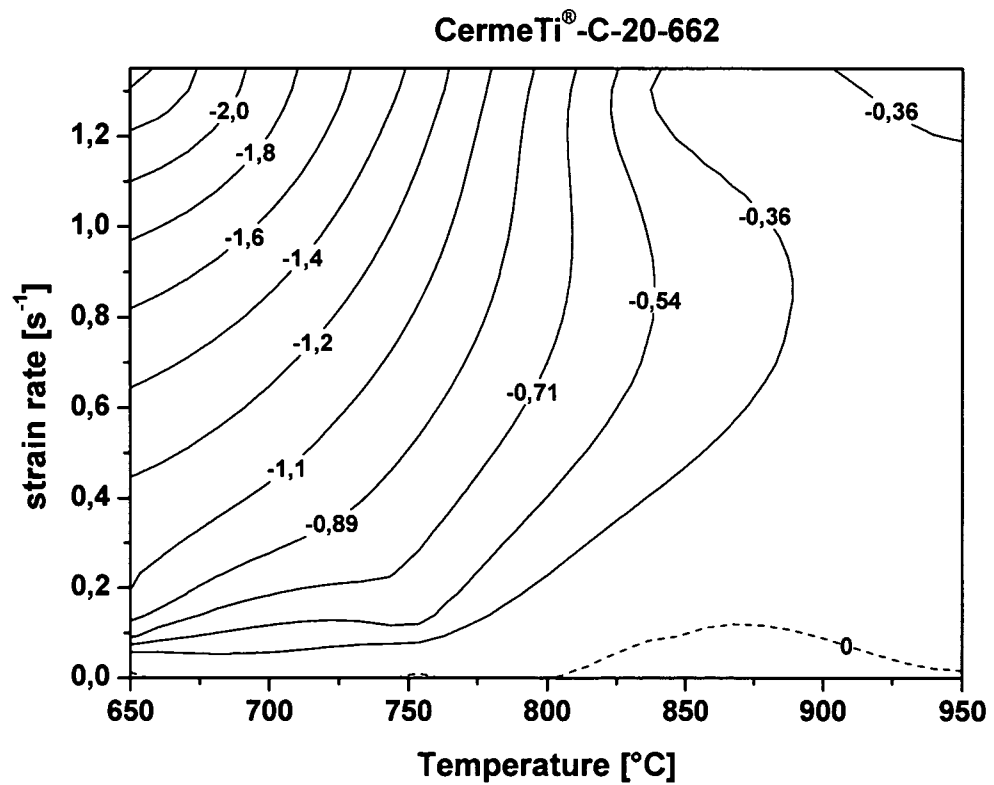


Figure 155. Instability map for CermeTi<sup>®</sup>-C-20-662 calculated at  $\epsilon = 0.3$  using the DMM.



From the DM model it can be said that:

- *Ti662 Ingot*. The highest dissipation range occurs at high temperatures and strain rates, where also stability of the flow is predicted. The instability of flow at low temperatures and high strain rates could be provoked by a shear band deformation.
- *CermeTi<sup>®</sup>-C-662*. The highest dissipation of the energy is in the range of high strain rates, while the instabilities of the flow is predicted between 650 and 850°C at the lowest strain rate.
- *CermeTi<sup>®</sup>-C-12-662*. For the composite material, high values of dissipation of the energy lay in the range of high temperatures and high strain rates, where also instability of in the flow is predicted, but also instabilities up to 850°C at the lowest temperatures are shown.
- *CermeTi<sup>®</sup>-C-662*. The composite reinforced with 20% of particles (only tested up to  $1.4\text{s}^{-1}$  strain rate) shows high dissipation of the energy at low strain rates. The instabilities of the flow are predicted in the whole range of strain rates and temperatures except between 800 and 950°C at the lowest strain rate.

Figure 156 to Figure 163 show the processing maps at  $\epsilon = 0.3$  ( $\eta\%$ ) calculated according to the modified DMM and the instability maps delimited by  $\kappa < 0$  which differs from the DMM. The behaviour of the materials predicted with this model shows that:

- *Ti662 Ingot*. Again, the highest dissipation range occurs at high temperatures and strain rates, but also at temperatures below 750°C and low strain rates. The stability of the flow is now predicted only for high strain rates between 650-800°C and 900-950°C.
- *CermeTi<sup>®</sup>-C-662*. The highest dissipation of the energy is in the range of temperatures higher than 850°C, where the instabilities of the flow are also predicted.
- *CermeTi<sup>®</sup>-C-12-662*. For the composite material, high values of dissipation of the energy lie in the range of high temperatures and high strain rates, while the flow instability is predicted in the range of temperatures lower than 800°C in the whole range of strain rates (except high strain rates and temperatures lower than 680°C) and around 850°C at the lowest strain rate.
- *CermeTi<sup>®</sup>-C-20-662*. The composite reinforced with 20% of particles (only tested up to  $1.4\text{s}^{-1}$  strain rate) shows high dissipation of the energy again at low strain rates. The instabilities of the flow are now predicted in the range of highest temperatures and highest strain ranges, as well as at the lowest temperatures and lowest strain rates.

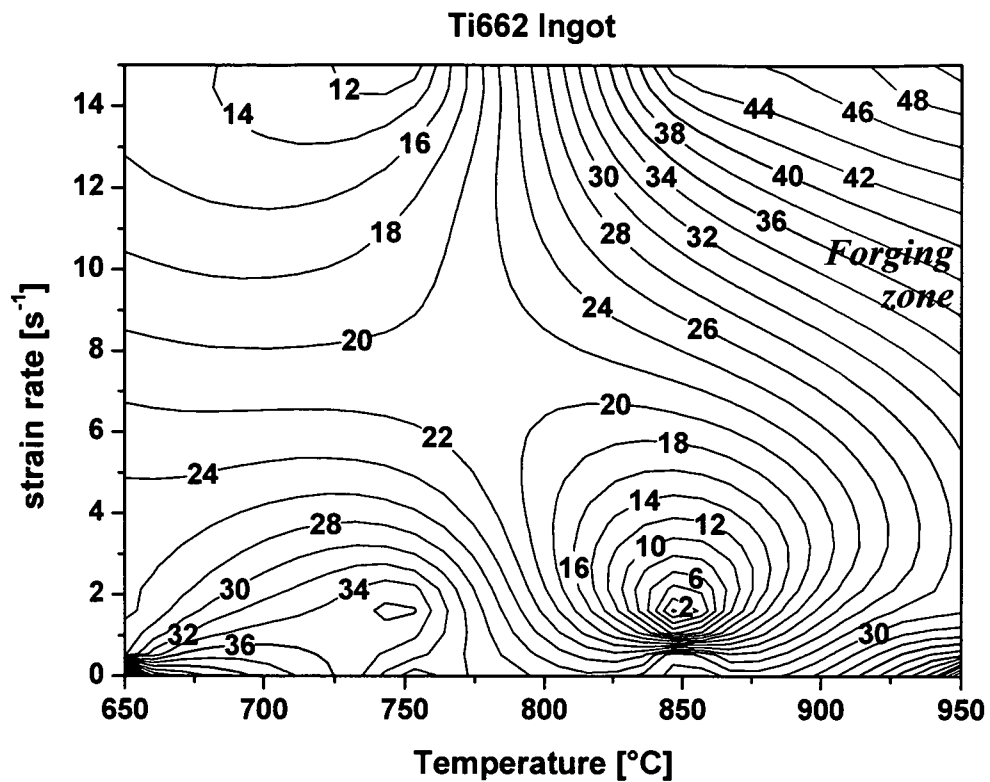


Figure 156. Power dissipation map for Ti662 ingot calculated at  $\epsilon = 0.3$  using the modified DMM.

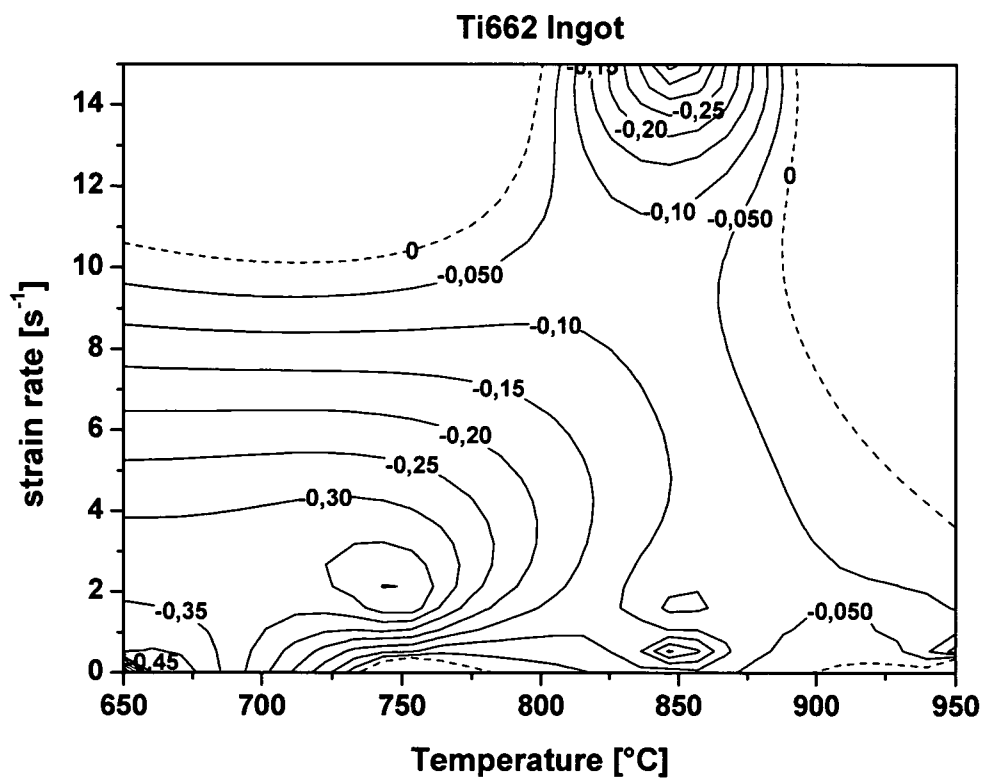


Figure 157. Instability map for Ti662 ingot calculated at  $\epsilon = 0.3$  using the modified DMM.

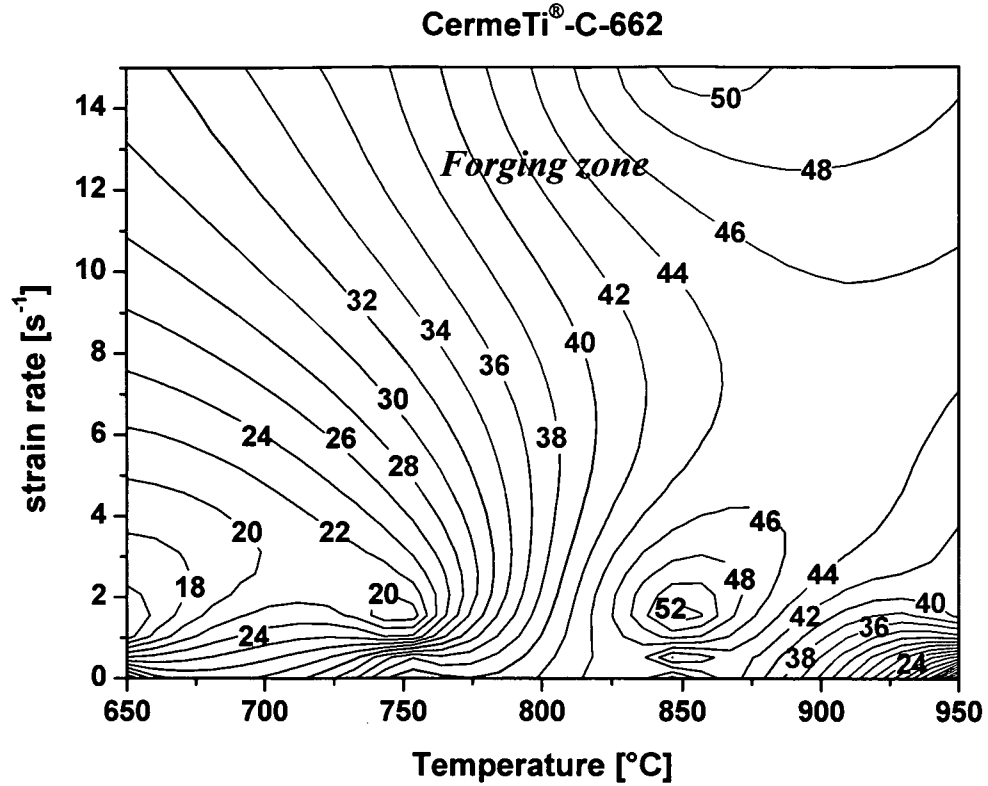


Figure 158. Power dissipation map for CermeTi®-C-662 calculated at  $\epsilon = 0.3$  using the modified DMM.

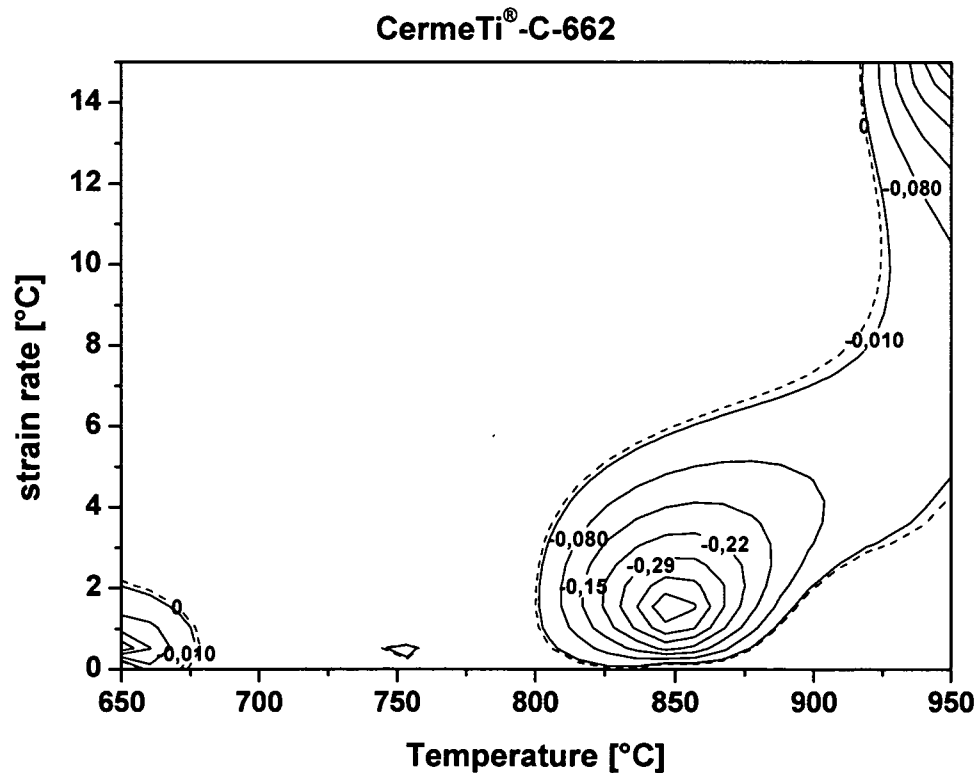


Figure 159. Instability map for CermeTi®-C-662 calculated at  $\epsilon = 0.3$  using the modified DMM.

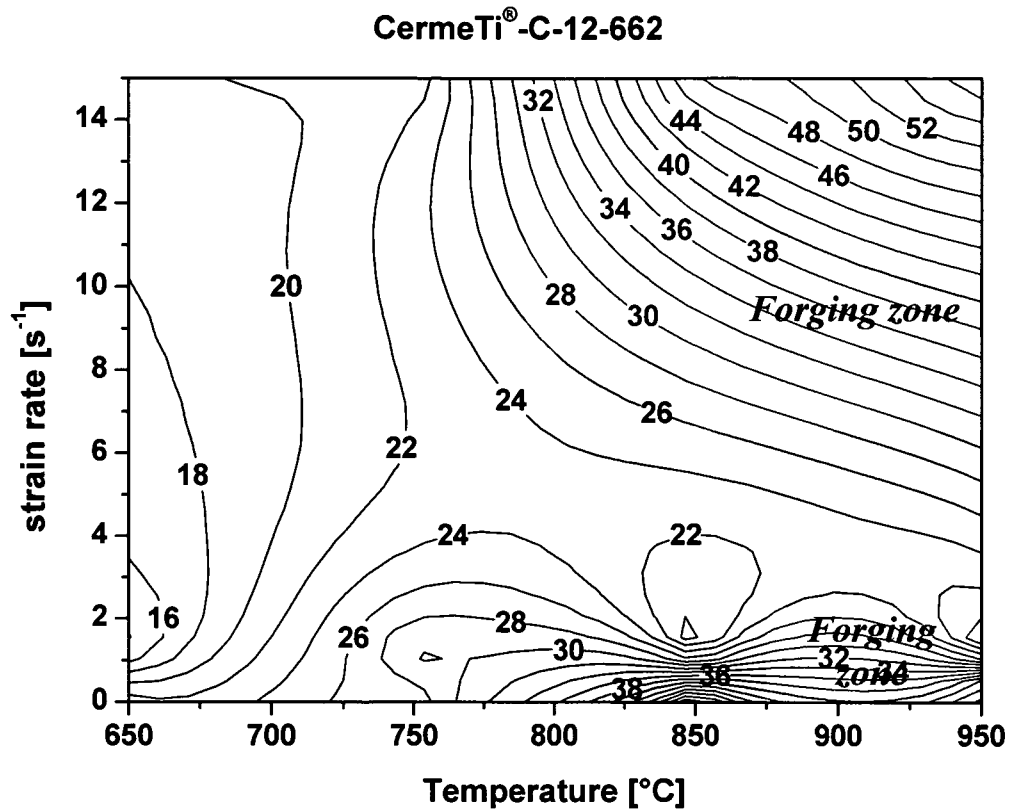


Figure 160. Power dissipation map for CermeTi®-C-12-662 calculated at  $\epsilon = 0.3$  using the modified DMM.

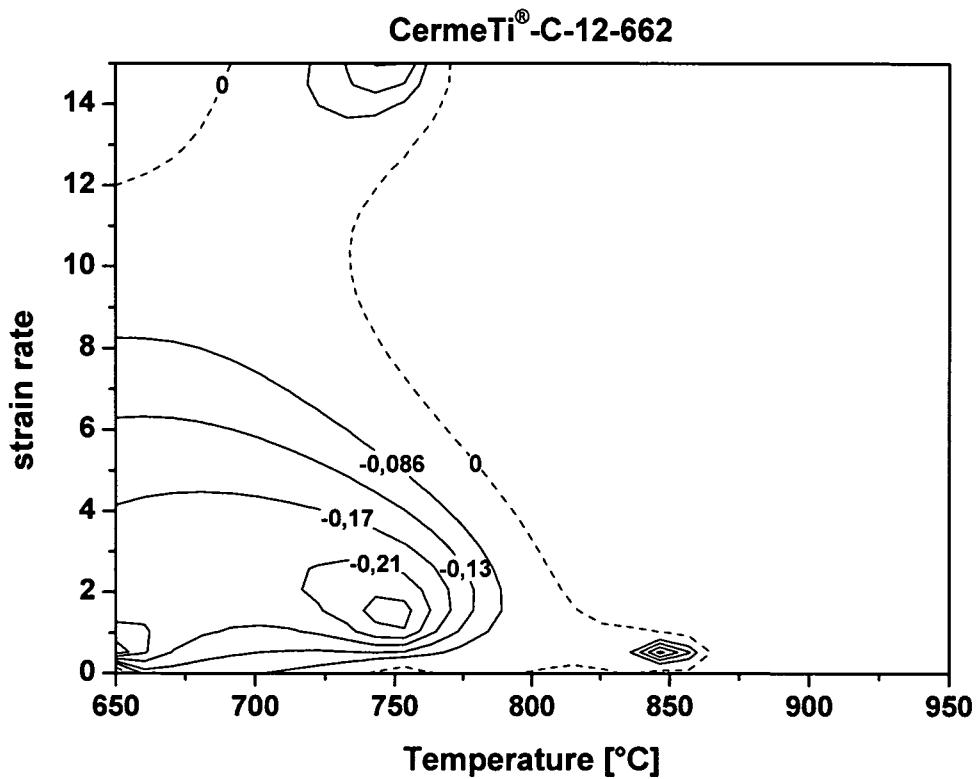


Figure 161. Instability map for CermeTi®-C-12-662 calculated at  $\epsilon = 0.3$  using the modified DMM.

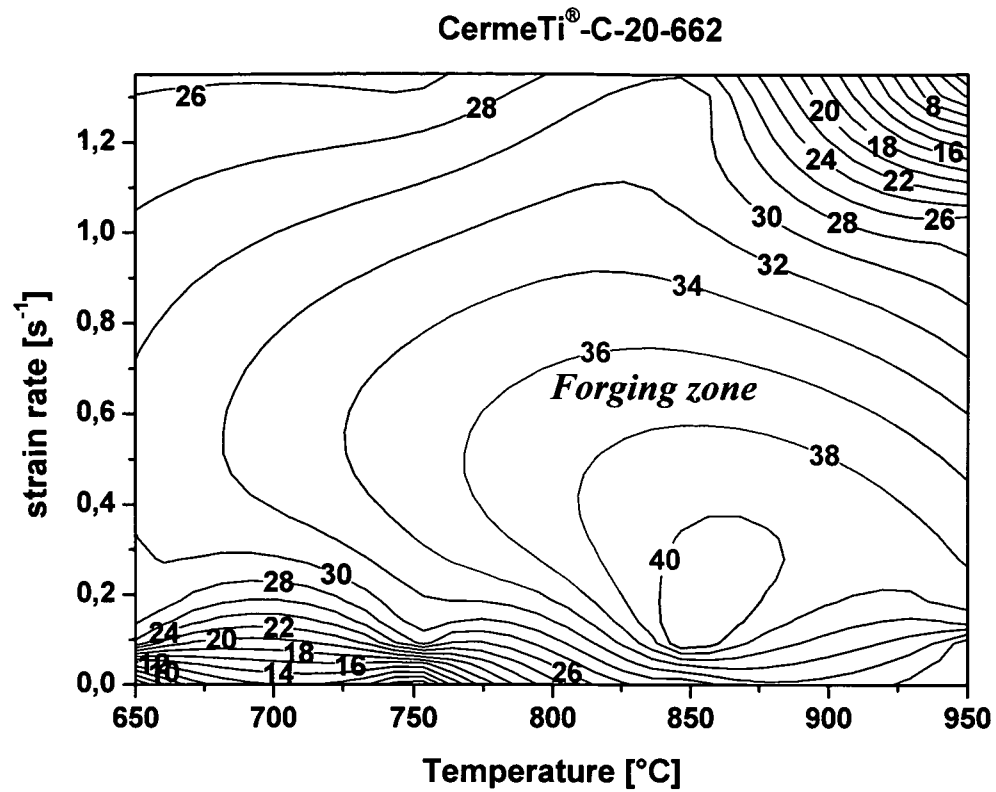


Figure 162. Power dissipation map for CermeTi®-C-20-662 calculated at  $\epsilon = 0.3$  using the modified DMM.

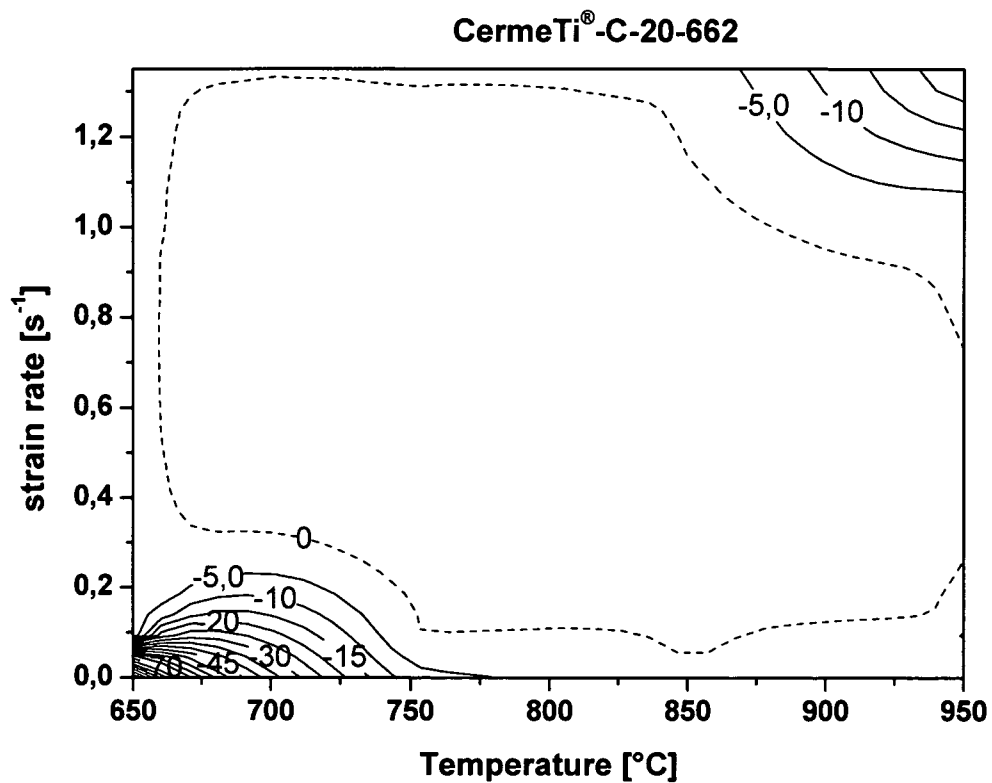
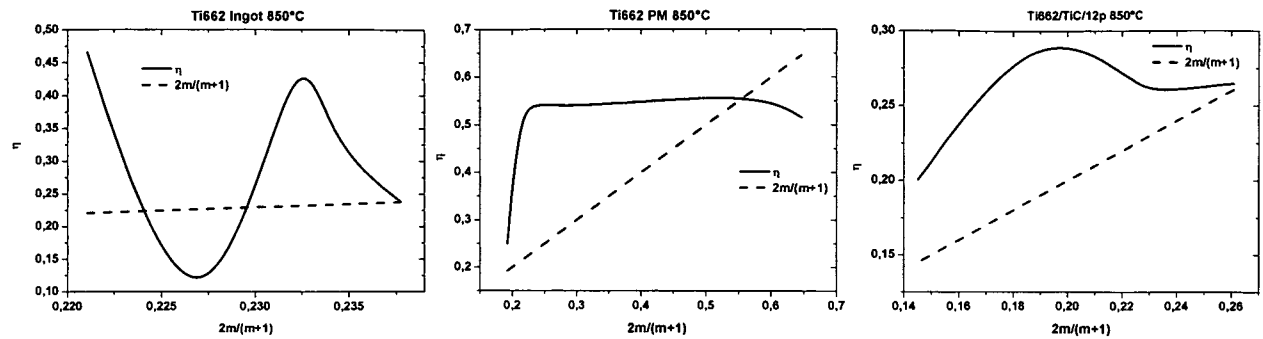


Figure 163. Instability map for CermeTi®-C-20-662 calculated at  $\epsilon = 0.3$  using the modified DMM.

Figure 164 shows that the power dissipation ( $\eta$ ) calculated using the DMM equations compared to those calculated using the modified DMM at 850°C for Ti662 Ingot, PM and reinforced with 12% TiC. The discrepancies are the result of the behaviour of the materials that clearly do not obey the power law.



**Figure 164.** Power dissipation  $\eta$  calculated using the Rao et al equations ( $\eta$  modified DMM) compared to those calculated using the Prasad et al model ( $2m/(m+1)$  DMM)

Figure 165 show an optical comparison of the values of dissipation power ( $\eta\%$ ) calculated using the DMM and the DMM modified, and it can be seen that the tendencies regarding the optimum regions are not much different.

The larger discrepancies between the two models are those of the Ti662 Ingot and Ti662 reinforced with 20%vol of TiC particles. In the first case, it has to be note that the material is a pre-deformed material, and that, although all the samples were taken from the ingot from the same direction of cogging (longitudinal), some differences between a sample from the centre of the ingot and from the border could influence in the quality of the data. In the second case, only 4 strain rate values were taken to fit a cubic spline.

Although the tendency in the energy dissipation is more or less the same for the two models, the predictions in the instabilities of the flow are quite different.

The complete deformation mechanisms can only be clarified with the help of the metallography and the shape of the flow curves, in order to choose the model, which fits best the flow behaviour of the tested materials (see discussion).

**DMM**

**modified DMM**

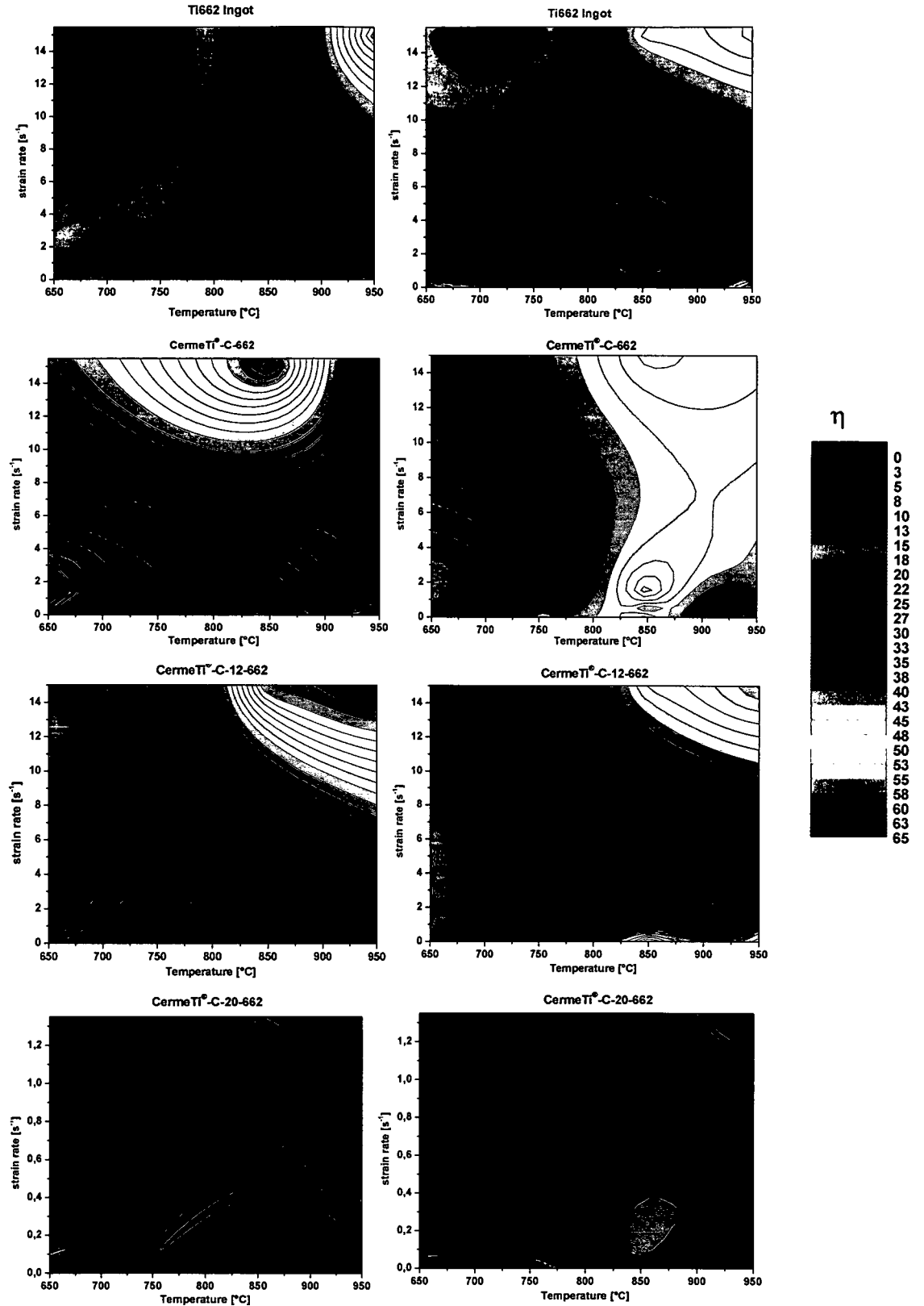


Figure 165. Comparison of power dissipation between the two models using the same scale for  $\eta$  %.

## 5.5 Wear mechanisms

Figure 166 shows the wear rate for the unreinforced CermeTi®-C-662 while that for the reinforced material CermeTi®-C-20-662 is shown in Figure 167.

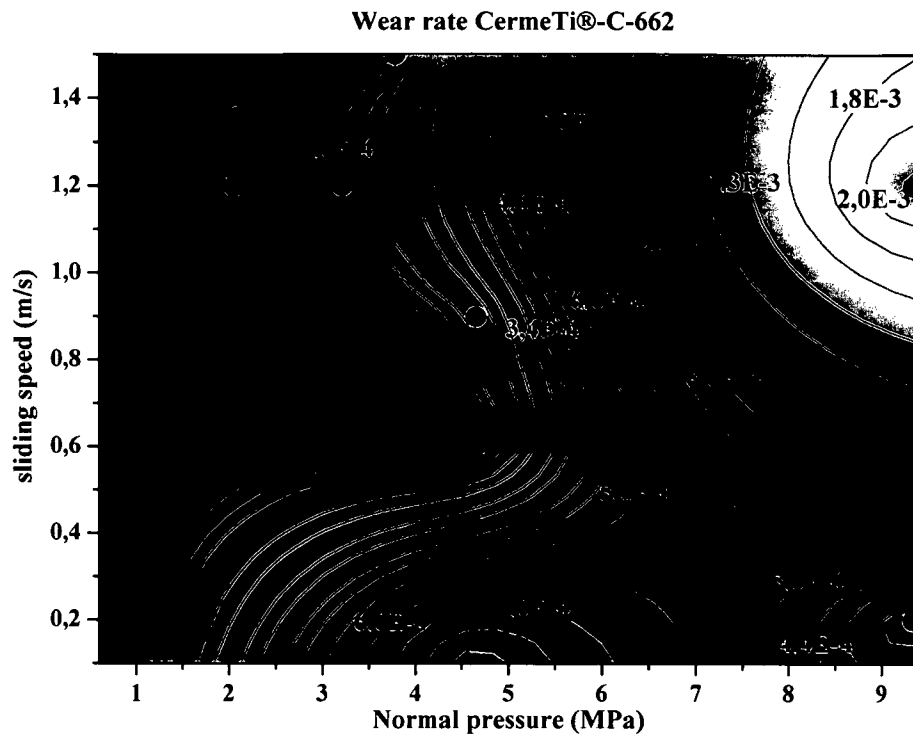


Figure 166. Wear rate as a function of the normal pressure and the sliding speed for the unreinforced Ti662.

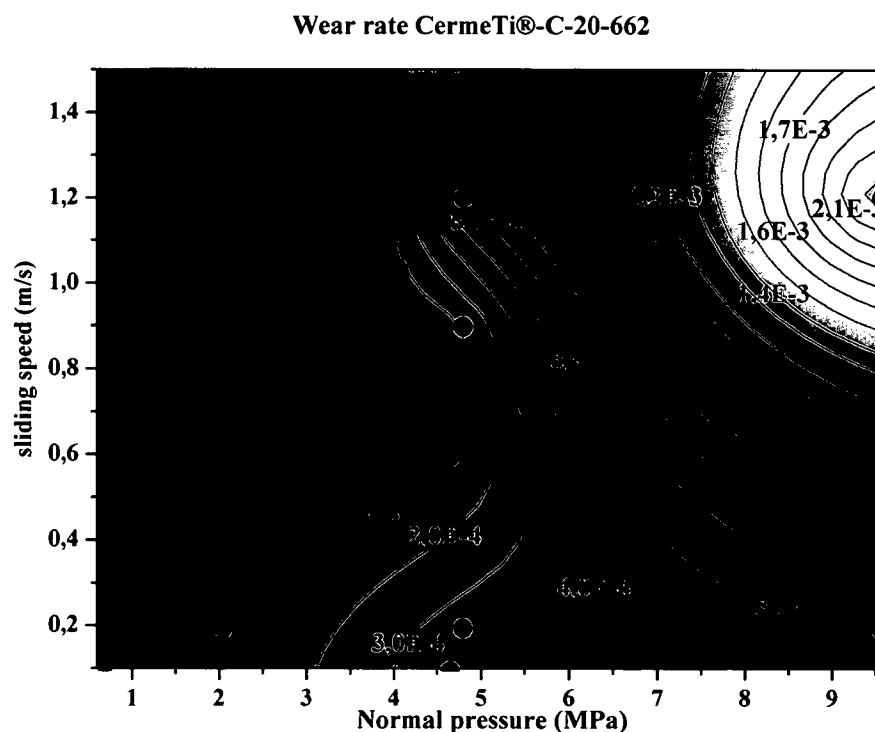


Figure 167. Wear rate as a function of the normal pressure and the sliding speed for the Ti662/TiC/20p.



The values of wear rate of the Ti662 PM Figure 166 compared to the composite of Ti662 reinforced with 20%vol of TiC particles Figure 167 show no sensible differences at pressures higher than 3 MPa. For both materials, the wear resistance is low at high pressures and high sliding speeds. The composite is more resistant to the dry sliding against steel at pressures lower than 3MPa for all the sliding speeds, and up to 7MPa for low sliding speeds.

All the experimental curves of friction coefficient vs. distance show values in the running-in state below the steady state values, except for some experiments with the CermeTi®-C-20-662 pins and one with the Ti664/SiC/15p, which exhibit an initial peak. In Figure 168 the friction coefficient of a CermeTi®-C-20-662 at 0.2 m/s sliding speed and 25.4N normal force is plotted with the distance.

It can be seen that the lowest values of friction coefficient agree with the tests that present a high initial value in the running in state. It suggests that during the running in state there is a time needed for the formation of the iron oxides, which lubricate the sliding between the two materials (pin and disc/ring). For the Ti664/SiC/15p, the only test that present a peak of the friction coefficient in the running in state, shows a very low friction coefficient in the steady – state and little formation of oxides.

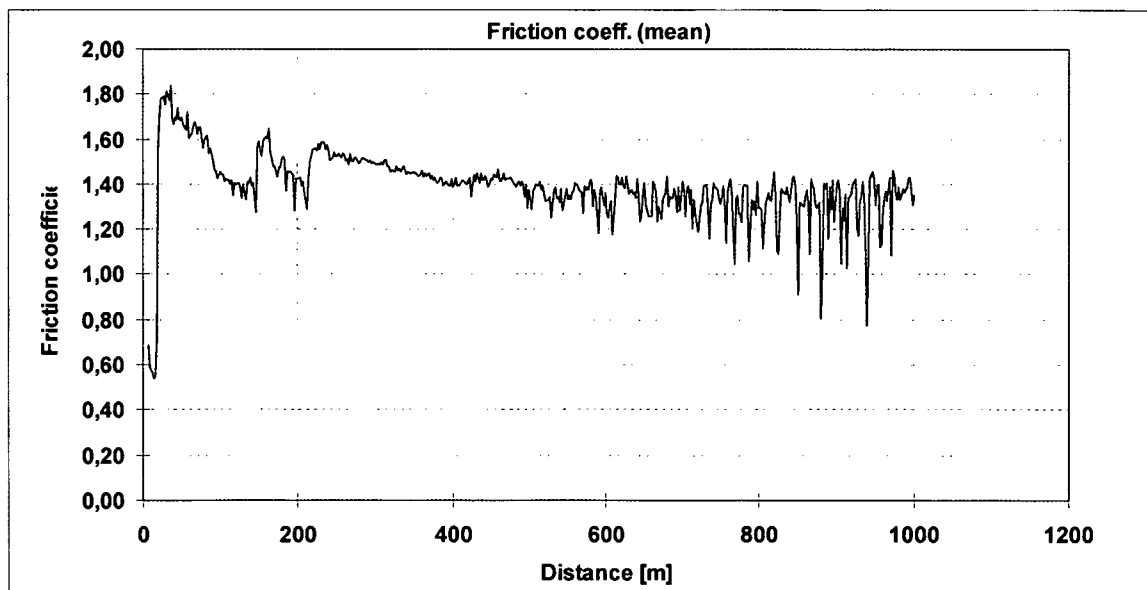


Figure 168. Friction coefficient plotted with the distance of a CermeTi®-C-20-662 running at 0.2 m/s sliding speed and 25.4N normal force.

The coefficient of friction obtained for the unreinforced alloy (Figure 169) increases abruptly with increasing normal pressures and sliding speeds, while more homogeneous coefficient of friction ( $\mu$ ) values are observed for the composite material (Figure 170).

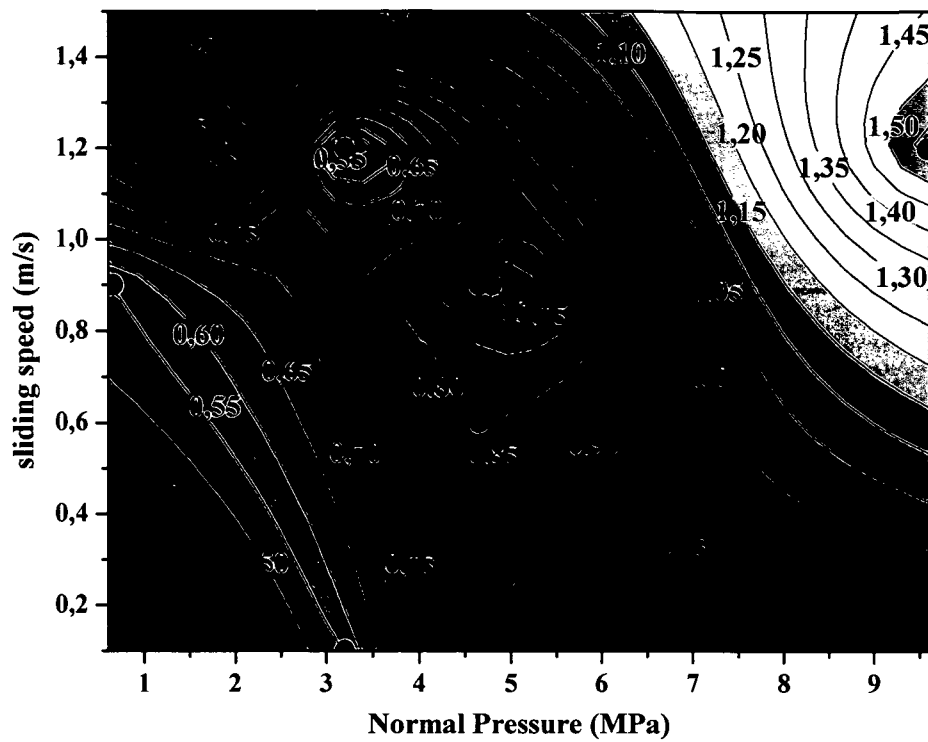
$\mu$  steady-state. CermeTi®-C-662

Figure 169. Friction values in the steady state as a function of the normal pressure and the sliding speed for the unreinforced Ti662 alloy.

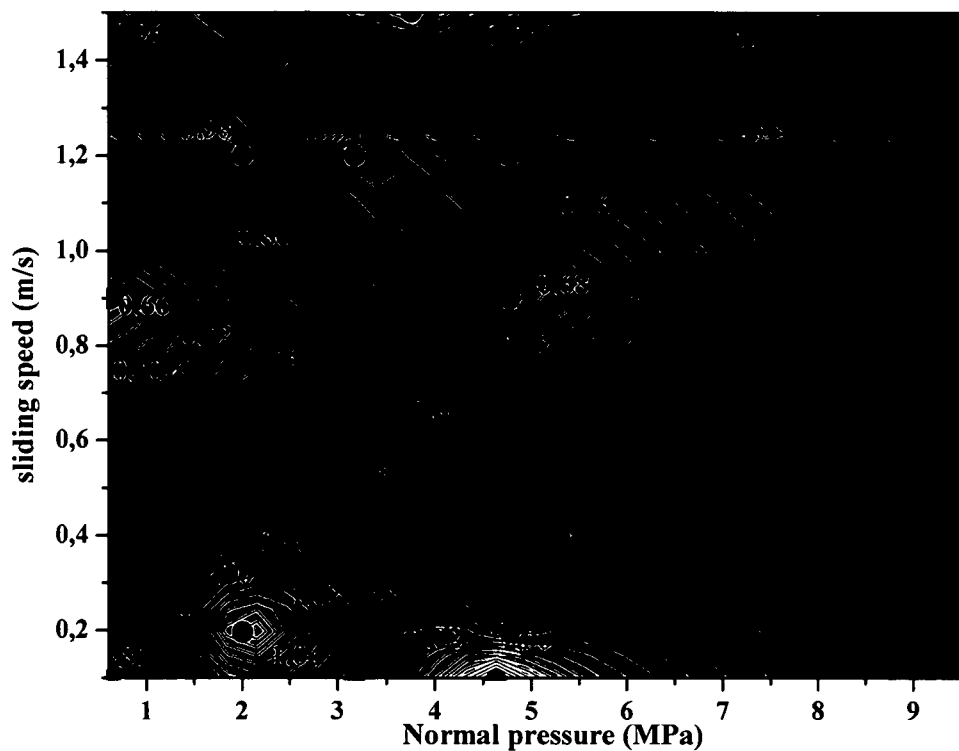
 $\mu$  steady-state. CermeTi®-C-20-662

Figure 170. Friction coefficient in the steady state for the Ti662 reinforced with 20% vol TiC particles dependent of the normal pressure and the sliding speed.

---

## 6 Discussion.

### 6.1 Analysis of the experimental methods.

#### 6.1.1 *Alpha-beta quantification with Image Analysis.*

Alpha and beta phases change their shapes, relation and alloy contents during heat treatments. Basically, two different methods were used in this work to study these transformations: image analysis of water quenched samples and dynamic dilatometry.

The quantification of  $\alpha/\beta$  ratio of the water-quenched samples was done using the image analysis. There are some problems inherent to the measurement method. First, the process of quenching cannot freeze the original microstructure. During quenching, the alpha phase grows at a rate that decreases by increasing the cooling rate. In an ideal case, the analysis of the phases should be done after an infinite cooling rate, i.e. at instantaneous quenching time, to retain the equilibrium phases. The experiments cooled with water result in the study of a microstructure, which is not the actual microstructure at high temperatures. Furthermore, the pictures measured using image analysis were taken with SEM in the BSE mode, with a resolution maximum of 0.5 $\mu\text{m}$ . Finally, the Image analysis itself is subjected to errors. The pictures at low magnifications (150x) loose resolution, and the contrast between the two phases is diffuse, especially for a lamellar microstructure and markedly edges. The high magnifications (2000x), on the other hand do not represent the whole microstructure, and many pictures are needed in order to have an average.

#### 6.1.2 *Dilatometry*

The dynamic dilatometry allows us the study of the phase changes during heating and/or cooling, with varying heating/cooling rates. The results would represent the equilibrium diagram in the ideal case of cooling and heating rates tending to zero.

By using this technique with titanium alloys, it is possible to say that:

- It is not possible to study the effect of the time at high constant temperatures above 850°C, due to the high reactivity of the titanium with both, the alumina and the SiO<sub>2</sub> holders.
- For high cooling rates, high purity inert gas is required.
- During cooling, some non-reproducible peaks in the CTE were registered.

- 
- At temperatures higher than 1000°C, also artefact in the reference platinum sample with the alumina holder was observed.
  - The beta transus temperature, a constant temperature for pure material, and a temperature at which all the alpha is transformed into beta for the titanium alloys is dependent on the rate of heating/cooling.

### 6.1.3 *Gleeble vs. Servotest.*

The flow data used to build the processing maps should be representative of the actual flow behaviour of the tested materials, and the temperature and strain rate should be constant during the experiment.

By using the Gleeble machine, the *gradient of temperature* along the sample provoked by the heating system results in a non uniform compressive deformation due to the dependence of the flow stress on the temperature resulting in the softening of the zone of the sample at higher temperatures. In the case of the titanium samples, this dependence is considerable high because the flow also depends on the  $\alpha/\beta$  ratio. The higher the temperature, the higher the quantity of the beta phase, and the softer the material. Furthermore, at temperatures near the beta transus, the percentage of beta content changes abruptly.

Due to the heating method, the *friction* between the anvil and the sample cannot be avoided at high temperatures with the common lubricants used in the industry, because all of them are electrical isolator (glass and ceramics).

Thus, the measurement of the deformation cannot be done along the sample, but in the transversal measurement, avoiding the relation  $A_1 \cdot l_1 = A_2 \cdot l_2$ , only valid for uniform deformation, with  $A_x$  constant along the sample at time  $x$ . The non-uniform deformation implies tensile deformation in the middle of the sample (multiaxial tension test) that is critical for the composites (see 6.2).

Finally, although the Gleeble<sup>®</sup> 1500 machine can reach high strain rates, the constant strain rates are achieved only up to  $4s^{-1}$ .

On the other hand, the parameters of compression such as temperature (at the measured point) and strain rate can be precisely measured and controlled, and constant strain rates are possible.

The experiments carried out with a SERVOTEST machine can be lubricated with glass, and the temperature in the furnace is more or less constant, and both correlations result in an uniform deformation (uniaxial tension test). On the other hand, the strain rate is commonly not easy to maintain constant during the test and the temperature of the furnace is recorded, but not that of

---

the sample. Finally, the change in length of the sample is not measured, but the whole movement of the anvil during the compression test.

## 6.2 Deformation behaviour.

### 6.2.1 Ti662 Ingot: globular microstructure.

The steady state that characterizes the flow behaviour between 750-950°C for strain rates up to 0.15 s<sup>-1</sup> and between 850 and 950°C up to 15 s<sup>-1</sup> suggests dynamic recrystallisation, superplasticity or rapid dynamic recovery [91].

The Zener-Hollomon parameter  $Z$  is defined as [117]:

$$Z = \dot{\epsilon} \exp\left(\frac{Q}{RT}\right) \quad \text{Equation 42}$$

where  $Q$  is the apparent activation energy,  $R$  the gas constant and  $T$  the temperature in K.

It has been found that normally the Zener-Hollomon parameter behaves as:

$$Z = c_1 \sinh(c_2 \cdot \sigma)^n \quad \text{Equation 43}$$

where  $n$  is the stress exponent, and  $c_1$  and  $c_2$  are constants.  $Z$  can be also expressed as

$$\sigma = \frac{1}{c_2} \ln \left[ \left( \frac{Z}{c_1} \right)^{\frac{1}{n}} + \left( \left( \frac{Z}{c_1} \right)^{\frac{2}{n}} + 1 \right)^{\frac{1}{2}} \right] \quad \text{Equation 44}$$

At low values of stress, or where the stress is independent of the strain rate, the previous equation reduces to Norton's creep law:

$$\dot{\epsilon} = A \sigma^n e^{\left(\frac{-Q}{RT}\right)} \quad \text{Equation 45}$$

where  $n$  is the stress factor ( $n=1/m$ ),  $Q$  is the apparent energy of activation of the deformation mechanism, and  $A$  is the frequency factor.

On the other hand, at high stress values,  $Z$  can be calculated as:

$$Z = c_4 \exp(c_5 \sigma) \quad \text{Equation 46}$$

where  $c_4$  and  $c_5$  are constants.

Figure 171 shows the variation of the flow compressive stress at 0.3 strain with the strain rate and the  $n$  values using the Equation 45. The high value of  $n = 12.9$  at  $650^{\circ}\text{C}$  means a value of  $m = 0.077$  that implies low dissipation of the power through metallurgical processes, in accordance with the dissipation map calculated through *DMM* (Figure 148) because we are considering the power law in both cases. On the other hand, the dissipation map calculated through *modified DMM* (Figure 156), shows moderate values of power dissipation at low strain rates. The pictures of the microstructures after compression at  $650^{\circ}\text{C}$  show shear bands of deformation at low strain rates while the flow curves show softening flow in concordance with both instability maps. But at high strain rates, (and  $\epsilon = 0.8$ ) modified DMM does not predict instabilities in the flow in contrast with the DMM. As in globular microstructures this can be only produced by cracking or flow instability, and the micrograph (Figure 66) show zones of growth of the alpha phase, it can be concluded that DDM predicts better the instable flow behaviour at  $650^{\circ}\text{C}$ .

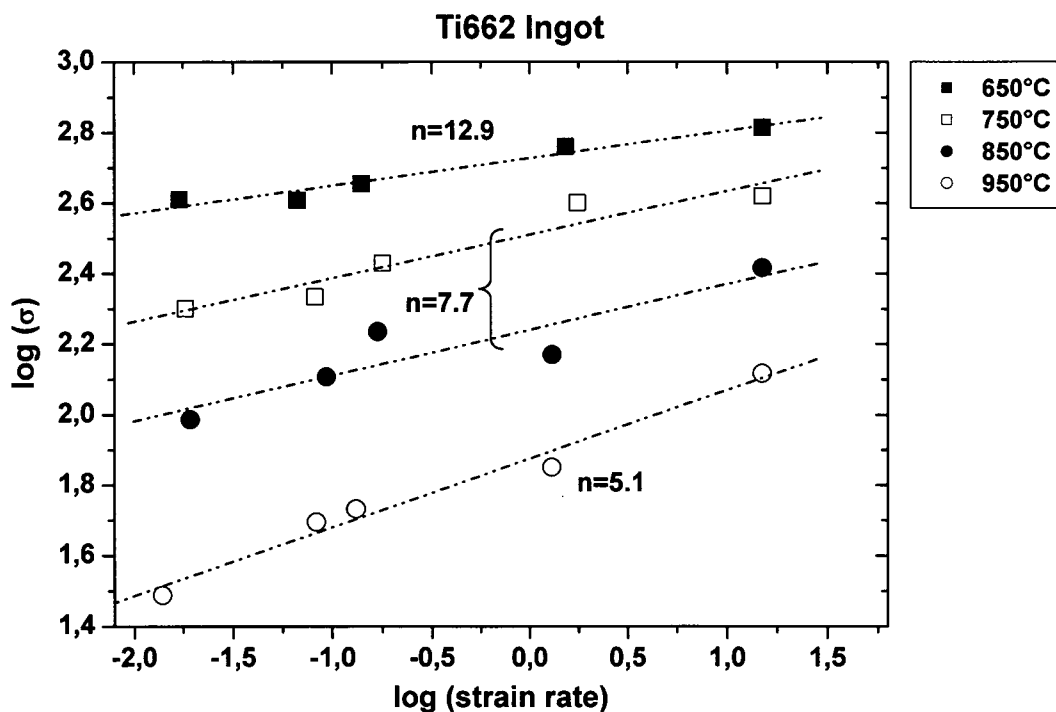


Figure 171. Variation of the flow stress at 0.3 strain with the strain rate to determine the stress exponent

The  $n$  value of 7.7 found for 750 and  $850^{\circ}\text{C}$  allows us to follow with the kinetic study at those temperatures. Figure 172 shows that it is possible to calculate the energy of activation of the hot deformation. It was found that the values of apparent energy jump from 350 kJ/mol to 530 kJ/mol alternatively. To test the applicability of Equation 45,  $Z$  was recalculated using  $Q = 350$  kJ/mol (that agrees with exponent value of the literature [91]) with Equation 42, and  $\log(\text{strain rate})$  was

plotted in Figure 173 against the log of the recalculated  $Z$ , giving a slope of approximately  $n=9$ . The plot shows a good agreement for temperatures of 750°C and 850°C.

The fluctuating energy of activation suggests instability in the flow due to changing deformation mechanisms. The *modified DMM* predicts instability of the flow in the whole strain rate range at temperatures between 750 and 850°C. In fact, comparing the microstructures, although both seem to be recrystallised, in agreement with the steady state shape of the flow curves, they are completely different if the compression test was done at 750°C and  $0.15\text{s}^{-1}$  (Figure 67) or at  $1.3\text{s}^{-1}$  (Figure 69).

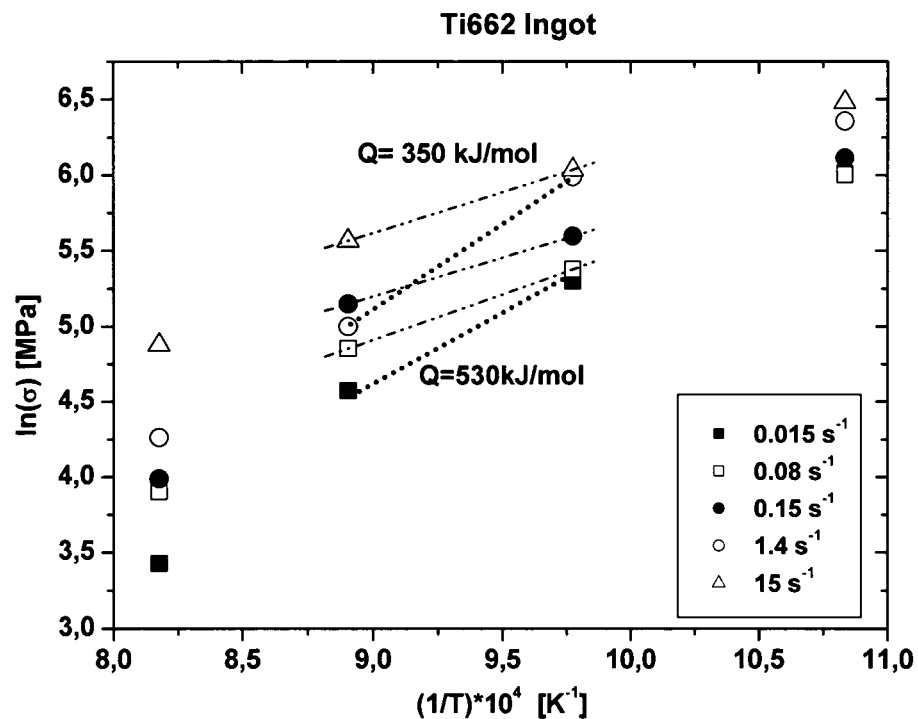


Figure 172. Apparent energy of activation at 750-850°C.

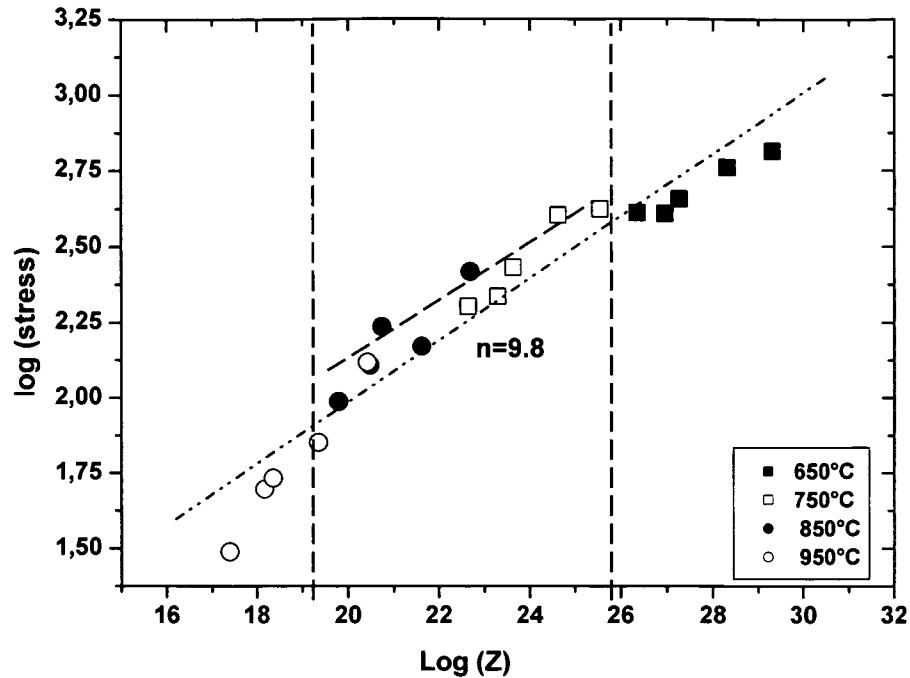


Figure 173. Log (Z) recalculated with equation 42, showing a good linear fit between 750 and 850°C.

The steady state flow at 950°C (in the beta range) suggests cracks, fast dynamic recovery, recrystallisation or instability of the flow. At strain rates above  $5\text{s}^{-1}$  both models predict stable flow (Figure 149 and Figure 157). As titanium and titanium alloys are characterized by a high stacking fault energy [118], high values of power dissipation are expected if dynamic recrystallisation occurs [119]. It is confirmed in the processing maps (Figure 148 and Figure 156), with values of  $\eta$  in the range of high temperatures and strain rates above  $5\text{s}^{-1}$  of 38 up to 50. Furthermore, the pictures at high strain rates and  $\epsilon = 0.8$  show polygonisation of the beta grains, suggesting also dynamic recrystallisation.



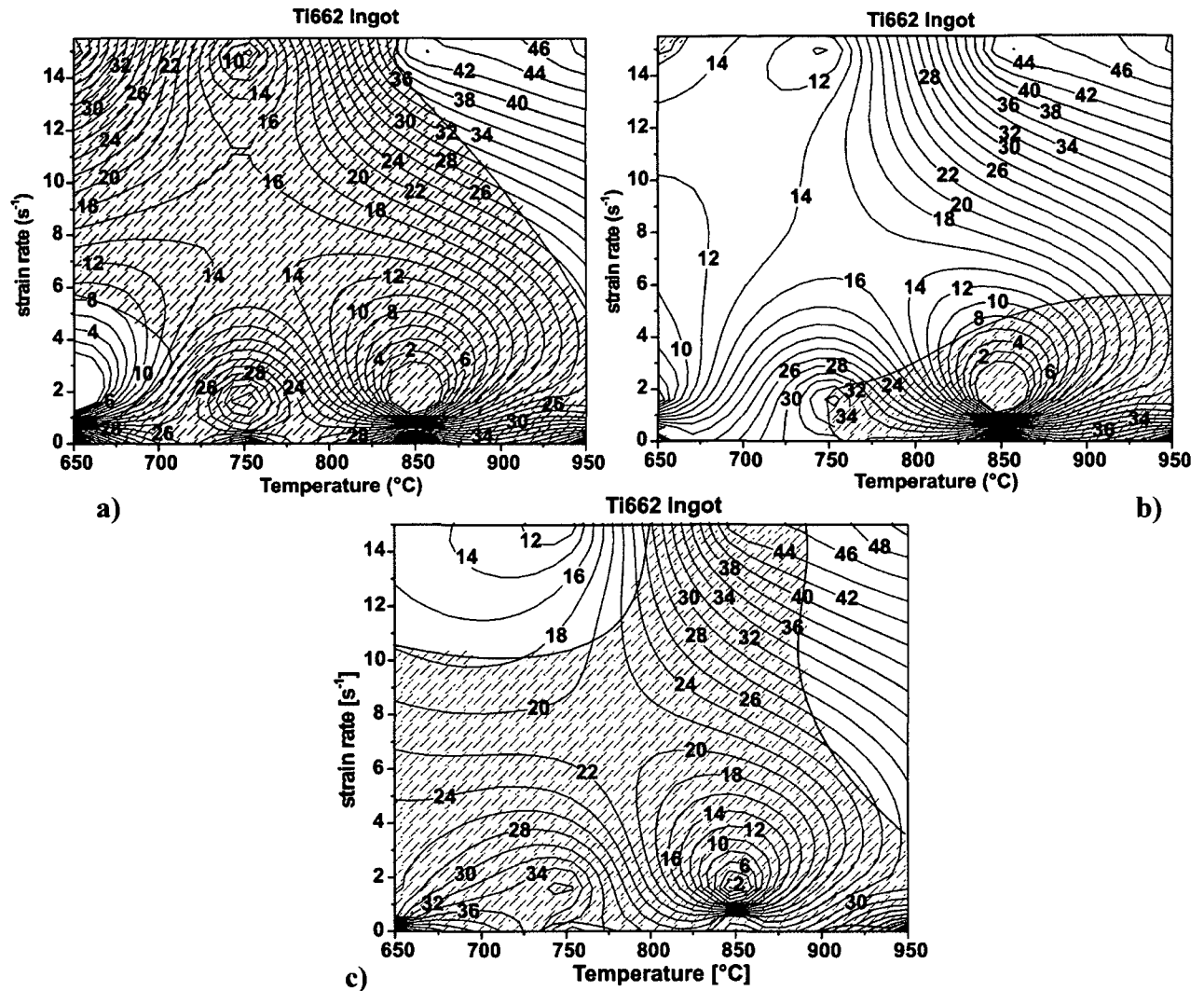


Figure 174. Processing maps and instability zones (dashed) calculated using the modified DMM at different true strains a)  $\epsilon = 0.1$ , b)  $\epsilon = 0.2$  and c)  $\epsilon = 0.3$  showing the evolution of the  $\eta$  and the  $g$  values.

The processing and stability maps were calculated using the modified DMM for true strains of 0.1 and 0.2 and compared to the 0.3 true strain maps, in order to follow the whole deformation process. Figure 174 shows stability of the flow at high strain rates and temperatures and instability at high temperatures and low strain rates for all the strain, and similar values of  $\eta$  for both zones. At low temperatures and high strain rates, the beginning of the deformation (0.1 strain) show high values of power dissipation and instability in the flow. This behaviour changes to a stable material flow at higher strains and lower power dissipation values. It suggests shear bands by starting the deformation, which can be stabilized during the deformation, as showed for copper [120].

---

### 6.2.2 Ti662 PM: lamellar microstructure.

The flow curves of the lamellar as received microstructures show a more markedly softening comparing to the ingot material Ti662.

In the alpha-beta range, softening occurs in the whole range of strain rates. According to [93], among the lamellar  $\alpha+\beta$  colonies, the grain boundary  $\alpha$  and the thin  $\beta$  layer at the  $\alpha$  grain boundaries, the colonies have the highest strength due to specific crystallographic orientation (Burgers) relationships, while the  $\beta$  phase is inherently soft at the deformation temperature. During deformation at elevated temperatures, prior  $\beta$  boundaries oriented at  $\sim 45^\circ$  of the compression direction will slide under a resolved shear stress, resulting in a stress concentration developed at the triple junction grain boundaries. Since the grain boundary  $\alpha$  is less hard than the colonies, the stress concentration may be relieved if the softening rate of grain boundaries  $\alpha$  exceeds the stress accumulation rate at the grain boundary  $\alpha$ / thin  $\beta$  interface and, if not, cracks or pores (as observed in all the micrographs) are expected to nucleate at this interface.

At temperatures lower than 700°C, instability of the flow is produced by the adiabatic flow that causes the increment in the temperature at strain rates of  $1.4 \text{ s}^{-1}$  of 15-20°C (Figure 132). At higher strain rates, no instabilities were predicted, but Figure 64 suggest dynamic recovery because of the formation of fine alpha probably during the cooling after the deformation.

At the lowest strain rate and 900-950°C, the steady state of the flow, and the high values of the power dissipation (higher than 46%) suggest super-plasticity of the beta grains as reported for Ti64 with starting lamellar microstructure [93].

The kinetic study shows that at low temperatures, a high value of  $n$  (10.3) is calculated (Figure 175), in concordance with the low values of  $\eta$  calculated by both models at strain rates lower than  $5 \text{ s}^{-1}$ . At high temperatures, a value of  $Q$  of 240 kJ/mol was calculated. This value is near the value of 153 kJ/mol [121] of selfdiffusion in beta.

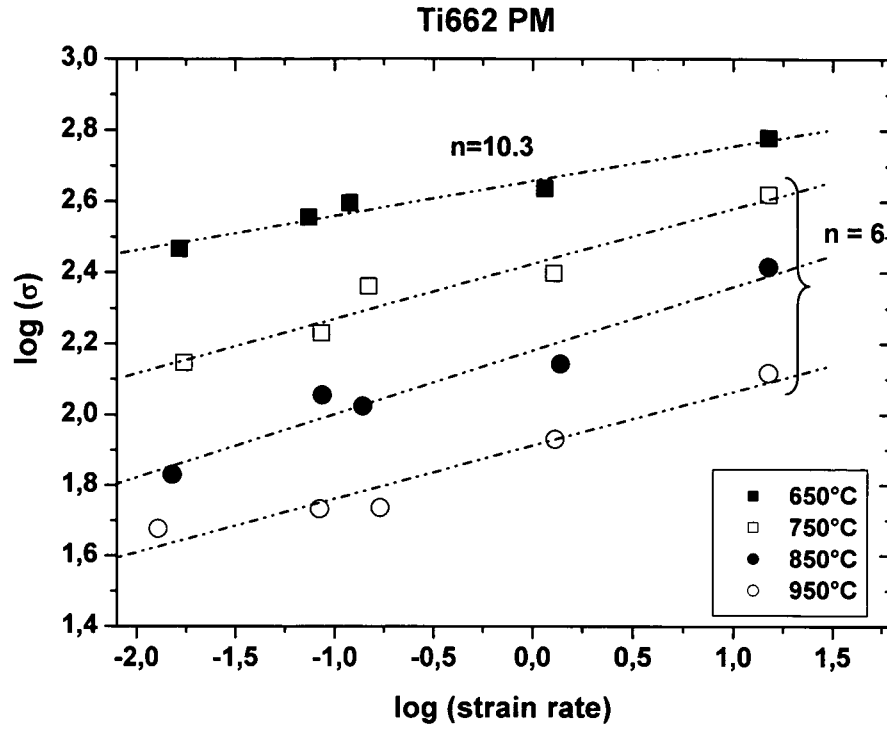


Figure 175. Variation of the flow stress at 0.3 strain with the strain rate to determine the stress exponent  $n$ .

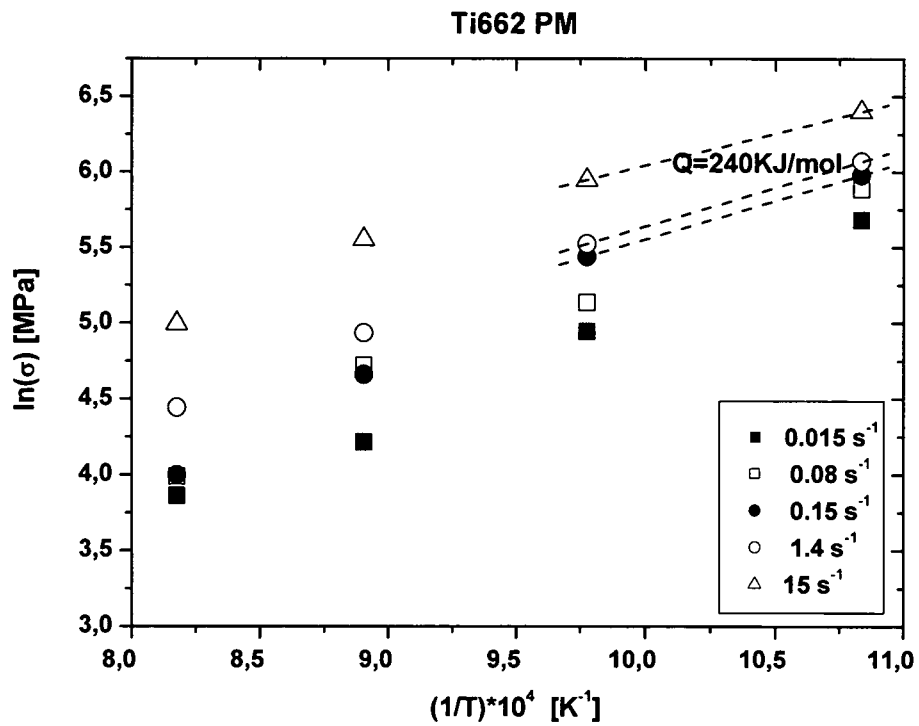


Figure 176. Apparent energy of activation between 850-950°C at strain rates higher than  $0.1 \text{ s}^{-1}$

Figure 177 shows a good correlation of  $Z$  using  $Q=240 \text{ kJ/mol}$ . The value of  $n$  is smaller than this calculated for 750°C-850°C.

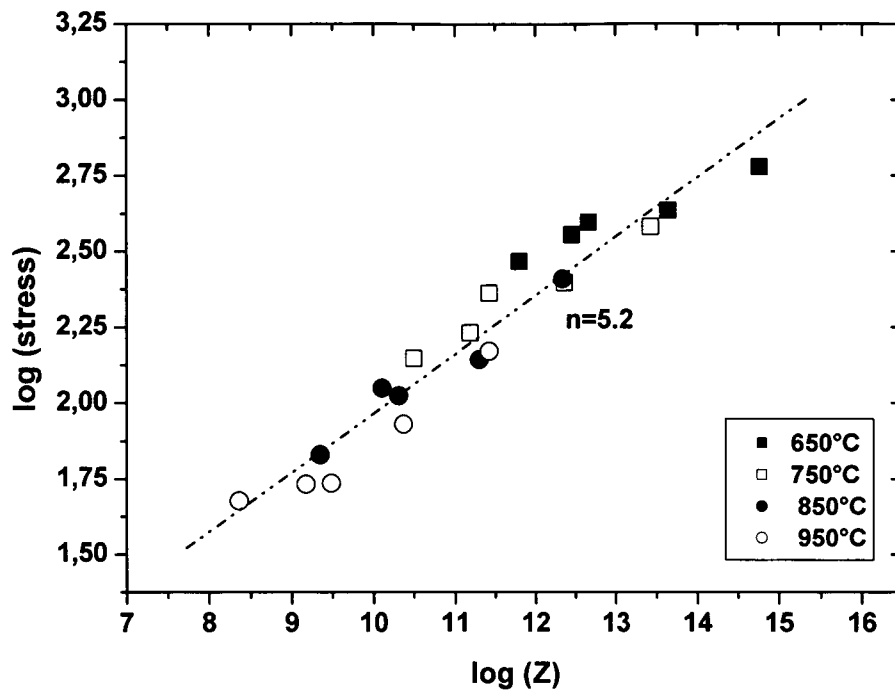


Figure 177. Linear fit with the recalculated Z using  $Q = 240 \text{ kJ/mol}$

Considering the effect of the holding time in the flow mechanisms, it is possible to say that:

The compression test at 750°C after a holding time of one hour at 1000°C, i.e. a temperature above the beta transus temperature (Figure 126) for the unreinforced material show lower values in the compression stress than the alloys heat treated below the beta transus temperature (900°C) before the compression at 750°C (Figure 125). It is due to the high rates of grain growth of the beta phase [23], which, by cooling down to the test temperature, result in large colonies of alpha inside large beta grains, in detriment to the compressive resistance. Furthermore, a large softening was observed due to the damage of the microstructure.

The processing and stability maps (modified DMM) for true strains of 0.1, 0.2 and 0.3 are showed in Figure 178. At high strain rates the  $\eta$  values increase gradually for all the temperatures with a stable flow (except at 925-950°C and  $\epsilon = 0.3$ ), indicating that the microstructural changes increases with the deformation up to superplasticity a high temperatures.

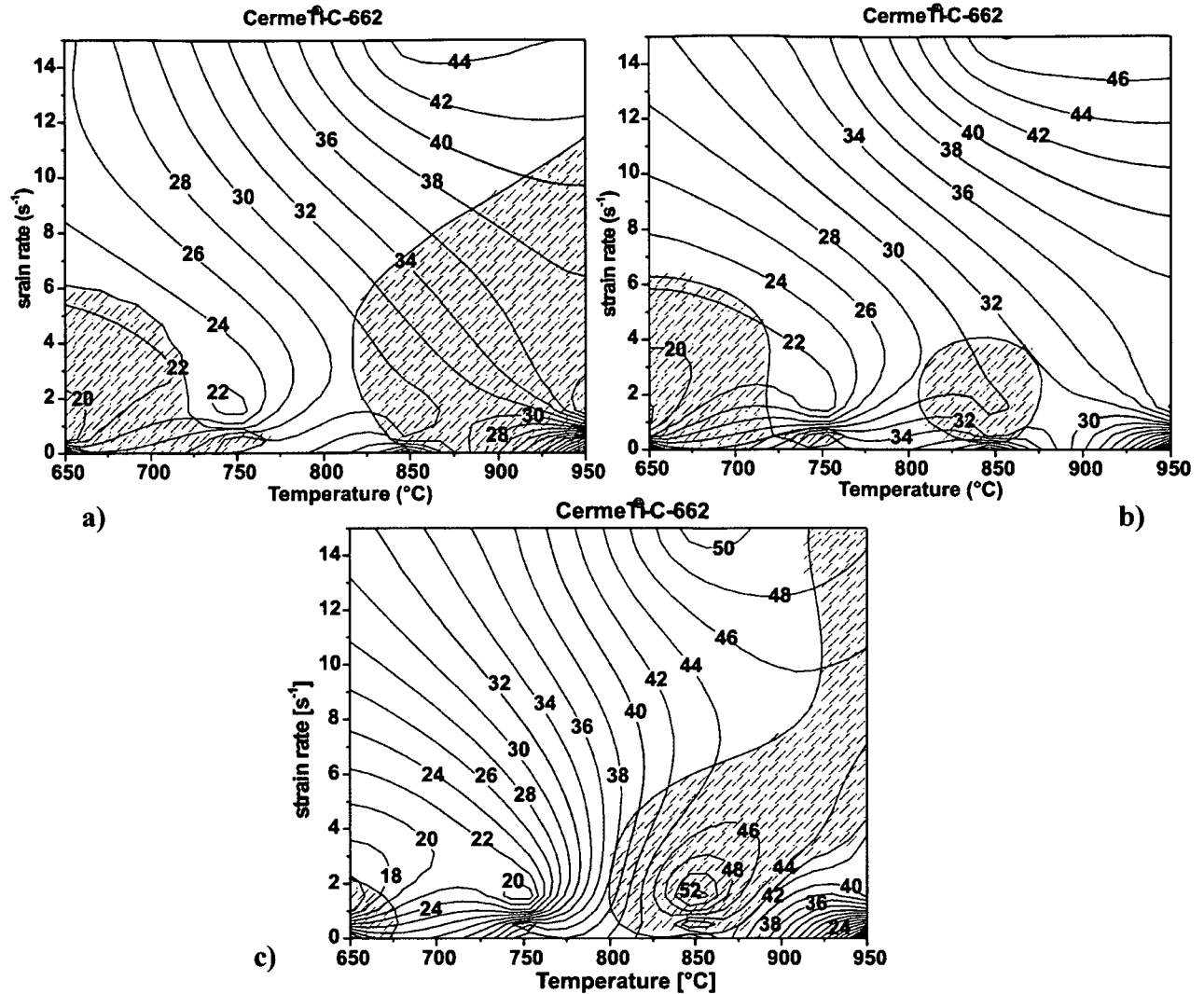


Figure 178. Processing maps and instability zones (dashed) calculated using the modified DMM at different true strains a)  $\epsilon = 0.1$ , b)  $\epsilon = 0.2$  and c)  $\epsilon = 0.3$  showing the evolution of the  $\eta$  and the  $g$  values.

### 6.2.3 Ti64 PM alloy: lamellae microstructure.

The most important difference between the Ti662 and the Ti64 alloys is the alpha/beta content. Not only the beta transus of Ti662 is lower than that of the Ti64, in about 50°C, but also its alpha content in the whole range of temperatures is lower in about 10%.

As the beta phase is softer than the alpha phase, it is valid to expect for the Ti662 alloy lower maximum compressive strength at the same temperature and strain rate compared to the values of the Ti64 alloy. This was observed for all the samples (compare Figure 118 with Figure 119), but this effect is less important with increasing the temperature, i.e. while increasing the beta content. On the other hand, as the relaxation of the produced stresses is relieved by cracks in the beta phase, the Ti662 alloy shows more softening. The softening due to kinking reported for Ti64 by

---

[95] , is also observed here (Figure 73), but not for Ti662, where mainly softening by cracks in the beta phase occurs.

#### **6.2.4 Composites. Influence of the TiC particles in the deformation behaviour.**

The strengthening that the TiC particles imparts to the matrices is high, even at high temperatures and long holding times.

Concerning to the dislocation strengthening mechanism, by increasing the test temperature, the internal stresses induced during cooling after material production decreases, and the generated dislocations as well as the strengthening tend to disappear. Furthermore, low or no CTE misfit exists between the TiC particles and the titanium alloy matrix, and it can be observed in the dilatometric tests, where similar values of thermal expansion between the matrix and the composite were observed (Figure 107). At high temperatures, or while holding the composites at elevated temperatures, the strength observed during compression does not decrease as shown in the holding time tests. Furthermore, after long heat treatments above the beta transus temperature, the particles avoid the extreme grain growth of the beta prior grains (Figure 88 compared with Figure 89) that would decrease the strength by testing the material at temperatures below the beta transus (Figure 126).

As we saw, comparing the pictures of the unreinforced material and the composite, a refinement of the grains was produced due to the reinforcement. Using the relation of Hall- Petch (Equation 6), and using  $\beta = 0.1 \text{ MPa}\sqrt{\text{m}}$ , the  $\Delta\sigma_{\text{YM}}$  obtained is about 40 MPa for 20%vol of particles of  $10\mu\text{m}$  , but the experimental stresses reach values up to 200 MPa higher than the matrix.

The strengthening mechanism can be explained as a combination of an increased density of dislocations produced by the little misfit, of faster growth of dislocation multiplication during deformation and to the refinement of the grains, but mainly due to the C diffusion from the TiC particles into the matrix during the production of the composite.

Although the heat treatments up to  $700^\circ\text{C}$  (even at long holding times, as 500 h) do not cause the diffusion of carbon from TiC toward the matrix [75], the carbon seems to diffuses during the processing step into the matrix, and the strengthening results from the interstitial alloying of the carbon. In our work, evidence of C poor TiC ( $\text{TiC}_x$  with  $x \approx 0.6$ ) was observed by diffractometry. The strengthening effect of the particles does not disappear above the  $\beta$ -transus temperature.

The Ti alloy matrix composites reinforced with TiC particles presents more softening than the respective matrices. It can be explained also with the stresses produced in the Widmanstätten

microstructure, but in this case, the stress is relieved by cracking or debonding of the particles. The phenomena can be explained by using the Figure 179, where a multiaxial tension system is represented. If we call:  $\sigma_I$  to the local stress,  $\sigma_P$  to the threshold compressive stress of the reinforcement, and  $\sigma_M$  to the threshold compressive stress of the matrix at the test temperature, then we have:

- At low temperatures of deformation  $\sigma_I$  is higher than  $\sigma_P$ , and the tensions relieve by breaking the particles (Figure 179a)) – the bigger the earlier –  $\sigma_I$  does not reach the  $\sigma_M$ , and no cracks in the matrix is then observed.
- At high compression temperatures  $\sigma_I$  is higher than  $\sigma_M$ , which in this case is very low (see the flow curves) and the tensions relieve by debonding of the particles, i.e. cracks in the matrix in the high stress concentration zones (Figure 179b)). As  $\sigma_I$  does not reach the  $\sigma_P$ , no cracks of the particles are observed.

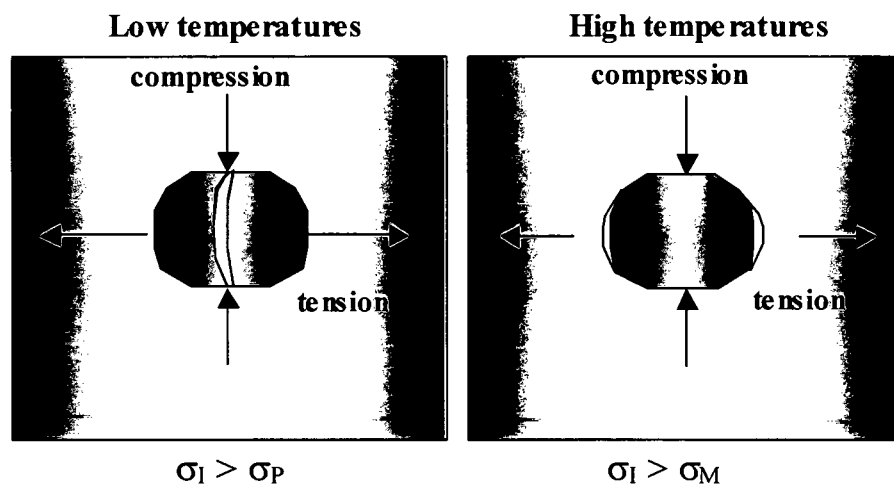


Figure 179. Stress situation for high and low temperatures.

- CermeTi<sup>®</sup>-C-12-662 composite

The kinetic study shows in Figure 180 a high correlation value for  $n$  at 650°C (14.4) in the whole strain rates range, i.e. a low  $m$  value related to low power dissipation values calculated using both DMM methods (Figure 152 and Figure 158).

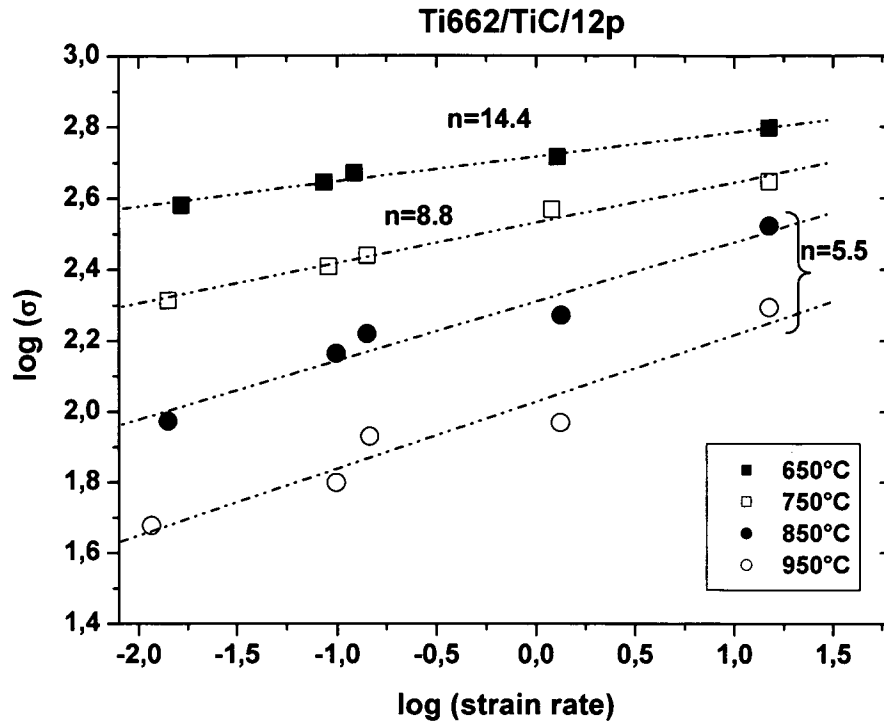


Figure 180. Variation of the flow stress at 0.3 strain with the strain rate to determine the stress exponent  $n$ .

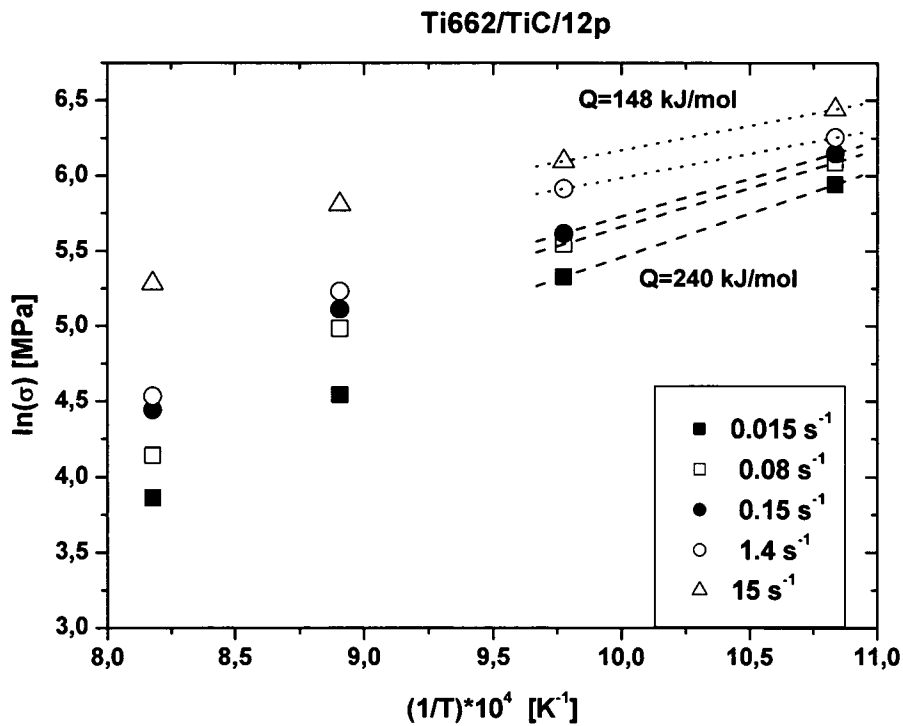


Figure 181. Apparent energy of activation between 850 and 950°C suggesting two different mechanisms of deformation

Figure 182 shows a good correlation for  $Z$ , with a  $n$  of about 5.2 for  $Q=240 \text{ kJ/mol}$ .



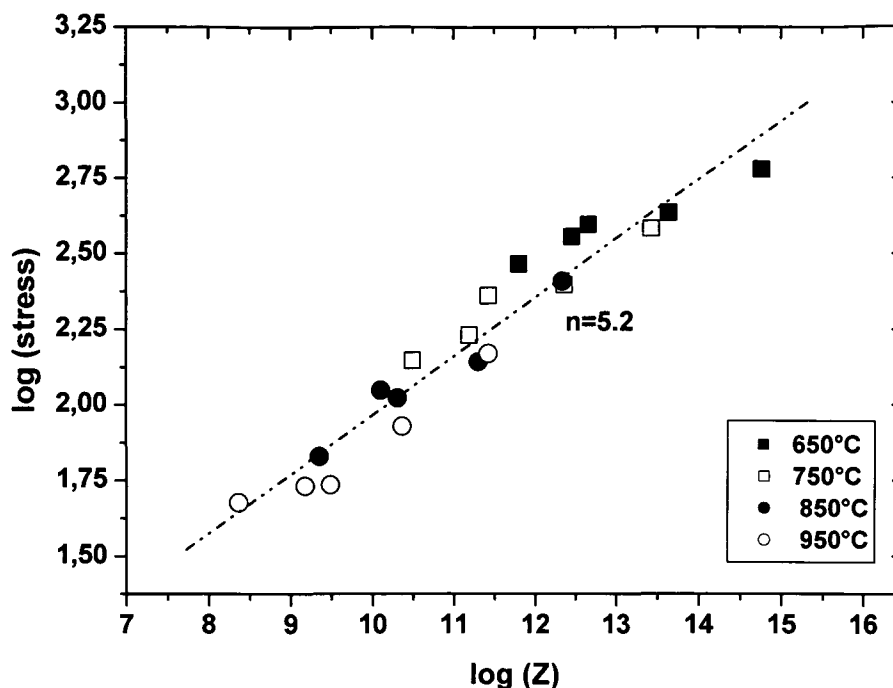


Figure 182. Recalculation of Z using  $Q=240$  kJ/mol

The prediction of instability done by the *modified DMM* (Figure 159) shows instability where cracking of the particles were observed (650-750°C). Furthermore, the dissipation of the energy at low temperatures is bad, and a registered increment of the temperature (Figure 120) of about 15-35°C results in flow instabilities. On the other hand, the *DMM* does not predict instability in the low temperature range, but only at high temperatures and high strain rates.

In the range of high temperatures and strain rates above  $5s^{-1}$ , high values of power dissipation were predicted (up to 56% at the highest strain rate), and it can be related to the recrystallisation of the beta phase, as observed in Figure 83, but also to the damage of the matrix produced after debonding of the particles.

The processing and stability maps (modified DMM) for true strains of 0.1, 0.2 and 0.3 are showed in Figure 183. The behaviour of the material is quite similar to the unreinforced Ti662: at high strain rates the  $\eta$  values increase gradually for all the temperatures with a stable flow (except at 675-775°C and  $\epsilon = 0.3$ ), indicating that the microstructural changes increases with the deformation up to instable breakage of the ceramic particles at low temperatures. The instabilities of the flow at low temperatures appear first at 0.3 strain, accompanied of higher values of  $\eta$ , suggesting that the cracks in the particles occur late during the deformation.

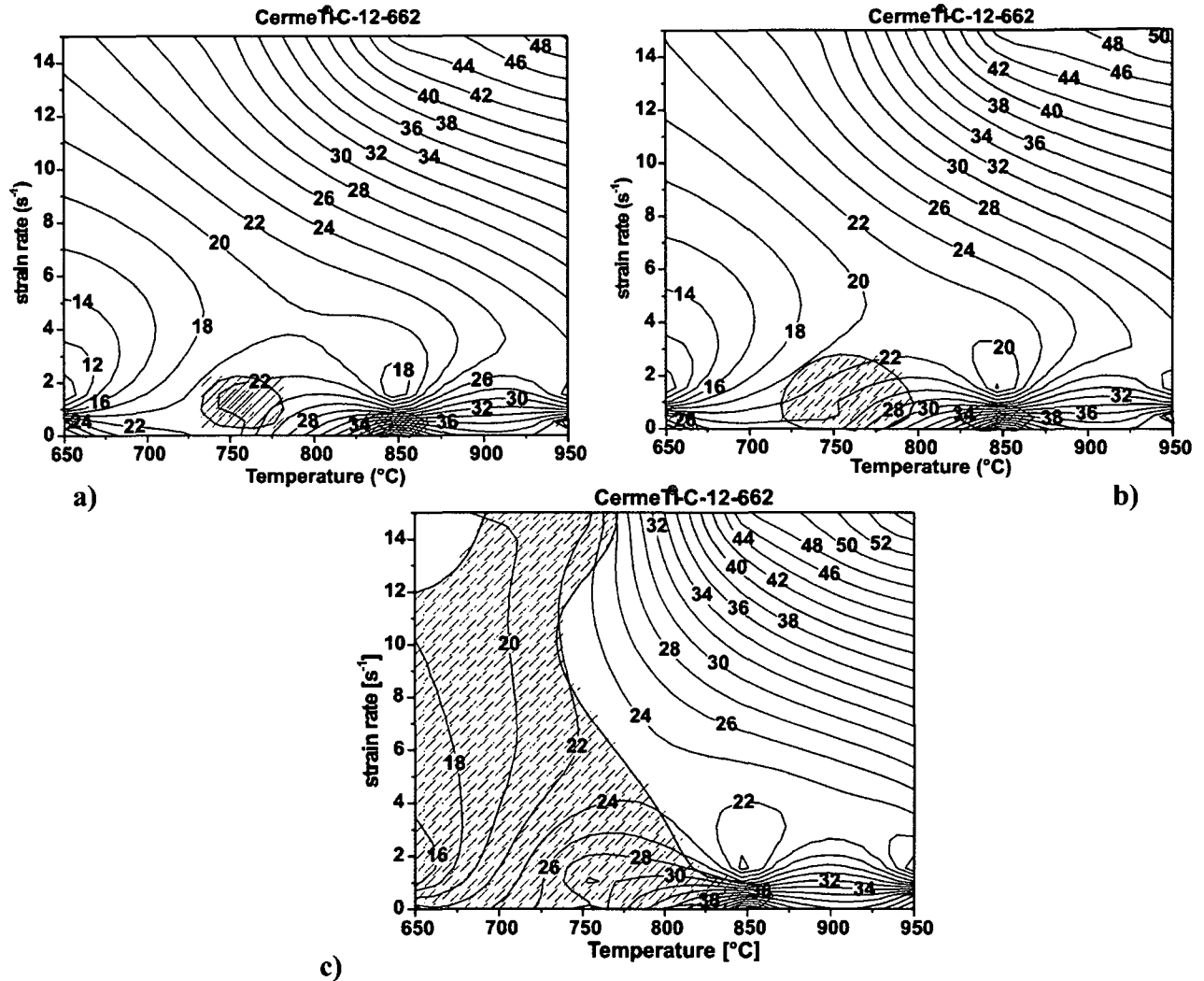


Figure 183. Processing maps and instability zones (dashed) calculated using the modified DMM at different true strains a)  $\epsilon = 0.1$ , b)  $\epsilon = 0.2$  and c)  $\epsilon = 0.3$  showing the evolution of the  $\eta$  and the  $g$  values.

#### - CermeTi<sup>®</sup>-C-20-662 composite

Compared to the composite reinforced with 12%vol of TiC particles, the CermeTi<sup>®</sup>-C-20-662 shows a slightly higher compression stress due to a higher production of dislocations and a more markedly softening due to the breakage of the particles.

Figure 184 shows that if the material is considered to behave linear, a high  $n$  value (that means low value of  $m$ ) at temperatures between 650 and 750°C can be observed, related also to the low values of energy dissipation calculated by the *modified DMM*. The negative values of  $\eta$  calculated using the *DMM* are unrealistic.

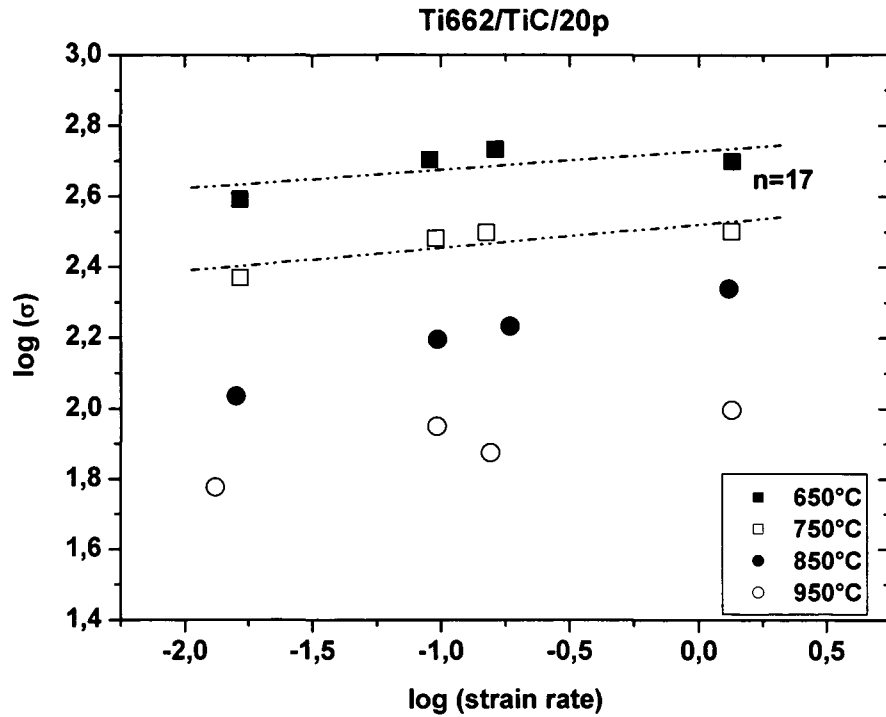


Figure 184. Variation of the flow stress at 0.3 strain with the strain rate

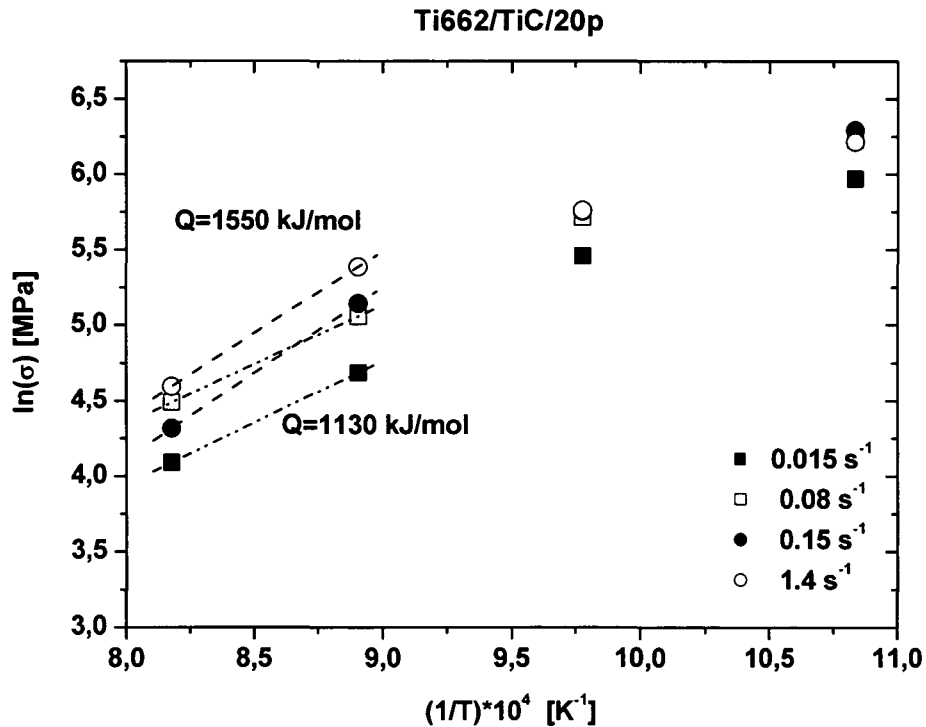


Figure 185. High activation energy predicted for 650-750°C.

A very high activation energy was found for low temperature deformation:  $Q$  approx 1130 kJ/mol at low strain rates (0.015-0.08 s<sup>-1</sup>), and  $Q$  approx 1550 kJ/mol at higher strain rates (0.15-1.4 s<sup>-1</sup>). The high activation energy has often been attributed to the existence of threshold stresses. In this

---

case, cracks not in the matrix but in the particles can be observed in the whole range of strain rates at low temperature.

*- Ti64/TiC/12p composite*

Again, the behaviour of this reinforced material is comparable to the Ti662/TiC/12p, with the most important difference in the matrix (alpha /beta content and beta transus temperature). In this case, it can be observed that the Ti64 reinforced is less ductile than the Ti662 reinforced also with 12%TiC particles. Furthermore, the maximum compressive stress is lower for the first alloy, and also the softening is less pronounced.

The relaxation of a part of the produced stresses during deformation is relieved by cracks in the beta phase. In the Ti64 there is less beta phase, and the cracks propagate through the ceramic particles.

#### **6.2.5 *Dynamic material model and modified DMM.***

The dynamic material model proposed by Prasad et al compares the behaviour of the material with that of a linear dissipator. Furthermore, it proposes also a method to determine the parameters of deformation that result in the instability of the flow. In this model the power law is considered to regulate the behaviour of the materials, even though  $\eta = m/(m+1)$  is dependent on the strain rate.

On the other hand, and using the same basic theory and criterion, Rao et al proposed the DMM modified to avoid this contradiction. Although the dissipation energy coefficient can be calculated by using both models without introducing important errors in monophase alloys, the instability calculations are erroneous if considering the power law.

Figure 165 shows that the tendency in the efficiency of power dissipation calculated using both models is more or less the same for all the materials, but the black zones calculated using the DMM represent zones where  $\eta$  is negative, what means the same as  $m$  is negative.

Finally, the zones of instability predicted by the modified DMM are more in accordance with the whole behaviour of the here studied materials.

#### **6.2.6 *Considerations for forging.***

From the studies done before, the parameters listed in Table 13 are suggested for forging:

**Table 13 parameters suggested for forging.**

Material	Parameters of Forging		Observations
	<i>strain rate (<math>s^{-1}</math>)</i>	<i>Temp (<math>^{\circ}C</math>)</i>	
<b><i>Ti662 Ingot</i></b>	Above $12s^{-1}$	650-800	Low dissipation of the energy
	Above $7s^{-1}$	900-950	High dissipation of the energy. DRX
<b><i>CermeTi<sup>®</sup>-C-662</i></b>	Above $8s^{-1}$	700-925	Above $2s^{-1}$ cracks
	Below $2s^{-1}$	900-950	
<b><i>CermeTi<sup>®</sup>-C-12-662</i></b>	Above $8s^{-1}$	800-950	Possibly debonding
	Below $2s^{-1}$	875-925	
<b><i>CermeTi<sup>®</sup>-C-20-662</i></b>	$0.2-0.8s^{-1}$	750-925	The forging produced a lot of cracks at the particles

The forging in an open die of the CermeTi<sup>®</sup>-C-20-662 is not recommended. The clusters of TiC particles results in the propagation of the cracks at low temperatures along the ceramic net, and the high percentage of ceramic results in an increment of the temperature that cannot be dissipated, resulting in low values of  $\eta$ .

Concerning to the Ti64 alloy reinforced with 15% vol of SiC particles, it is recommended to forge this material inside a titanium alloy ring at  $850^{\circ}C$  and a strain rate of  $1 s^{-1}$ . Of course, more tests should be carried out on this material.

As a general consideration for the metal matrix composites reinforced with ceramic, if the work-piece is forged inside a metal ring or in a close die, the tensile stresses perpendicular to the compression direction that break the ceramic particles can be decreased to increase the stability range.

Figure 186 shows a summary of the deformation mechanisms that occur at different strain rates and temperatures for all the Ti662 materials deformed up to 0.3 true plastic strain.

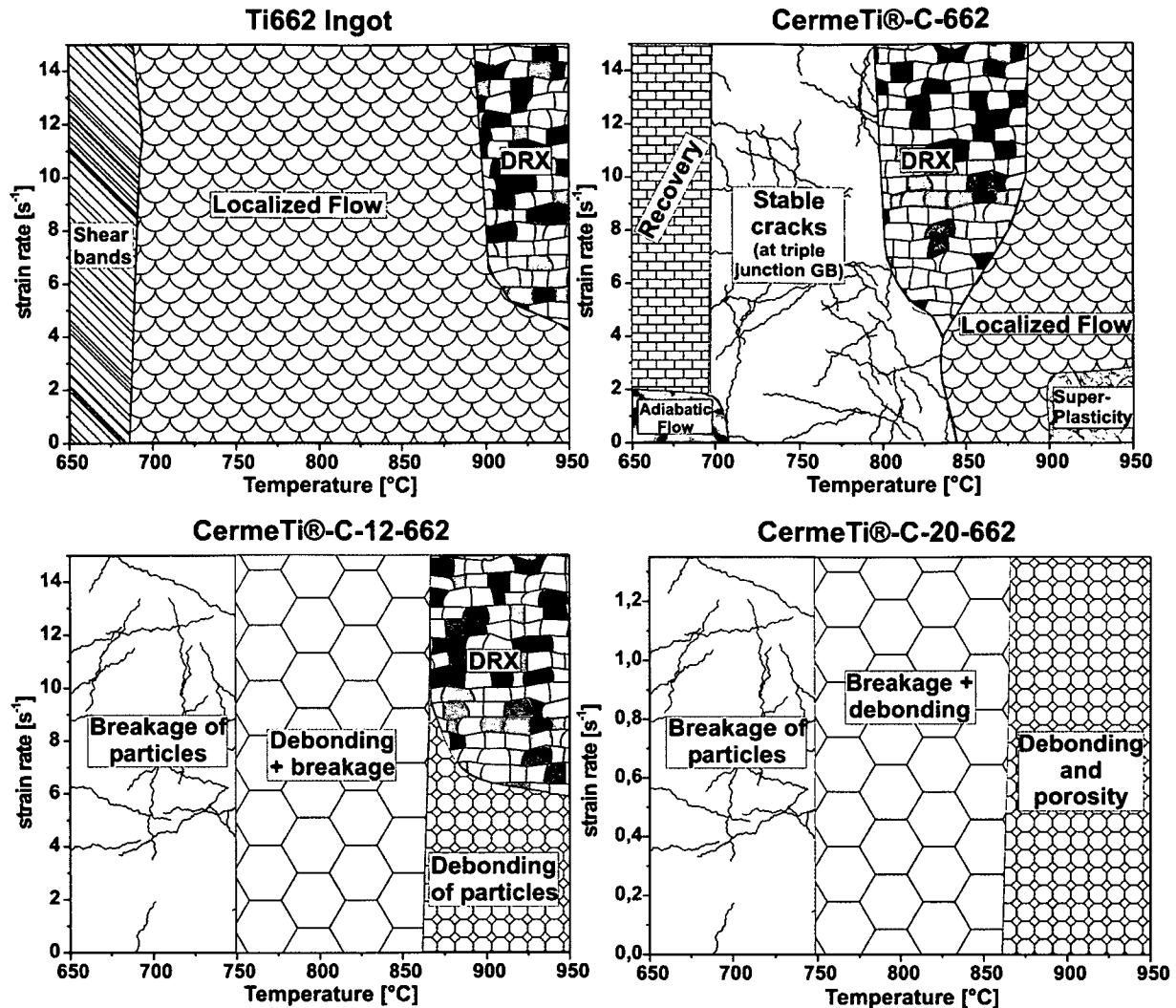


Figure 186. Deformation mechanisms depending on the temperature and the strain rate up to 0.3 strain for a) Ti662 Ingot b), Ti662 produced by PM c), Ti662 reinforced with 12% TiC and d) Ti662 reinforced with 20% of TiC.

## 6.3 Wear mechanisms.

### 6.3.1 Running-in state.

For the unreinforced material there are no important differences between the initial friction coefficient and this value in the steady state. The TiC reinforced alloy behaves differently depending on the parameters, but always presents higher values of friction coefficients than the unreinforced material due to the abrasive sliding mechanism.

The formation of iron oxides takes place in the running in state. The CermeTi®-C-20-662 produces scratches in the steel disc/ring at some pressures and sliding speeds. The removed material of the steel counterpart reacts with the oxygen of the atmosphere forming considerable

amounts of iron oxides, which does not occur with the unreinforced material. When this oxide remains between the two bodies, it will act as a lubricant, and the steady state coefficient of friction will decrease. If the pressure or the speed is high enough to remove the oxide layer, then the coefficient of friction will remain high. This running-in state would occur only the first time, and the peak of coefficient of friction should be taken account for design.

### 6.3.2 Steady state

During the steady-state the iron oxide layer can act as a lubricant, but also may break and disappear. At low sliding speeds and low pressures the iron oxides remains (Figure 130). The contact is in this case not any more between the two materials, but between each material and the iron oxide in between (Figure 187a). Due to the low hardness of the oxides the friction coefficient decreases.

If the oxide layer breaks and disappears due to the high pressure and/or sliding speed (Figure 187b)), the friction coefficient will be as high as in the running – in state, and will agree with the values that correspond to the governing wear mechanism: adhesive for the unreinforced alloy, and abrasive for the reinforced material.

Finally, the reinforced material can loose the particles due to the high friction coefficient values reached, and, in this case, the wear rate increases abruptly.

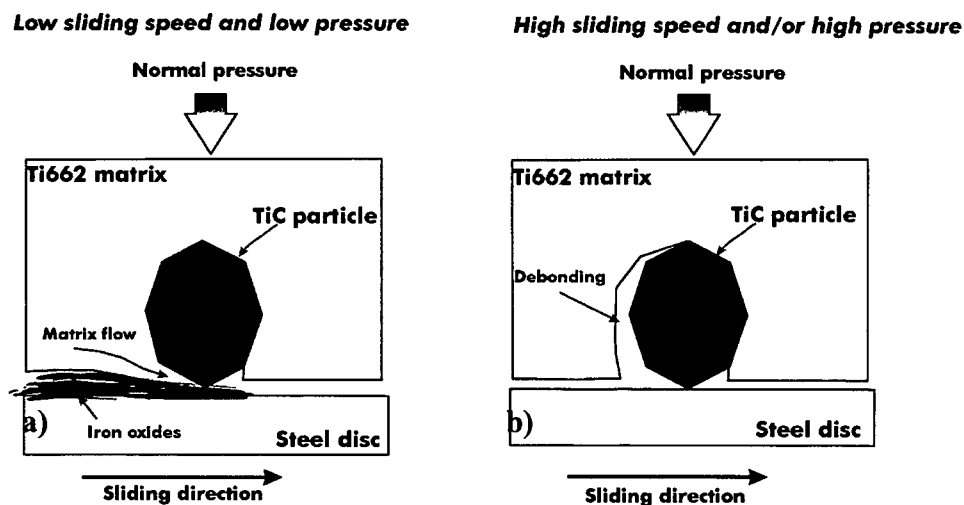


Figure 187. Wear mechanisms of the Ti662 reinforced with TiC particles (a) at low sliding speeds and low pressures, and (b) at high sliding speed and/or high normal pressure.

### 6.3.3 Wear behaviour.

Figure 188 and Figure 189 show schematic wear behaviour maps with the different friction and wear mechanisms. For the Ti662, (Figure 188) the main wear mechanism is the adhesive wear.

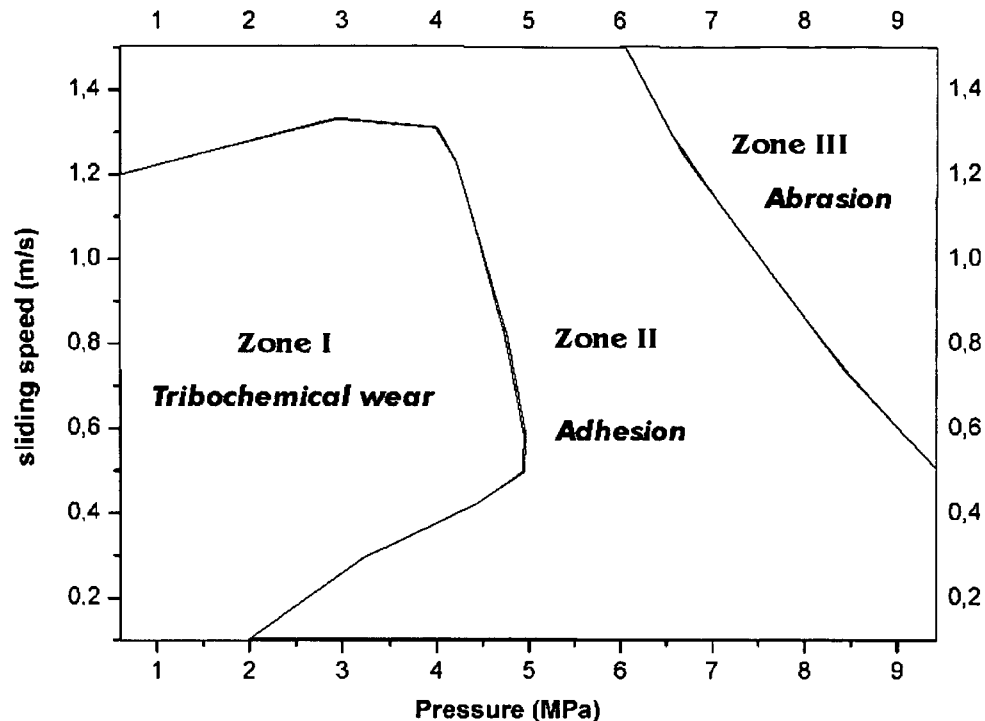


Figure 188. Wear mechanisms for the unreinforced Ti662.

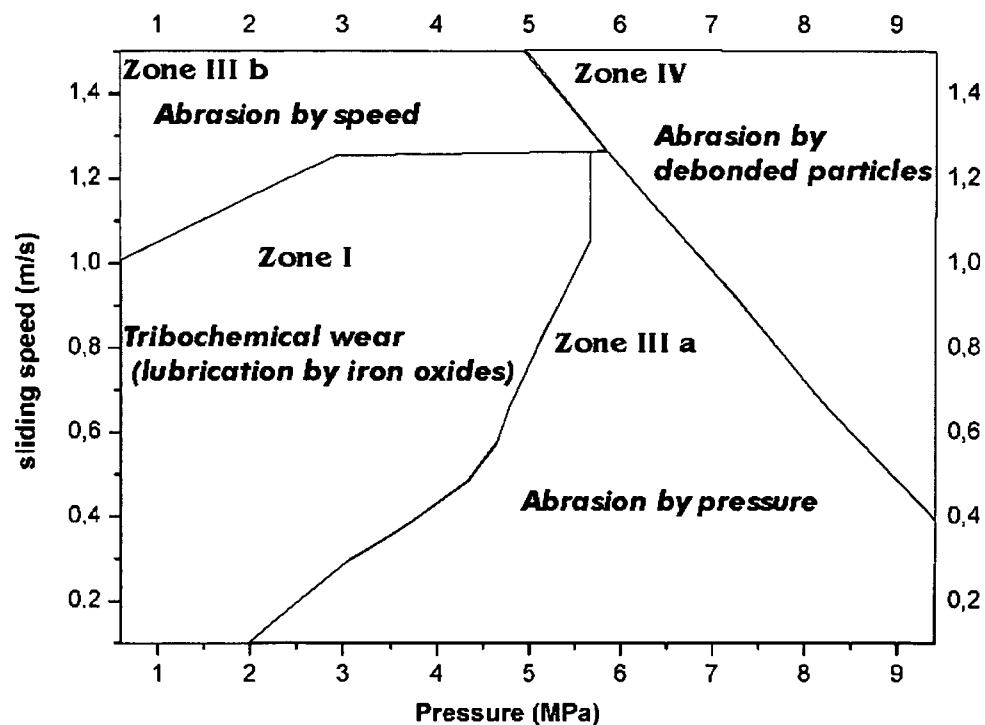


Figure 189. Wear resistance mechanisms for the Ti662 reinforced with 20%vol TiC particles.



For the reinforced material (Figure 189), four zones are distinguished: in zone I, oxidative wear is the most important mechanism. The lubrication by iron oxides results in low wear rates and low noise levels. Zone IV presents debonding of the particles due to the high sliding speeds that break the iron oxide layer and increase the friction. Zone II presents also debonding of the particles, but now the high pressure breaks the oxide layer. In zone III the wear, friction coefficient and noise reach unacceptable values.

#### 6.3.4 Interface damage.

The SiC reinforced composite show low friction coefficient and high wear rate at very low sliding speed and high pressure. The low friction coefficient could be due to the high amount of oxides formed, but debonding of the particles happens (the original interface reaction layer is very brittle), and high wear rate [122].

Figure 190 shows schematically the rupture of the brittle interface reaction zone, the formation of the oxides and the particle before debonding.

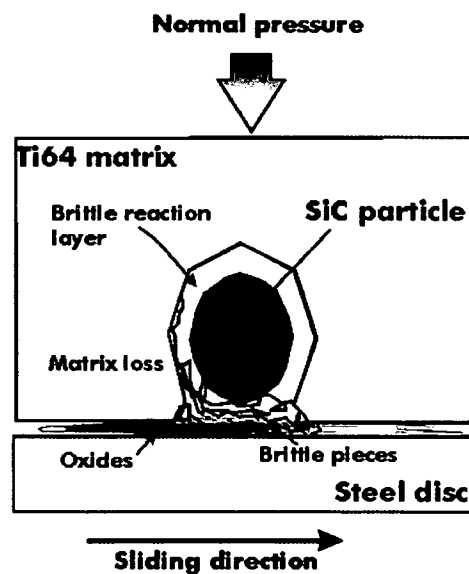


Figure 190. Wear mechanism of the SiC reinforced Ti64, showing the disintegration of the brittle particle interface reaction layer.

#### 6.3.5 TiC influence.

One of the motives for reinforcing a metal matrix with poor tribological properties with ceramic particles is to improve these properties.

As comparing the coefficient of friction results of the matrix and the Ti662 reinforced composite it can be seen that the values do not differ too much. But the values of the composite are more

---

homogeneous than those of the matrix by varying the wear parameters. This characteristic permits the use of the reinforced material for designs where the requirement of constant friction coefficient in a wide range of sliding speed and normal pressure is desired, for example for slowly moving levers or axis, but may be even for breaks.

On the other hand, the wear resistance of the Ti662 in the tested conditions does not improve while reinforcing with TiC particles. The reason of this seems to be the bad distribution of the ceramic particles that results in vast zones without particles that, in contact with another surface behaves like the matrix. In this way, the material can be thought as a net formed by MMC reinforced with 50% of TiC particles locally and the matrix with 0% of TiC particles

#### **6.4 Young's modulus.**

For the unreinforced alloy, it is important to remember that the Young's modulus is not only dependent on the temperature, but also on the texture of the alpha phase. The powder metallurgy material does not present texture, but the ingot material has the alpha grains oriented due to the cogging direction. As found for pure titanium Figure 191a), the Young's modulus is higher if the angle  $\Phi$  is 0 degrees with respect to the c-axis for a mono-crystal. For polycrystalline material without texture, a Young Modulus of 120 GPa is expected.

The preferred orientation of the alpha crystals in a alpha-beta alloys after deformation (such as rolling, cogging, etc.) is dependent on the alpha- beta alloying elements. In the case of the Ti662, the texture is in the direction showed in Figure 191b) (for rolled samples with 15% of beta content [24]), also confirmed by the pole figures (Figure 97).

The slightly higher values of Young's modulus found for the transversal sample (Figure 112) can be explained by the preferred orientation of the alpha phase with an angle  $\Phi$  smaller than 45°.

On the other hand, the values of the composites were up to 12% higher than expected with the rule of mixtures. If there is some diffusion of the C from the particles into the matrix, as suggests the results of the diffractometry (TiC poor in C), it acts as interstitial alloying element. As reported in previous works [24], it has been found that interstitial and substitutional alpha-stabilizing solutes slightly increase the modulus. The high values of Young's modulus of the composites can be attributed to the good bonding between the particles and the matrix, as shows the Halpin and Tsai model results.

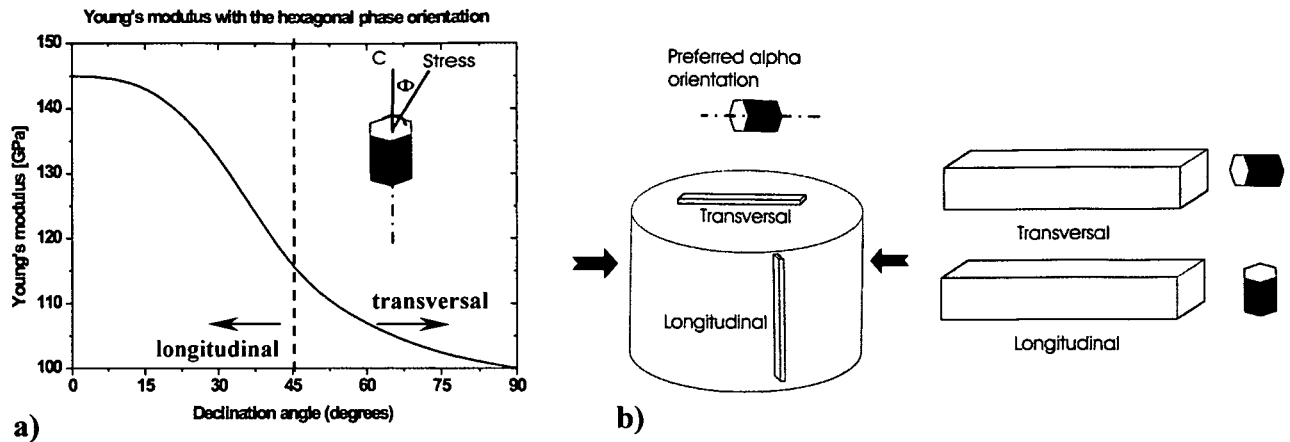


Figure 191. a) Young's modulus as a function of the alpha phase orientation [24] b) Preferred orientation of the alpha crystals in the sample during measurement of the Young's modulus

## 6.5 Alpha beta transformations.

The  $\alpha + \beta \rightarrow \beta$  and  $\alpha \rightarrow \beta$  transformation of the matrices and the composites were studied in this work by metallography, dilatometry and diffractometry.

The most important facts are:

- The transformation of the titanium alloyed with vanadium requires a minimal thermal activation for the diffusion of the vanadium into the alpha phase in order to transform it into a beta phase. This phenomena occurs at approximately 600°C, and it can be observed in the changes of the thermal expansion (Figure 143) due to an expansion in the beta phase provoked by the decrement of the vanadium content in the bcc cell.
- At the beginning, the diffusion is fast, although the temperature is not so high because of the large gradient of V (approx 28% in the beta phase and only 2% in the alpha phase) and because of the large specific surface. At this moment, the alpha phase is supersaturated in vanadium and transforms continuously into beta.
- By increasing the temperature, the specific alpha surface decreases by the consumption of the smaller alpha phase (see Figure 51) and the self-diffusion of the beta phase increases to homogenize the V distribution within the phases.
- By increasing the temperature, the beta transformation increases rapidly, as observed in the metallographic study (Figure 94), while the whole material decreases its volume (Figure 143) provoked by the phase transformation from the alpha phase to a denser beta phase.
- At the final beta transus temperature, the vanadium reaches an equilibrium concentration (4% in the case of Ti64, and 6% for Ti662).

- 
- In the beta phase the grains built new grain boundaries and grow, as can be observed in the micrographs after heat treatments above the beta transus temperature (Figure 92). This effect is also clear if comparing the maximum compression stress of a sample heat-treated in the alpha + beta field with a sample compressed after 1 hour of heat treatment in the beta field.

The compressive stress of the second sample is markedly lower than that of the first one.

The particles seem to have no effect up to the beta transus temperature. Although the beta transus temperature could not be determined by using dilatometry, the unreinforced samples deformed at 950°C and quenched show a higher content of beta phase than the composites (Figure 72 compared Figure 76). This could be due to the alpha stabilization provoked by the dissolved C. Finally, the particles avoid the grain growth of the beta phase.

## **6.6 Trials on the production of a new material**

The reinforcing of titanium alloys with ceramic particles is attractive in order to increase the strength, the stiffness and the wear resistance. The misfit in Young's modulus and CTE between SiC particles and the titanium alloys is larger than that between the TiC particle and the titanium alloys. Furthermore, SiC is lighter than TiC, but the high reactivity between SiC and Ti produces degrading interface reaction products. The reaction between SiC and titanium can be decreased by decreasing the time and/or the temperature of consolidation.

A method of powder metallurgy developed in USA called electric Field Assisted Sintering (FAST) reduces considerably the time of consolidation. In [123], Zavaliangos et al determined that the specific feature of FAST is the application of a pulsed electrical discharge to conventional strength of the oxide layer, using the mechanisms of electrical resistive sintering under pressure. This field activation enables sintering to higher densities in shorter times or at lower temperatures than conventional sintering. The activated sintering process has been shown for a large variety of powders. The engineering benefits of FAST densification relate to short processing time, no need for additives, prior cold compaction or controlled atmospheres. Actually it is used nowadays mainly to produce nanomaterials, avoiding the coarsening of the nanopowders [124, 125].

Another method called equal channel angular pressing (ECAP) have been developed in the last few years to obtain submicrometer grain structures in ductile alloys by imposing high levels of strains. But also some new projects [Bratislava] are concentrated in consolidation of powders for producing metal matrix composites at low temperatures of consolidation.

## 7 Conclusions.

The compression tests carried out by preheating the sample in furnace and deformed using the SERVOTEST machine results in an uniform deformation due to the homogeneous temperature and the possibility of using glass for high temperatures as lubricant. On the other hand, the control of the temperature and the non-linear strain rate can provoke some errors in the flow curves. The use of a Gleeble ® 1500 machine allows the control of the temperature and the strain rate at constant values during the deformation at the point of measurement of the transversal strain. Due to the bad thermal conductivity of the Titanium alloys, the contact with the cold anvils and the impossibility of using glass lubricant, there is a gradient of temperature and friction which results in a non uniform deformation (axial stress components) which finally results in a gradient of local stresses and strains.

The deformation behaviours of all the tested materials during hot compression are good represented with the modified Dynamic Mechanical Model. The best parameters for forging the Ti662 alloys (ingot and PM) and the composites are at high temperatures and strain rate. The composites are suggested to be only slightly deformed (to obtain the final shape of a piece) and at temperatures above 900°C. To avoid the axial tensions, it is also recommended the deformation in a closed die or inside a titanium ring.

The deformation of the globular microstructure results in high stress values due to the fine grain structure and in homogeneities (localized flow) due to the oriented alpha grains. The lamellar microstructure cracks at the triple junction grain boundaries where the maximum concentration of stresses occurs. In the case of the composite reinforced with 12% of TiC particles, this maximum stress concentration relaxes by particles breakage at low temperatures and by debonding at high temperatures. Furthermore, the Ti662 alloy is more easily deformed than the well-known Ti64 due to the lower content of alpha phase, resulting in lower required stress values.

The addition of the TiC particles improves markedly some mechanical properties. The good bonding between the particles and the matrix, the absence of secondary reactive brittle products, the diffusion of the C into the matrix from the particles to form an alloy rich in this interstitial element and the high elastic modulus of the particles results in these improvements. The Young's modulus, an important property when light weight rigid parts are required, is 13% and 23% higher than the matrix by reinforcing with 12 and 20% of particles at room temperature and much better by increasing the temperature, up to 16 and 25% higher than the matrix value at 350°C by

reinforcing with 12 and 20% of ceramic particles respectively. Furthermore, the strength values are much higher than those of the matrix, and the percentage of increment respect to the alloy increases markedly at temperatures near the beta transus, where the C solubility is higher.

The poor tribological properties of the titanium alloys are not strongly improved by the addition of the TiC particles. The main reason seems to be the bad distribution of the TiC particles that results in a material with large unreinforced zones, which behaves like titanium alloy. There is a slightly improvement of the wear resistance in the composite at low pressures, and the fact that the coefficient of friction of this material is more or less constant in the whole range of tested pressures and temperatures allowing this material for uses where these parameters change abruptly and homogeneity in the coefficient of friction values are required. Furthermore, if the wear partner is different from iron, the formation of Fe-oxides at low-normal pressures would not form a lubricant, then the wear results might be different.

The dilatometry applied to the titanium alloys at high temperatures to study the  $\alpha \rightarrow \beta$  and  $\alpha + \beta \rightarrow \beta$  transformations is possible, showing a range of temperatures from the V diffusion (600°C) up to the beta transus temperature where the volume changes. But some technical problems such as the reaction with the holders at very high temperatures should be solved. On the other hand, the material reinforced with TiC particles shows slightly lower CTE values than the matrix only near the beta transus temperature. This shows that the internal stresses induced by the difference of the CTE of the particles and the matrix is very low, suggesting other strengthening mechanisms of the material by the addition of TiC particles.

Finally, if a consolidation of Ti-alloy powder with SiC powder could be achieved without or with a fine interface layer, the recommended high forging temperatures may cause further reaction. Furthermore, the heat treatment possibilities would be limited and the application temperatures would remain low for high exposure times. Protection coating of the SiC particles would be an alternative, as seen in chapter 2 for the SiC monofilaments.

## 8 References.

- [1] Luo Guozhen, Zhen Quanpu and Deng Ju. Titanium '95. III, 2704. 1995.
- [2] M. Peters, C. Leyens: Titan und Titanlegierungen, Wiley VCH, Weinheim **2002**.
- [3] D.E. Alman, J.A. Hawk. Wear. 225-229.629 **1999**.
- [4] M. Ashby. Materials Selection in Mechanical Design. 2<sup>nd</sup> Edition. Ed. Butterworth-Heinemann. **2000**.
- [5] CES Selector Version 4,0 software, Granta Design, Cambridge **2002**.
- [6] Radhaskirshna B. Bhat, Seshacharyulu Tamirisakandala, Dale J. McEldowney, Daniel B. Miracle. *In press*. **2003**.
- [7] C.Poletti, W. Marketz, H.P Degischer. Ti-2003 Science and Technology. Vol IV. 2531-2538. **2003**.
- [8] S.C. Tjong, Z.Y. Ma. Materials Science and Engineering, 29. 49-113. **2000**.
- [9] Light Alloys. Metallurgy of the light metals. Au. I. J. Polmear. Ed. Halsted Press. Third edition. **1995**.
- [10] N.J. Welham. Minerals Engineering, Vol. 9, No. 12, pp. 1189-1200, **1996**.
- [11] R. M. Kelly, N. A. Rowson. Minerals Engineering, Vol 8, No. 11, pp. 1427-1438, **1995**.
- [12].Titanium. Engineering materials and processes. Gerd Lütjering and James Williams. Springer Editorial. **2003**.
- [13]. K. H. Rendigs. Proceedings of the Ti-2003 Science and Technology. Vol 4. 2659-2666. **2003**.
- [14] James C. Williams, Edgar A. Starke, Jr. Acta Materialia 51. 5775–5799. **2003**.
- [15]F.H. Froes , B. Trindade. Journal of Materials Processing Technology 153–154. 472–475. **2004**.
- [16] V.M. Anokhin, O.M. Ivasishin, A.N. Petrunko. Materials Science and Engineering. A243 269–272. **1998**.
- [17] A Choudhury, M Blum. Vacuum. Vol. 47. Iss. 6-8. 829 – 8311. **1996**.
- [18].Takao Hanawa. Science and Technology of Advanced Materials 3. 289–295. **2002**.
- [19] Mitsuo Niinomi. Materials Science and Engineering A243. 231–236. **1998**.
- [20] S. Niyomsoan, W. Grant, D.L. Olson, B. Mishra. Thin Solid Films 415. 187–194. **2002**.
- [21] Phase Diagrams of binary Titanium Alloys. ASM International. **1987**.
- [22] W. Szkliniarz and G. Smolka. Journal of Materials Processing Technology 53. 413-422. **1995**.
- [23] G. G. E. Seward, S. Celotto. D. J. Prio, J. Wheeler and R. C. Pond. Acta Materiala 52. 821-832. **2004**.
- [24]. Material Properties Handbook. Titanium Alloys (Eds.: R. Boyer, G Welsch, E.W. Collings). USA, **1994**.
- [25] Z. Ignjatov. Master Thesis. TuWien. **2005**.
- [26] G. E. Kiourtsidis, S. M. Skolianos, G. A. Litsardakis. Materials Science and Engineering A Vol. 382. 351–361. **2004**.
- [27] I. Bobic, M.T. Jovanovic, N. Ilic. Materials Letters Vol. 57. 1683– 1688. **2003**.

- [28] C. Tekmen, I. Ozdemir, U. Cocen, K. Onel. *Materials Science and Engineering A* 360 365-371. **2003**.
- [29] R. Mitra, V.S. Chalapathi Rao, R. Maiti, M. Chakraborty. *Materials Science and Engineering A* 379. 391–400. **2004**.
- [30] Feng Wang, T. Huimin Liu, Bin Yang. *Materials Characterization* 54. 446–450. **2005**.
- [31] C. Srinivasa Rao and G. S. Upadhyaya. *PII:SO261-3069*. 00015-5. **1996**.
- [32] J.B. Fogagnolo, F. Velasco, M.H. Robert, J.M. Torralba. *Materials Science and Engineering A* 342. 131-143. **2003**.
- [33] M. Adamiaka, J.B. Fogagnolo, E.M. Ruiz-Navas, L.A. Dobrzański, J.M. Torralba. *Journal of Materials Processing Technology* 155–156. 2002–2006. **2004**.
- [34] Alan C.F. Cocks. *Progress in Materials Science* 46. 201-229. **2001**.
- [35] E.A. Oliber, E.R. Benavidez, G. Requena, J.E. Fiscina, C.J.R. González Oliver. *Physica C* 384. 247–257. **2003**.
- [36] R. Sepúlveda, F. Arenas. *International Journal of Refractory Metals and Hard Metals* 19. 389-396. **2001**.
- [37] W. S. Coblenz, J. M. Dynys, R. M. Cannon and R. L. Coble. *Materials Science Research* 13. 141-157. **1980**.
- [38] M.C. Poletti, E.A. Oliber, J.E. Fiscina, L.F. García, J. Vivas Hohl, D.A. Esparza, C.J.R. González Oliver. *Jornadas SAM 2000 - IV Coloquio Latinoamericano de Fractura y Fatiga*, 1065-1072. **2000**.
- [39] G. O'Donnell, L. Looney. *Materials Science and Engineering A* 303. 292–301. **2001**.
- [40] A. Olszówka-Myalska, J. Szala, J. Cwajna. *Materials Characterization* 46. 189–195. **2001**.
- [41] Zhiwu Xu, Jiuchun Yan, Weiwei Zhao, Huibin Xu, Shiqin Yang. *Composites Science and Technology*. *In Press*. **2005**.
- [42] R. Leucht and H. J. Dudek. *Materials Science and Engineering A*. Vol 188, Iss 1-2. 201-210. **1994**.
- [43] J.C. Halpin and S.W. Tsai. *Environmental Factors in composite design*, Air Force Materials Laboratory, AFML-TR-67-423.
- [44] T.W. Clyne and P.J. Whithers. *An Introduction to Metal Matrix Composites*. Cambridge University Press. **1993**.
- [45] A. Roatta, R. E. Bolmaro. *Materials Science and Engineering A* 229. 182-191. **1997**.
- [46] A. Roatta, P.A. Turner, M.A. Bertinetti, R. E. Bolmaro. *Materials Science and Engineering A* 229. 203-218. **1997**.
- [47] W. S. Miller and F. J. Humphreys. *Scripta Metallurgica et Materialia*. Vol 25, Iss 1. 33-38. **1991**.
- [48] Tariq A. Khraishi, Lincan Yan, Yu-Lin Shen. *International Journal of Plasticity* 20. 1039–1057. **2004**.
- [49] R. A. Shatwell. *Materials Science and Engineering A*. Vol. 259. Iss.2. 162-170. **1999**.
- [50] P. Mogilevsky, A. Werner, H.J. Dudek. *Materials Science and Engineering A* Vol. 242. Iss. 1-2. 235-247. **1998**.



- [51] J. Shyue, W.O. Soboyejo, H.L. Fraser. *Scripta Metallurgica et Materialia*. Vol. 32. Iss. 10. 1695-1700. **1995**.
- [52] C. Leyens, F. Kocian, J. Hausmann, W. A. Kaysser. *Aerospace Science and Technology* 7. 201–210. **2003**.
- [53] Y.J. Kim, H. Chung, S.J.L. Kang. *Materials Science and Engineering A*. Vol 333, Iss 1-2. 343-350. **2002**.
- [54] Z.D. Cui, S.L. Zhu, H.C. Man, X.J. Yang. *Surface & Coatings Technology* 190. 309–313. **2005**.
- [55] P.B. Joshi, G.R. Marathe, N.S.S. Murti, V.K. Kaushik, P. Ramakrishnan. *Materials Letters* 56. 322–328. **2002**.
- [56] M.S. Selamat, L.M. Watson, T.N. Baker. *Journal of Materials Processing Technology* 142. 725–737. **2003**.
- [57] T. Furuta, T. Yamaguchi, Y. Shibata, T. Saito. *Titanium '99. Proceedings of the ninth world conference of titanium*. Pgs. 1917-1924. **1999**.
- [58] T.M.T. Godfrey, P.S. Goodwin, C.M. Ward-Close. *Titanium '99. Proceedings of the ninth world conference of titanium*. Pages 1868-1877. **1999**.
- [59] J. Lapin, L. Ondrus, O. Bajana. *Materials Science and Engineering A360*. 85-95. **2003**.
- [60] V. de Castro, T. Leguey, A. Muñoz, M.A. Monge, R. Pareja. *Materials Science and Engineering A*. *In press*. **2005**.
- [61] Ke Geng, Weijie Lu, Zhifeng Yang, Di Zhang. *Materials Letters* 57. 4054–4057. **2003**.
- [62] E. Zhanga, S. Zenga, B. Wang. *Journal of Materials Processing Technology* 125–126. 103–109. **2002**.
- [63] T.W. Clyne, H.M. Flower. *Titanium '92. Science and Technology*. 2467-2478. **1993**.
- [64] B.V. Radhakrishna Bhat 1, J. Subramanyam, V.V. Bhanu Prasad. *Materials Science and Engineering A325*. 126–130. **2002**.
- [65] M. Bram, F. Aubertin, J. Breme, *Titanium '99. Proceedings of the ninth world conference of titanium*, 1882-1889. **1999**.
- [66] Liang Zhenfeng, Li Diqian, Luo Kai. *Titanium '99. Proceedings of the ninth world conference of titanium*. 1890-1895. **1999**.
- [67] B. J. Kooi, M. Kabel, A.B. Kloosterman, J. Th. M. De Hosson. *Acta Materialia*. Vol 47. 3105-3116. **1999**.
- [68] W. Tong, G. Ravichandran, T. Christman and T. Vreeland Jr. *Acta metall, mater*. Vol. 43, No. 1. 235-250. **1995**.
- [69] S. Gorsse, Y. Le Petitcorps. *Composites Part A*. Vol 29A. 1221 – 1227. **1998**.
- [70] R. A. Shatwell. *Materials Science and Engineering A*. Vol 259. 162-170. **1999**.

- [71] P. Mogilevsky, A. Werner, H. J. Dudek. Materials Science and Engineering A. Vol 242. Iss 1-2. 235-247. **1998**.
- [72] J. M. Quenisset, J. F. Fromentin, Y. Le Peticorps, K. Debray, E. Martin. Composites Science and Technology. Vol 56. Iss 7. 767-775. **1996**.
- [73] G. Requena, D. Telfser, C. Hörist, H. P. Degischer. Materials Science and Technology, 18. 515. **2002**.
- [74] A.J. Wagoner Johnson, K.S. Kumar, C.L. Briant. Metallurgical and Materials Transactions A. Vol 34A. 1869-1877. **2003**.
- [75] C. Badini, G. Ubertalli, D. Puppo, P. Fino. Journal of Material Science 35. 3903-3912. **2000**.
- [76] Zhang Erlin, Zeng Songyan, Zhu Zhaojun . Journal of Materials Science. Vol 35. 5989-5994. **2000**.
- [77] S.V.S. Narayana Murty, B. Nageswara Rao, B.P. Kashyap. Journal of Processing Technology. *In press* . **2004**.
- [78] C. Gandhi and M. F. Ashby. Acta Metallurgica. Vol 27. 1565-1602. **1979**.
- [79] R. Raj. Metall. Trans. A. ; 12A(6): 1089-1097. **1981**.
- [80] G. Ganesan , K. Raghukandan, R. Karthikeyan and B. C. Pai. Materials Science and Engineering A. Vol. 369, Iss. 1-2. 230-235. **2004**.
- [81] B. S. L. Semiatin, V. Seetharaman and A. K. Ghosh. Phil. Trans. Royal Society Lond. A. 357, 1487-1512. **1999**.
- [82] Prasad,-Y.-V.-R.-K.; Gegel,-H.-L.; Doraivelu,-S.-M.; Malas,-J.-C.; Morgan,-J.-T.; Lark,-K.-A.; Barker,-D.-R. Metall. Trans. A. 15 A (10): 1883-1892. **1984**
- [83] S.V.S. Narayana Murty and B. Nageswara Rao. Journal of Materials Science Letters 17. 1203-1205. **1998**.
- [84] Hans Ziegler. Ed: E. Becker, B. Budiansky, H.A. Lauwerier and T. Koiter. An Introduction to thermomechanics. North-Holland Publishing Company. 2<sup>nd</sup> Ed. **1983**.
- [85] P. Cavalliere, E. Cerri, P. Leo. *In press* in Composite Science and Technology.
- [86] H. Ziegler. Some Extremum Progress in solid mechanics. Chapter II. Vol 4. **1963**.
- [87] S.V.S. Narayana Murty a, B. Nageswara Rao Materials Science and Engineering A254. 76–82. **1998**.
- [88] S.V.S. Narayana Murty, B. Nageswara Rao, B.P. Kashyap. Composites Science and Technology 63 119–135. **2003**.
- [89] S.V.S. Narayana Murty and B. Nageswara Rao. Journal of Materials Processing Technology 104. 103-109. **2000**.
- [90] S. Spigarelli, E. Cerri, P. Cavaliere and E. Evangelista. Materials Science and Engineering A. Vol. 327, Iss. 2 144-154. **2002**.
- [91] T. Seshacharyulu, S.C. Medeiros, W.G. Frazier, Y.V.R.K. Prasad. Materials Science and Engineering A284. 184-194. **2000**.

- [92] Nho-Kwang Park, Jong-Taek Yeom and Young-Sang Na. Journal of Materials Processing Technology. Vol. 130-131. 540-545. **2002**.
- [93] T. Seshacharyulu, S.C. Medeiros, W.G. Frazier, Y.V.R.K. Prasad. Materials Science and Engineering A.325. 112-125. **2002**.
- [94] Y.V.R.K. Prasad, T. Seshacharyulu. Materials Science and Engineering A243. 82-88. **1998**.
- [95] R.M. Miller, T.R. Bieler and S.L. Semiatin. Scripta Materialia, Vol. 40, No. 12, pp. 1387–1393, **1999**.
- [96] T. R. Bieler, S.L. Semiatin. International Journal of Plasticity 18. 1165–1189. **2002**.
- [97] T. Seshacharyulu, S.C. Medeiros, W.G. Frazier, Y.V.R.K. Prasad. Materials Letters. 47. 133-139. **2001**.
- [98] L.Y. Zeng, Y.Q. Zhao, P.S. Zhang, L. Zhou, A. Vassel. Proceeding of the Titanium International Congress 2003. 2609-2613. **2003**.
- [99] S. Gorsse, D.B. Miracle. Acta Materialia 51 2427–2442. **2003**.
- [100] Ke Geng , Weijie Lu , Di Zhang, Taokao Sakata , Hirotaro Mori. Materials and Design 24 409–414. **2003**.
- [101] P. Wanjara, R.A.L. Drew, J. Root, S. Yue. Acta Materialia 48. 1443-1450. **2000**.
- [102] C. Ouchi, H. Iizumi, S. Mitao. Materials Science and Engineering A243. 186-195. **1998**.
- [103] S.L. Soo, D.K. Aspinwall, R.C. Dewes. Journal of Materials Processing Technology 150. 116–123. **2004**.
- [104] K.P. Rao, Y.K.D.V. Prasad, E.B. Hawbolt. Journal of Materials Processing Technology 56. 897-907. **1996**.
- [105] N.E. Glover, C.L. Davis Scripta Materialia, Vol. 34, No. 5, pp. 675-684. **1996**.
- [106] Seung Chan Hong, Sung Hwan Lim, Hyun Seon Hong, Kyung Jong Lee, Dong Hyuk Shin, Kyung Sub Lee. Materials Science and Engineering A355. 241-248. **2003**.
- [107] H. Zhang, G.Y. Lin b, D.S. Peng, L.B. Yang, Q.Q. Lin. Journal of Materials Processing Technology 148. 245–249. **2004**.
- [108] L.X. Li, D.S. Peng, J.A. Liu, Z.Q. Liu, Y. Jiang. Journal of Materials Processing Technology 102. 138-142. **2000**.
- [109] L.X. Li, Y. Lou, L.B. Yang , D.S. Peng , K.P. Rao. Materials and Design 23. 451–457. **2002**.
- [110] Engineered materials reference book. (2nd Edition). ASM International. **1994**.
- [111] C.Stocker, R.Sonnleitner, G.E. Nauer, J.L.Castillo, C.Poletti, A.Afjehi-Sadat. 39. Metallographie Tagung. *In Press*. **2005**.
- [112] Takashi Taguchi, Yuji Yamauchi, Yuko Hirohata, Tomoaki Hino, Masana Nishikawa. Applied Surface Science 237. 321–325. **2004**.
- [113] SGTE Phase diagram collection. <http://web.met.kth.se>. from M. Pasjunen, unpublished work. **1989**.
- [114] P. Y. Chevalier, Termochimica Acta, 141. 217-226. **1998**.

- [115] I. Ohnum, Y. Fujita, H. Mitsui, K. Ishikawa, R. Kainuma, K. Ishida *Acta materiala*. 48 3113-3123. **2000.**
- [116] J. Cruz Fernandes, C. Anjinho, P.M. Amaral, L. G. Rosa, J. Rodriguez, D. Martinez, F. A. C. Oliveira, N. Shohoji. *Materials Chemistry and Physics*. Vol 77, Iss 3. 711-718. **2003.**
- [117] *Recrystallization and Related Annealing Phenomena*. F.J. Humphreys and M. Harherl. Ed Pergamon. **1996.**
- [118] M.H. Yoo, S.R. Agnew, J.R. Morris, K.M. Ho. *Materials Science and Engineering A*319–321 87–92. **2001.**
- [119] Prasad, Y.V.R.K.; Seshacharyulu, T. *International Materials Reviews* Volume 43, Issue 6 . 243-258. **1998.**
- [120] Y.V.R.K. Prasad and K.P. Rao. *Materials Science and Engineering A*. Vol 391, Iss 1-2. 141-150. **2005.**
- [121] N.E.W. de Reza, C.M. Libanati, *Acta Metall*. 16. 1297-1305. **1968.**
- [122] C. Poletti, W. Marketz, A. Merstallinger, T. Schubert, P. Degischer. *Materialwissenschaft und Werkstofftechnik. Reibung und Verschleiß*, 35. 741-749. **2004.**
- [123]. Joanna R. Groza, Antonios Zavaliangos. *Materials Science and Engineering A*287 . 171–177. **2000.**
- [124] V.Y. Kodash, J.R. Groza, K.C. Cho, B.R. Klotz, R.J. Dowding. *Materials Science and Engineering In Press*. **2004.**
- [125] TJ. Goodwin, S.H. Yoo, I Matteazzi, and J.R. Groza. *NanoStructured Materials*. Vol. 8. No. 5. pp. 559-566.**1991.**

# LEBENS LAUF

## ■ Personalangaben.

*Name:* Maria Cecilia POLETTI  
*Personalausweis Nr.:* 25.298.809N  
*Staatsangehörigkeit:* Argentinien.  
*Geburtsdatum:* 16. August 1976.  
*Geburtsort:* Cutral Co - Provinz Neuquén - Argentinien.  
*Eltern:* Chem. Technisch Ricardo Carlos Poletti und Frau Griselda Matilde Cazalla  
*Familienstand:* Ledig.  
*Adresse:* Burggasse 93/14. A-1070 Wien, Österreich  
*Tel Nr.:* 0043-1-  
*E-mail Adresse:* cpoletti@mail.zserv.tuwien.ac.at  
*Arbeitadresse:* Institut für Werkstoffwissenschaft und Werkstofftechnologie. TUWien. Karlsplatz 14/308. A-1040. Wien. Österreich  
*Telefonnummer.:* 0043 1 58801-30813

## ■ Ausbildung

*Grundschule:* März 1982 - Dezember 1982  
Cristo Rey Grundschule, Caseros, Provinz Buenos Aires.  
  
März 1983 - Dezember 1983  
Jean Piaget Grundschule, Neuquén, Provinz Neuquén  
  
März 1984 - Dezember 1989  
125 Grundschule, Neuquén, Provinz Neuquén  
  
*Gymnasium:* März 1990 - Dezember 1994  
C.P.E.M. N°12 Gymnasium, Neuquén, Provinz Neuquén.  
Abschluss als Absolvent der Handelsschule.  
  
*Universität:* März 1995 - November 2001  
5 Jahr Studium Chemiker-Ingenieur (Technische Chemie) an der Ingenieurwesen Fakultät, Staatliche Comahue Universität, Neuquén, Argentinien. Durchschnittnote: 8,2/10  
*Oktober 2000-April 2001*  
*Diplomarbeit:* Beitrag zur Charakterisierung von kurzfaserverstärktem Schnellarbeitstahl. Unter der Leitung von: O. Univ. Prof. Dipl. Ing. techn. H. P. Degischer In Institut für Werkstoffwissenschaft und Werkstofftechnologie, TUWien gemacht.  
Diplomandenseminar: sehr gut (1)

## ■ Sprache

*Spanisch:* Muttersprache  
*English:* sehr gut in Schrift, Lesen und in mündlicher Ausdruck.  
*Deutsch:* gut in Schrift, Lesen und mündlicher Ausdruck.  
*Portugiesisch:* gut in lesen  
*Italienisch:* gut in lesen

## ■ Arbeitstätigkeiten

*April 1998-Februar 2000*

Hilfsassistentin am Physikalische Chemie für Chemie Ingenieur Studenten. Ingenieurwesen Fakultät, Staatliche Comahue Universität, Neuquén, Argentinien.

*Februar 1999-Juli 1999*

Hilfsassistentin am Algebra und Geometrie für Ingenieurwissenschaft Studenten. Ingenieurwesen Fakultät, Staatliche Comahue Universität, Neuquén, Argentinien.

*Juni 1999-August 2000*

Teilnehmerin aus der Forschungsgruppe Neue Technologien und Moderne Werkstoffe. Prof. Dr. Dipl Ing. Julio A. Vivas Hohl. Ingenieurwesen Fakultät, Staatliche Comahue Universität, Neuquén. Argentinien.

*November 2001-Juli 2002*

Junior Engineer bei Tecfor Ingenieria GmbH, Neuquén, Argentinien. Ich war beschäftigt mit dem Studium von den Technischen und Chemischen Prozessen in der Öl und Chemischen Industrie.

*September 2002-zu der Zeit.*

Projektass. im Institut für Werkstoffwissenschaft und Werkstofftechnologie. TUWien. Doktoratstudentin. Thema des Doktorstudium: Titanlegierung und Titan Matrix Verbundwerkstoffe. Ich bin beschäftigt mit Charakterisierung der physikalische und mechanische Eigenschaften des Leichtlegierungen (hauptsächlich mit Titanlegierungen) und des Verbundwerkstoffe, auch als Labor und Seminarübung Hilfeassistentin, und in der Betreuung eines Diplomarbeit Student.

## ■ Stipendium.

*Februar 2000-März 2000.*

Forschungssommerstipendium in der Atomforschungszentrum Bariloche, Balseiro Institut. Neuquén, Argentinien.

## ■ Veröffentlichungen

- « Efecto de la adición de SrO en la sinterización de superconductores de  
M. Cecilia Poletti

YBa2Cu3O7-d ». M.C. Poletti, E.A. Oliber, J.E. Fiscina, L.F. García, J. Vivas Hohl, D.A. Esparza und C.J.R. González Oliver. Jornadas SAM 2000 - IV Coloquio Latinoamericano de Fractura y Fatiga, Agosto 2000, 1065-1072

- « Ti-Matrix Composites for Future High Performance Applications ». W. Marketz (V), C. Poletti, H.P. Degischer. Forum für Metallurgie und Werkstofftechnik. Mai 2003. Leoben. Berg- und Hüttenmännische Monatshefte (BHM), 148 (2003), 9; S. 376 - 379.
- "Hot Formability of a Particle Reinforced Ti-Alloy" C. Poletti (V), W. Marketz, H.P. Degischer. 10th World Conference on Titanium Ti-2003, July 2003. Hamburg, Germany.
- „TiC Partikel verstärkte Ti-Legierung“ (Poster). C. Poletti, W. Marketz, H.P. Degischer. Verbundwerkstoffe und Werkstoffbunde. Juli 2003. Wien, Österreich.
- "Hot Compression of Ti-alloys and Titanium Matrix Composites". (Poster). C. Poletti, W. Marketz, H.P. Degischer. Junior EuroMat 2004 Sept. 2004.- Lausanne. Switzerland.
- "Wear and Friction Coefficient of Particle Reinforced Ti-Alloys". C. Poletti (V), A. Merstallinger, Th. Schubert, W. Marketz, H.P. Degischer. DGM Reibung und Verschleiß 2004. März 2004. Fürth, Deutschland. 35 (2004), 10/11; S. 741 - 749.
- "Flow rating at high temperatures of particle reinforced Ti-alloys". M. C. Poletti (V); W. Marketz; H. P. Degischer. Verbundwerkstoffe und Werkstoffverbund. April 2005. Kassel, Deutschland.

## ■ Anders

- Teilnehmerin im 3. Argentinische Kongress für Chemie Ingenieur Studenten. Provinz Santa Fe, Argentinien. Oktober 1998. Kurs "Krümmung von Flüssen"
- Teilnehmerin im 4. Argentinische Kongress für Chemie Ingenieur Studenten. Provinz Córdoba, Argentinien. September 1999. Kurs "Toxikologie und Industriell Sicherheit"
- Studentenberater von der Fakultät. Teilnehmerin an der Forschungs- und Veröffentlichungs- Komitee. (1999)
- Teilnehmerin der Studienrates des Studenten Zentrums der Ingenieurwesen Fakultät, Staatliche Comahue Universität, Neuquén. (1998-2000)
- Assistent der Gruppe für Edition und Design der Zeitschrift des Studenten Zentrums der Ingenieurwesen Fakultät, Staatliche Comahue Universität, Neuquén. (1999-2000).
- Teilnehmerin in der „Titan und Titanlegierung“ Tagung, im DLR, Köln, Deutschland. März 2003. Vorsitz: Dr. Ing. Manfred Peters, Direktor des Materialwissenschaftsinstitut in DLR, Köln.
- Teilnehmerin in der „Fundamentals of Titanium“ Tagung organisiert bei TIMATEC in der „Light Alloys Exhibition“ in Brescia, Italien. April 2004
- Sport: Volleyball und Schwimmen